ENS DE LYON

THÈSE
en vue de l'obtention du grade de Docteur, délivré par
l'ÉCOLE NORMALE SUPERIEURE DE LYON

École Doctorale N° 52
PHAST - Physique et Astrophysique

Discipline : Physique

Soutenue publiquement le 17/09/2026, par :

Louis SADDIER

Bistable dynamics of the ocean circulation in Antarctic ice-shelf cavities

---

Dynamique bistable de la circulation océanique sous les plateformes de glace antarctiques

Devant le jury composé de :

REESE, Ronja	Professeure Northumbria University	Rapporteure
LAPEYRE, Guillaume	Directeur de recherche ENS - PSL / CNRS	Rapporteur
CHILLÀ, Francesca	Professeure des universités ENS de Lyon	Examinatrice
LE BARS, Michael	Directeur de recherche Aix Marseille Université / CNRS	Examinateur
HERBERT, Corentin	Chargé de recherche HDR ENS de Lyon / CNRS	Directeur de thèse
COUSTON, Louis-Alexandre	Maître de conférences HDR Université Claude Bernard Lyon 1	Co-directeur de thèse

Laboratoire de Physique UMR 5672
École normale supérieure de Lyon
46, Allée d'Italie,
69364 Lyon cedex 07

École Doctorale Physique et
Astrophysique EDPHAST 52
Université de Lyon
92, rue Pasteur, CS 30122,
69361 Lyon cedex 07

Remerciements

Ces trois années passées à l'ENS de Lyon achèvent finalement mon parcours scolaire. C'est donc l'occasion pour moi de remercier les personnes qui m'ont aidées et soutenues lors de ce travail de thèse, mais aussi plus largement mon entourage.

Je remercie tout d'abord mes rapporteurs Ronja Reese et Guillaume Lapeyre pour la relecture attentive de ce manuscrit, ainsi que mes examinateurs Michael Le Bars et Francesca Chillà. J'ai pris plaisir à vous présenter mon travail et j'ai beaucoup apprécié les discussions que nous avons eu ensemble et qui ont apporté d'intéressantes ouvertures.

Ensuite, je remercie mes directeurs de thèse Louis Couston et Corentin Herbert pour la confiance qu'ils m'ont accordée pendant ces trois années. À vos côtés, j'ai énormément appris, tant sur le plan scientifique que sur le plan humain. Louis, grâce à ton organisation sans faille, ton sens du détail mais aussi tes nombreux conseils pour présenter et valoriser mes travaux. Ils m'ont permis de gagner confiance en moi au cours de cette thèse. Corentin, grâce à ton sens de l'écoute et ton pragmatisme dans ta manière d'aborder des problèmes scientifiques. Je retiens également nos nombreuses discussions qui grâce à ton intérêt pour une multitude de sujets m'ont beaucoup appris. Je voudrais finalement vous remercier pour votre enthousiasme et votre encadrement exemplaire qui m'ont permis d'aborder cette thèse joyeusement et sereinement.

I would also like to thank Chris Bull for his patience while I was learning to use the NEMO ocean model. Your involvement in my PhD project was invaluable, as none of the numerical simulations carried out during this work would have been possible without your help and advice. I was also very touched by your regular follow-ups despite the distance, and I have very good memories of my stay in Newcastle!

Ensuite de manière un peu plus pragmatique, je remercie l'ENS Paris-Saclay pour le financement de ma thèse ainsi que le Laboratoire de Physique de l'ENS de Lyon pour son accueil. En particulier, mon travail dans le laboratoire a été beaucoup facilité par ses gestionnaires Fatiha, Erika, Nadine, Laurence et Christelle, ainsi que par les membres du service informatique Denis et Hervé. Je remercie également le mésocentre de calcul du CBPsmn pour la mise à disposition de ses ressources qui ont permis la réalisation de mes simulations numériques, ainsi que Cerasela pour son aide précieuse dans l'utilisation de la plateforme. Au laboratoire, j'ai également rencontré de nombreux chercheurs avec qui j'ai eu plaisir à interagir : Antoine, Fanny, Irena, Guillaume, Rémi, Jason, Chinthaka, Yingpu, Nicolas, Éric et Laurent. Merci à Gaël et Romain de vous être assurés du bon déroulement de ma thèse, ainsi qu'à Sylvain, Tommaso et Julien de m'avoir permis d'enseigner à vos côtés.

Si j'ai beaucoup apprécié le cursus de thèse, c'est aussi grâces aux nombreux doctorants qui m'ont entouré quotidiennement et qui animent la vie du laboratoire. Merci à Bastien, François, Francis, Antoine, Gauthier pour les babyfoots même si tu n'étais pas très bon, Valeria, Alessandro, Sebastian, Elian, Nicolas, Kassandra et Romane pour les « petit badminton ? », Brice, François, Samuel, Antonin, Matthieu, Julie, Corentin, Wandrille, aux potos Antoine et Johan, Jette, Guillaume, Maud... Merci à Brivaël, Tim et Clément pour le roadtrip mémorable à l'EGU et en Italie, on reparle quand vous voulez du Frazil Ice Project. Merci aussi aux membres de la réunion TOPIC-BG : Julie, le flambeau est bien passé à August !

Avec un peu de recul, mon goût pour la physique s'est aussi développé grâce à des enseignants qui ont réussi à me captiver par leurs cours. Je suis particulièrement reconnaissant envers Jean-Philippe Garayt, Natacha Van Hauwaert, Jean-Philippe Oury et Christophe Texier.

Lors de ces années passées à Lyon, j'ai pu vivre avec de nombreux colocataires. Merci à toutes et à tous de m'avoir supporté, mais aussi d'avoir largement contribué à mon épanouissement et à faire de ces années lyonnaises de si bons souvenirs. Un merci tout particulier à Orlane, Camille, Laurène, Clément et Karla !

Merci à mes acolytes « lyonnais » Valentin, Laurent, Elena, Mélanie, Baptiste, Simon, Diane, Pierre et Maike de me sortir de chez moi de temps en temps pour profiter de la vie, à mes acolytes « parisiens » Théophile, Florian, Romain, Paul, Tristan et Léo que je retrouve très vite ! Et à mes acolytes « triestini » Hiromi et Fede pour l'aventure italienne.

Je vais maintenant m'attaquer aux vieux copains avec qui j'évolue depuis un petit bout de temps et qui commencent à bien me connaître. Je vais essayer de ne pas trop en faire mais quand même un peu si jamais il vous prend l'envie de télécharger ma thèse. Merci à Thomas, Zib, Lilian et Élise (temps record de 10h de bus pour venir me voir soutenir), Tato (temps record de 17 ans d'amitié à ce jour !), Fabus (multi-récipiendaire de médailles de bronze), Théo, Ewan, Eliot, Léa, Soso, Lulu, Meurianne, Elo bhl, Julio, Youyou, Kik, les Flos. Et comme dirait Théo, c'est vraiment super lourd d'être votre pote.

Merci Claire pour tout le soutien que tu m'as apporté cette année et pour tout le positif que tu ramènes où que tu ailles. Et puis aussi merci de m'avoir fait découvrir le concept des fermes-auberges dans les Vosges.

Enfin, je voudrais remercier ma famille. Mes cousins, cousines, oncle et tantes à qui je tente souvent d'expliquer avec plus ou moins de succès mon travail de recherche. Mes grands-parents à qui je dédie cette thèse, j'ai toujours été ébahi par tout ce que vous savez et par tout ce que vous nous avez transmis. Ma nièce Lou qui vient juste d'arriver. Je remercie bien sûr mes parents qui me choient toujours autant. M'apprendre ce qu'était une parabole alors que je m'amusais à lancer des cailloux a peut-être contribué à la naissance d'une vocation. Enfin, je remercie ma sœur, pour l'exemple que tu m'as toujours montré, et mon frère, pour les heures passées ensemble à chercher cette épée en bois enterrée au fond du jardin.

Contents

1 Introduction **1**
- 1.1 Uncertainties in a changing climate . . . 1
- 1.2 The Antarctic cryosphere and Southern Ocean environment . . . 5
  - 1.2.1 The Antarctic Ice Sheet mass budget . . . 5
  - 1.2.2 The Southern Ocean . . . 7
- 1.3 Tipping points and bistability . . . 13
  - 1.3.1 Tipping points in the climate system . . . 13
  - 1.3.2 Tipping points and bistability . . . 15
  - 1.3.3 Tipping points in Antarctic ice-shelf cavities . . . 17
- 1.4 A hierarchy of climate models . . . 18
  - 1.4.1 From the microscale physics to the global Earth dynamics . . . 18
  - 1.4.2 The compromise between realism and understanding . . . 19
  - 1.4.3 Theory development across the climate models hierarchy . . . 20
- 1.5 Outline . . . 22

2 Bistable dynamics of ice-shelf cavities in a low-dimensional box model **25**
- 2.1 Introduction . . . 25
- 2.2 Presentation of the model . . . 27
  - 2.2.1 Low-dimensional model setup . . . 27
  - 2.2.2 Equilibrium states and hysteresis . . . 31
- 2.3 Application to Antarctic ice-shelf cavities . . . 32
  - 2.3.1 Data . . . 32
  - 2.3.2 Bistability for a broad range of forcing parameters . . . 35
  - 2.3.3 Bistability for a broad range of parameterization choices . . . 37
  - 2.3.4 Dense Shelf Water outflow . . . 40
  - 2.3.5 Discussion . . . 42
- 2.4 Analytical and graphical solutions . . . 45
  - 2.4.1 Simplified model equations . . . 45
  - 2.4.2 Equilibrium states and stability . . . 47
  - 2.4.3 Graphical solutions . . . 48
  - 2.4.4 Asymptotic analytical results . . . 54
  - 2.4.5 From irreversibility to reversibility: cusp bifurcation . . . 55
- 2.5 Conclusion . . . 59

3 Bistable dynamics of ice-shelf cavities in an idealized numerical ocean model **69**
- 3.1 Introduction . . . 69

3.2 Methods . . . 70
3.2.1 Model description . . . 70
3.2.2 Spatial domain and forcing . . . 71
3.3 Results . . . 73
3.3.1 Two modes of circulation . . . 73
3.3.2 Hysteresis experiments . . . 77
3.3.3 Scaling laws . . . 80
3.4 From irreversible to reversible regime transitions . . . 87
3.4.1 Impact of salt stratification . . . 87
3.4.2 Impact of the large scale circulation: from no-slip to free-slip lateral boundaries . . . 89
3.4.3 Impact of subgrid-scale dissipation: changing the horizontal viscosity 91
3.5 Discussion and conclusion . . . 93

4 Numerical sensitivity of vertical motion and basal melting 99
4.1 Introduction . . . 99
4.2 Numerical schemes: truncation error and stability . . . 100
4.3 Vertical motion and horizontal viscosity . . . 101
4.3.1 Grid-scale noise . . . 101
4.3.2 Horizontal viscosity . . . 105
4.4 Vertical resolution and topographic Rossby waves . . . 110
4.4.1 Impact of the spatial resolution on the basal mass loss . . . 111
4.4.2 Topographic Rossby waves . . . 113

5 The response of an ice-shelf cavity to time-dependent forcing 121
5.1 Introduction . . . 121
5.2 Response of an ice-shelf cavity to various forcing timescales . . . 123
5.2.1 Insights from low-dimensional models . . . 123
5.2.2 Response to transient surface forcing with NEMO simulations . . . 128
5.3 Seasonal and interannual polynya variability . . . 134
5.3.1 Impact of the seasonal cycle on ice-shelf cavity transitions . . . 135
5.3.2 Interannual stochastic winter surface forcing . . . 137
5.4 Conclusion . . . 143

Conclusion 147

Bibliography 151

Chapter 1

Introduction

1.1 Uncertainties in a changing climate

Human activities have profoundly altered the Earth's climate system since the beginning of the industrial era. Over the past century, observations have revealed an unequivocal increase in global mean surface temperature, accompanied by widespread changes in the atmosphere, the ocean, the cryosphere, and the biosphere [Eyring et al., 2021]. This long-term warming is primarily driven by the increase in atmospheric greenhouse gas concentrations, particularly carbon dioxide, resulting from the massive extraction and combustion of fossil fuels (coal, oil, gas). The underlying physical mechanism is well understood: greenhouse gases absorb part of the infrared radiation emitted by the Earth's surface and re-emit it both toward space and back toward the surface, as illustrated in Fig. 1.1(a). This anthropogenic enhancement of the greenhouse effect has created a persistent radiative imbalance of approximately 1 $W.m^{-2}$, causing the Earth system to accumulate heat [von Schuckmann et al., 2023]. As shown in Fig. 1.1(b), more than 90% of this excess heat is absorbed by the ocean owing to its large heat capacity, while the remainder warms the atmosphere and continents or contributes to the melting of the cryosphere.

The Earth's energy budget is not uniformly distributed across latitudes. While the tropics receive a surplus of solar energy, the polar regions experience a net energy deficit. This meridional energy gradient drives the large-scale circulation of both the atmosphere and the ocean. Consequently, perturbations to the Earth's energy budget can lead to substantial reorganizations of these circulations [Marino et al., 2026], affecting all components of the climate system. As a result, climate change not only increases global temperatures (Fig. 1.2(a)) but also alters many other aspects of the Earth system, including precipitation patterns [Trenberth, 2011], the frequency and intensity of extreme heat waves [Mora et al., 2017], the rapid decline of Arctic sea ice (Fig. 1.2(b)), and the acidification of the oceans through the enhanced uptake of atmospheric carbon dioxide (Fig. 1.2(c)). Among these impacts, global mean sea-level rise stands out as one of the most significant long-term societal challenges because of its persistence over millennia and its consequences for coastal populations (Fig. 1.2(d,e)).

Although the existence of anthropogenic climate change is unequivocal, projecting its future evolution remains challenging because climate projections are affected by several

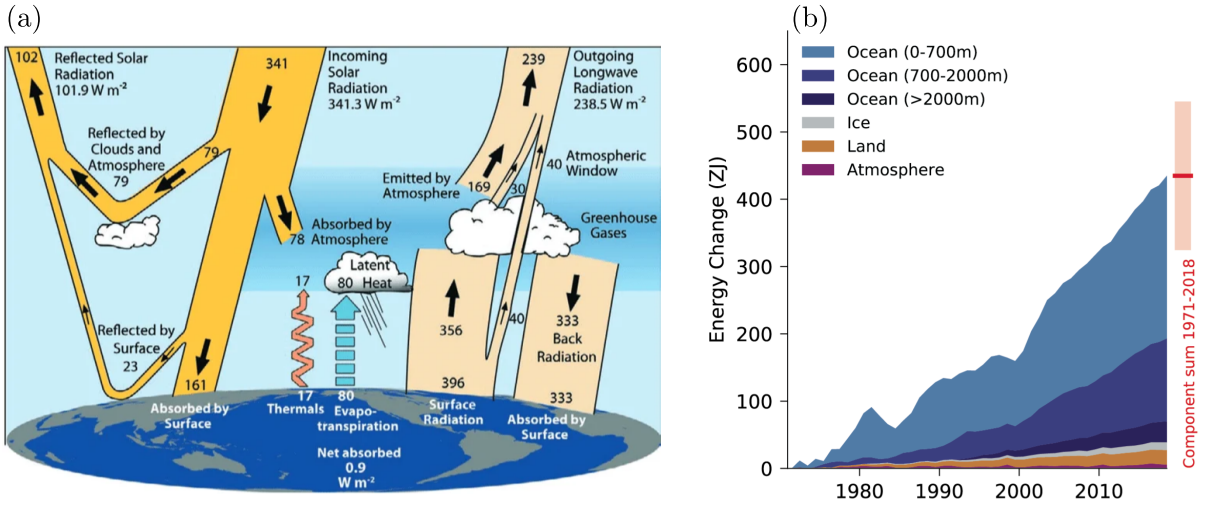

Figure 1.1: (a) Summary sketch of the Earth's radiative budget from [Trenberth et al., 2009]. (b) Distribution of the energy excess among the different climate components. Figure from the AR6 IPCC report [Fox-Kemper et al., 2021].

sources of uncertainty. These uncertainties arise from three main factors whose relative importance evolves depending on projection timescales (Fig. 1.3). Up to a few decades, uncertainty is dominated by the internal variability of the climate system (orange). Chaotic fluctuations associated with atmospheric and oceanic circulation can temporarily amplify or mask the long-term warming trend, limiting the predictability of the climate evolution. At intermediate timescales, uncertainties associated with climate models become increasingly important (blue). They reflect our incomplete understanding and imperfect representation of physical processes governing the climate system. Finally, on longer timescales, uncertainties associated with future greenhouse-gas emissions become dominant (green). Since future emissions depend on societal, economic and political choices, climate projections are usually expressed using several Shared Socioeconomic Pathway (SSP) scenarios representing different possible futures (see the colored box at the end of this section for more details).

Sea-level rise (SLR) is also subject to the combination of these different sources of uncertainty. While the contribution from the thermal expansion of the ocean is comparatively well constrained, the uncertainty associated with climate models mainly arises from the future evolution of the Greenland and Antarctic ice sheets. Together, these ice sheets contain enough ice to raise global mean sea level by approximately 7 m and 60 m, respectively, if completely melted. Although such changes would occur over millennial timescales, even partial destabilization could substantially increase sea-level rise over the coming centuries (Fig. 1.2(d,e)). Reducing these uncertainties requires a better understanding of the physical mechanisms governing ice-sheet evolution. Among these, interactions between the ocean and Antarctic ice shelves have emerged as a major source of uncertainty. They exert a strong control on the stability of the grounded ice sheet and may trigger self-perpetuating feedbacks capable of accelerating ice loss, potentially leading to tipping points. The remainder of this introduction is therefore organized as follows. We first introduce the Antarctic cryosphere and the Southern Ocean, with a particular focus on the physical processes controlling Antarctic ice-sheet evolution. We then present

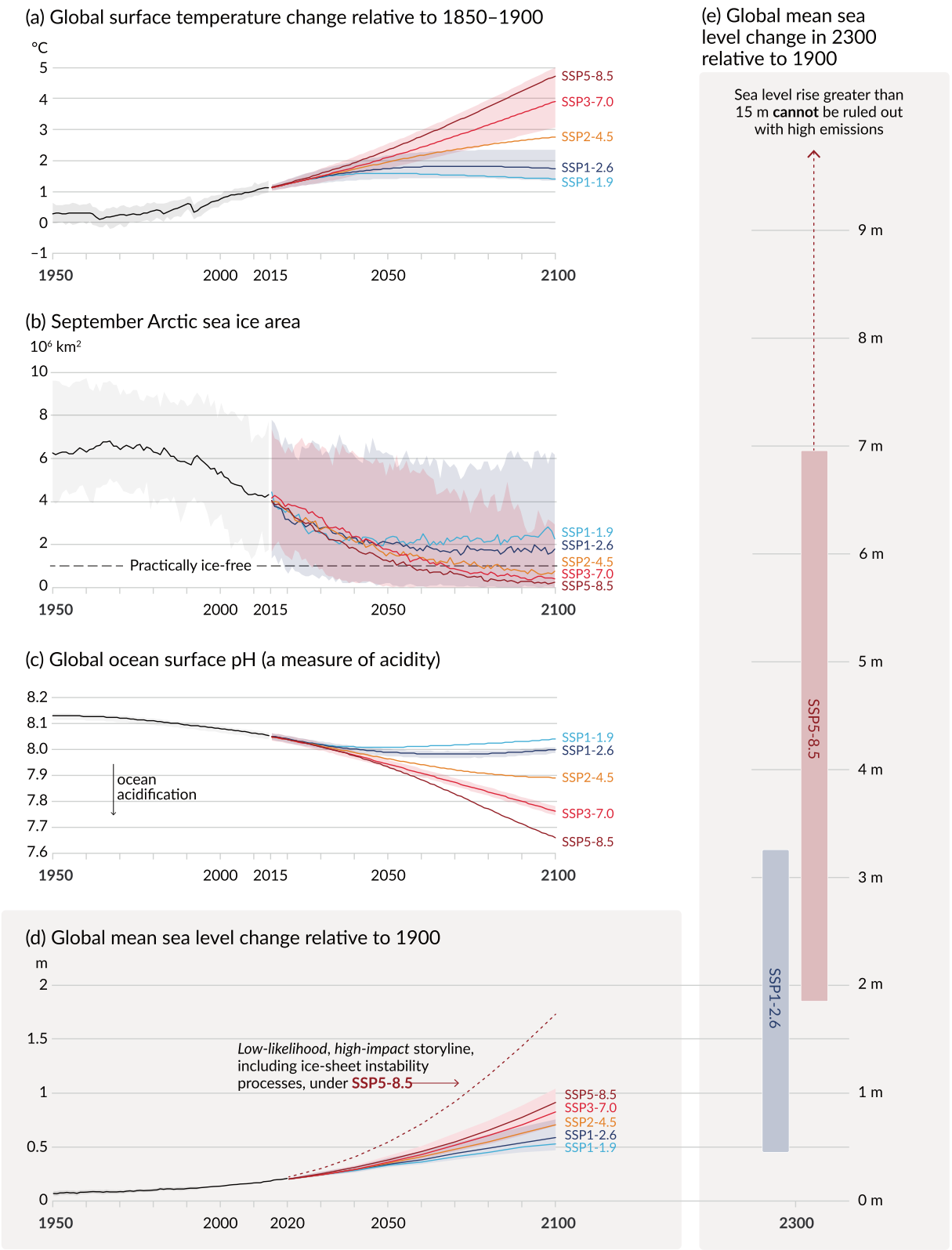

Figure 1.2: IPCC projections of the impacts of global warming on various components of the climate system: (a) global surface temperature, (b) summer Arctic sea-ice extent, (c) ocean acidification, and (d) and (e) global mean sea-level rise by 2100 and 2300, respectively. Figures from the AR6 IPCC report [Masson-Delmotte et al., 2021].

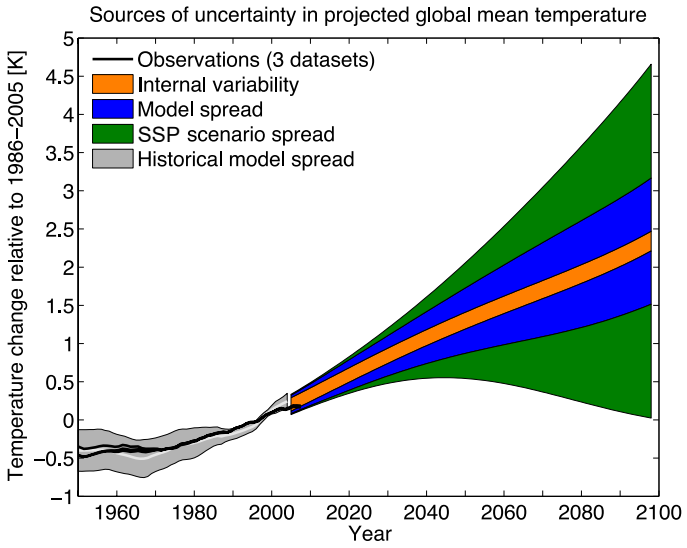

Figure 1.3: Projection of global mean surface temperatures. Observations and historical model spread are represented until 2005 in black and gray, respectively. Then, from 2005, the orange shading represents the uncertainty caused by internal variability within an intermediate SSP scenario, and within a single climate model. The blue shading represents the uncertainty among several climate models within the same intermediate SSP scenario. Finally, the green shading represents the uncertainty among all SSP scenarios considered by the IPCC. Figure from the AR5 IPCC report [Kirtman et al., 2014].

the concept of climate tipping points before discussing the hierarchy of climate models used in climate science, emphasizing the importance of idealized models for developing a mechanistic understanding of climate system processes.

What are the IPCC and the SSP scenarios ?

The **IPCC** (Intergovernmental Panel on Climate Change, also known as GIEC in French) is the United Nations body responsible for assessing climate change science. It brings together international scientists to produce transparent assessment reports that synthesize the existing scientific literature on climate change, its impacts, and possible adaptation and mitigation strategies.

The **SSP scenarios** (for Shared Socioeconomic Pathways) are used as assumptions of IPCC projections on how human society, economy, and politics might evolve. They are indexed from 1 to 5. SSP1 being an ideal "sustainability" scenario in which the world cooperates to tackle the climate crisis, and SSP5 being the worst "growth at all costs" scenario in which the use of fossil resources are strongly privileged regardless of their environmental impact and of alternative sources of energy. In between, SSP2 to SSP4 are the more plausible scenarios testing business as usual policies (2), weaker international cooperation (3), and the increase of socioeconomic inequalities (4). The SSP scenarios are associated with a power imbalance number ranging from 1.9 to 8.5 representing the net radiative energy flux imbalance [$W.m^{-2}$] expected by the year 2100.

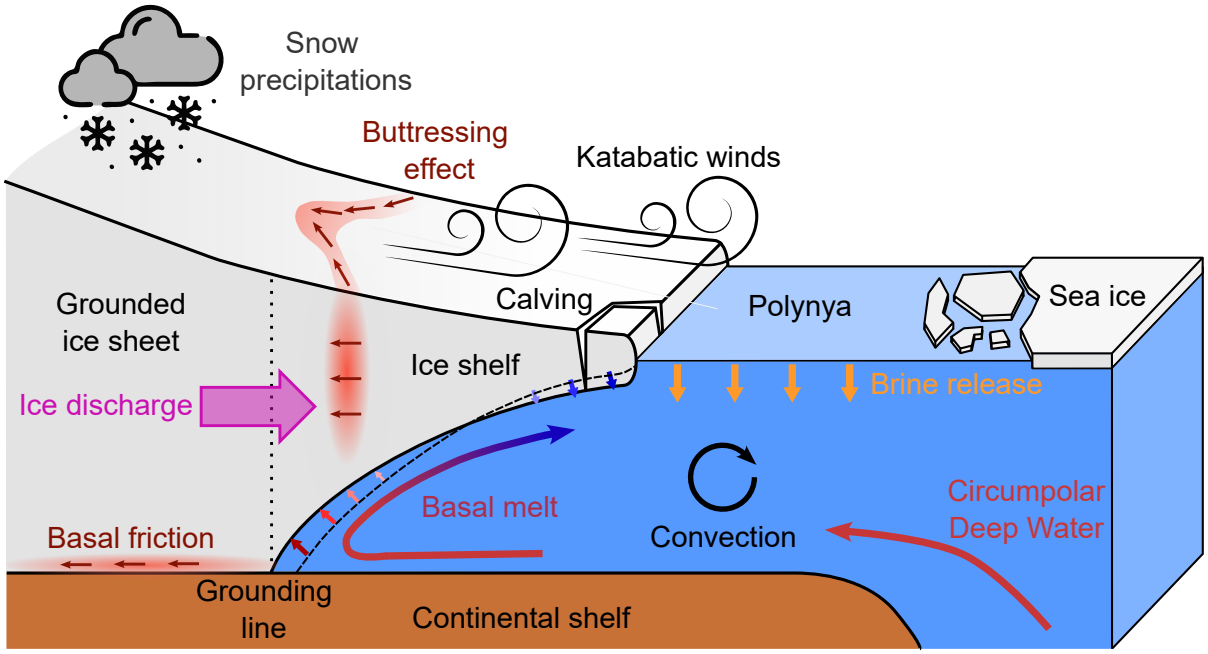

Figure 1.4: Sketch representing the various physical processes involved at the interface of the ice sheet, the ice shelf, the atmosphere, and the ocean. Note the presence of some processes not discussed in the main text, such as calving (producing icebergs), which represents half of the ice-shelf mass loss but does not contribute directly to the AIS mass budget if the calved ice already crossed the grounding line.

1.2 The Antarctic cryosphere and Southern Ocean environment

In the previous section, we described how anthropogenic climate change is altering the Earth's climate system, with particularly pronounced impacts in polar regions. We also highlighted the large uncertainties that remain regarding the future evolution of the AIS and the associated implications for SLR. The present section introduces the mass budget of the AIS and the physical characteristics of the Southern Ocean. Particular attention is given to ice-shelf cavities, where interactions between the ocean and the cryosphere control basal melting and strongly influence the Antarctic contribution to future SLR.

1.2.1 The Antarctic Ice Sheet mass budget

The mass budget of the AIS only accounts for the ice that is grounded on the continental shelf (Fig. 1.4). Indeed, only grounded ice contributes directly to SLR once it is discharged to the ocean. Ice shelves, the floating extensions of the ice sheet, are already displacing seawater and therefore do not directly affect sea level when they melt or calve. On the one hand, the mass gain of the AIS is primarily provided by snowfall. Over time, successive snow layers accumulate and undergo compaction, forming firn and eventually glacial ice. On the other hand, the mass loss of the ice sheet arises from several processes. The dominant contribution is the discharge of ice across the grounding line, where grounded ice transitions to floating ice and enters the ocean [Fowler and Ng, 2020]. A smaller

contribution comes from surface ablation processes, including sublimation and surface meltwater runoff. Surface melting remains limited over most of Antarctica because of the cold atmospheric conditions, but it can become significant in warmer regions such as the Antarctic Peninsula [Trusel et al., 2015]. Although ice shelves are not directly included in the AIS mass budget, they exert a strong control on the rate at which grounded ice is discharged into the ocean. The ocean temperatures are generally above the freezing point of seawater beneath the ice shelves and lead to basal melting. Basal melting influences the dynamics of the AIS through several mechanisms. Firstly, enhanced melting near the grounding line induces its retreat. As the grounding line migrates inland, ice that was previously grounded is now floating and is no longer part of the grounded ice-sheet mass budget. Secondly, ice shelves provide a resistive mechanical force opposed to the glacier flow through a process known as buttressing [Gudmundsson et al., 2019]. The lateral confinement of ice shelves within embayments, together with local contacts with topographic pinning points, generates resistive stresses that oppose the seaward flow of ice. The thinning of the ice shelves because of basal melting weakens their buttressing capacity, leading to an acceleration of grounded ice flow [Bett et al., 2026].

Key cryospheric glossary

The **Antarctic Ice Sheet (AIS)** is the grounded part of the ice mass that covers the Antarctic continent.

Ice shelves are the floating extensions of the AIS. They should not be confused with the **continental shelf** which is the submerged portion of the Antarctic continent, nor with the **sea ice** which is frozen seawater. While ice-shelf thickness can reach several hundreds meters, sea-ice thickness is often limited from 1 to 10 meters.

The **grounding line** marks the delineation between the grounded AIS and the floating ice shelves. When ice flows through the grounding line, it contributes to sea-level rise: this is the phenomenon of **ice discharge**.

Because one third of the AIS is grounded below sea level, it may be vulnerable to dynamical instabilities that can lead to rapid grounding-line retreat. One of the most important is the Marine Ice Sheet Instability (MISI), which occurs when the ice sheet is grounded on a retrograde bed slope, i.e., a bed that deepens inland [Weertman, 1974, Schoof, 2007]. In such a configuration, the grounding line retreats into deeper water. As a result, the ice thickness at the grounding line increases and allows a greater ice discharge into the ocean. The resulting increase in ice flux removes mass from the upstream ice sheet, leading to further ice-sheet thinning and grounding-line retreat. This positive feedback results in a self-sustained retreat of the ice sheet until a prograde bed slope is reached. Retrograde bed slopes are common beneath several sectors of West Antarctica, making these regions particularly susceptible to MISI [Rosier et al., 2021, Favier et al., 2014]. The buttressing effect reduces ice discharge across the grounding line and therefore counteracts the MISI. Future intrusions of warm ocean waters into ice-shelf cavities may substantially enhance basal melting, leading to ice-shelf thinning and a weakening of their buttressing capacity. Whether such ocean-driven changes are sufficient to initiate or amplify MISI remains highly uncertain and constitutes a large source of uncertainty in

projections of the AIS mass loss. The dashed curve in Fig. 1.2(d) illustrates that sea-level projection increase and showcase larger uncertainty when including the contribution of such dynamical instabilities [Robel et al., 2019].

1.2.2 The Southern Ocean

We now turn to the main characteristics of the Southern Ocean. Because basal mass loss from Antarctic ice shelves is largely controlled by ocean-ice interactions, understanding the circulation of the Southern Ocean and the pathways of the various water masses reaching ice-shelf cavities is essential for understanding the present and future evolution of the AIS mass budget.

The Antarctic Circumpolar Current

The Southern Ocean is the oceanic region that surrounds Antarctica. Its northern boundary is commonly defined by the 60°S parallel for administrative purposes. From an oceanographic perspective, a more physically grounded boundary is the Antarctic Polar Front [Sallée et al., 2008], represented by the thick black line on Fig. 1.5. It is the zone of convergence between cold Antarctic waters and warmer mid-latitude waters, and is characterized by a strong meridional temperature gradient. The Southern Ocean is the only oceanic region on Earth that is uninterrupted by continents in the zonal direction. As a consequence, the large scale westerly winds at these latitudes can continuously transfer momentum to the ocean, generating a strong circumpolar circulation. This circulation, known as the Antarctic Circumpolar Current (ACC), is the strongest ocean current on Earth. Its transport is estimated to be approximately 173 Sv [Donohue et al., 2016] ($1\,\mathrm{Sv} = 10^6\,\mathrm{m^3 s^{-1}}$). For comparison, the total global river runoff into the oceans is about 1.2 Sv. As emphasized by Fig. 1.5, the ACC is the central component of the global ocean circulation, linking the Atlantic, Indian, and Pacific Oceans. The ACC is also a region of upwelling, where deep waters originating from the mid-latitude oceans rise toward the surface [Bennetts et al., 2024] (light purple arrows transforming into green arrows in Fig. 1.5). These waters are referred as Circumpolar Deep Waters (CDW). They play a central role in the present thesis because these relatively warm ($\approx 1 - 2\,^\circ\mathrm{C}$) and saline waters induce high basal melt rate when they intrude ice-shelf cavities.

Sea ice and polynyas

One of the characteristics of the Southern Ocean is its sea-ice cover, whose extent varies seasonally. Sea ice forms when atmospheric conditions are sufficiently cold for seawater to freeze at the ocean surface. Sea ice influences the ocean through both mechanical and thermodynamic processes. Mechanically, it transmits atmospheric momentum to the ocean and thereby affects ocean circulation. Thermodynamically, it modifies the properties of the underlying water masses through the exchange of freshwater. When sea ice forms, freshwater is removed from the ocean surface. As a result, the salt contained in seawater becomes concentrated, increasing the salinity and density of surface waters. This process is commonly referred to as brine rejection. Conversely, when sea ice melts, freshwater is released into the ocean, reducing surface salinity and stabilizing the water column. As sea ice is transported by winds and ocean currents, it redistributes freshwater

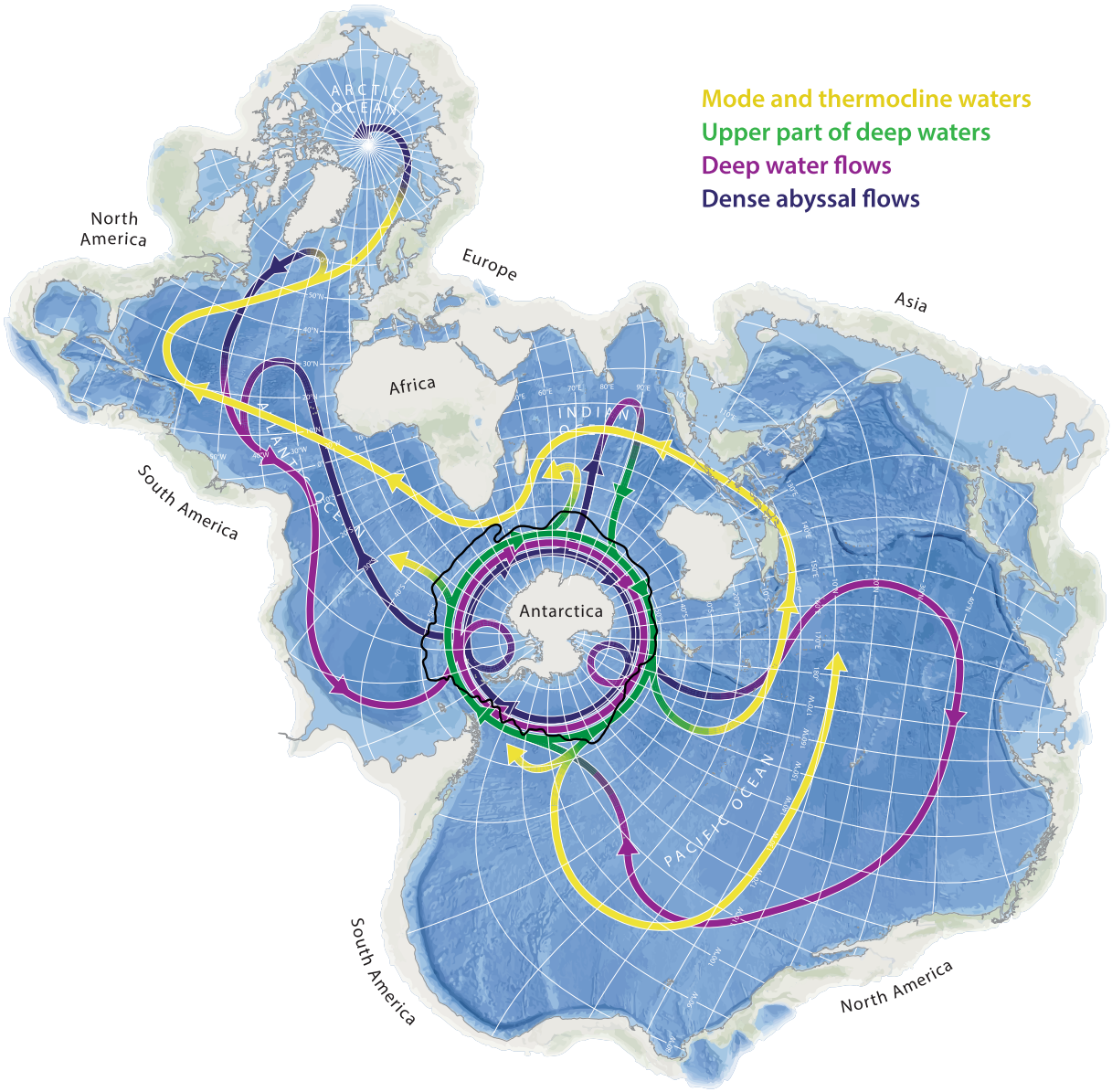

Figure 1.5: Spilhaus cartographic projection of Earth. This representation allows focusing on the ocean rather than the continents. From this point of view, it is clear that the Southern Ocean is the central component of the global ocean circulation. Idealized (and non-exhaustive) pathways of the ocean circulation are represented from yellow colors for surface currents to dark purple colors for the deepest currents. The thick black line represents the Antarctic Polar Front. Figure from [Meredith, 2022].

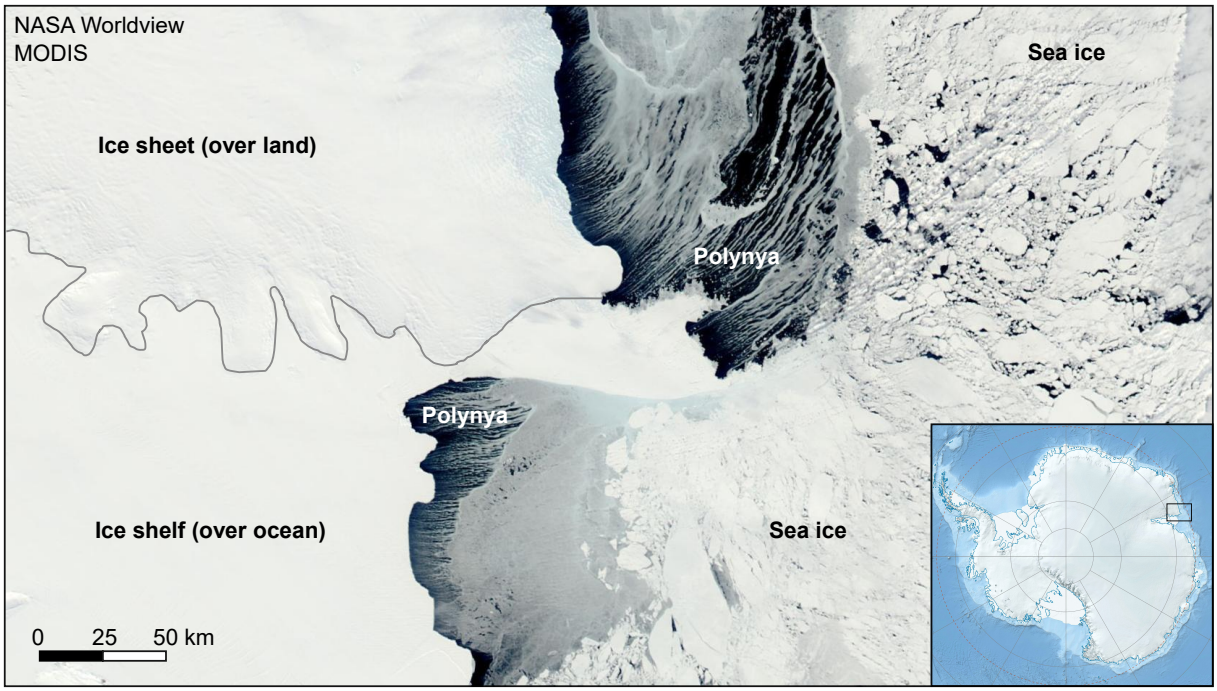

Figure 1.6: Photography from the satellite MODIS of the western part of the Amery ice-shelf front. The grounded ice sheet and the floating ice shelf are delineated by the light gray line. This photography represents the opening of coastal polynyas during a katabatic winds event pushing sea ice offshore. White streaks are indicative of the wind direction, and result from the aggregation of newly formed frazil ice in Langmuir circulation cells. Source: NASA Worldview (`https://worldview.earthdata.nasa.gov/`).

and salt across the Southern Ocean, influencing its density stratification and water-mass formation [Bennetts et al., 2024].

Regions of particular interest in the Southern Ocean are the polynyas, which are areas of open waters surrounded by sea ice. They allow direct exchanges between the ocean and the atmosphere as these regions are not insulated by a sea-ice layer. They are rich ecosystems as photosynthetic organisms can develop and sustain marine life [Golledge et al., 2025]. Polynyas can be categorized depending on their location and formation mechanisms. Coastal polynyas are located at the front of ice shelves or along the Antarctic coastline. They are distinguished from offshore polynyas that are located away from the coast. Two formation mechanisms are usually discussed. On the one hand, sensible heat polynyas open when warm waters upwell and melt the sea ice. They remain open as long as the ocean brings sufficient sensible heat at the sea surface to prevent ice freezing from the atmosphere. One example of this type of polynya is the Weddell Polynya, an offshore polynya that opens intermittently in the Weddell Sea [Naughten et al., 2019]. Its formation mechanisms remain an active area of research, although seabed topography, wind, and deep vertical mixing are thought to play an important role in facilitating the upward transport of oceanic heat [Gülk et al., 2024, Narayanan et al., 2024]. On the other hand, latent heat polynyas open through the mechanical action of the wind or due to the divergence of sea-ice motions, which is sometimes observed near topographic barriers. In the case of coastal polynyas, gravity-driven katabatic winds blow from the continent to the sea, pushing sea ice away from the ice-shelf front and opening coastal

latent heat polynyas [Thompson et al., 2020, Ushio and Wakatsuchi, 1993]. As the sea-ice is pushed away, the cold polar atmosphere freezes the ocean surface which is not anymore insulated by sea ice. This newly formed ice takes the form of microscopic to millimetric ice crystals, also known as frazil ice, that in turn are also advected by the katabatic winds. These areas are therefore regions of intense brine release into the ocean and large latent heat fluxes to the atmosphere, owing to the continuous formation of sea ice [Noel et al., 2025]. Note that in the following and until the end of this manuscript, the language abuse "coastal polynya" will be used to refer to "coastal latent heat polynya" as they will be the main focus of this thesis, despite the existence of coastal sensible heat polynyas. Fig. 1.4 sketches the interplay between katabatic winds, coastal polynyas, and sea ice. A more realistic representation is provided by a photography from the satellite MODIS in Fig. 1.6 that represents the western part of the Amery ice-shelf front and Prydz Bay. This photography was taken during a strong katabatic wind event, with sea ice pushed away from the coastline. Coastal polynyas are clearly visible as they appear as dark regions adjacent to the coastline. The elongated white streaks observed within these polynyas are indicative of frazil ice formation and wind direction. These streaks result from the aggregation of frazil ice crystals within Langmuir circulation cells, driven by the nonlinear interaction between wind-induced surface currents and surface waves [Herman et al., 2020].

Deep convection and Dense Shelf Water formation

The two polynya formation mechanisms described above have very different consequences on water-mass transformation. While the sensible heat polynyas are characterized by ice melting and surface freshwater releases, the latent heat polynyas are characterized by ice freezing and surface brine rejections. In the latter case, the brine release densifies the ocean surface, such that enough sea-ice production in these very localized zones can trigger deep convection events; the water column undergoes upward and downward vertical motions to tend back to a stable density stratification [Ohshima et al., 2022, Kusahara et al., 2010]. The dense and saline water masses formed within polynyas are referred to as Dense Shelf Water (DSW) as they are created on the Antarctic continental shelf. Deep convection and DSW formation under coastal polynyas have major global impacts. First, large volumes of DSW can spread over and out of the continental shelf, and further sink into the abyss entraining surrounding waters to form Antarctic Bottom Waters (AABW) [Schmidt et al., 2023] (see Fig. 1.7(a)). Primary production zones for DSW around Antarctica are shown in Fig. 1.7(b) and include the Weddell Sea, the Ross Sea, the Adélie Coast, and Prydz Bay. DSW formation is an essential component of the global overturning circulation depicted in Fig. 1.5 and of AABW production [Rintoul et al., 2026]. Indeed, there are in fact few regions on Earth where dense water formation occur. Other regions on Earth featuring dense water formation lie in the North-Atlantic region, and are connected to the Atlantic Meridional Overturning Circulation (AMOC). A corollary of this process is the ventilation of the global deep ocean. DSW formed in coastal polynyas originate from surface waters that have recently exchanged oxygen with the atmosphere. As these waters sink and fill the abyssal ocean, they supply oxygen to deep waters, with important consequences for marine ecosystems on a global scale [Rintoul et al., 2026]. The second major impact of DSW formation is that it can prevent CDW from intruding onto the continental shelf and into ice-shelf cavities. By replacing relatively warm CDW with cold

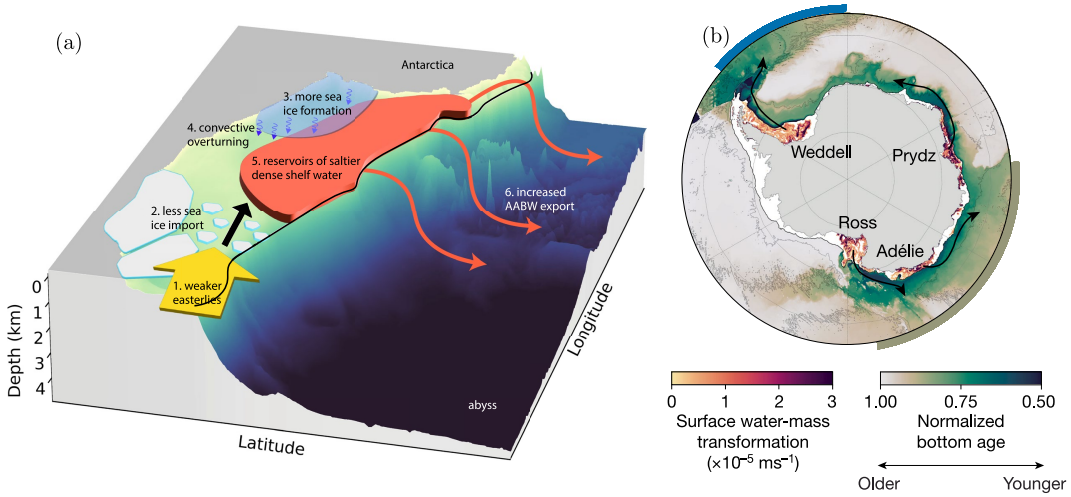

Figure 1.7: (a) Sketch representing the formation of DSW in coastal polynyas, which transforms into AABW when leaving the continental shelf. In this figure, the impact of easterly winds on AABW export is emphasized. Figure from [Schmidt et al., 2023]. (b) Ocean-sea-ice numerical simulation (ACCESS-OM2-01, 1/10° resolution) [Moorman et al., 2020]. The yellow to purple color map shows the surface water-mass transformation, which is the DSW formation volume flux by unit surface. Black arrows show the DSW pathways out of the continental shelf which are linked to AABW formation. The normalized bottom age of the abyssal regions (gray to green colors) represents the last time abyssal waters were at the surface of the ocean. Green patches therefore represent the pathways of newly formed AABW. Figure from [Abram et al., 2025].

DSW, whose temperature is close to the seawater freezing point (≈ -2, °C), basal melt rates are strongly reduced, thereby limiting mass loss from the AIS.

Modes of circulation within ice-shelf cavities

Fig. 1.8 summarizes the different circulation regimes that can develop within ice-shelf cavities depending on the water masses occupying them. Three circulation modes are commonly distinguished [Silvano et al., 2016]. We first discuss Mode 2, as it is associated with CDW, which were first introduced in this thesis. In Mode 2, relatively warm CDW that has upwelled south of the ACC crosses the continental shelf. When entering the ice-shelf cavity, CDW comes into contact with the ice shelf and induces high basal melt rates. The resulting meltwater is fresher and therefore more buoyant than the surrounding waters. It rises along the slope of the ice shelf, forming an ascending meltwater plume [Hewitt, 2020, Lazeroms et al., 2018]. This plume drives an overturning circulation within the cavity. This circulation constitutes a positive feedback mechanism: enhanced basal melting strengthens the buoyancy forcing associated with the meltwater plume, which in turn intensifies the overturning circulation and increases the transport of oceanic heat toward the ice shelf. As a result, basal melting can be further enhanced [Jourdain et al., 2017]. This circulation is particularly important because direct exchanges between the open ocean and the cavity are often limited by the ice-shelf front thickness. The ice front acts as a topographic barrier that restricts barotropic (i.e., depth-independent) flows [Grosfeld et al., 1997], making buoyancy-driven overturning a key mechanism for transporting

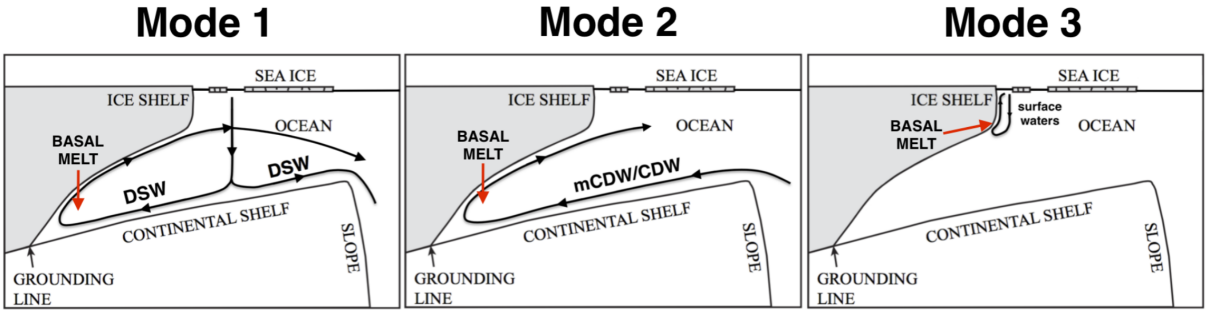

Figure 1.8: The three main circulations modes identified in Antarctic ice-shelf cavities. Mode 1 is supplied by deep DSW intrusion and results in low basal melt rates. Mode 2 is supplied by deep CDW intrusion and results in high basal melt rates. Mode 3 is supplied by Antarctic surface water and is responsible for basal melt rates enhanced close to the front of the ice shelf. Figure from [Silvano et al., 2016].

heat into the cavity. The description of the meltwater plume and the study of the ice-ocean interface are active fields of research because of their major impacts on ice-shelf mass losses [Rosevear et al., 2024, Hewitt, 2020]. Indeed, their description often relies on parameterizations of the turbulent entrainment and melting that does not necessary succeed in capturing the various regimes observed at small scales in the ice-ocean boundary layer. In particular, the combined effects of temperature and salinity on seawater density strongly influence the stratification and turbulent mixing of the ice-ocean boundary layer. These processes control the transport of heat toward the ice and therefore the rate at which melting occurs [Collin et al., 2026, Couston, 2024].

In Mode 1 (see Fig. 1.8), deep waters enter the cavity and similarly drive an overturning circulation beneath the ice shelf. However, the circulation strongly differs from that of Mode 2 because of the very different properties of the intruding waters. While Mode 2 is characterized by the intrusion of relatively warm CDW, Mode 1 involves the inflow of DSW, which is formed on the continental shelf through sea-ice production and brine rejection. As a result, the thermal driving, defined as the difference between the ocean temperature and the local freezing temperature at the ice-ocean interface, is much smaller in Mode 1 ($\approx 0.3\,^{\circ}\mathrm{C}$) than in Mode 2 ($\approx 3\,^{\circ}\mathrm{C}$). In Mode 1, the ascending meltwater plume may even become supercooled as it rises along the basal slope of the ice shelf. This occurs because the local freezing temperature decreases with increasing pressure and therefore increases as the plume ascends toward shallower depths. Under these conditions, ice crystals can form and accrete beneath the ice shelf [Kulessa et al., 2014].

Finally, Mode 3 involves the intrusion of Antarctic Surface Water (AASW) beneath the ice-shelf front. In this case, relatively light surface waters sink below the ice-shelf draft near the front of the cavity and can induce basal melting in this region. Several mechanisms may promote these intrusions, including wind-driven Ekman transport [Zhou et al., 2014], eddies [Årthun et al., 2013], and tides [Silvano et al., 2016]. Although the penetration depth of AASW is generally limited compared to that of CDW or DSW, this melting regime can be significant in cavities already experiencing a Mode 1 circulation. During summer, solar heating can substantially warm the ocean surface, increasing the thermal driving of intruding AASW. In large ice shelves such as Ross ice shelf, these seasonal intrusions have been shown to account for a large fraction of the total basal

melt, despite being largely confined to the shallower portion of the cavity [Stewart et al., 2019].

Key oceanographic glossary

The **Antarctic Circumpolar Current (ACC)** is the strong clockwise oceanic current forced by westerly winds that surrounds the Antarctic continent.

Circumpolar Deep Waters (CDW) are warm ($\approx 1-2\,°C$) and saline waters that upwell south of the ACC. If intruding the continental shelf and reaching ice-shelf cavities, they induce high basal melt rates.

Polynyas are areas of open waters surrounded by sea ice. They are opened by the action of the wind (latent heat polynyas), or by the intake of heat by the underneath ocean (sensible heat polynya). We can find them along the coast or offshore.

Dense Shelf Waters (DSW) are cold ($\approx -2\,°C$) and saline waters formed at the surface of coastal polynyas. If reaching the seafloor, they can push CDW away toward the shelf break and replace them in ice-shelf cavities, resulting in low basal melt rates.

Antarctic Bottom Waters (AABW) are dense waters initiated by the sinking of DSW and flushed out of the continental shelf. They represent 36% of the global ocean volume and are a key component of the global overturning circulation. The double "A" of the acronym differentiates AABW from Arctic Bottom Water (ABW).

1.3 Tipping points and bistability

1.3.1 Tipping points in the climate system

When introducing the AIS mass budget, we discussed the Marine Ice Sheet Instability (MISI), a mechanism that may trigger a self-sustained retreat of the grounding line in West Antarctica. Because this retreat can continue even after the initial forcing has ceased, WAIS is often regarded as a climate tipping element. In this context, a tipping point corresponds to a level of global warming beyond which a climate threshold is crossed. Current estimates place the West AIS collapse warming threshold between approximately 1.5 °C and 3.0 °C above pre-industrial temperatures [Armstrong McKay et al., 2022]. Climate tipping points are generally characterized by three properties: abruptness, irreversibility, and self perpetuation once initiated [Armstrong McKay et al., 2022]. Abruptness refers to the relatively short timescale of the transition. For the collapse of the West AIS, the transition is estimated to occur over timescales ranging from about 500 years to 13 kyr [Feldmann and Levermann, 2015, Armstrong McKay et al., 2022], which is rapid compared with the roughly 100 kyr periodicity of the last glacial cycles. The irreversibility of this retreat has been demonstrated in numerical simulations showing that once the ice sheet has retreated beyond a critical point, lowering global temperatures or reducing basal melting is insufficient to restore its initial state [Rosier et al., 2021, Garbe et al., 2020]. Finally, the self-sustained nature of the retreat arises from the positive feedback associated with MISI on retrograde bed slopes in West Antarctica [Schoof, 2007, Weertman, 1974].

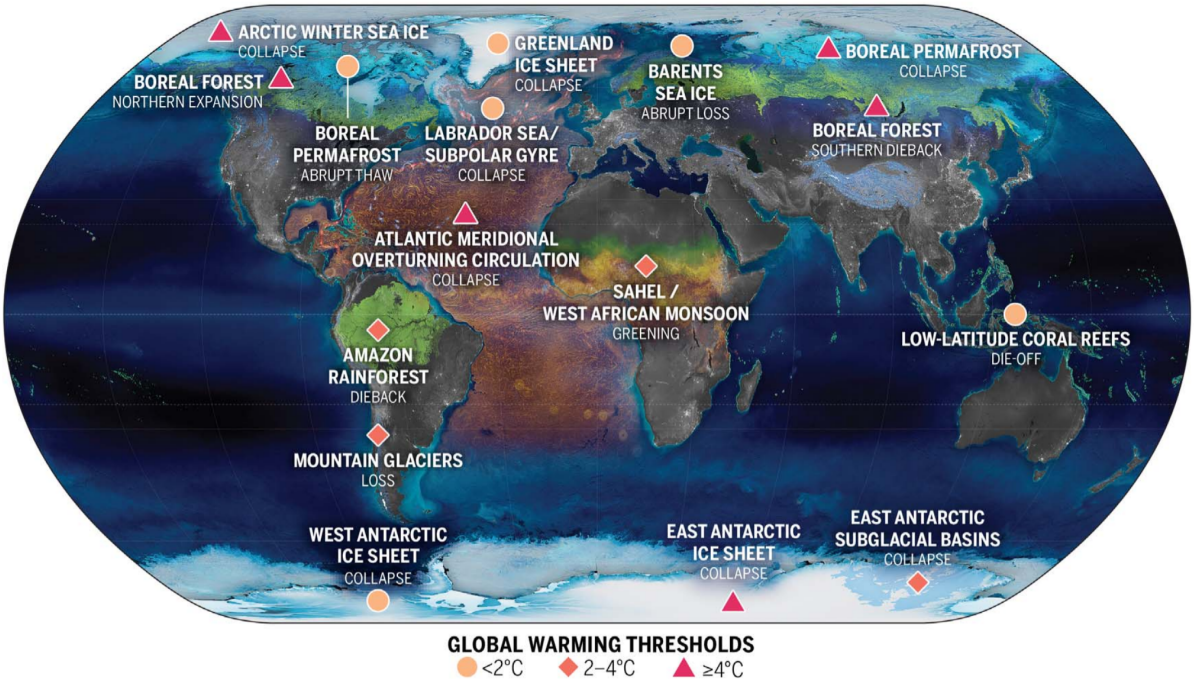

Figure 1.9: Location of the climate tipping points identified by [Armstrong McKay et al., 2022]. Circles, squares and triangles indicate the global temperature increase threshold beyond which a tipping point is triggered. Figure from [Armstrong McKay et al., 2022].

MISI and the collapse of the West AIS are not the only examples of climate tipping points. Several other tipping elements have been identified within the cryosphere, the biosphere, the ocean, and the atmosphere [Lenton et al., 2008] (see Fig. 1.9). Another prominent example is the Amazon rainforest. Deforestation and climate change reduce forest cover and weaken the recycling of atmospheric moisture by vegetation. As less moisture is returned to the atmosphere through evapotranspiration, precipitation decreases over the interior of the basin, spurring additional forest loss. This positive feedback may drive an abrupt transition toward a much drier ecosystem, with profound consequences for biodiversity and the global carbon cycle [Zemp et al., 2017]. As a last example of major climate tipping element, we now turn our attention to the Atlantic Meridional Overturning Circulation (AMOC). One key component of the AMOC is the formation of dense waters in the North Atlantic promoted by surface cooling. An increased freshwater input from melting ice sheets reduces surface salinity, weakens deep-water formation, and slows the overturning circulation. This weakening further decreases the northward transport of salty waters, leading to additional freshening of the North Atlantic and reinforcing the initial perturbation [Stommel, 1961]. This positive feedback gives rise to two possible stable circulation states and may trigger an abrupt transition to a much weaker AMOC if a critical freshwater forcing is exceeded [Rahmstorf, 2024].

A colloquium at the Institut Henri Poincaré was dedicated in October 2023 to gather the French scientific community to discuss the scientific challenges linked to these climate tipping points. A summary report that I contributed to was produced by PhD student and postdoctoral researchers to summarize the contributions and discussions that took place during this week [Beylat et al., 2024].

1.3.2 Tipping points and bistability

Climate tipping points are often interpreted using the framework of bistable dynamical systems. Such systems are commonly represented by a double-well potential, featuring two local minima corresponding to stable equilibrium states. These minima are separated by an unstable equilibrium (the separatrix), which divides the basins of attraction of the two stable states. Within this framework, three main classes of tipping can be distinguished. Firstly, a bifurcation-induced tipping occurs when changes in the external forcing progressively modify the potential landscape until one of the stable equilibria disappears, forcing the system to transition to the alternative state. Secondly, a noise-induced tipping results from internal variability or stochastic perturbations that drive the system across the separatrix despite the persistence of two stable equilibria. Finally, a rate-induced tipping can occur when environmental conditions change so rapidly that the system is unable to track its evolving initial attractor. A transition is then initiated if the system remains in the attraction basin of the other attractor. As in the noise-induced case, no bifurcation has occurred since the two equilibria have remained stable during the transition.

These three types of tipping are represented in Fig. 1.10. The top panel represents the stable equilibrium states (black solid line) of a climate variable x as well as its separatrix (black dashed line), as a function of an environmental parameter μ. For the bifurcation-induced tipping (in red), the trajectories of the system are shown when μ is increasing and decreasing. They are not following the same path as the critical thresholds to go from one regime to another have different values. The increasing and decreasing trajectories thus form a hysteresis curve. The red system trajectories do not exactly follow the black steady-state equilibria, illustrating that the finite rate of change of μ prevents the system from instantaneously adapting to its equilibrium state. As a result, the transition occurs slightly beyond the critical thresholds. The five panels in the middle represent the energy landscape associated to various values of μ. As μ approaches a critical value, one of the potential wells becomes progressively shallower. At the critical μ value, the curvature of the potential at this point vanishes, corresponding to a saddle-node bifurcation. Beyond this bifurcation, the associated stable equilibrium no longer exists, and the system evolves toward the remaining stable state. On the bottom row, we show the other two tipping categories. In contrast with the bifurcation-induced tipping, these two tipping are not triggered by a stability change of one of the fixed points. In the case of noise-induced tipping (in green), the transition rate $k_{1\to2}$ depends both on the barrier energy ΔV that has to be crossed and the amplitude of the noise (exemplified with the Arrhenius law with thermodynamic notations in Fig. 1.10, where k_B is the Boltzmann constant, and T is the system temperature). Finally, for the case of the rate-induced tipping (in blue), the double well potential is shifted towards higher x values. This shift occurs over a time τ_{env}. If the response time of the system τ_{sys} is fast enough, the system will simply track the potential minimum it was already in. However, for $\tau_{\text{sys}} \gg \tau_{\text{env}}$, the system does not have the time to adapt to the fast shift of the potential and ends up in the basin of attraction of the other stable state.

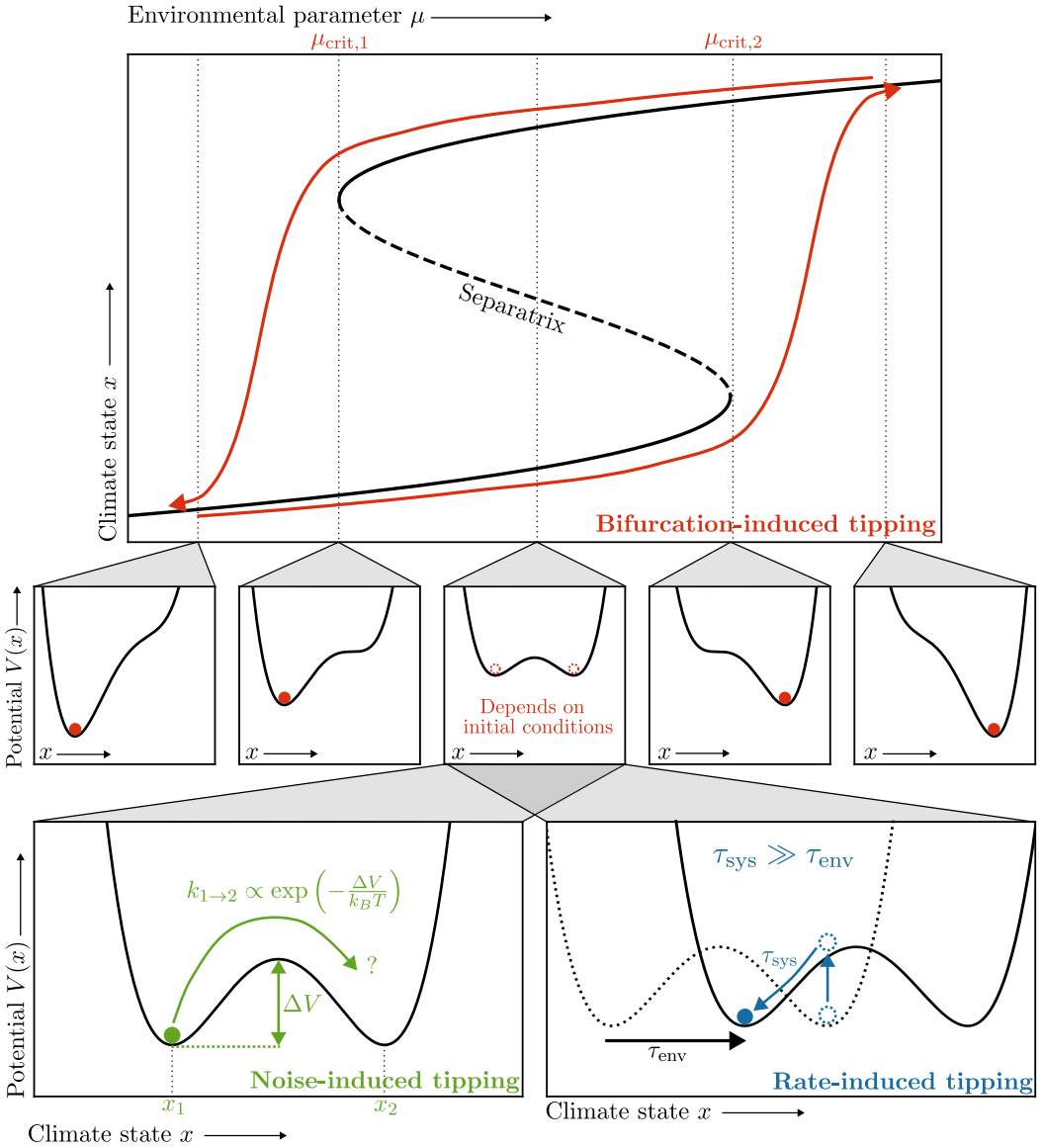

Figure 1.10: Graphical representations of tipping within a bistable system. The state of the system $x(t)$ follows the canonical time dynamics $\mathrm{d}x = -V'(x)\mathrm{d}t + \sqrt{2k_BT}\mathrm{d}W_t$, where $V(x) = \frac{1}{4}x^4 - \frac{1}{2}x^2 - \mu x$, W_t is the Wiener process, and k_BT is the associated strength of the noise. The top panel represents the fixed points of the system (solid for stable, and dashed for unstable) as a function of the parameter μ. Saddle-node bifurcations occur at $\mu_{\text{crit},1}$ and $\mu_{\text{crit},2}$. Bifurcation-induced tipping are represented in red. The other panels represent the energy landscape $V(x)$ for various μ values (middle row), and exemplify noise-induced (green) and rate-induced (blue) tipping.

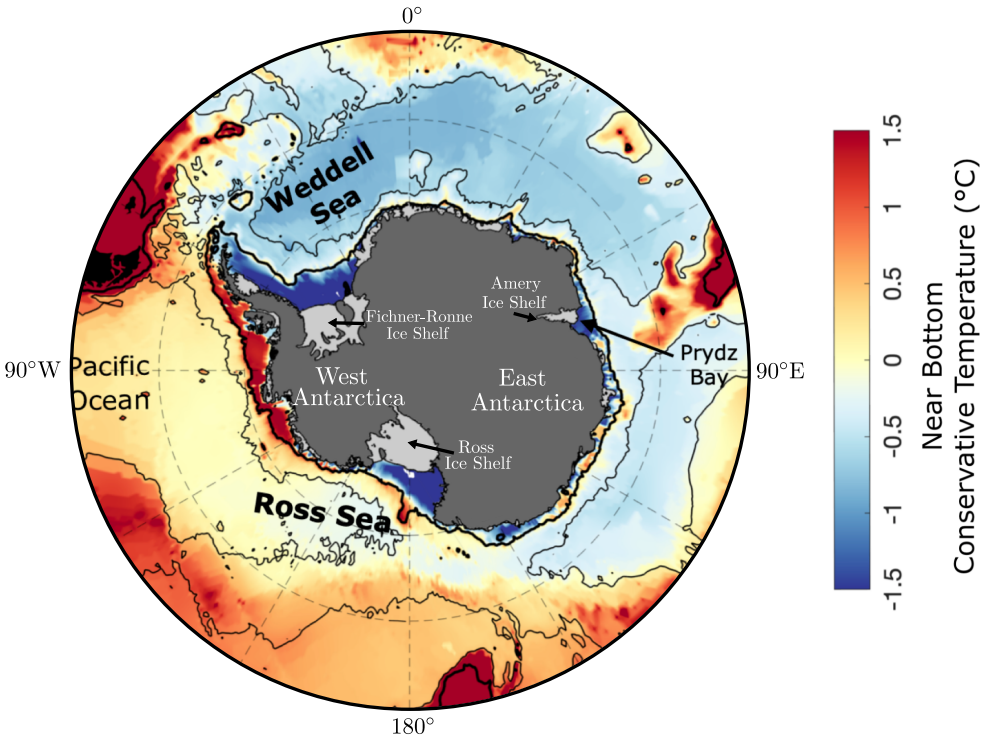

Figure 1.11: Conservative temperatures near the bottom of the water column around Antarctica. The AIS is represented in dark gray whereas the ice shelves are represented in light gray. The thick black solid line represents the 1000 m isobath hence is indicative of the continental shelf break, and the thin black solid line represents the 4000 m isobath. Figure adapted from [Silvano et al., 2023].

1.3.3 Tipping points in Antarctic ice-shelf cavities

We have shown that Antarctic ice-shelf cavities can present two markedly different circulation regimes (discarding Mode 3, whose impact is highly localized). Cavities supplied with DSW experience weak basal melting (Mode 1), whereas cavities invaded by CDW undergo much stronger melting (Mode 2). These two regimes differ not only in their melt rates but also in the structure of the circulation within the cavity. This naturally raises the question of whether Antarctic ice-shelf cavities may themselves undergo tipping dynamics, which constitutes the core question addressed by this thesis. More specifically, can a cavity abruptly and irreversibly transition from a cold DSW-dominated state to a warm CDW-dominated state? Such a transition would substantially enhance basal melting and could trigger a tipping cascade by promoting ice-sheet instabilities such as MISI.

Currently, East Antarctic ice shelves remain relatively stable and filled with DSW while those in West Antarctica are filled with CDW and account for most of the observed mass loss [Paolo et al., 2015,Galton-Fenzi et al., 2025]. These regional contrasts are largely controlled by the properties of water masses intruding the continental shelf [Thompson et al., 2018] and differences in surface buoyancy fluxes at the front of the Antarctic ice shelves [Silvano et al., 2016], as illustrated by Fig. 1.11.

Evidence of possible cold-to-warm transitions in ice-shelf cavities has been put forth for past climates [Suganuma et al., 2025] and regional studies suggest that such transitions may occur under future climate forcing for the Filchner-Ronne [Hellmer et al., 2012,

Hellmer et al., 2017, Hazel and Stewart, 2020, Daae et al., 2020, Naughten et al., 2021, Haid et al., 2023, Hoffman et al., 2024, Song et al., 2025] and Amery ice shelves [Jin et al., 2025, Haid et al., 2023], and within most Antarctic ice-shelf cavities under the SSP5-8.5 scenario [Mathiot and Jourdain, 2023, Mathiot et al., 2026].

The main positive feedback that could drive and sustain such a transition has been identified as the release of meltwater beneath the ice shelf [Hellmer et al., 2017, Hazel and Stewart, 2020, Moorman et al., 2023]. When CDW intrudes into an ice-shelf cavity, the resulting high basal melting produces large amounts of buoyant freshwater. This meltwater rises along the basal slope of the ice shelf and ends at the sea surface at the ice-shelf front, where it strengthens the stratification of the water column. Consequently, DSW produced by sea-ice formation in coastal polynyas is less able to convect to the seafloor and replenish the cavity. The reduction in DSW formation favors further intrusions of warm CDW, reinforcing the initial perturbation and making the warm circulation regime self-sustaining. Conversely, when the cavity is filled with DSW, basal melt rates remain weak and only limited amounts of meltwater are released. The surface layer is therefore less stratified, allowing buoyancy losses in coastal polynyas to maintain deep convection and sustain DSW formation. This, in turn, promotes the persistence of the cold circulation regime.

The high computational cost and complexity of forcing schemes in realistic configurations restrict systematic investigation of the steady response of an ice-shelf cavity to incremental variations of external conditions. As a result, a quantitative understanding of the physical mechanisms and positive feedback driving these transitions and their thresholds is lacking. Specifically, only a limited number of studies have examined the reversibility of these regime transitions. Past works exploring the reversibility of ocean circulations have focused on the Amundsen Sea [Caillet et al., 2023], the Filchner-Ronne ice shelf [Hazel and Stewart, 2020, Haid et al., 2023, Reese et al., 2026, Naughten et al., 2026, Hellmer et al., 2017], the Ross ice shelf [Naughten et al., 2026], and pan-Antarctic configurations [Mathiot et al., 2026], but with diverging conclusions. Although some studies found irreversible dynamics [Hellmer et al., 2017, Naughten et al., 2026, Hazel and Stewart, 2020] or hints of hysteresis behaviors [Haid et al., 2023] for the case of the Filchner-Ronne ice-shelf cavity, others reported reversible transitions [Mathiot et al., 2026, Reese et al., 2026]. Quantifying the reversibility of cold-to-warm transitions is yet critical for assessing their potential short and long terms impacts, particularly in scenarios where the external forcing may weaken or reverse, or simply exhibits temporal variability. The conflicting conclusions reached by previous studies highlight the difficulty of characterizing the nonlinear dynamics of Antarctic ice-shelf cavities using realistic numerical models alone. As a result, complementary modelling approaches are needed to increase our understanding of physical mechanisms governing these regime transitions and their dynamical properties.

1.4 A hierarchy of climate models

1.4.1 From the microscale physics to the global Earth dynamics

Climate dynamics involve processes spanning a large range of spatial scales, from the micrometer scale of viscous dissipation to the Earth's circumference (4×10^4 km). As a

result, the climate system possesses a very large number of degrees of freedom that cannot be fully resolved within a single numerical model. Instead, different modeling approaches have been developed to represent various range of spatial scales.

At the smallest scales, Direct Numerical Simulations (DNS) solve the Navier-Stokes equations without introducing turbulence parameterizations. Because all turbulent motions down to the Kolmogorov scale must be explicitly resolved, DNS are computationally limited to domains of only a few meters. They are therefore mainly used to investigate localized processes, such as turbulent boundary layers [Couston, 2024] or few convective plumes [Sohail et al., 2020]. Large Eddy Simulations (LES) overcome this limitation by explicitly resolving only the largest turbulent motions while representing the effects of unresolved eddies through subgrid-scale closures. By removing the need to resolve the Kolmogorov scale, LES can be applied to domains ranging from hundreds of meters to tens of kilometers. In the context of convection, they allow for example the study of the self-aggregation of convective plumes in the atmosphere [Bretherton and Blossey, 2017]. At the planetary scale, General Circulation Models (GCMs) provide a practical description of the climate system. Their horizontal resolution typically ranges from one to several tens of kilometres, allowing simulations of the global atmosphere and ocean. Achieving such large computational domains requires additional approximations in the governing equations. For example, ocean GCMs often assume the hydrostatic balance, which neglects vertical accelerations in the vertical momentum equation. This approximation is generally justified because the depth of the ocean is much smaller than its horizontal extent (aspect ratio $\sim 10^{-3}$) and because the ocean is strongly stratified. However, it breaks down in regions of deep convection where the aspect ratio of convective patterns get closer to one and where the ocean is weakly stratified. Since convective plumes cannot be explicitly resolved, their effects on the vertical transport of heat and salt must be represented through convective parameterizations [Giordani et al., 2020, Legay et al., 2025]. The highest level of complexity is reached by Earth System Models (ESMs), which couple GCMs describing the atmosphere and the ocean with other models tackling the other climate components (e.g., sea ice, ice sheet, land surface). These components continuously exchange physical quantities such as momentum, heat, freshwater, or carbon. By explicitly representing these interactions, ESMs provide the most comprehensive framework currently available for simulating the response of the Earth system to anthropogenic forcing and projecting future climate change.

1.4.2 The compromise between realism and understanding

Although ESMs provide the most realistic representation of the climate system, their complexity also constitutes one of their main limitations. Because they are built upon numerous physical parameterizations and empirical parameters, their simulations inevitably exhibit biases. Quantifying and reducing these biases is therefore an active area of research. In particular, Model Intercomparison Projects (MIPs) compare the behavior of multiple ESMs under standardized experimental protocols. In the context of ice-ocean interactions in Antarctic ice shelves, several generations of MIPs with increasing level of realism have emerged to compare ice-sheet-ocean coupled models within regional configurations [Hunter, 2006, Asay-Davis et al., 2016, Yung et al., 2026, De Rydt et al., 2024].

Beyond model uncertainty, the complexity and computational cost of ESMs make them

poorly suited for the investigation of specific climate processes. A central idea to overcome this issue is often to accept that greater realism does not necessarily imply greater understanding [Held, 2005, Dijkstra, 2013]. Thus, simpler models deliberately lower their level of realism in order to isolate or get a better control of the fundamental processes they aim to study. This is the case of Earth System Models of Intermediate Complexity (EMICs). These models typically employ simplified geometries, reduced spatial resolution, or idealized couplings between climate components, resulting in lower computational costs than ESMs. The lower complexity of these models does not mean that they are less suited to investigate complex scientific questions. On contrary, their efficiency allows large ensembles and millennial-scale simulations to be performed, making it for example possible to investigate statistical climate properties that would be prohibitively expensive with ESMs (see e.g., [Mascolo et al., 2025] for the statistical characterization of extreme heatwaves over France). A complementary approach consists in using GCMs in idealized configurations. By simplifying the forcing, geometry, or boundary conditions, these models make it possible to isolate the response of the climate system to a single physical process while retaining much of the underlying dynamics. They also provide a convenient framework for systematically assessing the impact of different physical parameterizations.

At the simplest end of the climate models hierarchy are low-dimensional models, which can be integrated in a few seconds on modern computers. Although they neglect much of the complexity of the climate system, they have repeatedly provided fundamental insights into its dynamics. For example, the one-dimensional atmospheric model of Manabe and Wetherald [Manabe and Wetherald, 1967] predicted the warming of the troposphere and cooling of the stratosphere associated with increasing atmospheric CO_2 concentrations. Stommel's box model [Stommel, 1961] raised the question of the existence of multiple stable ocean circulation states, while Lorenz's model revealed the chaotic nature of atmospheric dynamics [Lorenz, 1963]. Low-dimensional models still remain widely used because they provide a powerful framework for identifying the feedback mechanisms and nonlinear interactions governing climate variability.

More recently, machine-learning approaches have emerged as powerful complements to traditional climate models. They are increasingly used to emulate computationally expensive model components, improve parameterizations, and extract information from the growing volume of available data. Although they have often been criticized for their limited interpretability, recent advances in physics-informed machine learning begin to address this limitation by incorporating prior physical knowledge such as conservation laws into their learning process, therefore improving the physical consistency of these models [Kashinath et al., 2021].

1.4.3 Theory development across the climate models hierarchy

Having introduced the different categories of climate models, a natural question arises: which type of model is most appropriate for investigating a given climate process? The answer depends primarily on the scientific question being addressed [Dijkstra, 2013]. The development of the modern theory of the Atlantic Meridional Overturning Circulation (AMOC) provides an illustrative example of how models of various degrees of complexity are used in a complementary way.

The possibility that the ocean circulation could exhibit multiple stable states was first

proposed by Stommel with the use of a simple box model [Stommel, 1961]. At the time, the scarcity of ocean observations prevented a direct investigation of the large-scale circulation. Instead, Stommel developed a conceptual model to explore how differences in surface heat and freshwater forcing between low and high latitudes could shape the global overturning circulation. Subsequent conceptual studies extended this framework to investigate the dynamical consequences of ocean bistability. For example, Welander examined the possibility of self-sustained oscillations [Welander, 1982], whereas Cessi investigated noise-induced transitions [Cessi, 1994]. These studies shared the same objective of improving the fundamental understanding of the dynamics associated with multiple circulation equilibria. Once the existence of multiple equilibria had been established in conceptual models, the next challenge was to understand their spatial structure and required moving beyond zero-dimensional box models. In this context, [Cessi and Young, 1992] developed a two-dimensional numerical model in the meridional–depth plane, capable of representing the spatial structure of two bistable states. The robustness of AMOC bistability was subsequently assessed through an intermediate-complexity model intercomparison [Rahmstorf et al., 2005]. These results progressively established a consensus that the AMOC may indeed possess multiple stable states. Consequently, more realistic models were used to address increasingly quantitative questions. For example, recent studies used high-resolution GCMs to characterize the properties of the collapsed AMOC state [van Westen et al., 2025], and recent ESMs investigated the impacts on the European climate of such collapse [van Westen and Baatsen, 2025].

The progression outlined above suggests a gradual increase in model complexity accompanying the development of AMOC theory. In reality, this evolution has been far less linear. The growing concern over a potential AMOC collapse during the twenty-first century and the need for ocean observations motivated the deployment of extensive observing systems across the North Atlantic, providing an unprecedented view of the circulation. These observations challenged several aspects of the existing theoretical framework. They revealed that the AMOC exhibits substantially larger intrinsic variability than previously simulated by climate models. They also highlighted a stronger influence of wind forcing in the eastern Atlantic and different long-term trends from those simulated by GCMs [Srokosz and Bryden, 2015]. These discrepancies between observations and models have reinforced the importance of exploiting the entire hierarchy of climate models. Conceptual models have been revised to incorporate processes identified in observations and realistic simulations, such as the influence of wind-driven forcing on the overturning circulation [Cimatoribus et al., 2014]. Conversely, missing processes have been identified in high complexity models, such as the coupling of ocean GCMs with dynamic ice-sheet models to accurately represent Greenland freshwater discharge [Rahmstorf, 2024]. Thus, the AMOC theory development constantly moves back and forth across the hierarchy of climate models. Simple models study progressively more realistic feedback by incorporating key processes identified in numerical simulations and observations, while complex models become more interpretable through the physical mechanisms uncovered by conceptual studies. Together, these complementary approaches provide an increasingly coherent framework for understanding the observed behavior of the AMOC.

At the end of his editorial *Why We Are Oceanographers* [Stommel, 1989], Stommel expressed the concern that the increasing complexity of numerical models might eventually outpace our ability to understand them (which concern is raised nowadays by

machine-learning approaches). Yet, the history of AMOC research suggests a different perspective. Increasing model complexity has not replaced conceptual understanding but has rather reinforced the need for a continuous dialogue between observations and models of all complexities. Observations motivate new theories, conceptual models propose physical mechanisms, and realistic simulations assess their robustness while simultaneously revealing new phenomena that inspire further observations and conceptual developments. Stommel's earlier remark in the same editorial that "when it comes to the phenomenology of the ocean, there are more discoveries than predictions" is perhaps the best illustration of this idea. Observations drive scientific discovery and the hierarchy of climate models provides the tools needed to explain, test, and progressively understand them.

1.5 Outline

The objective of this thesis is not to explore the full hierarchy of climate models. Instead, we use models of intermediate and low complexity to address questions that are difficult to investigate with high-fidelity simulations. In particular, while previous studies using realistic models have reached contrasting conclusions regarding the reversibility of cold-to-warm transitions in Antarctic ice-shelf cavities, lower-complexity models are well suited to investigate such questions because they provide a clearer understanding of the underlying mechanisms. More specifically, this thesis addresses the following questions. Can cold-to-warm transitions in Antarctic ice-shelf cavities be irreversible? If so, which physical processes promote or inhibit bistability? On which environmental parameters does the nature of the transition depend? Finally, are the mechanisms identified in simplified models relevant to real Antarctic ice shelves? To answer these questions, we aim to (*i*) characterize the steady-state response of an ice-shelf cavity to quasi-static coastal-polynya forcing, a problem that is generally beyond the reach of high-realism configurations because of their computational cost and forcing complexity; and (*ii*) investigate the response of ice-shelf cavities to time-varying forcing in lower-complexity frameworks, thereby providing fundamental insight into regime transitions under seasonal and interannual forcing.

To achieve these objectives, we combine two complementary levels of the climate models hierarchy. The first is a low-dimensional box model coupling an ice-shelf cavity to the adjacent continental shelf. Its simplicity makes it possible to explore large regions of parameter space while easily incorporating observations of ice-shelf geometry, CDW properties, and coastal-polynya characteristics. The second is an idealized three-dimensional configuration performed with the ocean GCM NEMO [Madec et al., 2024]. Although its geometry and forcing are deliberately simplified, it retains the essential ocean dynamics required to investigate the physical mechanisms identified by the conceptual model and to assess their robustness in a more realistic setting.

In this context, this thesis is organized as follows.

In **Chapter 2**, we develop the low-dimensional box model and apply it to nine Antarctic ice shelves to investigate their propensity to exhibit bistable circulation regimes under steady coastal-polynya forcing. We further analyze the model from a dynamical systems theory perspective to characterize the bifurcations governing these transitions.

In **Chapter 3**, we move to the next level of the climate-model hierarchy using the ocean GCM NEMO. Through quasi-static experiments performed in an idealized configuration, we investigate the steady response of an ice-shelf cavity to coastal-polynya forcing

and identify the roles of thermocline dynamics and large-scale circulation at the ice-shelf front in controlling the reversibility of regime transitions.

In **Chapter 4**, which is more technical and less directly related to bistability, we describe the tuning of the numerical schemes and parameterizations of the NEMO configuration in order to minimize spurious numerical artifacts. This study also leads us to investigate the occurrence of topographic Rossby waves within the cavity.

Finally, in **Chapter 5**, we apply time-varying forcing to both the low-dimensional model and the NEMO configuration. We focus in particular on seasonal coastal-polynya forcing and investigate how its stochastic interannual variability influences regime transitions.

Chapter 2

Bistable dynamics of ice-shelf cavities in a low-dimensional box model

Summary

We demonstrate that brine rejection in coastal polynyas promotes bistable dynamics in ice-shelf cavities. We develop a generic low-dimensional box model featuring warm and cold circulation modes and apply it to nine ice-shelf cavities. We find that most ice-shelf cavities are in a bistable regime and are therefore susceptible to irreversible abrupt transitions for a realistic range of sea-ice formation rates. Bistability is robust to changes in cavity parameterization. However, the vertical mixing scheme at the ice-shelf front can be tuned to make the transitions reversible. We give graphical and asymptotic model solutions, providing scaling laws for basal melt rates and transition thresholds. We highlight that the system undergoes a cusp bifurcation, inducing either reversible or irreversible regime transitions depending on the Circumpolar Deep Water temperature.

The Sections 2.2 and 2.3 of this chapter are mainly based on [Saddier et al., 2026]. In contrast, Section 2.4 is largely unpublished and presents more technical aspects of the dynamical systems characterization of the low-dimensional box model.

2.1 Introduction

The development of box models in oceanography is closely tied to the broader emergence of computational tools and dynamical systems theory. Starting in the 1960s, the arrival of "minicomputers" made it possible and more accessible to numerically integrate relatively simple nonlinear systems. Climate science has both contributed to and benefited from the development of dynamical systems theory. The model of Lorenz [Lorenz, 1963], implemented on a LGP-30 desk computer (see Fig.2.1a), stands as a landmark example. This system of three ordinary differential equations, representing simplified atmospheric convection, provided the first robust numerical demonstration of deterministic chaos. While sensitivity to initial conditions had already been anticipated by Henri Poincaré for the three-corps problem [Poincaré, 1890] and by Jacques Hadamart when he investigated the motion of free particles on negative curvature surfaces [Hadamard, 1898], Lorenz's work



(a) The LGP-30 desk computer (1956). *Source:* https://en.wikipedia.org/wiki/LGP-30



(b) The HP-97 desktop calculator (1976). *Source:* https://fr.wikipedia.org/wiki/HP-97

Figure 2.1: Computer used by dynamical systems pioneers.

made this concept explicit thanks to graphical representations of the system, and foundational for modern chaos theory. In a context of climate forecasting, it also emphasized the intrinsic finite predictability of complex systems such as the atmosphere.

In oceanography, the same conceptual approach led to the development of idealized box models. Henry Stommel introduced a minimal model of thermohaline circulation based on buoyancy-driven fluxes between ocean boxes [Stommel, 1961]. Despite its simplicity, the model revealed a key property of the ocean circulation system: the existence of multiple steady states, laying the foundation for the concept of bistability in oceanography. In subsequent decades, miniaturization of computer enabled further exploration of reduced dynamical systems. With his desktop calculator HP-97 (see Fig.2.1b), Pierre Welander demonstrated self-sustained oscillations in a mixed-layer box model, only subject to heat and salt fluxes from the atmosphere and from the deep ocean. His results highlighted the richness of nonlinear feedbacks that can arise even in highly simplified frameworks, and gave insights on thermohaline driven climate variability.

In a similar spirit, box model approaches were extended to more complex cryospheric systems, such as ice-shelf cavities. D. Olbers and H. Hellmer [Olbers and Hellmer, 2010] developed a box model of an ice-shelf cavity in which the ocean exchanges heat and salt with both the ice shelf and the atmosphere at the ice-shelf front in coastal polynyas. Building on this framework, [Reese et al., 2018] developed the PICO model (Potsdam Ice-shelf Cavity mOdel), focusing on basal melt rates beneath ice shelves, discarding the ocean front boxes of the Olbers and Hellmer model. The PICO model serves for instance as a low-computational boundary condition for ice-sheet models, providing basal melt rates beneath ice shelves. More recently, the works of [Hazel and Stewart, 2020] and [Moorman et al., 2023] have shifted attention toward ocean dynamics at the front of ice shelves, rather than within the cavity itself. Both studies reveal bistable ocean circulation induced by surface buoyancy fluxes within coastal polynyas. They identify a meltwater positive feedback that self-sustains two distinct circulation regimes: a warm regime in which Circumpolar Deep Water (CDW) intrudes the cavity, and a cold regime in which CDW are replaced by Dense Shelf Water (DSW). Although these studies account for water column

dynamics beneath the polynya, including the ability to track the thermocline depth in the model of [Moorman et al., 2020], they do not explicitly represent the meltwater feedback associated with basal melting at the ice–ocean interface. Instead, they rely on cavity parameters that are tuned for specific ice shelves, limiting the generalizability of their results to other regions.

In this chapter, we investigate the competition between CDW and DSW in filling ice-shelf cavities. We develop a low-dimensional model of coupled cavity and near-front ocean dynamics, starting back from the box model of [Olbers and Hellmer, 2010], which allows for both a representation of the ice–ocean interface within the ice-shelf cavity, and a description of heat and salt fluxes within the polynya. We apply our model to several ice-shelf cavities and assess the impact of changing the parameterizations for basal ice melting, cavity ocean circulation and vertical mixing scheme on the results. We uncover bistable dynamics for a wide range of realistic ocean and polynya conditions, suggesting that deep convection dynamics in polynyas can drive irreversible transitions.

The chapter is organized as follows. In Section 2.2 we introduce the model, and the solution method. In section 2.3, we apply the model to nine Antarctic ice-shelf cavities. We show the melt rate as a function of the control parameters, and for different parameterization choices, highlighting the existence of broad bistable regions. We comment on the results in light of recent observations and realistic simulations and discuss model limitations for future research directions. Finally in Section 2.4, we give graphical and asymptotic model solutions, providing scaling laws for basal melt rates and transition thresholds. We highlight that the system undergoes a cusp bifurcation, inducing either reversible or irreversible regime transitions. This last section can be read independently of the previous sections.

2.2 Presentation of the model

2.2.1 Low-dimensional model setup

We construct a low-dimensional box model for ocean dynamics near and inside ice-shelf cavities. Our formulation combines the PICO box-slicing approach [Reese et al., 2018], which captures the decrease in melt rates along the meltwater plume path, with a representation of vertical mixing at the ice-shelf front [Olbers and Hellmer, 2010], which has been identified as a driver of hysteresis behavior [Hazel and Stewart, 2020, Moorman et al., 2023]. We focus on steady-state dynamics.

Our model consists of N_{PICO} cavity boxes"$\mathrm{c}_1, \ldots, \mathrm{c}_{N_{\mathrm{PICO}}}$" [1], one coastal polynya box "p", and one deep water box "d" (Fig. 2.2(a)). We denote by $V_{c,1}, \ldots, V_{c,N_{\mathrm{PICO}}}$, V_p, V_d their volume, respectively, and by $\mathcal{A}_{c,1}, \ldots, \mathcal{A}_{c,N_{\mathrm{PICO}}}$ and $\mathcal{A}_p$ the horizontal areas of the cavity and polynya boxes. The box volumes do not impact steady states (as can be inferred from Eq. (2.6a)-(2.6h)) hence will not be discussed further in this chapter.

The box temperatures T_i and salinities S_i ($i \in \{\mathrm{c}_1, \ldots, \mathrm{c}_{\mathrm{N_{PICO}}}, \mathrm{p}, \mathrm{d}\}$) evolve under

[1] We propose an alternative formulation to the discrete number of cavity boxes used in the PICO model by deriving a continuous 1D limit of PICO in Appendix 2.5. For simplicity, we will keep the discrete PICO model in the following.

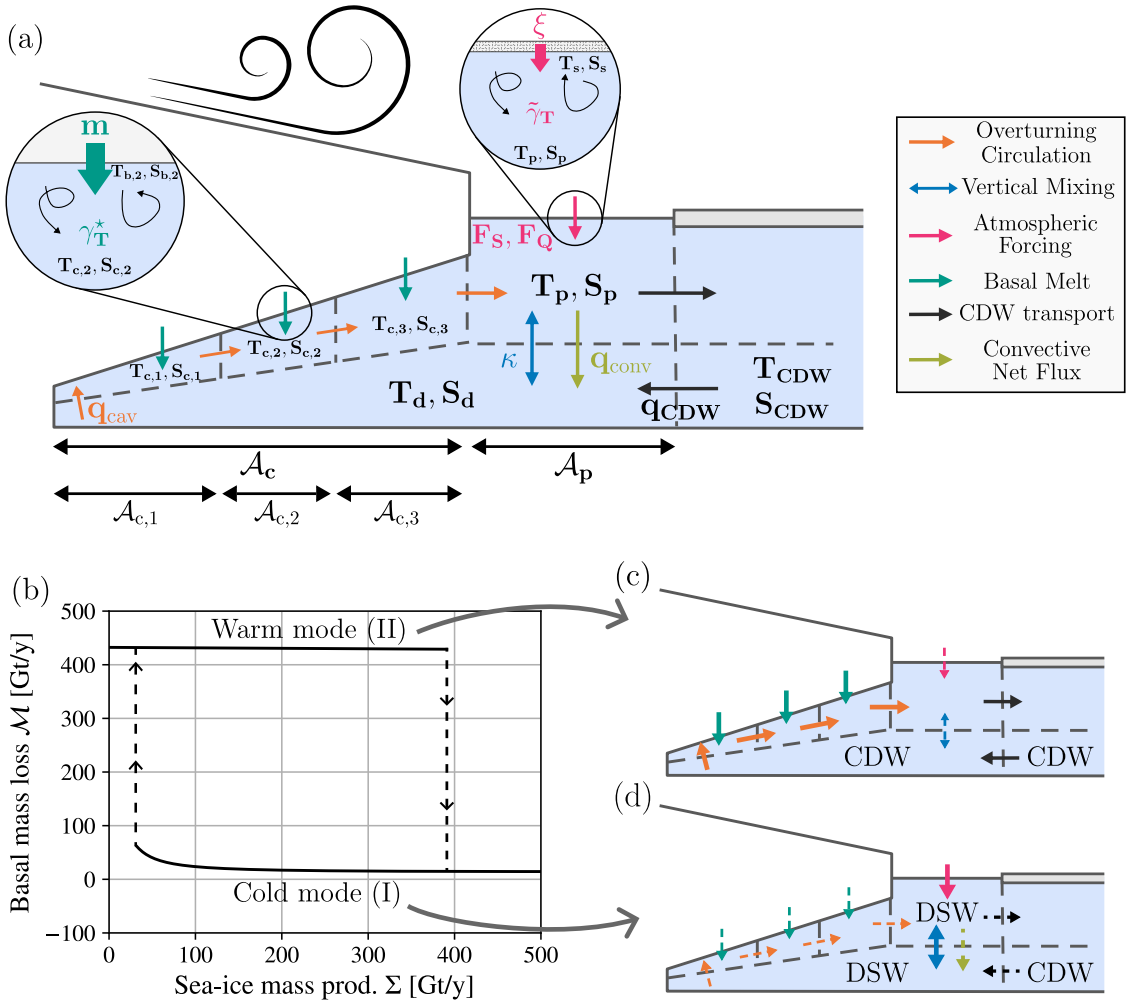

Figure 2.2: (a) Schematic of our low-dimensional box model (with $N_{\mathrm{PICO}} = 3$). (b) Basal mass loss $\mathcal{M} = \rho_{\mathrm{ice}} \mathcal{A}_c m$ for the Amery ice shelf obtained from our low-dimensional model as a function of the sea-ice mass production $\Sigma = \rho_{\mathrm{ice}} \mathcal{A}_p \xi$. The forcing parameters T_{CDW}, S_{CDW} and ξ are set to their inter-annual means, such that we vary Σ through variations in $\mathcal{A}_p$ only. Dashed lines represent transition thresholds. (c,d) Circulation in the warm (II) and cold (I) regimes, respectively, with thicker arrows denoting stronger fluxes [Silvano et al., 2016].

conservation equations, with density ρ_i given by the linearized equation of state

$$\frac{\rho_i}{\rho_\star} = 1 - \alpha(T_i - T_\star) + \beta(S_i - S_\star), \tag{2.1}$$

where $\alpha\,[°C^{-1}]$ and $\beta\,[(g.kg^{-1})^{-1}]$ are constant thermal expansion and haline contraction coefficients. All model parameters are listed in Table 2.1.

The vertical mixing velocity $\kappa\,[m.s^{-1}]$ between the "p" and "d" boxes depends on density stratification. A low value $\kappa = \kappa_{\text{diff}}$ models diffusive exchanges when the stratification is stable while a high value $\kappa = \kappa_{\text{conv}} \gg \kappa_{\text{diff}}$ models deep convection when the stratification is unstable [Olbers and Hellmer, 2010, Moorman et al., 2023, Welander, 1982, Hazel and Stewart, 2020].

As in the PICO model [Reese et al., 2018], the cavity overturning transport $q_{\text{cav}}\,[m^3.s^{-1}]$ is proportional to the density difference between the plume and the underlying waters at the grounding line,

$$q_{\text{cav}} = C(\rho_d - \rho_{c,1}). \tag{2.2}$$

This proportionality arises from rotational two-dimensional plume theory where cross-cavity plume flow dominates and tends towards geostrophic balance with along-cavity pressure gradient terms. The parameter $C\,[m^6 s^{-1} kg^{-1}]$ combines the effects of rotation and the along-cavity slope of the ice shelf base [Hewitt, 2020]. C should therefore vary spatially, but here we adopt a uniform value identified as optimal for general use across warm and cold cavity ice shelves [Reese et al., 2018]. This parameterization yields a melt-rate sensitivity to ocean temperature consistent with three-dimensional idealized simulations [Holland et al., 2008]. A key assumption of the model is that the overturning is sustained exclusively by deep waters (box "d"), that can either originate from the intrusion of CDW with temperature $T_{\text{CDW}}\,[°C]$ and salinity $S_{\text{CDW}}\,[g/kg]$ through a volume transport $q_{\text{CDW}}\,[m^3.s^{-1}]$, or a net volume flow $q_{\text{conv}}\,[m^3.s^{-1}]$ linked to deep convection sourced from box "p". For simplicity, we express q_{conv} as a fraction $r \in [0, 1]$ of the cavity overturning such that $q_{\text{conv}} = r q_{\text{cav}}$. We set $r = 0$ in the warm stably stratified mode. Volume conservation in boxes "p" and "d" requires

$$q_{\text{CDW}} + q_{\text{conv}} = q_{\text{cav}} \Rightarrow q_{\text{CDW}} = (1 - r) q_{\text{cav}}. \tag{2.3}$$

We remark that our model predicts CDW intrusions based on q_{cav} and r only, thus omitting shelf-break processes [Thompson et al., 2018, Lanham et al., 2025], which we discuss in Section 2.3.5.

We model the ice-shelf melt rate $m\,[m.s^{-1}]$ with the 2-equations formulation [Holland and Jenkins, 1999], neglecting ice salinity, conductive heat flux through the ice shelf, and the supplementary heat flux induced by the meltwater advection at the ice-ocean interface [Jenkins et al., 2001]:

$$\begin{cases} T_b = aS_c + b - ch_c & \text{liquidus equation,} \\ m = \frac{\rho_\star c_\star}{\rho_{\text{ice}} \mathcal{L}} \gamma_T^\star [T_c - T_b(S_c, h_c)] & \text{heat balance equation,} \end{cases} \tag{2.4}$$

where a, b and c characterize the liquidus, T_b and h_c are the temperature and depth at the ice-ocean interface (interface salinity $S_b = S_c$ in the 2-equation formulation), $c_\star\,[J.kg^{-1}.°C^{-1}]$ is the specific heat capacity, $\mathcal{L}\,[J.kg^{-1}]$ is the latent heat and $\gamma_T^\star\,[m.s^{-1}]$ is the effective turbulent heat transfer. Finally, we model air-sea fluxes at the polynya

Table 2.1: Box model parameters split into five categories. The PICO parameters are based on [Reese et al., 2018] and assumed common to all cavities [Menthon et al., 2025]. The polynya parameters are based on [Olbers and Hellmer, 2010] (κ_{diff} , κ_{conv}), and assumed common to all cavities.

	Parameter	**Symbol**	**Value**	**Unit**
PICO	Salinity coefficient of the liquidus	a	-0.0572	°C/(g/kg)
	Constant coefficient of the liquidus	b	0.0788	°C
	Depth coefficient of the liquidus	c	7.59×10^{-4}	°C/m
	Thermal expansion coefficient	α	7.5×10^{-5}	$°C^{-1}$
	Salt contraction coefficient	β	7.7×10^{-4}	$(g/kg)^{-1}$
	Reference temperature	$T_\star$	0	°C
	Reference salinity	$S_\star$	34	g/kg
	Latent heat of fusion	$\mathcal{L}$	3.34×10^5	J/kg
	Heat capacity of sea water	$c_\star$	3974	J/kg/°C
	Density of ice	ρ_{ice}	910	kg/m^3
	Reference density of sea water	$\rho_\star$	1033	kg/m^3
	Ice-shelf effective turbulent heat transfer velocity	$\gamma_T^\star$	2×10^{-5}	m/s
	Overturning strength	C	1×10^6	$m^6/kg/s$
Polynya	Diffusive vertical mixing velocity	κ_{diff}	1×10^{-7}	m/s
	Convective vertical mixing velocity	κ_{conv}	1×10^{-3}	m/s
	Polynya effective turbulent heat transfer velocity	$\tilde{\gamma}_T$	4×10^{-4}	m/s
	Convective net flux / overturning circulation ratio	r	0	-
Cavity	Cavity volume	V_{cav}	-	m^3
	Number of PICO boxes	N_{PICO}	-	-
	Cavity horizontal area	$\mathcal{A}_c$	-	m^2
	Horizontal area of cavity box i	$\mathcal{A}_{c,i}$	-	m^2
	Depth of the ice-ocean interface of cavity box i	$h_{c,i}$	-	m
Forcing	CDW temperature	T_{CDW}	-	°C
	CDW salinity	S_{CDW}	-	g/kg
	Polynya area	$\mathcal{A}_p$	-	m^2
	Sea-ice formation rate	ξ	-	m/s
	Sea-ice mass production	Σ	$\rho_{\text{ice}}\mathcal{A}_p\xi$	kg/s
Output	Overturning circulation	q_{cav}	-	m^3/s
	Flushing time of the cavity	τ_{flush}	$V_{\text{cav}}/q_{\text{cav}}$	s
	Basal melt rate	m	-	m/s
	Basal mass loss	$\mathcal{M}$	$\rho_{\text{ice}}\mathcal{A}_c m$	kg/s

surface through a brine release term F_S [g.m^{-2}.s^{-1}] and a heat exchange term F_Q [W.m^{-2}]. We use the sea-ice formation rate ξ [m.s^{-1}] as control parameter so that

$$\begin{cases} F_S = \rho_{\text{ice}} \xi S_p, \\ F_Q = \rho_\star c_\star \tilde{\gamma}_T (T_s - T_p), \end{cases} \tag{2.5}$$

with $\tilde{\gamma}_T$ [m.s^{-1}] the effective turbulent heat transfer below the polynya. Eq. (2.5) assumes the interface at freezing temperature $T_s = aS_p + b$, with salinity $S_s = S_p$. The heat release to the atmosphere is $-F_Q + \rho_{\text{ice}} \mathcal{L} \xi$ [Haid and Timmermann, 2013].

Applying heat and salt balances to each box leads to the model equations:

$$V_p \dot{T}_p = q_{\text{cav}}(T_{c,N_{\text{PICO}}} - T_p) - \mathcal{A}_p \kappa (T_p - T_d) + \mathcal{A}_p \tilde{\gamma}_T [T_s(S_p) - T_p], \tag{2.6a}$$

$$V_p \dot{S}_p = q_{\text{cav}}(S_{c,N_{\text{PICO}}} - S_p) - \mathcal{A}_p \kappa (S_p - S_d) + \frac{\rho_{\text{ice}}}{\rho_\star} \mathcal{A}_p \xi S_p, \tag{2.6b}$$

$$V_d \dot{T}_d = (1-r) q_{\text{cav}}(T_{\text{CDW}} - T_d) + (\mathcal{A}_p \kappa + r q_{\text{cav}})(T_p - T_d), \tag{2.6c}$$

$$V_d \dot{S}_d = (1-r) q_{\text{cav}}(S_{\text{CDW}} - S_d) + (\mathcal{A}_p \kappa + r q_{\text{cav}})(S_p - S_d), \tag{2.6d}$$

$$V_{c,1} \dot{T}_{c,1} = q_{\text{cav}}(T_d - T_{c,1}) - \mathcal{A}_{c,1} \gamma_T^\star [T_{c,1} - T_b(S_{c,1}, P_b)], \tag{2.6e}$$

$$V_{c,1} \dot{S}_{c,1} = q_{\text{cav}}(S_d - S_{c,1}) - \mathcal{A}_{c,1} \frac{c_\star}{\mathcal{L}} \gamma_T^\star [T_{c,1} - T_b(S_{c,1}, P_b)] S_{c,1}, \tag{2.6f}$$

$$V_{c,j} \dot{T}_{c,j} = q_{\text{cav}}(T_{c,j-1} - T_{c,j}) - \mathcal{A}_{c,j} \gamma_T^\star [T_{c,j} - T_b(S_{c,j}, P_b)], \tag{2.6g}$$

$$V_{c,j} \dot{S}_{c,j} = q_{\text{cav}}(S_{c,j-1} - S_{c,j}) - \mathcal{A}_{c,j} \frac{c_\star}{\mathcal{L}} \gamma_T^\star [T_{c,j} - T_b(S_{c,j}, P_b)] S_{c,j}, \tag{2.6h}$$

with $j \in \{2, \dots, N_{\text{PICO}}\}$. The parameter r affects box "d" only (i.e. Eqs. (2.6c)-(2.6d)) and has a negligible impact on the system's dynamics. In the cold regime, vertical mixing dominates over CDW inflows, i.e. $q_{\text{cav}} \ll \mathcal{A}_p \kappa_{\text{conv}}$, ensuring that box "d" is primarily influenced by box "p" rather than offshore CDW, regardless of the downwelling flux q_{conv}. Accordingly, we set $r = 0$ from now.

2.2.2 Equilibrium states and hysteresis

We solve numerically Eq. (2.6a)-(2.6h) at steady state with $\kappa = \kappa_{\text{conv}}$ or $\kappa = \kappa_{\text{diff}}$ to obtain the equilibrium convective and diffusive solutions, respectively. The equilibrium states are always stable, as we will later see in Section 2.4.2, but not necessarily physically consistent. An equilibrium is physical only if the underlying regime agrees with the density stratification at the ice-shelf front, which we define as

$$\sigma = \frac{\rho_p - \rho_d}{\rho_\star} = -\alpha(T_p - T_d) + \beta(S_p - S_d), \tag{2.7}$$

where $\sigma > 0$ (resp. $\sigma < 0$) is indicative of an unstable (resp. stable) stratification such that the vertical mixing scheme is

$$\kappa = \begin{cases} \kappa_{\text{diff}} & \text{if } \sigma \leq 0, \\ \kappa_{\text{conv}} & \text{if } \sigma > 0. \end{cases} \tag{2.8}$$

Fig. 2.2(b) shows the melt rates of the Amery ice shelf as a function of sea-ice mass production Σ predicted by our model, which we recall approximates the cavity dynamics as a simple steady warm or cold circulation mode. For low Σ ($\leq 30\,\mathrm{Gt/y}$), both κ_{conv} and κ_{diff} yield a stable water column, such that the warm diffusive regime is the only physical solution. For high Σ ($\geq 390\,\mathrm{Gt/y}$), the water column is, conversely, unstable and the convective state is the only physical solution. Importantly, both solutions exist for a continuous range of intermediate Σ, which define the domain of bistability. In the bistable regime, the final equilibrium state depends on the initial conditions. Thus, if we increase and then decrease Σ incrementally, basal melt follows an irreversible hysteresis trajectory, as found in previous low-dimensional models [Moorman et al., 2023, Hazel and Stewart, 2020]. The hysteresis arises from positive feedback loops. In the warm mode, high meltwater production stabilizes the water column, reinforcing the diffusive state. In the cold mode, low meltwater production promotes an instable water column, reinforcing the convective state [Moorman et al., 2023, Hazel and Stewart, 2020].

2.3 Application to Antarctic ice-shelf cavities

We aim to apply the complete system of equations derived in Section 2.2.1 to nine Antarctic ice-shelf cavities (Fig. 2.3), spanning a broad range of ice-shelf sizes, and CDW and polynya conditions. Observations classify the large Ross, Filchner-Ronne, and Amery cavities, as well as the medium Riiser-Larsen and Roi Baudouin cavities, as cold convective (mode I; Fig. 2.2(d)), while the smaller Dotson, Pine Island, Totten, and Moscow University cavities are warm diffusive (mode II; Fig. 2.2(c)) [Dinniman et al., 2016, Nøst et al., 2011, Li et al., 2023, Hirano et al., 2023]. We note that our model does not capture the mode III regime that features warm surface waters entering the cavity [Silvano et al., 2016]. It also does not allow for combinations of modes within the same cavity [Silvano et al., 2016, Tinto et al., 2019].

2.3.1 Data

When applying our model, we subdivide each cavity in boxes with characteristics prescribed according to [Burgard et al., 2022] (Fig. 2.3). We estimate the properties of CDW from [Burgard et al., 2022], who ran regional ocean simulations of several ice shelf cavities with the general circulation model NEMO [Madec et al., 2024]. The data set provides annual means of temperature and salinity profiles at various distances from the front of the ice shelves (see Fig. 2.17 and Fig. 2.18 in Appendix 2.5). We force our model with the temperature and salinity of CDW at depth $z = h_{\mathrm{front}}$, where h_{front} is the mean water depth at the front of the ice shelf. For all ice shelves, we use offshore profiles, after the continental shelf break to primarily capture CDW properties.

We constrain ξ using March to October sea-ice formation rates from [Nakata et al., 2021], which together account for 96% of total sea-ice production. The coastal polynya area $\mathcal{A}_p$ combines all cells in the dataset experiencing sea-ice formation rates in excess of 0.5m/30d (Fig. 2.3) and within a prescribed geographical mask. Yearly averages for $\mathcal{A}_p$ and ξ assume no polynyas, no freezing, nor positive buoyancy fluxes from November to February. All forcing parameters are listed in Table 2.2.

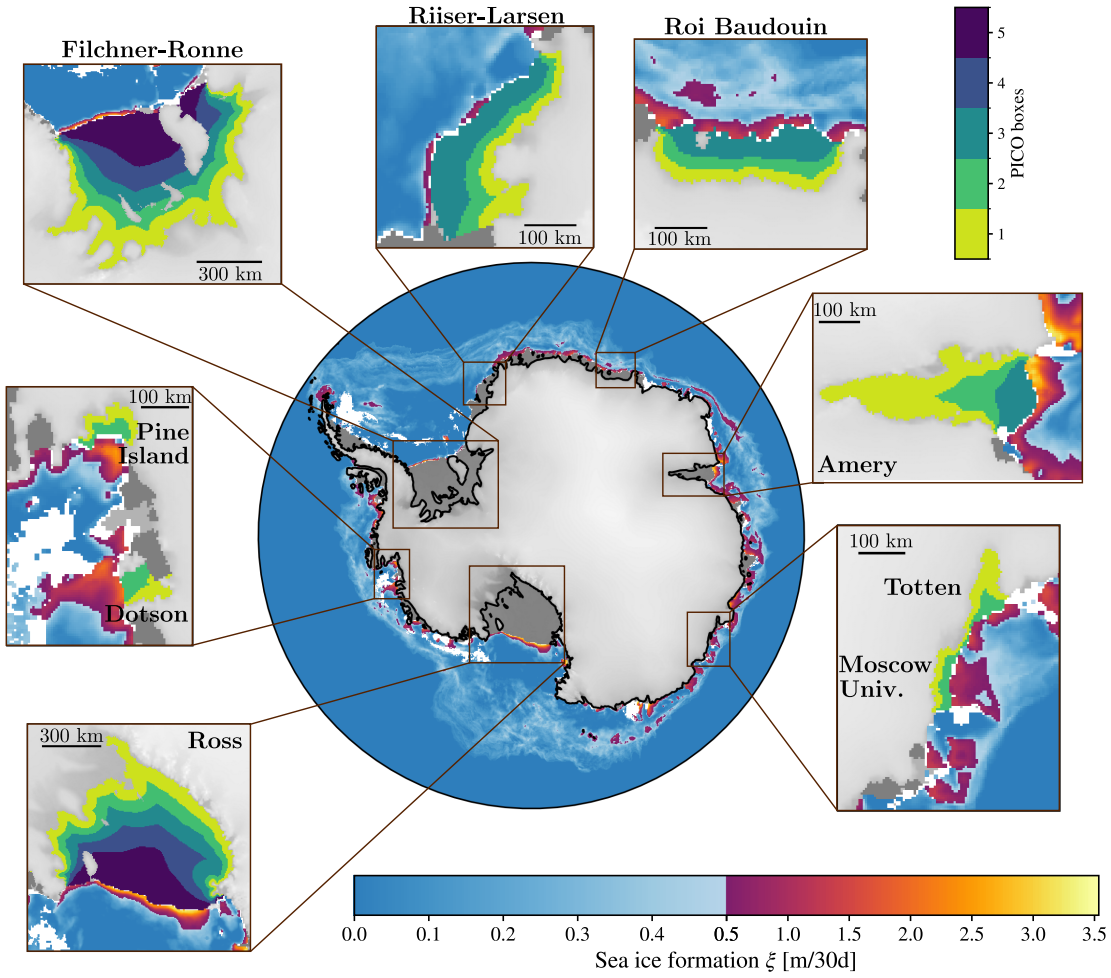

Figure 2.3: Sea-ice formation rates (April 2007) [Nakata et al., 2021]. The nine Antarctic ice shelves selected to test our model are shown in the insets. The colorbar for freezing rates is split in two to enhance contrasts above the threshold of 0.5 m/30d, which we used to identify coastal polynyas areas $\mathcal{A}_p$. White cells denote regions with land-fast sea ice or sea-ice concentration below 30% in open water [Nakata et al., 2021] and are masked. We show the PICO cavity boxes $\mathcal{A}_{c,j}$, $j \in \{1, \ldots, 5\}$ using the light green to dark blue colormap [Burgard et al., 2022].

Table 2.2: Forcing parameter values (inter-annual means). We also report the horizontal surface area of ice-shelf cavities $\mathcal{A}_c$ for comparison with the polynya area $\mathcal{A}_p$.

Cavity	$\mathbf{T}_{\mathrm{CDW}}$ **[°C]**	$\mathbf{S}_{\mathrm{CDW}}$ **[g/kg]**	$\mathcal{A}_\mathbf{p}$ $[\times\mathbf{10^3}\,\mathrm{km}^2]$	ξ **[m/y]**	$\mathcal{A}_\mathbf{c}$ $[\times\mathbf{10^3}\,\mathrm{km}^2]$	$\mathbf{T}_{\mathrm{surf}}$ **[°C]**	$\mathbf{S}_{\mathrm{surf}}$ **[g/kg]**
Ross	1.78	34.69	23.85	10.94	469.28	-1.71	33.75
Filchner-Ronne	0.02	34.55	5.52	8.9	416.61	-1.66	33.85
Amery	0.62	34.64	5.36	13.84	58.83	-1.35	34.06
Dotson	1.8	34.71	8.11	8.4	4.94	-1.53	33.58
Pine Island	1.95	34.68	1.63	7.29	5.73	-1.51	33.56
Riiser-Larsen	0.6	34.64	1.72	6.33	41.82	-1.54	34.0
Roi Baudouin	0.54	34.58	3.76	8.7	32.98	-1.21	33.92
Totten	1.08	34.68	3.68	7.28	6.58	-0.74	34.05
Moscow Univ.	1.16	34.66	0.34	4.91	5.67	-0.7	34.04

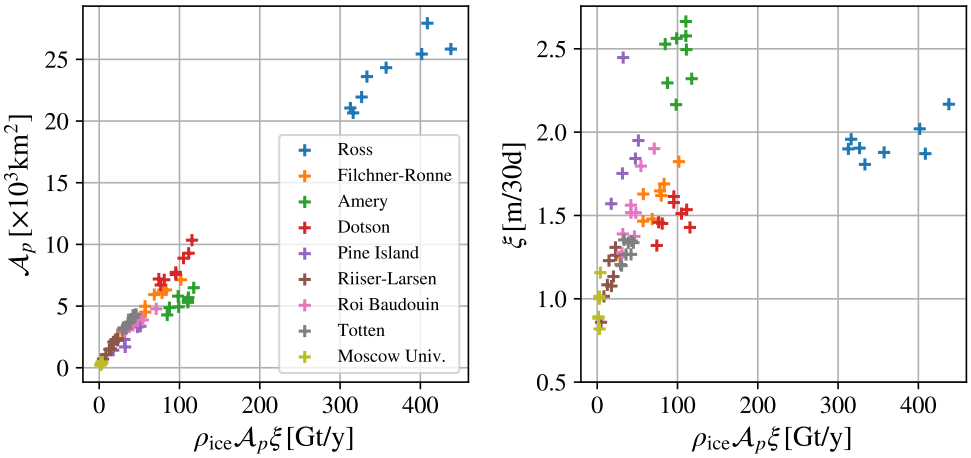

Figure 2.4: $\mathcal{A}_p$ and ξ as a function of $\Sigma = \rho_{\text{ice}}\mathcal{A}_p\xi$. Each data point represents a yearly average (with 8 years of data for each ice shelf).

Table 2.3: Correlation coefficients $r[\mathcal{A}_p, \mathcal{A}_p\xi]$ and $r[\xi, \mathcal{A}_p\xi]$ computed for each ice shelf, where $r[X, Y] = \frac{\text{Cov}[X,Y]}{\sigma_X \sigma_Y}$ is based on annual means for the forcing parameters (see Fig. 2.4). A global correlation analysis combining the data series from all ice shelves is also performed.

Cavity	$\mathbf{r}[\mathcal{A}_\mathbf{p}, \mathcal{A}_\mathbf{p}\xi]$	$\mathbf{r}[\xi, \mathcal{A}_\mathbf{p}\xi]$
Ross	0.89	0.63
Filchner-Ronne	0.98	0.93
Amery	0.83	0.2
Dotson	0.94	0.43
Pine Island	0.95	0.27
Riiser-Larsen	0.98	0.87
Roi Baudouin	0.91	0.90
Totten	0.97	0.66
Moscow Univ.	0.90	0.67
All	0.99	0.49
All (without Ross)	0.91	0.73

In our experiments, we vary the sea-ice mass production $\Sigma = \rho_{\text{ice}}\mathcal{A}_p\xi$, by varying $\mathcal{A}_p$ only (except in Fig. 2.6), i.e. fixing ξ to its inter-annual mean, because it has been reported that Σ correlates more strongly with $\mathcal{A}_p$ than ξ [Haid and Timmermann, 2013]. We have verified that $\mathcal{A}_p$ correlates more strongly than ξ with the sea-ice mass production rate for polynya parameters inferred from [Nakata et al., 2021]. Fig. 2.4 shows $\mathcal{A}_p$ and ξ as a function of $\rho_{\text{ice}}\mathcal{A}_p\xi$. We find that $\mathcal{A}_p$ follows a linear trend while ξ shows a non-monotonic evolution, suggesting that $\mathcal{A}_p$ is a better proxy for sea-ice formation than ξ (at least on interannual timescales), which is confirmed quantitatively by a computation of correlation coefficients provided in Table. 2.3.

2.3.2 Bistability for a broad range of forcing parameters

Fig. 2.5(a-i) shows the basal mass loss $\mathcal{M}$ of all selected ice shelves as a function of CDW temperatures T_{CDW} and sea-ice mass production Σ. The diffusive (warm) mode is stable below the black solid lines while the convective (cold) mode is stable above the black dashed lines. The gray regions are the bistable regions, wherein both modes are stable. The small white regions (e.g. to the bottom left for Riiser-Larsen) have equilibrium states that are not physical, hence exhibit oscillating dynamics [Welander, 1982]. These regions are observed for values T_{CDW} below $-1.9\,^{\circ}\mathrm{C}$, as predicted in Section 2.4.3. We classify cavities based on their flushing times $\tau_{\mathrm{flush}} = V_{\mathrm{cav}}/q$ to anticipate the response of the cavities to transient forcings [Holland, 2017], which we discuss in Section 2.3.5, and study specifically in Chapter 5.

The key result of this chapter is that our low-dimensional model predicts bistable behavior for all ice-shelf cavities over a broad range of plausible parameters, encompassing or close to values inferred from observations and realistic model studies (white crosses and diamonds). For fixed T_{CDW}, the system transitions from a convective to a diffusive regime with decreasing sea-ice production and from a diffusive to a convective regime with increasing sea-ice production. In the warm mode, the basal melt increases with T_{CDW}, as cavity water masses are largely controlled by CDW properties. However, it is insensitive to sea-ice production Σ because the two-value mixing scheme limits mixing before transition to the cold mode, consistent with [Moorman et al., 2023]. In the cold mode, the basal melt dependence on T_{CDW} and Σ is complex though relatively weak, because both T_p and T_{CDW} influence deep water properties. Both the diffusive-to-convective and convective-to-diffusive sea-ice formation thresholds increase with T_{CDW}, since higher meltwater production stabilizes the water column and reinforces the diffusive regime.

Fig. 2.5(j) shows the size of the bistable region, i.e. the difference in sea-ice mass production thresholds $\Sigma_{\mathrm{warm}\to\mathrm{cold}} - \Sigma_{\mathrm{cold}\to\mathrm{warm}}$, as a function of the basal melt difference $\mathcal{M}_{\mathrm{warm}} - \mathcal{M}_{\mathrm{cold}}$ between the warm and cold modes for each cavity (one circle denotes one cavity), when T_{CDW} is set to its inter-annual average. The size of the bistable region closely matches, though slightly underestimates, the basal mass-loss difference, suggesting that basal mass-loss difference before and after a regime shift can be used to quantify the irreversibility of the transition. This result will be analytically proved with asymptotic hypothesis on the box model in Section 2.4.4 (see Eq. (2.30)).

Table 2.4 shows the model outputs m and q for each mode, considering interannual means for forcing parameters (shown by white diamonds in Fig. 2.5, which correspond to Table 2.2 parameters). Melt rates are compared with those obtained by [Rignot et al., 2013].

Although the stability regions in Fig. 2.5 show similar trends for all ice shelves with the forcing parameters, we observe that a rescaling collapsing all stability lines on a universal closed curve is not possible. Firstly, the number of cavity boxes differ from one cavity to another, which especially affects the basal melt rates of large cavities that can support refreezing. Another reason is that $\mathcal{A}_p$ and ξ, whose values differs between cavities, do not affect the system dynamics in the same way. While ξ affects only the surface salt flux (see Eq. (2.6b)), $\mathcal{A}_p$ affect both the surface salt flux and the vertical mixing (see Eqs. (2.6a)-(2.6d)). Thus, stability maps Fig. 2.5 are plotted for a fixed value of ξ, varying only $\mathcal{A}_p$, as mentioned in Section 2.3.1. To assess the impact of both $\mathcal{A}_p$ and ξ, Fig. 2.6 shows stability maps in the $\xi \times \mathcal{A}_p$ phase space, setting T_{CDW} to its interannual mean.

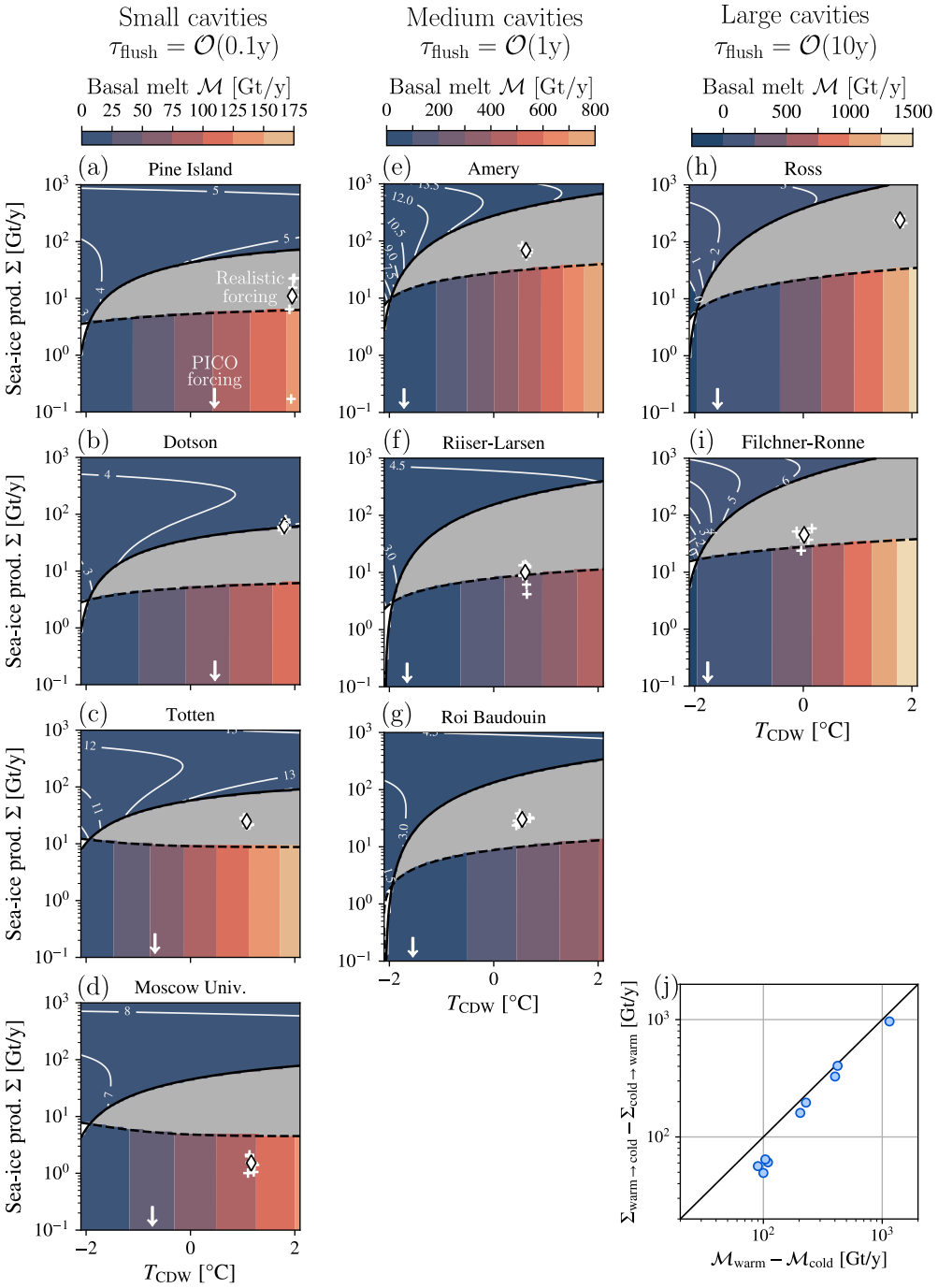

Figure 2.5: Basal mass loss $\mathcal{M}$ as a function of CDW temperatures T_{CDW} and sea-ice mass production Σ for small (a-d), medium (e-g) and large (h,i) cavities classified by flushing time, with forcing parameters S_{CDW} and ξ set to their inter-annual means. The bistable region is colored in gray, such that the black solid and dashed lines highlight the warm-to-cold and cold-to-warm thresholds, respectively. The annual means for Σ [Nakata et al., 2021] and T_{CDW} [Burgard et al., 2022] are shown by white crosses (8 between 2003 and 2010 for each cavity) while the inter-annual average is shown by a white diamond. The white arrows indicate PICO T_{CDW} forcings [Reese et al., 2018]. Each panel is computed on a 120×120 grid of $\mathcal{A}_p$ and T_{CDW}. (j) Size of the bistable region in terms of sea-ice mass production versus basal mass-loss difference between the warm and cold modes, assuming inter-annual averages for ξ, T_{CDW}, and S_{CDW} for each cavity.

Table 2.4: Key box model diagnostics considering the model parameters listed in Table 2.1 and the forcing parameters listed in table 2.2 ($1\,\mathrm{Sv} = 10^6\,\mathrm{m}^3/\mathrm{s}$). We do not show any data when the regime is unstable ; for instance, our box model predicts that the warm diffusive regime is unstable for the Dotson ice-shelf cavity, which is why there is no data in the first two columns. We also show the melt rates from [Rignot et al., 2013] for comparison.

Cavity	$\mathbf{m}^{\mathrm{warm}}$ **[m/y]**	$\mathbf{q}_{\mathrm{cav}}^{\mathrm{warm}}$ **[Sv]**	$\mathbf{m}^{\mathrm{cold}}$ **[m/y]**	$\mathbf{q}_{\mathrm{cav}}^{\mathbf{cold}}$ **[Sv]**	$\mathbf{m}_{\mathbf{Rignot}}$ **[m/y]**
Ross	2.71	0.83	0.01	0.13	0.1±0.1
Filchner-Ronne	1.17	0.6	0.06	0.23	0.3±0.1
Amery	8.06	0.51	0.58	0.19	0.6±0.4
Dotson	-	-	1.11	0.05	7.8±0.6
Pine Island	24.74	0.23	3.79	0.1	16.2±1
Riiser-Larsen	6.66	0.3	0.67	0.12	0.2±0.2
Roi Baudouin	7.07	0.26	0.26	0.07	0.4±0.4
Totten	20.58	0.25	3.22	0.11	10.5±0.7
Moscow Univ.	18.78	0.17	-	-	4.7±0.8

As expected, low values of $\mathcal{A}_p$ and ξ favor the warm mode whereas high values of these parameters favor the cold mode. A bistable zone (in gray) is observed over a broad range of plausible parameters. Surprisingly, the cold mode remains stable in certain regions where $\xi < 0$ (gray regions on the left of the vertical dotted line). This is due to the effect of temperature on water density (Eq. (2.1)). The atmosphere cools the surface of the ocean and tends to destabilize the water column, hence supporting the cold mode. The warm mode melt rates have a very small response to the variation of $\mathcal{A}_p$ and ξ since the vertical mixing coefficient κ_{diff} is very small in this regime. However, the cold mode melt rates increase when $\mathcal{A}_p$ decreases, because less DSW can mix with CDW via the mixing flux $\mathcal{A}_p \kappa_{\mathrm{conv}}$.

2.3.3 Bistability for a broad range of parameterization choices

We now test the sensitivity of the bistable dynamics to different parameterization choices, considering both model parameters and functional forms. We select the Amery ice-shelf cavity without loss of generality as other cavities behave similarly (see Fig. 2.19 and Fig. 2.20 in Appendix 2.5). We first provide results on the dependence of the stable equilibrium states with PICO parameters, i.e. $\gamma_T^\star$ and C. Fig. 2.7(a,b) compares basal melt rates in the $\gamma_T^\star \times \mathcal{A}_p$ and $C \times \mathcal{A}_p$ parameter spaces. Increasing $\gamma_T^\star$ enlarges the bistable region because of the strengthening of the meltwater positive feedback loop (Fig. 2.7(a)). The melt rate of the diffusive regime increases with $\gamma_T^\star$ before a maximum is reached at $\gamma_T^\star \approx 3 \times 10^{-4}$ m/s. This non-monotonic behavior, which is observed for all large cavities, is due to the presence of large freezing areas at large $\gamma_T^\star$, which decrease the integrated melt rate and stem from the intense melt-induced cooling in the deepest cavity box. Fig. 2.7(b) show that the integrated melt rate increases with the overturning strength C. However, the meltwater also becomes increasingly diluted within the overturning water mass as C increases, such that the positive feedback loop weakens, resulting in a non-monotonic behavior of the warm-to-cold threshold as a function of C. This behavior is also observed in the low-dimensional model of [Moorman et al., 2020] with a non-monotonic behavior of the treshold when varying the inflowing volume flux in the cavity.

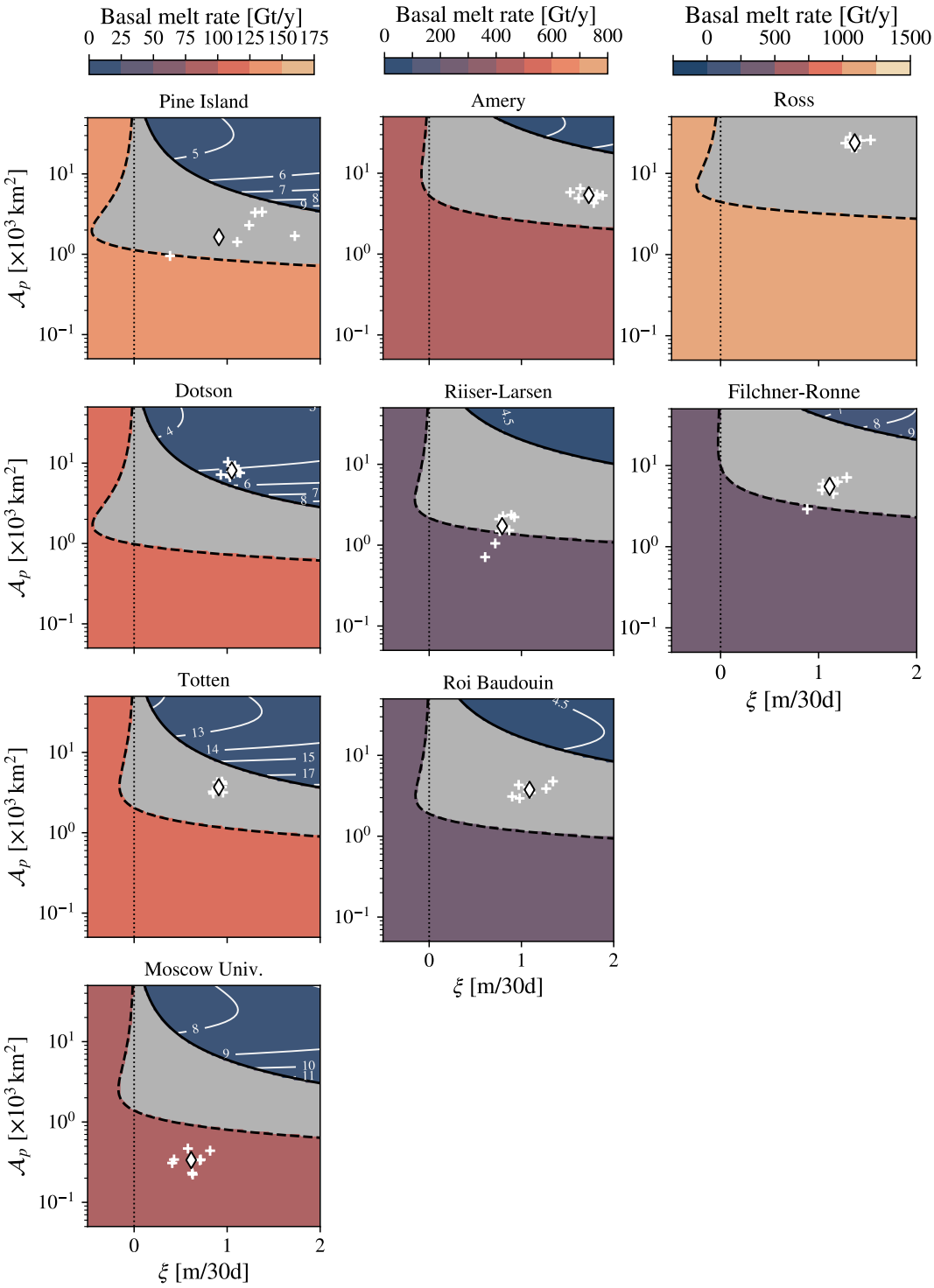

Figure 2.6: Basal mass loss $\mathcal{M}$ as a function of freezing rate ξ and polynya area $\mathcal{A}_p$, with forcing parameters S_{CDW} and T_{CDW} set to their inter-annual means. The bistable region is colored in gray, such that the black solid and dashed lines highlight the warm-to-cold and cold-to-warm thresholds, respectively. The vertical dotted lines represent $\xi = 0$.

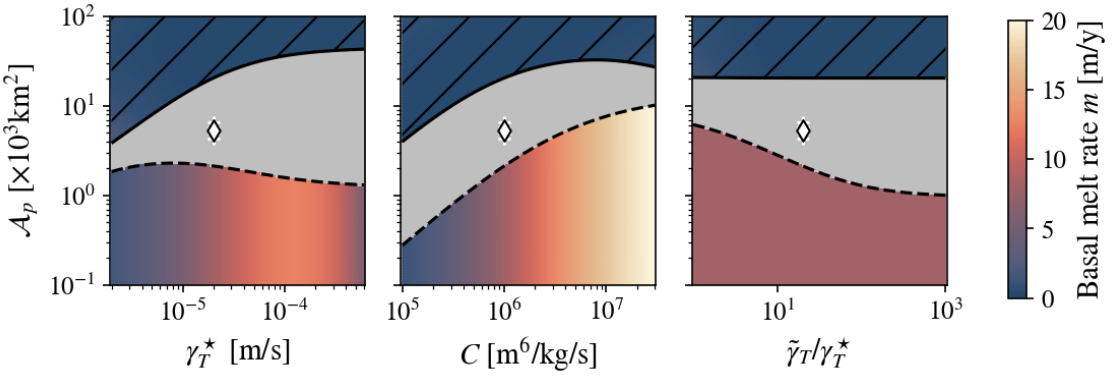

Figure 2.7: Basal melt rate beneath the Filchner–Ronne Ice Shelf as a function of the PICO parameters $\gamma_T^\star$ (a) and C (b), and of the effective turbulent heat transfer coefficient beneath the polynya, $\tilde{\gamma}_T$ (c), which is not included in the standard PICO formulation. Hatched regions indicate convective monostable regimes.

Fig. 2.7(c) shows the impact of mixing at the atmosphere-ocean interface, i.e., $\tilde{\gamma}_T$ (relative to $\gamma_T^\star = 2 \times 10^{-5}$ m/s) on the basal melt rate m. We expect $\tilde{\gamma}_T \geq \gamma_T^\star$ because dense brine rejections at the sea surface enhance mixing with box "p". The limiting case $\tilde{\gamma}_T \to +\infty$ is equivalent to setting $T_p = T_s$ (see Eq. (2.6a)) as in the [Hazel and Stewart, 2020] low-dimensional model. Increasing $\tilde{\gamma}_T$ increases the size of the convective region, because a higher $\tilde{\gamma}_T$ results in cooler surface water masses, reducing the basal melt rates.

We then test the impact of changing the functionality of parameterizations for processes inside the cavity, namely the overturning circulation q_{cav} and the effective turbulent heat transfer $\gamma_T^\star$, to test other choices than those done in PICO [Reese et al., 2018]. We denote by $q_{\text{cav}}^{\text{ref}} = 0.19\,\text{Sv}$ the reference circulation that is predicted by our default box model when the cavity is in the convective regime. The first row of Fig. 2.8 shows the basal mass loss $\mathcal{M}$ as a function of T_{CDW} and Σ when (a) $q_{\text{cav}} = q_{\text{cav}}^{\text{ref}}$ and $\gamma_T^\star$ are both constant, (b) $q_{\text{cav}} = C(\rho_d - \rho_{c,1})$ and $\gamma_T^\star$ is constant (our standard box model), and (c) $q_{\text{cav}} = C(\rho_d - \rho_{c,1})$ and $\gamma_T^\star = \Gamma q_{\text{cav}}$, i.e. the heat transfer coefficient is circulation dependent with $\Gamma = 1.2 \times 10^{-10}\,\text{m}^{-2} = \gamma_T^\star / q_{\text{cav}}^{\text{ref}}$, as in most regional ice-shelf ocean simulations [Asay-Davis et al., 2016]. The three cases present a bistable region, highlighting the robustness of the irreversibility of transitions against cavity parameterization changes. Both the basal mass loss (in the diffusive regime) and the size of the bistable region increase when we implement variable (in contrast to constant) cavity parameterizations. This is because variable parameterizations can enhance or contribute to additional positive feedback loops in the system. When q_{cav} and $\gamma_T^\star$ are constants, the only positive feedback stems from the release of meltwater, which stabilizes the water column [Hazel and Stewart, 2020, Moorman et al., 2023]. When we instead use $q_{\text{cav}} = C(\rho_d - \rho_{c,1})$, a new positive feedback is introduced: higher meltwater production within the cavity lowers $\rho_{c,1}$, and thus increases q_{cav}, delivering additional heat to the cavity. This parameterization yields mode-dependent overturning strengths: weak in the cold mode and strong in the warm mode (see Table 2.4), consistent with [Song et al., 2025]. Finally, setting $\gamma_T^\star = \Gamma q_{\text{cav}}$ further amplifies the meltwater feedback loop, since increased circulation increases meltwater production. With this last parameterization choice, the basal melt rate scales quadratically with the thermal driving of the cavity, as found in previous 3D

numerical simulations of ice shelf cavities [Holland et al., 2008]. The derivation of this scaling can be done analytically with a simplified model framework (see Appendix 2.5).

Finally, we discuss the impact of the vertical mixing scheme, keeping $q_{\text{cav}} = C(\rho_d - \rho_{c,1})$ and $\gamma_T^\star$ constant. We test in Fig. 2.8(d,e,f) the impact of a smooth dependence of κ on the density difference, i.e. of the form [Moorman et al., 2023, Welander, 1982]

$$\kappa = \frac{\kappa_{\text{conv}} - \kappa_{\text{diff}}}{2} \tanh\left(\frac{\rho_p - \rho_d}{\Lambda}\right) + \frac{\kappa_{\text{conv}} + \kappa_{\text{diff}}}{2}, \tag{2.9}$$

where $\Lambda\,[\text{kg/m}^3]$ is a smoothening parameter that regularizes the step function. We show the results in Fig. 2.8(d,e,f) for $\Lambda = 0.15, 0.30, 0.45\,\text{kg/m}^3$. The bistable region shrinks as Λ increases, consistent with [Moorman et al., 2023]. For $\Lambda > \Lambda_c = \mathcal{O}(0.1)\,\text{kg/m}^3$, the bistable region disappears, such that the transition between the two modes become continuous and reversible. We show in Section 2.4.5 that this change of behavior results from the collapse of two saddle-node bifurcations into a single stable equilibrium, characteristic of a cusp bifurcation. The value of Λ_c is comparable to the range of density differences observed during warm-to-cold transitions [Haid et al., 2023]. Consequently, we are in the critical case where the system should lie between the two extreme regimes: κ behaves as a step function because the variations of $\rho_p - \rho_p$ are bigger than Λ_c, leading to irreversible dynamics, and κ behaves linearly because the variations of $\rho_p - \rho_p$ are smaller than Λ_c ($\tanh(x) \sim x$ when $x \to 0$), leading to reversible dynamics.

2.3.4 Dense Shelf Water outflow

We observe anomalously large salinities in the convective regime (see e.g., S_d in Fig. 2.9(b)), because the surface outflow q_{CDW} is much smaller than the mixing volume flux $\mathcal{A}_p\kappa_{\text{conv}}$, such that the polynya salinity is trapped within the overturning flow. In a convective configuration, this excess of salt is not unphysical as we expect the formation of DSW transforming into Antarctic Bottom Water (AABW) once it flows down the continental slope. To test the impact of DSW formation on our results, we augmented our standard model with a counter-clockwise overturning circulation q_{DSW} at the ice-shelf front representing the DSW outflow, as sketched in Fig. 2.9(a). Specifically this led to the modification of Eqs. (2.6a)-(2.6d) as

$$\begin{aligned} V_p\dot{T}_p = {} & q_{\text{cav}}(T_{c,N_{\text{PICO}}} - T_p) - \mathcal{A}_p\kappa(T_p - T_d) + \mathcal{A}_p\tilde{\gamma}_T[T_s(S_p) - T_p] \\ & + q_{\text{DSW}}(T_{\text{surf}} - T_p), \end{aligned} \tag{2.10a}$$

$$V_p\dot{S}_p = q_{\text{cav}}(S_{c,N_{\text{PICO}}} - S_p) - \mathcal{A}_p\kappa(S_p - S_d) + \frac{\rho_{\text{ice}}}{\rho_\star}\mathcal{A}_p\xi S_p + q_{\text{DSW}}(S_{\text{surf}} - S_p), \tag{2.10b}$$

$$V_d\dot{T}_d = (1-r)q_{\text{cav}}(T_{\text{CDW}} - T_d) + (\mathcal{A}_p\kappa + rq_{\text{cav}} - q_{\text{DSW}})(T_p - T_d), \tag{2.10c}$$

$$V_d\dot{S}_d = (1-r)q_{\text{cav}}(S_{\text{CDW}} - S_d) + (\mathcal{A}_p\kappa + rq_{\text{cav}} - q_{\text{DSW}})(S_p - S_d), \tag{2.10d}$$

where T_{surf} and S_{surf} are the surface temperatures and salinities northward of box "p". In practice, T_{surf} and S_{surf} are water properties at the sea surface extracted from the data set of [Burgard et al., 2022], using offshore profiles to minimize the impact of meltwater

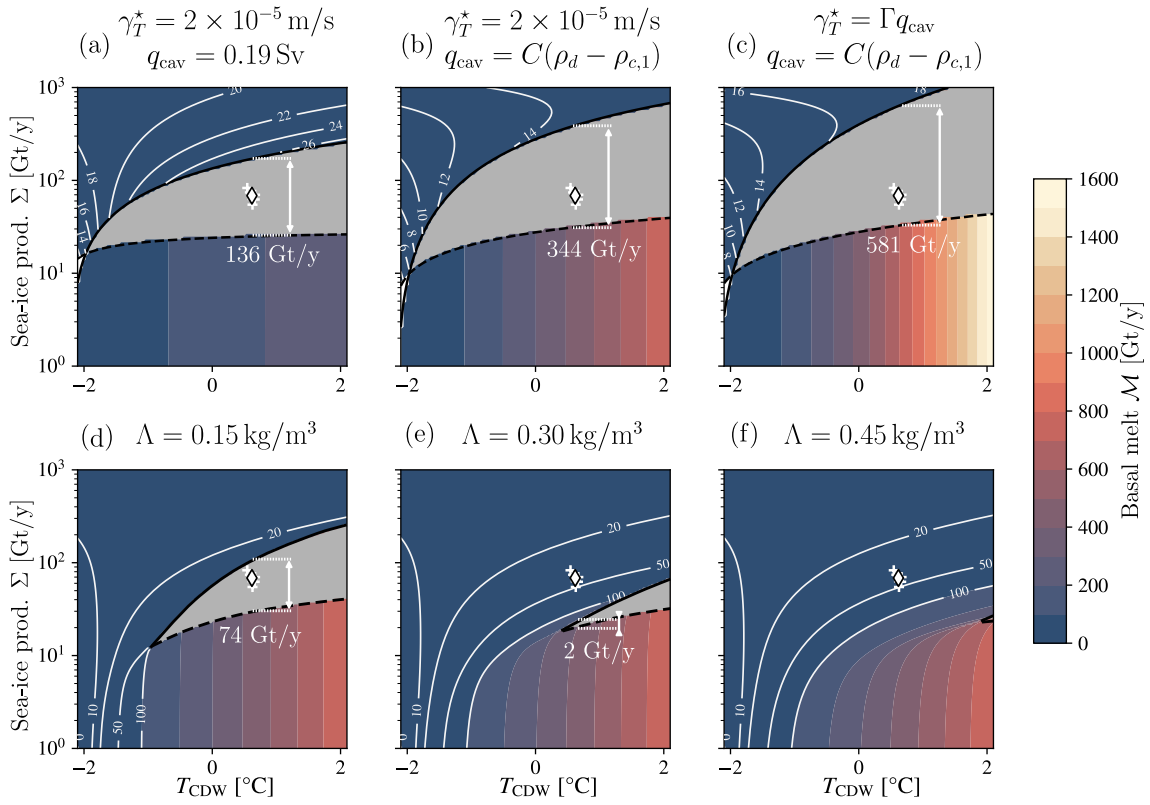

Figure 2.8: Basal mass loss $\mathcal{M}$ for the Amery ice shelf as a function of T_{CDW} and Σ, for different cavity parameterizations: (a) constant q_{cav} and $\gamma_T^\star$, (b) $q_{\mathrm{cav}} = C(\rho_d - \rho_{c,1})$ and constant $\gamma_T^\star$, and (c) $q_{\mathrm{cav}} = C(\rho_d - \rho_{c,1})$ and $\gamma_T^\star = \Gamma q_{\mathrm{cav}}$. In (d,e,f), we use a smooth parameterization for vertical mixing (Eq. (2.9)), varying the smoothening density step Λ.

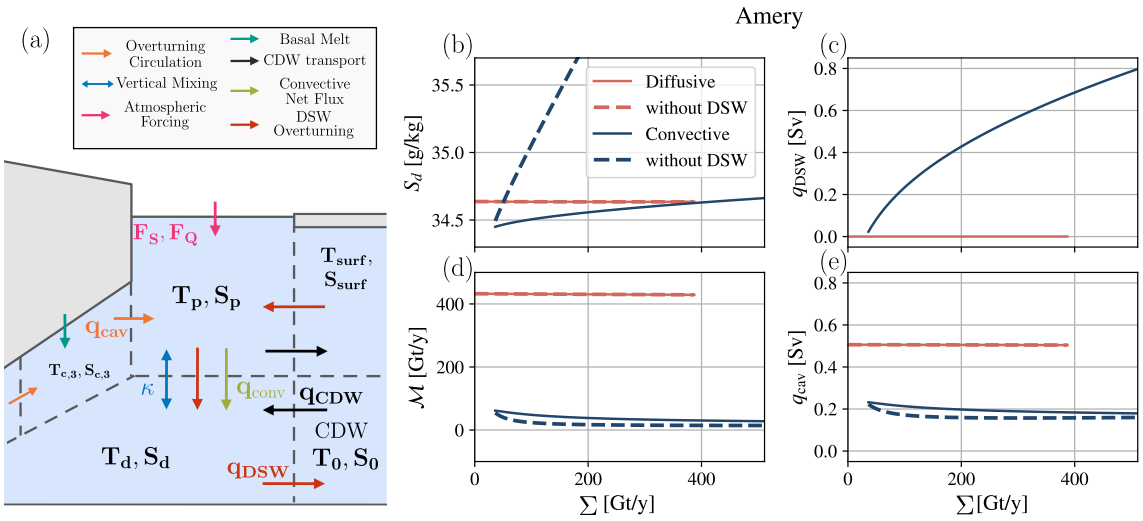

Figure 2.9: (a) Schematic of the box model including DSW overturning. (b)-(e) Comparison of key output for the Amery ice shelf obtained with our standard box model, using $r = 0$ (dashed lines), and the box model including DSW outflow (solid lines). The output, which we show as functions of sea-ice mass production Σ, are (b) the salinity in the deep ocean box, (c) the strength of the DSW flow ($1\,\mathrm{Sv} = 10^6\,\mathrm{m}^3/\mathrm{s}$) (which is 0 when DSW outflow is not included), (d) the basal mass losses, and (e) the cavity overturning strength. The blue (resp. red) color denotes the convective (resp. diffusive) regime.

coming out of the cavity. We assume that the DSW overturning flow can be modelled as a gravity current at the continental shelf break, such that

$$q_{\mathrm{DSW}} = \max\{0, C_{\mathrm{DSW}}(\rho_d - \rho_{\mathrm{CDW}})\}, \tag{2.11}$$

where C_{DSW} characterizes the strength of the DSW overturning flow. Fig. 2.9(c) shows q_{DSW} for the Amery ice shelf. In the convective regime, the DSW outflow increases with the sea-ice mass production Σ and thus with brine rejection, whereas in the diffusive regime we do not observe DSW formation, as expected. Fig. 2.9(b) shows that the anomalous excess of salinity is mitigated by the DSW outflow. Fig. 2.9(d,e) show that the thresholds for the transitions, the basal melt rates and the cavity overturning strength are not significantly affected by the addition of DSW formation.

Table 2.5 shows the values of the DSW overturning volume fluxes using interannual mean forcing from Table 2.2.

2.3.5 Discussion

We have applied a generic low-dimensional model of sub ice-shelf seas to nine ice-shelf cavities and identified their stable equilibrium states (warm diffusive or cold convective) for a broad range of forcing parameters. Using realistic forcing values (white diamonds in Fig. 2.5), the predicted states are consistent with the actual cavity states (bistability remains consistent with observations, as either state may occur), except for the Dotson ice-shelf cavity, which we predict to be convective while observations suggest a diffusive regime [Miles et al., 2016]. A possible explanation is that our model does not take into account teleconnections, and specifically the input of meltwater from adjacent warm cavities, which [Silvano et al., 2018] showed can impact the Dotson and Totten ice-shelf

Table 2.5: DSW outflow considering the model parameters listed in Table 2.1 and the forcing parameters listed in table 2.2 ($1\,\mathrm{Sv} = 10^6\,\mathrm{m}^3/\mathrm{s}$). We do not show any data for the Moscow University ice shelf as our model predicts that the cold regime is unstable.

Cavity	$\mathbf{q}_{\mathrm{DSW}}$ **[Sv]**
Ross	0.44
Filchner-Ronne	0.06
Amery	0.15
Dotson	0.14
Pine Island	0.03
Riiser-Larsen	0.01
Roi Baudouin	0.09
Totten	0.1
Moscow Univ.	-

cavities by favoring the diffusive mode. Our model predicts plausible basal mass losses (see comparison with [Rignot et al., 2013] in Table 2.4). We remark that it underestimates convective-regime melt rates for the Ross and Filchner–Ronne ice shelves, likely due to the absence of mode III [Silvano et al., 2016]. For these two ice shelves, we thus expect that the sea-ice production threshold for cold-to-warm transitions is underestimated, as freshwater fluxes from the cavity to the polynya box "p" are underestimated. Conversely, melt rates in the diffusive regime for warm cavities (e.g., Pine Island) are overestimated. This is because CDW transformation processes other than with polynyas are not represented though they are expected to decrease CDW temperatures [Tamsitt et al., 2021] (see Fig. 2.17). Thus, we expect that the model overestimates the sea-ice production threshold of the warm-to-cold transition for warm cavities. We note that PICO melt rates better match observations because they are forced with observed continental-shelf deep-water properties (see white arrows in Fig. 2.5). In contrast, our model infers these water properties (box "d") from offshore CDW and polynya forcing, allowing predictions of warm regime melt rates for currently cold cavities.

We have shown that reductions in sea-ice mass production Σ can induce convective-to-diffusive tipping (and vice versa), in agreement with previous studies that demonstrated cold-to-warm regime shifts when the continental shelf freshens using both realistic simulations [Hellmer et al., 2017, Daae et al., 2020, Hazel and Stewart, 2020, Naughten et al., 2021, Haid et al., 2023, Mathiot and Jourdain, 2023, Caillet et al., 2023, Jin et al., 2025] and low-dimensional models [Hazel and Stewart, 2020, Moorman et al., 2023]. For cold cavities, an estimate of how far they stand from the critical threshold of a cold-to-warm transition is given by their distance from the black dashed line in the phase space of Fig. 2.5(a-i). This dashed line is easier to cross varying Σ than T_{CDW}, though higher T_{CDW} can also move cavities closer to the transition threshold, consistent with realistic modeling studies that linked CDW warming to transitions [Jin et al., 2025, Mathiot and Jourdain, 2023, Daae et al., 2020] and low-dimensional models [Moorman et al., 2023]. A future reduction in coastal polynya extent would therefore facilitate cold-to-warm transitions in ice-shelf cavities [Golledge et al., 2025]. Bistability is robust across cavity parameterizations, but its extent depends on their contribution to the meltwater positive feedback loop.

A limitation of our model stems from the omission of continental shelf–break dynamics

that can modulate CDW inflows onto the shelf, possibly through (positive or negative) large-scale feedback [Thompson et al., 2018, Lanham et al., 2025]. [O'Connor et al., 2025] recently showed that increased stratification on the Amundsen Sea continental shelf could lead to stronger shelf-break CDW undercurrent, enhancing CDW on-shelf intrusions. Such a positive feedback between CDW inflow and stratification, if represented in our model, would not impact the existence of the diffusive and convective modes but would extend the region of bistability. The inclusion of additional CDW modification pathways would be a natural direction for future model development. The neglect of DSW outflow in our model is another limitation that results in anomalously high salinities in convective cavities, since q_{CDW} (the only pathway out of the system) is much smaller than the mixing flux $\mathcal{A}_p \kappa_{\mathrm{conv}}$ that traps salinity within the system. This excess salinity may be interpreted as a signature of dense shelves, which usually feature salty DSW outflows across the shelf break [Thompson et al., 2018]. We tested the sensitivity of our results to DSW outflows by adding an anti-clockwise circulation on the shelf in our box model. Considering DSW outflows constrains salinity to more realistic values but has limited impact on the transition thresholds and model outputs.

We restricted our attention to steady solutions, which is a valid approximation when dynamical fluctuations occur on long time scales compared to the flushing time τ_{flush} of a cavity [Holland, 2017]. Shorter-term variability (e.g., seasonal fluctuation of surface buoyancy fluxes) is expected to induce more complex dynamics and thus should be explicitly modeled for reliable predictions. On the one hand, cavity inertia may damp fast fluctuations and allow critical thresholds to be transiently crossed without regime shifts. On the other hand, chaotic behaviors or noise-induced bifurcations may arise [Dijkstra, 2013]. Temporal variability does not affect the bistable cavity dynamics, as bistability is an equilibrium property identified from the steady-state analysis of the system. Understanding how temporal variability interacts with multiple equilibrium cavity states nonetheless represents an important avenue for future research, which cannot be addressed with our current model formulation but is well-suited for regional simulations. The Chapter 5 of this manuscript will indeed be dedicated to study the dynamics of ice-shelf cavities when a transient forcing is imposed. Fig. 2.5 shows our model results in groups ordered by flushing times to identify critical time scales for regime shifts. Ice-sheet time scales are much longer than the longest flushing times of ice-shelf cavities. Thus, our steady-state model provides an appropriate means of including oceanic tipping points in ice-sheet simulations that parameterize basal melting [Khrulev et al., 2025, Garbe et al., 2020, Kreuzer et al., 2021].

The reversibility of transitions in ice-shelf cavities remains debated within the community. For the Filchner-Ronne ice shelf, several studies reported an hysteresis [Hellmer et al., 2017, Hazel and Stewart, 2020, Haid et al., 2023], while [Reese et al., 2026] found a reversible transition. Similarly, [Moorman et al., 2023] observed hysteresis in the Dotson cavity using a low-dimensional model, while [Caillet et al., 2023] reported reversible transitions in Amundsen Sea cavities with a regional ocean model. Here, we have shown that both types of transition are possible, depending on the vertical mixing scheme at the ice-shelf front. This suggests that improved representations of vertical mixing in ocean simulations (e.g., Eddy-Diffusivity Mass-Flux [Giordani et al., 2020, Gülk et al., 2024]) are essential to reliably predict not only deep convection but also regime shifts in ice-shelf cavities.

Take-Home Messages

1. We presented a low-dimensional box model of ice-shelf cavities capturing polynya-induced transitions between cold and warm circulation regimes.
2. Several Antarctic ice-shelf cavities are in a bistable regime and are susceptible to irreversible abrupt transitions.
3. Bistability is robust against changes in cavity parameterizations but is sensitive to the vertical mixing scheme at the ice-shelf front.

2.4 Analytical and graphical solutions

We now propose to investigate in detail the low-dimensional model within the framework of dynamical system theory. We first provide analytical results obtained for a simplified version of the model. We analyze the stability of the fixed points and we derive scaling laws for the basal melt rates and the transition thresholds. Then, we propose graphical interpretations for the system dynamics. Finally, we characterize the bifurcation behavior of the system more precisely, showing that it can be classified as a cusp bifurcation.

2.4.1 Simplified model equations

The steady-state solutions presented previously are obtained by solving Eqs. (2.6a)-(2.6h) numerically. Here we provide a simplified and non-dimensionalized set of equations to further characterize the properties of the two modes and discuss the influence of the control parameters. For simplicity, we set $r = 0$ and we use a single cavity box. The first approximations we implement are related to exchange terms at the ice-ocean interfaces. Let us decompose $S_c = S_\star + S'_c$ and $S_p = S_\star + S'_p$ ($S_\star$ being the reference salinity). The hypotheses that make the governing equations tractable analytically, which we have verified are valid for the range of conditions considered, are:

(H1): $\left|\frac{S'_c}{S_\star}\right| \ll 1$, which allows to simplify the thermal driving term in the cavity as

$$\begin{aligned} T_c - T_b(S_c, h_c) &= T_c - aS_c - b + ch_c \\ &= T_c - aS_\star - b + ch_c + \mathcal{O}\left(\frac{S'_c}{S_\star}\right) \\ &= T_c - T_b(S_\star, h_c) + \mathcal{O}\left(\frac{S'_c}{S_\star}\right), \end{aligned} \tag{2.12}$$

and the salinity flux in the cavity as

$$\mathcal{A}_c \frac{c_\star}{\mathcal{L}} S_c \gamma_T^\star [T_c - T_b(S_c, h_c)] = \mathcal{A}_c \frac{c_\star}{\mathcal{L}} S_\star \gamma_T^\star [T_c - T_b(S_\star, h_c)] + \mathcal{O}\left(\frac{S'_c}{S_\star}\right), \tag{2.13}$$

where Eq. (2.12) simply implies that salinity-induced variations of thermal driving are neglected at leading order.

(H2): $\left|\frac{S'_p}{S_\star}\right| \ll 1$, which, similarly to (H1), allows to simplify the thermal driving term in the polynya box at leading order as

$$T_p - T_s(S_p) = T_p - T_s(S_\star) + \mathcal{O}\left(\frac{S'_p}{S_\star}\right), \tag{2.14}$$

and the salinity flux in the polynya box as

$$\frac{\rho_{\text{ice}}}{\rho_\star} S_p \mathcal{A}_p \xi = \frac{\rho_{\text{ice}}}{\rho_\star} S_\star \mathcal{A}_p \xi + \mathcal{O}\left(\frac{S'_p}{S_\star}\right). \tag{2.15}$$

Eqs. (2.6a)-(2.6h) can be rewritten under hypotheses (H1) and (H2) at steady states as

$$0 = q_{\text{cav}}(T_c - T_p) - \mathcal{A}_p \kappa (T_p - T_d) + \mathcal{A}_p \tilde{\gamma}_T [T_s(S_\star) - T_p], \tag{2.16a}$$
$$0 = q_{\text{cav}}(S_c - S_p) - \mathcal{A}_p \kappa (S_p - S_d) + \frac{\rho_{\text{ice}}}{\rho_\star} S_\star \mathcal{A}_p \xi, \tag{2.16b}$$
$$0 = q_{\text{cav}}(T_{\text{CDW}} - T_d) + \mathcal{A}_p \kappa (T_p - T_d), \tag{2.16c}$$
$$0 = q_{\text{cav}}(S_{\text{CDW}} - S_d) + \mathcal{A}_p \kappa (S_p - S_d), \tag{2.16d}$$
$$0 = q_{\text{cav}}(T_d - T_c) - \mathcal{A}_c \gamma_T^\star [T_c - T_b(S_\star, h_c)], \tag{2.16e}$$
$$0 = q_{\text{cav}}(S_d - S_c) - \mathcal{A}_c \frac{c_\star}{\mathcal{L}} S_\star \gamma_T^\star [T_c - T_b(S_\star, h_c)]. \tag{2.16f}$$

We non dimensionalize Eqs. (2.16a)-(2.16f) to clearly identify the independent control parameters. To this end, we define the non-dimensional temperatures x_i and salinities y_i as

$$x_i = \frac{T_i - T_b(S_\star, h_c)}{T_s(S_\star) - T_b(S_\star, h_c)} \quad \text{and} \quad y_i = \frac{S_i - S_{\text{CDW}}}{S_\star}, \quad i \in \{p, d, c\}. \tag{2.17}$$

The density difference σ between boxes "p" and "d" now reads

$$\sigma = \frac{\rho_p - \rho_d}{\rho_\star} = -\tilde{\alpha}(x_p - x_d) + \tilde{\beta}(y_p - y_d), \tag{2.18}$$

with $\tilde{\alpha} = (T_s - T_b)\alpha$ and $\tilde{\beta} = S_\star \beta$ the non-dimensional thermal expansion and haline contraction coefficients. We now consider that the circulation is prescribed rather than buoyancy driven (i.e., $q_{\text{cav}} = \text{cst}$). Then, the steady-state solutions are fully prescribed by four normalized environmental parameters

$$\begin{cases} f_S = \frac{\rho_{\text{ice}}}{\rho_\star} \frac{\xi}{\gamma_T^\star} & \text{normalized surface salt flux,} \\ x_{\text{CDW}} = \frac{T_{\text{CDW}} - T_b(S_\star, h_c)}{T_s(S_\star) - T_b(S_\star, h_c)} & \text{normalized CDW temperature,} \\ \chi = \frac{q_{\text{cav}}}{\mathcal{A}_c \gamma_T^\star} & \text{normalized overturning circulation,} \\ \Phi = \frac{\mathcal{A}_p}{\mathcal{A}_c} & \text{normalized polynya area,} \end{cases} \tag{2.19}$$

and three model parameters

$$\begin{cases} k = \kappa / \gamma_T^\star & \text{normalized vertical mixing velocity,} \\ \delta = \frac{c_\star}{\mathcal{L}}(T_s - T_b) & \text{Stefan number of the cold mode,} \\ g = \tilde{\gamma}_T / \gamma_T^\star & \text{normalized surface mixing velocity of box "p".} \end{cases} \tag{2.20}$$

The dynamical system Eqs. (2.16a)-(2.16f) can be recast in matrix form using the dimensionless variables as

$$M_k X + F = 0, \quad k = \begin{cases} k_{\text{diff}} & \text{if } \sigma \leq 0\,, \\ k_{\text{conv}} & \text{otherwise,} \end{cases} \tag{2.21}$$

with

$$X = \begin{pmatrix} x_p \\ x_d \\ x_c \\ y_p \\ y_d \\ y_c \end{pmatrix}, \qquad F = \begin{pmatrix} \Phi g \\ \chi x_{\text{CDW}} \\ 0 \\ \Phi f_s \\ 0 \\ 0 \end{pmatrix}, \tag{2.22}$$

and

$$M_k = \left(\begin{array}{ccc|ccc} -\chi - \Phi k - \Phi g & \Phi k & \chi & 0 & 0 & 0 \\ \Phi k & -\chi - \Phi k & 0 & 0 & 0 & 0 \\ 0 & \chi & -\chi - 1 & 0 & 0 & 0 \\ \hline 0 & 0 & 0 & -\chi - \Phi k & \Phi k & \chi \\ 0 & 0 & 0 & \Phi k & -\chi - \Phi k & 0 \\ 0 & 0 & -\delta & 0 & \chi & -\chi \end{array}\right), \tag{2.23}$$

hence is linear, thanks to (H1)-(H2) and the assumption of constant overturning (this last assumption can be in fact relaxed as shown in Appendix 2.5). Here, X is the dynamical state vector, F represents the external forcing, and M_k is a triangular block matrix with the upper left and lower right blocks accounting for temperature and salinity effects, respectively. The lower left block has a single non-zero term due to basal melting, which couples the temperature and salinity variables.

2.4.2 Equilibrium states and stability

When q_{cav} is prescribed, χ does not depend on the dynamical variables x_i and y_i ($i \in \{p, d, c\}$). Thus, Eq. (2.21) is a fully linear forced set of equations and the equilibrium states are given by

$$X_k = -M_k^{-1} F, \quad k \in \{k_{\text{diff}}, k_{\text{conv}}\}\,. \tag{2.24}$$

We aim to determine how these fixed points react to small perturbations, i.e., to characterize their dynamical stability. The study of the eigenvalues of the matrix M_k allows quantifying the response of the system to such perturbations along its characteristic directions. The system is attracted back to the fixed point along a characteristic direction if the associated eigenvalue is negative, and repelled otherwise. Thus, a fixed point is linearly stable if and only if the real parts of all its eigenvalues are negative. Here, M_k is a block triangular matrix, which we can rewrite as follows:

$$M_k = \begin{pmatrix} M_T & 0_3 \\ M_{TS} & M_S \end{pmatrix}, \tag{2.25}$$

with M_T, M_S and M_{TS} three 3×3 matrix. Its eigenvalues are solutions of $\det(\lambda I_3 - M_T) = 0$ and $\det(\lambda I_3 - M_S) = 0$, which are third-order polynomial equations in λ. The real part of

the eigenvalues of M_T and M_S can be shown to be negative thanks to the Rough-Hurwitz stability criterion. Let us write the characteristic polynomial of matrix M_S as

$$P_S(\lambda) = \lambda^3 + \chi(3+2u)\lambda^2 + \chi^2(3+4u)\lambda + \chi^3(1+u)\,, \tag{2.26}$$

with $u = \Phi k/\chi$ the ratio between the mixing volume flux and the overturning volume flux. Rewriting more generally all third-order polynomials as $P(\lambda) = \sum_{i=0}^{3} a_i\lambda^i$, the Rough-Hurwitz criterion guarantees that the solutions are linearly stable if and only if $a_i > 0\ \forall i \in \{0,\dots,3\}$ and $a_2a_1 - a_3a_0 > 0$, which is always true in our case since the two equivalent criteria $\chi > 0$ and $u \geq 0$ for our case are naturally satisfied.

We can similarly show that the eigenvalues of M_T have negative real parts. Let us denote by $w = \Phi g/\chi$ the ratio between the surface mixing volume flux and the overturning volume flux. Then, the coefficients of the characteristic polynomial read

$$\begin{cases} a_3 = 1, \\ a_2 = 1 + \chi(3+2u+w), \\ a_1 = \chi(2+2u+w) + \chi^2[3+4u+w(2+u)], \\ a_0 = \chi^2[1+2u+w(1+u)] + \chi^3(1+u)(1+w), \end{cases} \tag{2.27}$$

and can be shown to satisfy the Rough-Hurwitz stability criterion as long as $\chi > 0$, $u \geq 0$ and $w \geq 0$, which are conditions that are also naturally satisfied.

2.4.3 Graphical solutions

The previous section allowed to define the fixed points (see Eq. (2.24)) and prove their dynamical stability. Here, we adopt a graphical approach to verify the existence conditions of the fixed points discussed in Section 2.2.2. The phase plane $(y_p - y_d) \times (x_p - x_d)$ is divided into two zones by the solution of the density equation $\sigma = 0 \Leftrightarrow (y_p - y_d) = \frac{\tilde{\alpha}}{\tilde{\beta}}(x_p - x_d)$ (black dotted line in Fig. 2.10). Above this line, only the convective regime exists, whereas below it, only the diffusive regime exists. We show in Fig. 2.10 the steady-state solutions X_k in the $(y_p - y_d) \times (x_p - x_d)$ plane obtained for values of k in $[0, +\infty[$ (black solid curves). The point $(0,0)$ is reached for $k \to +\infty$ as it reflects a perfect vertical mixing of boxes "p" and "d". The other extremity of the curve is obtained for $k = 0$ when no exchanges occur between the two boxes. Fig. 2.10(a,b) show cases where the imposed forcing only allow to reach a single regime as the entire black solid curve is contained within the same zone: diffusive in (a) for $f_S = 0$ and convective in (b) for $f_S = 0.1$. We set the value of $k_{\text{conv}} = 20$ and $k_{\text{diff}} = 0.2$ to find the steady state solutions for the cold mode (blue dot) and the warm mode (res dot), respectively. We represent the velocity field $(\dot{x}_p - \dot{x}_d, \dot{y}_p - \dot{y}_d)$ associated to these specific solutions in their existence region. Even when the fixed lie outside their respective existence regions, they remain attractors for trajectories originating within those regions. For example, in Fig. 2.10(b), if the initial state of the system lies in the diffusive zone, it evolves toward the red dot, as indicated by the black arrows. Once the black-dotted line is crossed, the system enters the convective zone, whose attractor is the blue dot. Consequently, the system reaches the convective steady state, even though it initially started in the diffusive region. However, we can also impose forcing conditions that allow both steady-state solutions to exist and be stable, as in Fig. 2.10(c), for intermediate values of f_S. In this bistable case, the final state of the system is conditioned on its initial position

within the $(y_p - y_d) \times (x_p - x_d)$ plane. In Fig. 2.10(d), we also vary x_{CDW} and set it to zero, such that CDW temperatures are lower than surface temperatures, which is very unrealistic in Antarctic marginal seas. However, imposing this forcing is of theoretical interest since in this case the meltwater feedback becomes negative. Specifically, the convective mode now brings relatively warm waters into the cavity, stabilizing the water column under the polynya, while the diffusive mode now brings relatively cold waters in the cavity, destabilizing the water column. Consequently, both steady-state solutions do not respect their existence condition, resulting in the system oscillating between the two solutions, similar to the heat-salt oscillator model proposed by [Welander, 1982]. This work was investigating the dynamics of a surface mixed layer subject to heat and salt surface forcing.

With a standard forcing $x_{\mathrm{CDW}} > 1$ ($T_{\mathrm{CDW}} > T_s$), the solutions of the system can be obtained for multiple values of the forcing parameter f_S. Fig. 2.11(a) shows the steady-state solutions of the system in the $(y_p - y_d) \times (x_p - x_d)$ plane. Curve colors range from blue ($f_S = 0$) to green ($f_S = 0.11$) depending on the imposed f_S parameter value. Starting from $f_S = 0$, the only possible state is the warm state (red dot) as the whole curve lies in the diffusive zone. Then, increasing slowly f_S, the system follows the dashed line trajectory and remains attracted by the warm steady-state solution as long as it remains in the diffusive zone. However, when crossing the dotted line $\sigma = 0$, the system enters the convective zone and becomes attracted by the cold steady-state solution (blue dot) associated with the same f_S values, resulting in a jump in the $(y_p - y_d) \times (x_p - x_d)$ plane. The system then remains attracted to the cold steady-state solution while still lying within the convective zone. If f_S is subsequently decreased, the line $\sigma = 0$ is not crossed at the same value of f_S but follows a hysteresis trajectory.

Fig. 2.11(b) shows the value of x_c, the dimensionless temperature in the cavity, associated to the quasi-static trajectory, which also characterizes the basal melt rate since $m = \gamma_T^\star \delta \frac{\rho_\star}{\rho_{\mathrm{ice}}} x_c$. We recover the hysteresis behavior for the basal melt rate observed in Fig. 2.2(b) and now have a graphical understanding of the transition thresholds thanks to Fig. 2.11(a).

The same quasi-static experiments can be performed by varying other forcing parameters. Fig. 2.12 shows results varying x_{CDW} (CDW temperature), χ (CDW inflow), and Φ (polynya area). They all result in hysteresis behaviors. However, the trajectories in the $(y_p - y_d) \times (x_p - x_d)$ phase plane are more complex since, contrary to f_S, these forcing affect both the temperature and the salinity of the system. One consequence is that the basal melt rate response is not constant but varies within each regime.

Flip-flop dynamics: the case of the Filchner ice-shelf cavity

To close this section, we return to the flip-flop dynamics regime, which was previously excluded because it is not expected under realistic forcing conditions associated with CDW or DSW intrusions into ice-shelf cavities. The development of flip-flop dynamics requires deep water intruding the cavity colder than DSW formed at the sea surface. This condition is unrealistic for most cavities that have CDW as the intruding water mass, since CDW is always warmer than DSW.

The Filchner-Ronne ice shelf is constitued of two ice shelves that merge south of the Berkner Island. The eastern Filchner ice shelf is smaller than the western Ronne ice shelf

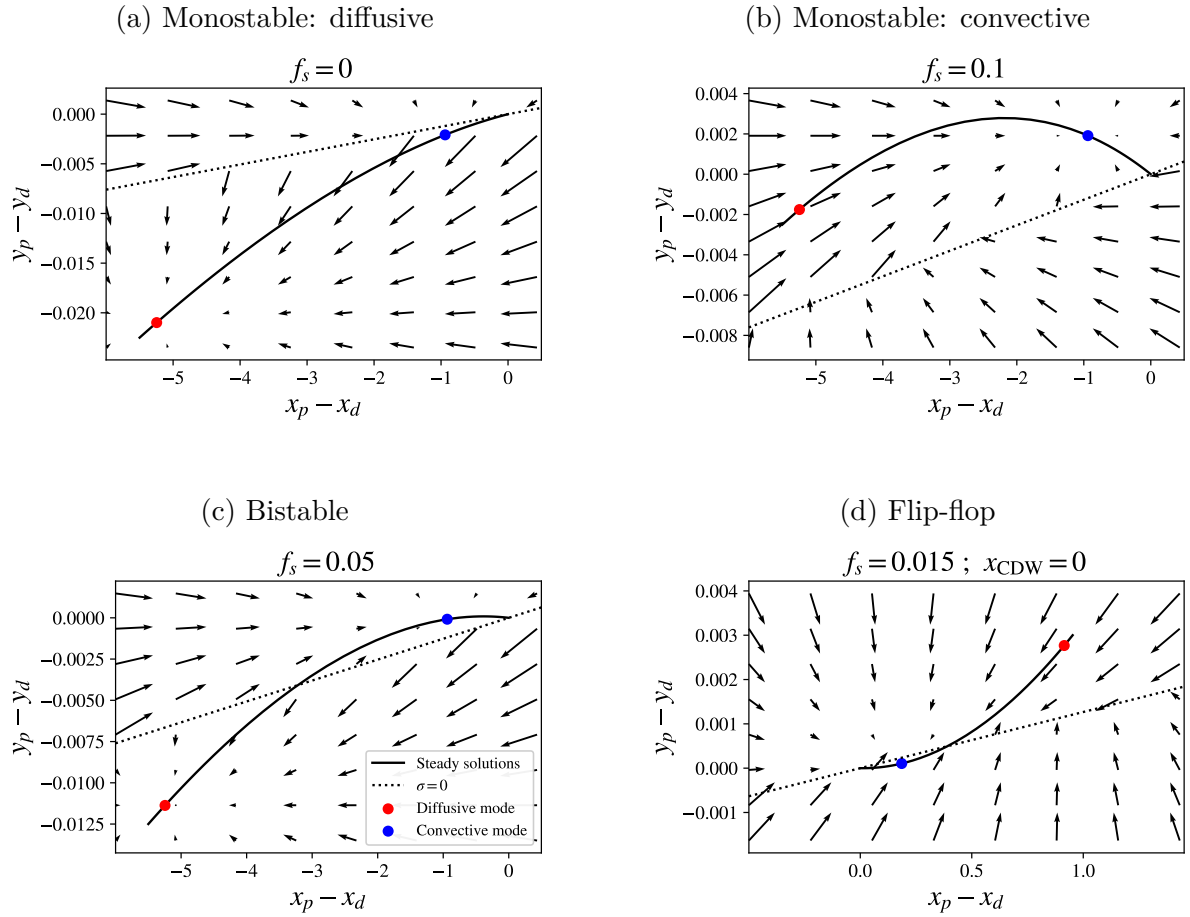

Figure 2.10: Diagrams of solutions in the phase plane $(y_p - y_d) \times (x_p - x_d)$ for different values of f_S. The dotted line indicates $\sigma = \frac{\rho_p - \rho_d}{\rho_\star} = 0$. Above (resp. below) this line lies the domain of existence of the convective (resp. diffusive) regime. The black solid line indicates all possible steady states for values of $k \in [0, +\infty[$. The red dot corresponds to the solution obtained with $k_{\mathrm{diff}} = 0.2$ whereas the blue dot is obtained for $k_{\mathrm{conv}} = 20$. The field of arrows represents the velocity field $(\dot{x}_p - \dot{x}_d, \dot{y}_p - \dot{y}_d)$. Other parameters are set to $\chi = 0.5$, $\Phi = 0.1$, $g = 10$, $x_{\mathrm{CDW}} = 7$ and $\delta = 5 \times 10^{-3}$.

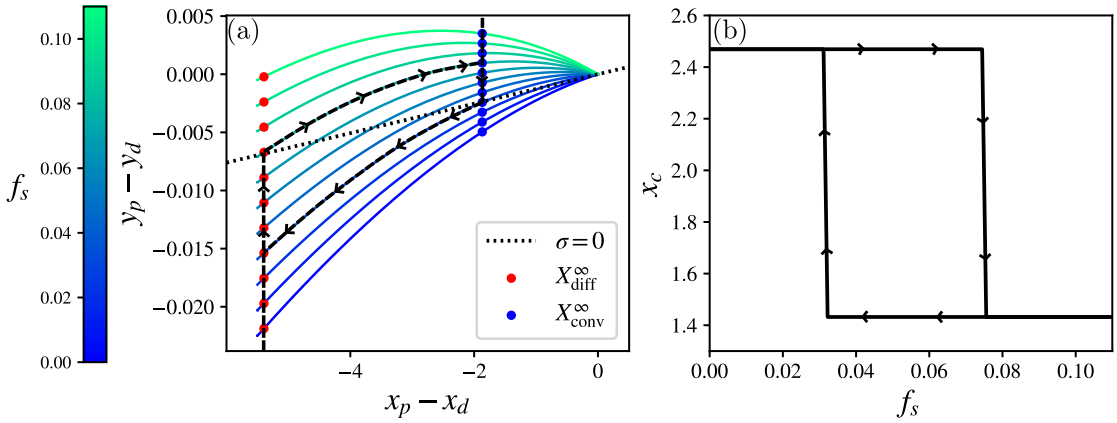

Figure 2.11: Steady state solutions in phase space. (a) Blue dots and red dots represent convective and diffusive steady states, respectively, for different values of f_s. The dashed black line shows a quasi-static experiment in the $(y_p - y_d) \times (x_p - x_d)$ space, increasing f_s from 0 to 0.11, and then decreasing it back. (b) Associated steady-state values for x_c. In both plots, $\chi = 0.5$, $\Phi = 0.1$, $g = 10$, $x_{\text{CDW}} = 7$, $\delta = 5 \times 10^{-3}$, $k_{\text{diff}} = 0.08$ and $k_{\text{conv}} = 8$.

(see Fig. 2.13). The Filchner ice-shelf cavity exhibits sometimes exceptional dynamics due to its two-openings geometry that permits intrusions of both DSW at its front and bottom water coming from the deep part of the adjacent Ronne ice shelf. The latter water mass can be colder than DSW formed at the front of the Filchner ice shelf, making flip-flop dynamics plausible. More specifically, the front of the Filchner ice-shelf cavity is either filled by High Salinity Shelf Water (HSSW) ($T_{\text{HSSW}} \approx -1.9\,^{\circ}\text{C}$, $S_{\text{HSSW}} \approx 34.8\,\text{g/kg}$), which are DSW formed at the front of the Berkner island, or by Ice Shelf Water (ISW) ($T_{\text{ISW}} \approx -2.25\,^{\circ}\text{C}$, $S_{\text{ISW}} \approx 34.9\,\text{g/kg}$), which are super-cooled waters coming from the deep part of the Ronne ice shelf cavity, which is connected to the Filchner ice-shelf cavity on its eastern side [Janout et al., 2021, Hattermann et al., 2021]. These two regimes of circulation are commonly referred as the Berkner mode and the Ronne mode (see Fig. 2.13 [Janout et al., 2021]). Recent observational studies emphasized that the dominance of these two modes has alternated on interannual time scales [Janout et al., 2021, Hattermann et al., 2021].

The Filchner ice shelf is currently subject to cold conditions, such that CDW intrusions are not observed as they barely reach the continental shelf [Thompson et al., 2018]. As a consequence, our low-dimensionnal model should consider for the deep box "d" an intrusion of ISW coming from the grounding zone instead of CDW (see Fig. 2.2). In practice, this means replacing T_{CDW} and S_{CDW} by T_{ISW} and S_{ISW} in Eqs. (2.6c) and (2.6d). As $T_{\text{ISW}} < T_{\text{HSSW}}$, flip-flop dynamics become possible. We test the hypothesis of flip-flop dynamics by implementing ISW properties in our box model. Fig. 2.14 shows the temperature and the salinity of a single cavity box configuration. Here, we recover an interannual variability in the system (approximately 4 years), by imposing constant forcing. Note that this oscillating dynamics is not obtained so easily, as it is very sensitive to model parameters and forcing (surface salt flux, box volumes, vertical mixing). For example, the volumes of the boxes, which is set empirically in our model (with the PICO method [Reese et al., 2018]) because it does not impact the steady states, can impact time-

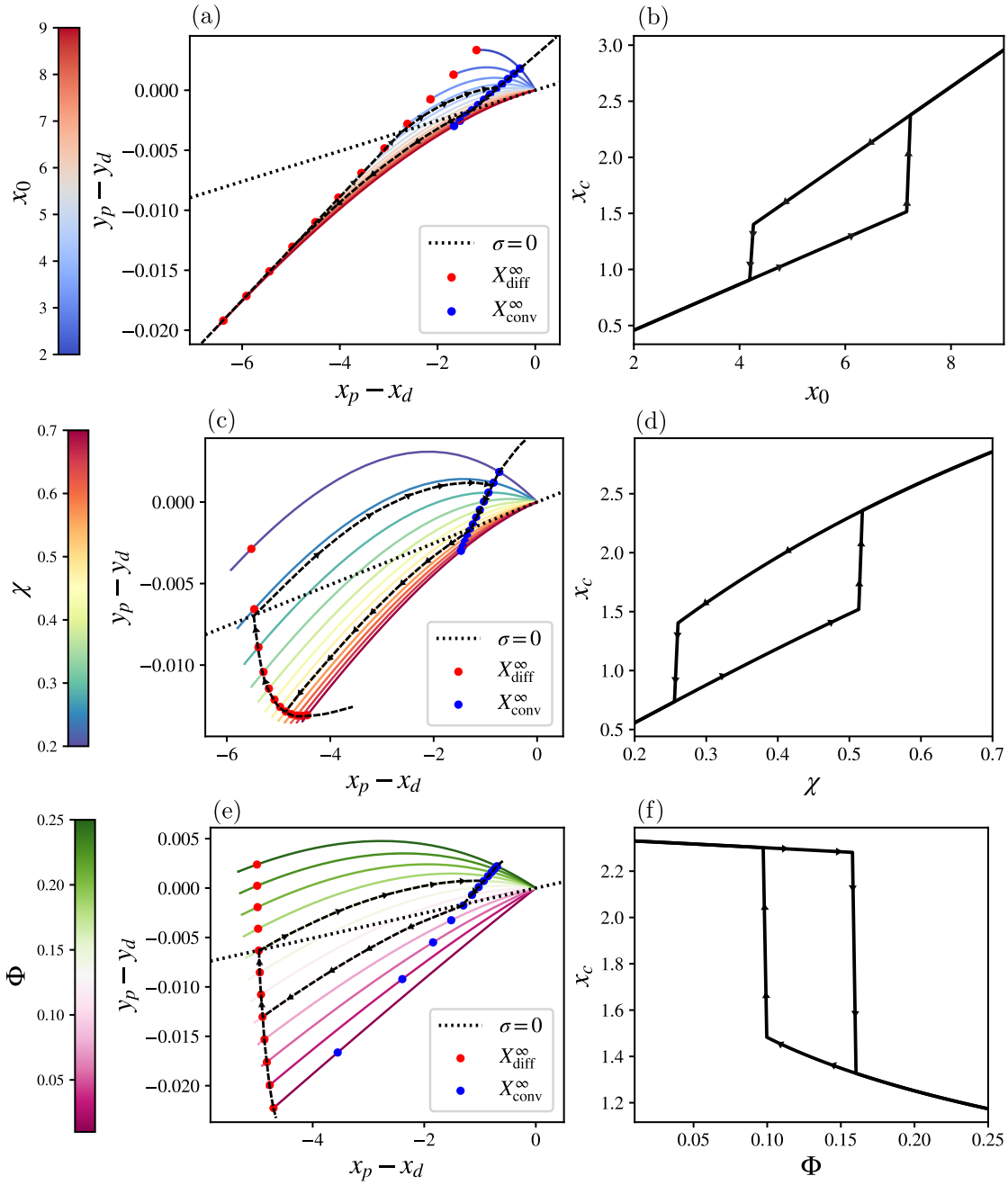

Figure 2.12: Steady-state solutions as a function of the forcing parameters. (a,c,e) Blue dots and red dots represent convective and diffusive steady states, respectively, for different values of x_{CDW} (a), χ (c), and Φ (e). The dashed black lines show the trajectories of quasi-static experiments, in which the corresponding forcing parameter is increased and then decreased. (b,d,f) Associated steady-state values of x_c. Unless specified on the horizontal axis or in the color bars, the parameter values are $\chi = 0.5$, $\Phi = 0.1$, $g = 10$, $x_{\text{CDW}} = 7$, $\delta = 5 \times 10^{-3}$, $k_{\text{diff}} = 0.1$, and $k_{\text{conv}} = 10$.

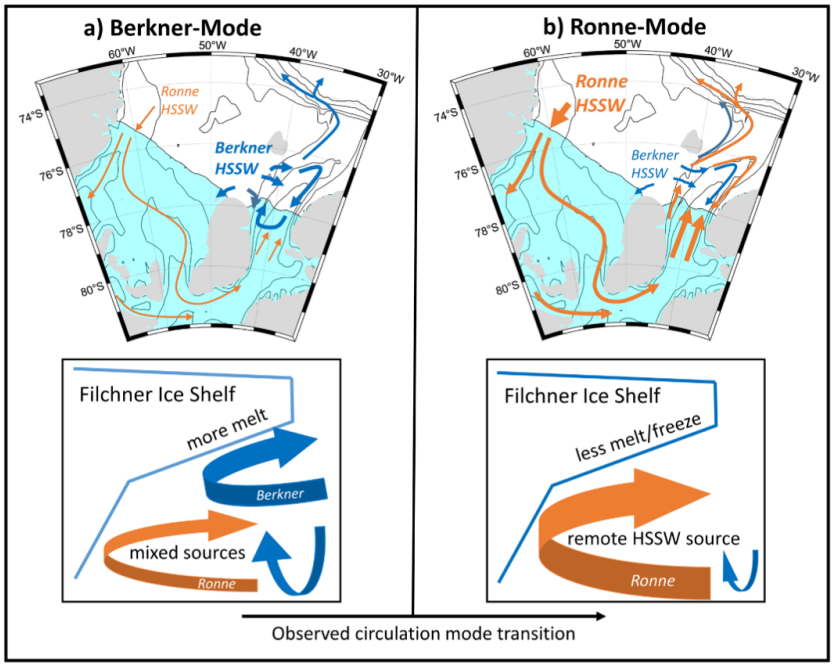

Figure 2.13: Illustrations of the Filchner-Ronne ice-shelf cavity dynamics. (a) In the Berkner mode, High Salinity Shelf Water (HSSW) forms at the sea surface due to sea-ice formation along the front of Berkner island and intrudes into the Filchner cavity. (b) In the Ronne mode HSSW from Ronne transforms into super-cooled Ice Shelf Water (ISW) that upwells along the Filchner ice-shelf slope. This figure comes from [Janout et al., 2021].

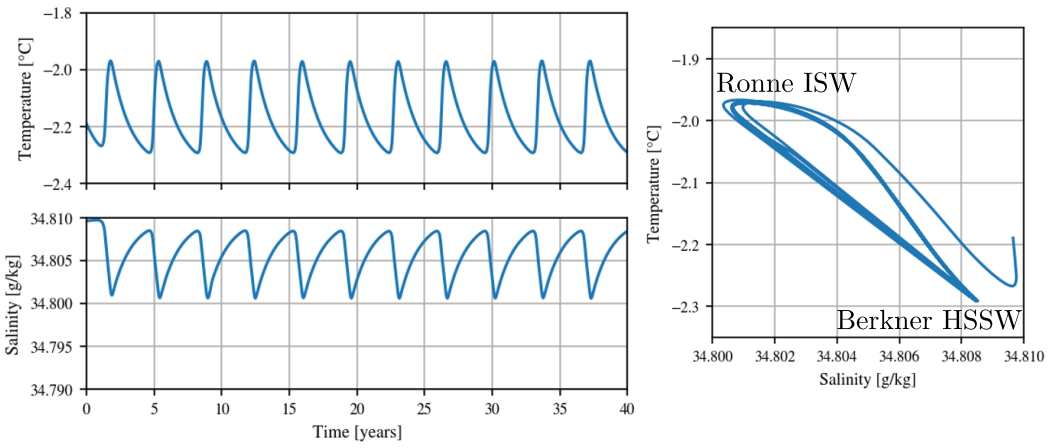

Figure 2.14: Cavity temperature and salinity obtained in a single cavity model configuration. We impose constant surface salt flux and intruding water properties, which are this time ISW properties instead of CDW properties. Diagrams on the left show time series of temperature and salinity, while the rightmost plot shows the corresponding limit cycle in $T - S$ space. Note that the salinity is in fact varying very little in time, with an amplitude of order 0.01 g/kg.

dependent dynamics. The vertical mixing coefficient is another parameter that can have a large impact on the transition time scales. This is visible in Fig. 2.14, where transition timescales depend on the direction of the transition, i.e. differing between the Berkner to Ronne and Ronne to Berkner transitions. As $\kappa_{\text{conv}} \gg \kappa_{\text{diff}}$, the destratification of the water column occurs very abruptly, which induces a very abrupt Berkner-to-Ronne transition. On the contrary, the Ronne-to-Berkner transition is slower as refilling of the ice-shelf cavity and polynya boxes with ISW is linked to q_{cav}. We conclude that flip-flop dynamics in the Filchner ice-shelf cavity is theoretically plausible but note that additional work would be needed to better constrain all parameters that impact the temporal dynamics of the system. Transient dynamics in Antarctic ice-shelf cavities will be explored in Chapter 5 with the help of a three-dimensional ocean model.

2.4.4 Asymptotic analytical results

Using the assumptions (H1) and (H2), i.e., neglecting the salinity-induced variations of thermal driving at leading order, we can express x_c from Eq. (2.24) in the asymptotic limits $k \to 0$ for the diffusive regime and $k \to \infty$ for the convective regime as

$$x_c = \begin{cases} \frac{\chi}{1+\chi} x_{\text{CDW}} + \mathcal{O}(k) & \text{for } k \to 0\,, \\ \frac{\chi(\Phi g + \chi x_{\text{CDW}})}{\Phi g + (2+\Phi g)\chi + \chi^2} + \mathcal{O}\left(\frac{1}{k}\right) & \text{for } k \to +\infty\,. \end{cases} \tag{2.28}$$

Thus, we find that the melt rate does not depend on the surface salt flux f_S in both regimes but varies linearly with the CDW temperature x_{CDW}, as shown in Figs. 2.11 and 2.12(a), respectively. The polynya area Φ and the heat transfer coefficient g below the polynya only appear in the expressions for x_c and m when $k \to +\infty$, in agreement with the fact that surface waters impact ice-shelf basal melt rates in the convective regime only. Nonetheless, Fig. 2.12(c) shows decreasing x_c as a function of Φ in the diffusive regime. This is due to a higher order term proportional to k_{diff}. In the limit $g \to +\infty$, the convective solution reduces to $x_c = \frac{\chi}{1+\chi}$.

The domain of existence of each regime is always bounded by $\sigma = 0$, i.e. the polynya and deep water boxes have the same density. Thus, the normalized integrated sea-ice production rates Φf_S that define the thresholds for the cold-to-warm and warm-to-cold transitions are found by solving equation $\sigma = 0$ when $k \to \infty$ and $k \to 0$, respectively. In the limit $g \to \infty$, using the analytical solution for X_k–the vector containing the temperatures and the salinities of the fixed point associated to the vertical mixing value k–in each regime, we can estimate the size of the bistable region from the difference in Φf_S for each threshold, i.e.

$$(\Phi f_S)_{\text{warm}\to\text{cold}} - (\Phi f_S)_{\text{cold}\to\text{warm}} = \delta \frac{\chi}{1+\chi}(x_{\text{CDW}} - 1), \tag{2.29}$$

meaning that the bistable region becomes increasingly large as x_{CDW} increases, and vanishes when $x_{\text{CDW}} = 1$ ($T_{\text{CDW}} = T_s$). Eq. (2.29) can be rewritten in dimensional form to provide a prediction for the range of total sea-ice mass production rates that support bistable dynamics as

$$(\rho_{\text{ice}} \mathcal{A}_p \xi)_{\text{warm}\to\text{cold}} - (\rho_{\text{ice}} \mathcal{A}_p \xi)_{\text{cold}\to\text{warm}} = (\rho_{\text{ice}} \mathcal{A}_c m_{\text{diff}}) - (\rho_{\text{ice}} \mathcal{A}_c m_{\text{conv}}). \tag{2.30}$$

Eq. (2.30) shows that the size of the bistable region in terms of sea ice production is directly linked to the meltwater production difference between the diffusive mode and the convective mode.

Taking the same asymptotic limits, our model recovers the low-dimensional formulation of [Hazel and Stewart, 2020]. First, taking $g \to +\infty$ gives $x_p = 1$, corresponding to $T_p = T_s$ as in [Hazel and Stewart, 2020]. Then, x_d reads

$$x_d = \frac{\chi x_{\mathrm{CDW}} + \Phi k}{\chi + \Phi k}. \tag{2.31}$$

In [Hazel and Stewart, 2020], the cavity is filled either by Warm Deep Water at temperature T_{CDW} in the diffusive mode, or by High Salinity Shelf Water at $T_p = T_s$ in the convective mode. These two regimes are recovered in our model for $k \to 0$ ($x_d = x_{\mathrm{CDW}}$) and $k \to +\infty$ ($x_d = 1$), respectively. The non-dimensional polynya salinity then reads

$$y_p = -\frac{\delta}{1+\chi} x_d + \frac{\Phi f_S}{\chi}, \tag{2.32}$$

or equivalently in dimensional form

$$S_p = S_{\mathrm{CDW}} - \frac{\sigma_{\mathrm{melt}}}{\rho_\star q_{\mathrm{cav}}} + \frac{\sigma_{\mathrm{polynya}}}{\rho_\star q_{\mathrm{cav}}}, \tag{2.33}$$

with $\sigma_{\mathrm{polynya}} = S_\star \rho_{\mathrm{ice}} \mathcal{A}_p \xi$ and

$$\sigma_{\mathrm{melt}} = \frac{c_\star \rho_\star q_{\mathrm{cav}} S_\star}{\mathcal{L}\left(1 + \frac{q_{\mathrm{cav}}}{\mathcal{A}_c \gamma_T^\star}\right)} (T_d - T_b). \tag{2.34}$$

[Hazel and Stewart, 2020] express $\sigma_{\mathrm{melt}} = f_{\mathrm{melt}} C_{\mathrm{melt}} (T_d - T_b)$, with $f_{\mathrm{melt}} C_{\mathrm{melt}} = 2.4 \times 10^8\,\mathrm{g/s/^\circ C}$ calibrated from regional simulations of the Filchner-Ronne cavity. Using our theoretical derivation, we find $f_{\mathrm{melt}} C_{\mathrm{melt}} = 1.6 \times 10^8\,\mathrm{g/s/^\circ C}$, showing surprisingly good agreement given the simplicity of our cavity model. We note that [Finucane and Stewart, 2024] also recover Eq. (2.34), while providing an additional constraint for q_{cav} thanks to geostrophic considerations. Nonetheless, our expression of σ_{melt} contains the extra factor $\left(1 + \frac{q_{\mathrm{cav}}}{\mathcal{A}_c \gamma_T^\star}\right)^{-1}$ which is not captured by [Finucane and Stewart, 2024] who provide a scaling based on a heat balance argument but miss the fact that all the heat that enters the cavity does not contribute to basal melting. Our extra-factor results from the equilibrium between fluxes entering and exiting the cavity box. It quantifies the fraction of heat brought to the cavity that will induce basal melt. For large cavities, $\frac{q_{\mathrm{cav}}}{\mathcal{A}_c \gamma_T^\star} \to 0$ such that $\left(1 + \frac{q_{\mathrm{cav}}}{\mathcal{A}_c \gamma_T^\star}\right)^{-1} \to 1$, meaning that all the heat entering the cavity is used to melt ice. In contrast, for small cavities, $\left(1 + \frac{q_{\mathrm{cav}}}{\mathcal{A}_c \gamma_T^\star}\right)^{-1} \sim \frac{\mathcal{A}_c \gamma_T^\star}{q_{\mathrm{cav}}}$, meaning that heat exchanges at the ice-ocean interfaces are limited by the turbulent flux $\mathcal{A}_c \gamma_T^\star$, such that the heat excess ends to the sea surface at the front of the polynya.

2.4.5 From irreversibility to reversibility: cusp bifurcation

In this section, we make again the hypothesis (H1) and (H2) to simplify our equations and we apply constant parameterizations for q_{cav} and $\gamma_T^\star$. We can therefore use the

dimensionless variables introduced in Section 2.4.1. In this simplified framework, the only nonlinearity arises from the step-function definition of the vertical mixing scheme (Eq. (2.8)). This simple parameterization allows the system to be studied as two distinct linear systems depending on the density stratification beneath the polynya. We now relax the step-function assumption for vertical mixing and introduce the continuous parameterization based on the density difference $\sigma = \frac{\rho_p - \rho_d}{\rho_\star}$ (in dimensionless form)

$$k = \frac{k_{\text{conv}} + k_{\text{diff}}}{2} + \frac{k_{\text{conv}} - k_{\text{diff}}}{2} \tanh\left(\frac{\sigma}{\lambda}\right), \tag{2.35}$$

where $\lambda = \Lambda/\rho_\star$ is a smoothing parameter that regularizes the step function.

We will show that introducing this nonlinearity gives rise to a cusp bifurcation (or *fronce* bifurcation in French). A cusp bifurcation is characterized by the coalescence of two saddle-node bifurcations at the critical point (called the cusp point) in parameter space. Along the direction transverse to the saddle-node curves at the cusp point, the system instead undergoes a supercritical pitchfork bifurcation.

Equation (2.24) can still be used to compute the steady state associated with each value of the vertical mixing coefficient k, although k now varies continuously between k_{conv} and k_{diff}. Since $k(\sigma)$ in Eq. (2.35) is bijective, each value of k uniquely determines σ. In turn, σ depends on the state variables x_p, y_p, x_d, and y_d, which themselves depend on k through Eq. (2.24). As a result, the solutions for σ must satisfy the following self-consistent equation

$$\sigma = -\tilde{\alpha}\{x_p[k(\sigma)] - x_d[k(\sigma)]\} + \tilde{\beta}\{y_p[k(\sigma)] - y_d[k(\sigma)]\} = \mathcal{F}(\sigma). \tag{2.36}$$

Figure 2.15 presents a graphical solution of Eq. (2.36) for $\lambda = 3 \times 10^{-5}$ (sharp transition; top row) and $\lambda = 2 \times 10^{-4}$ (smooth transition; bottom row), and for different surface salt fluxes f_S (see color bars). The solutions correspond to the intersections between the colored solid curves $\mathcal{F}(\sigma)$ and the dashed black identity line (left-hand panels). For fixed f_S, the system is monostable if the solution is unique and bistable if three solutions exist. In the latter case, the middle solution is unstable and connects two saddle-node bifurcations. The transition between monostable and bistable regimes occurs when two solution branches merge in a saddle-node bifurcation.

For a sharp transition (top row), a bistable region exists with two stable branches, leading to a hysteresis cycle when varying f_S, as shown in the upper-right panel of Fig. 2.15. In contrast, when the transition is smooth, the system remains monostable for all values of f_S, and the transition between convective and diffusive modes becomes fully reversible (lower-right panel). More generally, bistability occurs when the slope of $\mathcal{F}$ becomes sufficiently large for multiple intersections with the identity line to exist. Indeed, the condition $\max \mathcal{F}'(\sigma) > 1$ is necessary for multiple solutions to exist. When the smoothing parameter λ becomes sufficiently large, this condition is no longer satisfied and the hysteresis disappears.

An important feature of the transition from irreversible to reversible dynamics is the critical point at which the two saddle-node bifurcations merge, i.e., the cusp point where the dashed and solid black lines meet in Fig. 2.8(d,e,f). At this point, there exists a direction in parameter space (x_{CDW}, f_S) along which the system undergoes a supercritical pitchfork bifurcation.

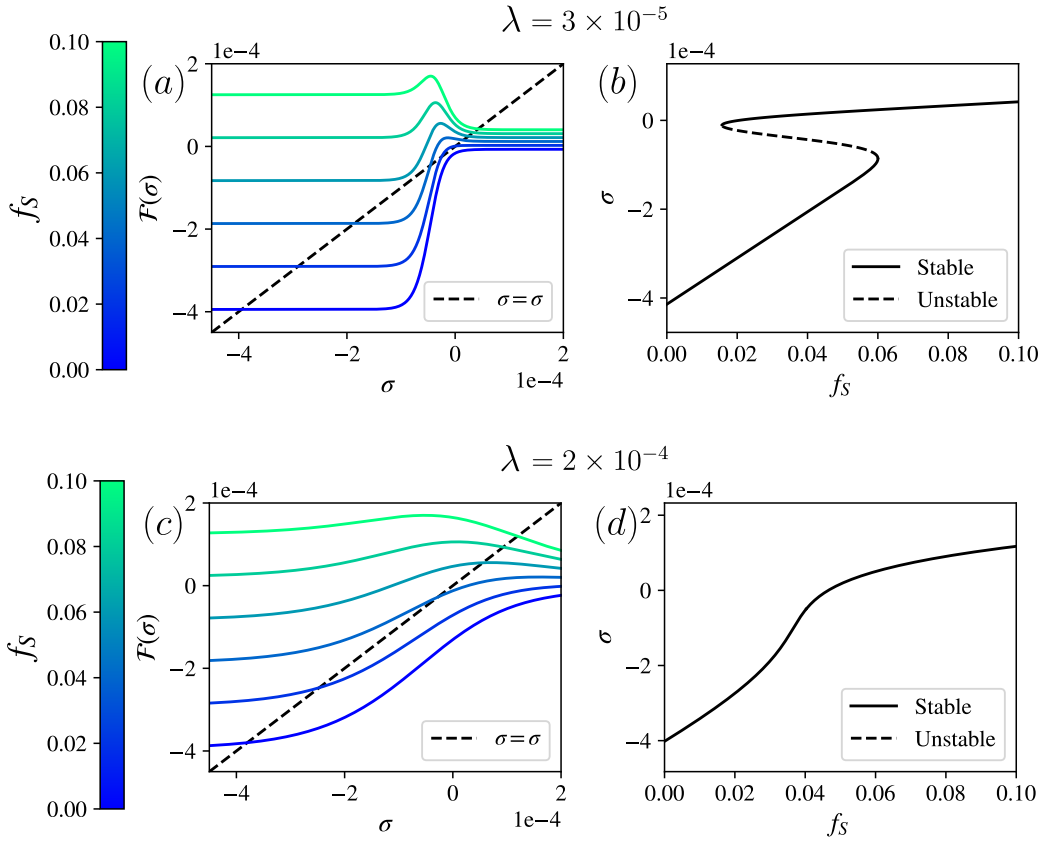

Figure 2.15: Graphical solutions of Eq. (2.36) for two values of λ. (a,c) The solutions correspond to the intersections between the colored solid curves $\mathcal{F}(\sigma)$ and the dashed black identity line. (b,d) Solutions as a function of the surface salt flux f_S. Dashed segments indicate unstable solutions. For small λ, hysteresis occurs because two stable branches coexist over a finite range of f_S values (b), whereas for larger λ the transition becomes reversible (d).

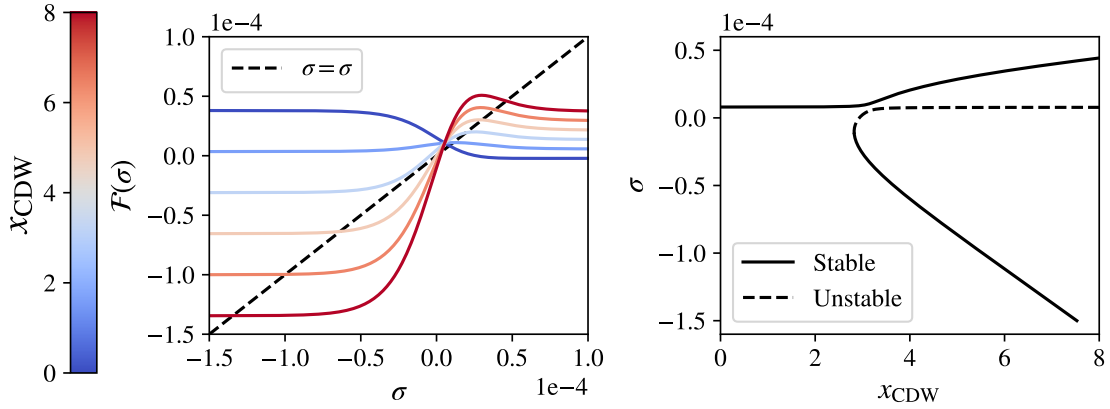

Figure 2.16: Graphical solutions of Eq. (2.36) with f_S fixed at its critical value. (a) The solutions correspond to the intersections between the colored solid curves $\mathcal{F}(\sigma)$ and the dashed black identity line. (b) Solutions as a function of x_{CDW}. The parameter g has been taken to infinity in order the supercritical pitchfork bifurcation along the x_{CDW} direction.

The parameters of the model can be tuned such that the x_{CDW} direction alone can exhibit a supercritical pitchfork bifurcation. Fig. 2.16 shows the same diagnostics as in Fig. 2.15 but highlights the dependence on x_{CDW} in this case. The graphical solution of the self-consistent equation in Fig. 2.16(a) shows that an intersection between $\mathcal{F}(\sigma)$ and the identity line exists for all values of x_{CDW}. This fixed point is stable when $\mathcal{F}'(\sigma) < 1$. When $\mathcal{F}'(\sigma) > 1$, the fixed point becomes unstable and two new stable branches emerge: a convective branch corresponding to $\sigma > 0$, and a diffusive branch corresponding to $\sigma < 0$ (Fig. 2.16(b)).

Note that the bifurcation shown here is only an approximate supercritical pitchfork bifurcation. In practice, the exact direction in parameter space that produces a perfectly symmetric supercritical pitchfork bifurcation is a linear combination of several parameter directions. Identifying this direction would require a more detailed analysis of the unstable branches associated with the saddle-node bifurcations.

Take-Home Messages

1. Graphical representations allow to predict the final state of the system from its initial conditions and highlight the hysteresis behavior.
2. The size of the bistable region is directly linked to the meltwater production difference between the warm and cold modes.
3. The system undergoes a cusp bifurcation, inducing either reversible or irreversible regime transitions depending on the CDW temperature and vertical mixing parameterization.

2.5 Conclusion

In this chapter, we developed a low-dimensional box model of ice-shelf cavity circulation capable of capturing transitions between cold and warm regimes driven by sea-ice production in coastal polynyas. Our analysis shows that several Antarctic ice shelves lie in bistable zones, making them susceptible to abrupt and irreversible transitions. Despite its conceptual simplicity, the model allows testing and discussing parameterizations choices to identify critical physical processes that could impact bistability. We demonstrate that bistability is robust under different parameterizations of cavity dynamics. These parameterizations all yield one or several positive feedback loops, hence support a bistable dynamics. We show that the extent of the bistable region is in fact directly related to the difference in meltwater production between the warm and cold modes. However, we identify the vertical mixing parameterization as critical for the emergence of bistability. When a smooth parameterization of vertical mixing as a function of density stratification is employed, the system undergoes a cusp bifurcation. Consequently, transitions between the two regimes are reversible for low CDW temperatures, but become irreversible above a critical CDW temperature.

Appendix

Temperature and salinity profiles

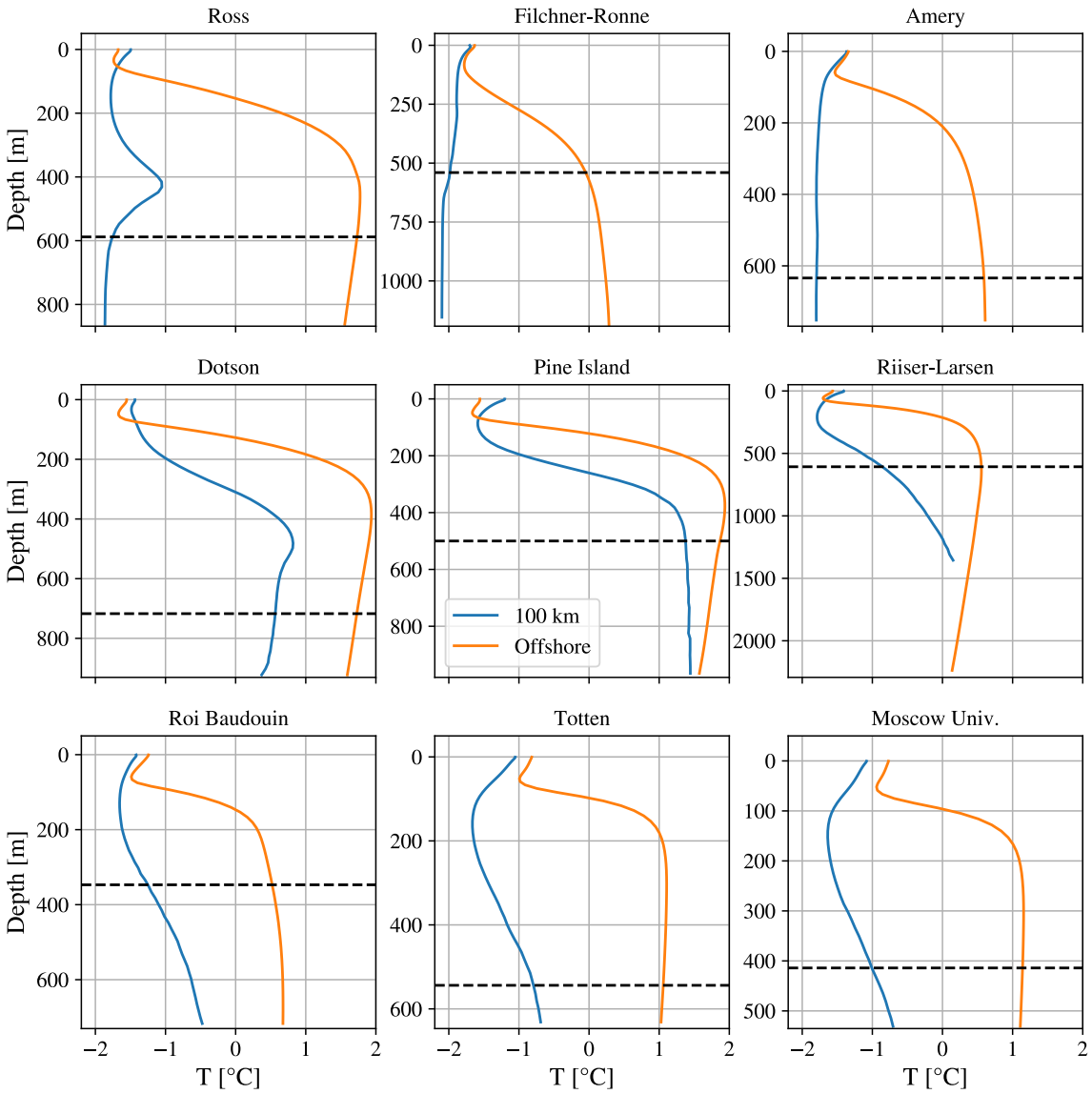

Figure 2.17: Vertical profiles of potential temperature (inter-annual means) 100 km away from the ice-shelf front (blue) or offshore past the continental shelf break (orange) [Burgard et al., 2022]. The profiles are drawn down to the maximum depth at the front of each ice shelf and the horizontal dashed black lines highlight h_{front}, the mean depth along the ice-shelf front.

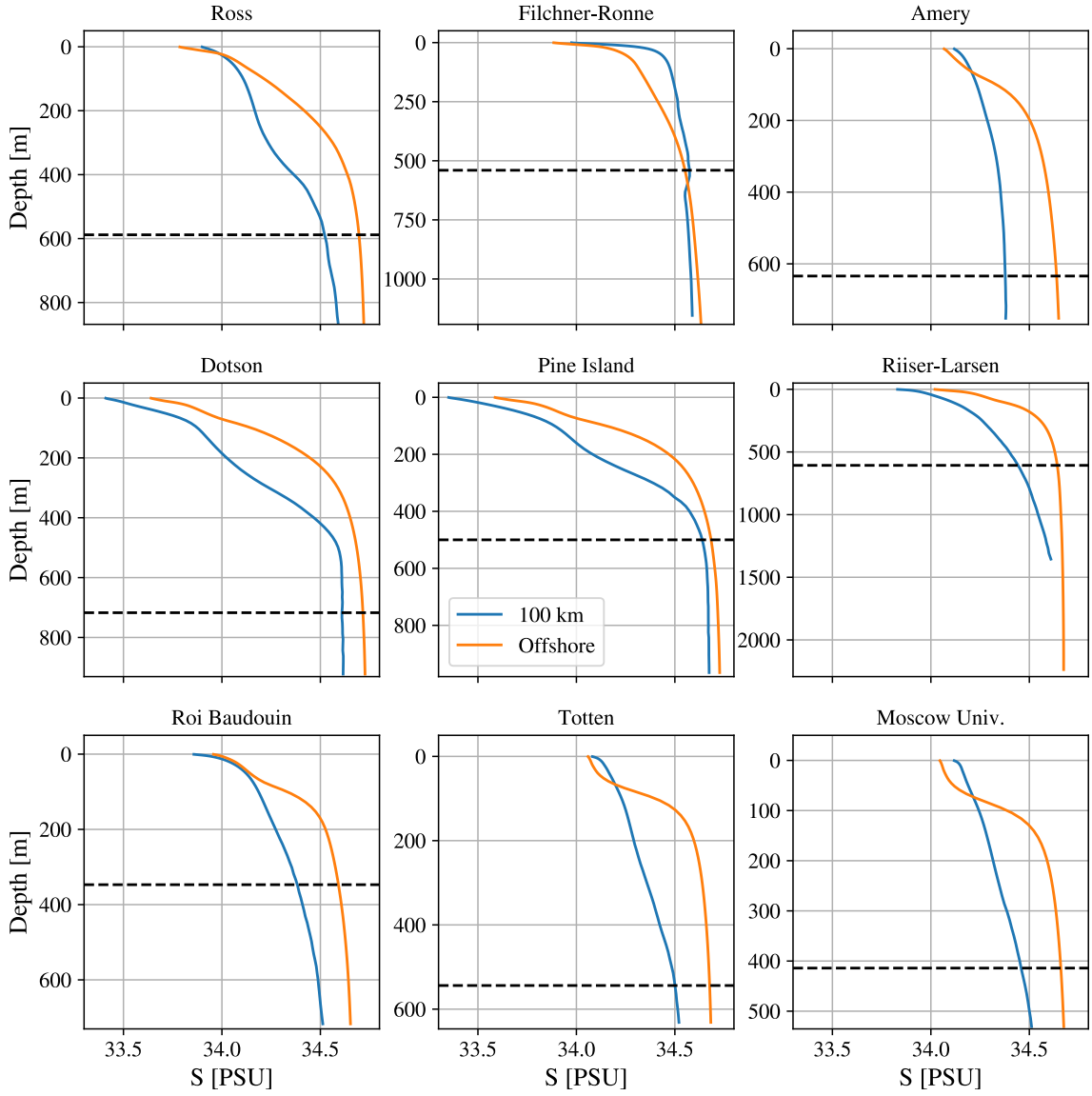

Figure 2.18: Same as in Fig. 2.17 but with vertical profiles showing salinity instead of potential temperature [Burgard et al., 2022].

Basal mass loss maps for other parameterizations

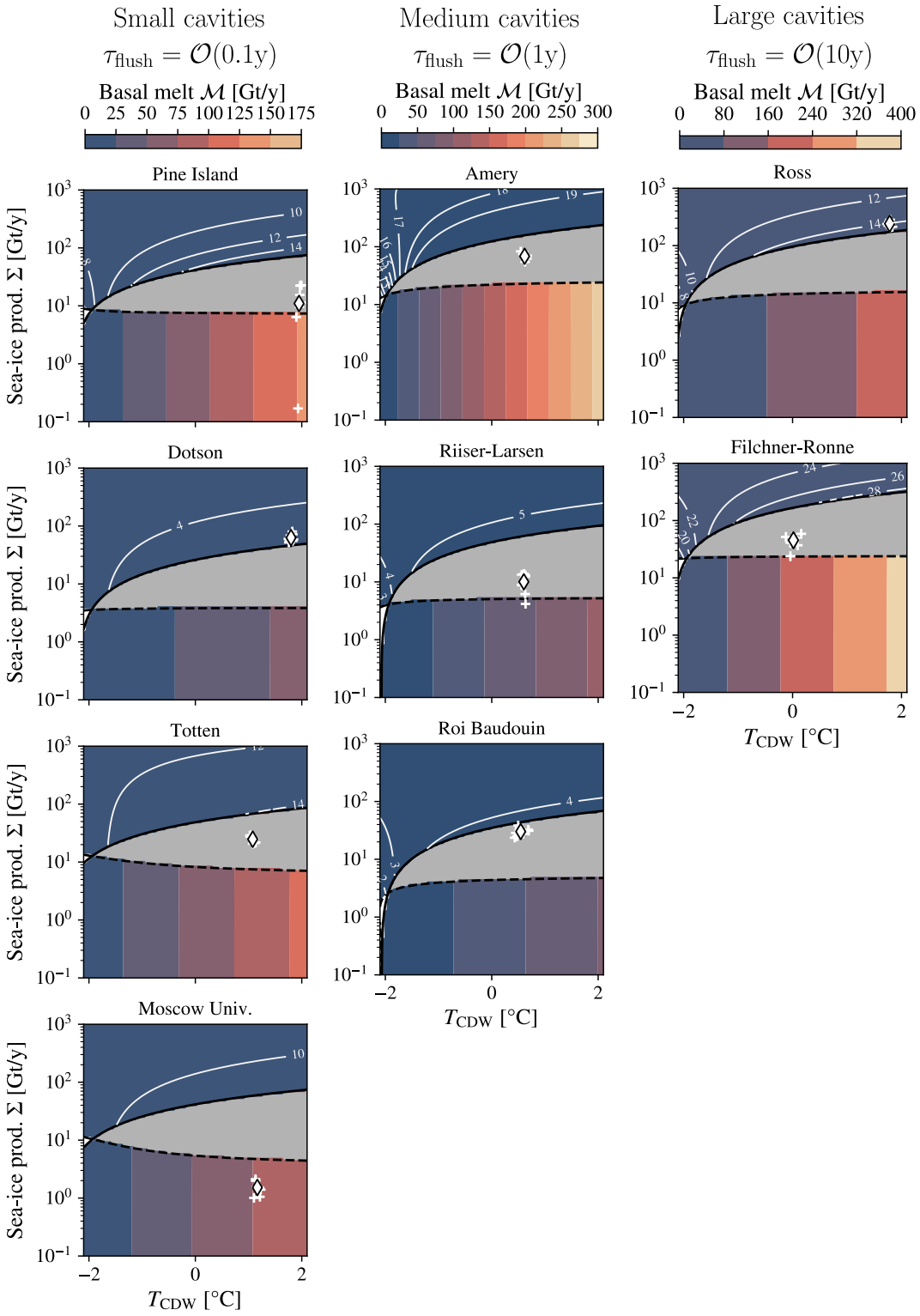

Figure 2.19: Same as Fig. 2.5 but with constant q_{cav} and $\gamma_T^\star$.

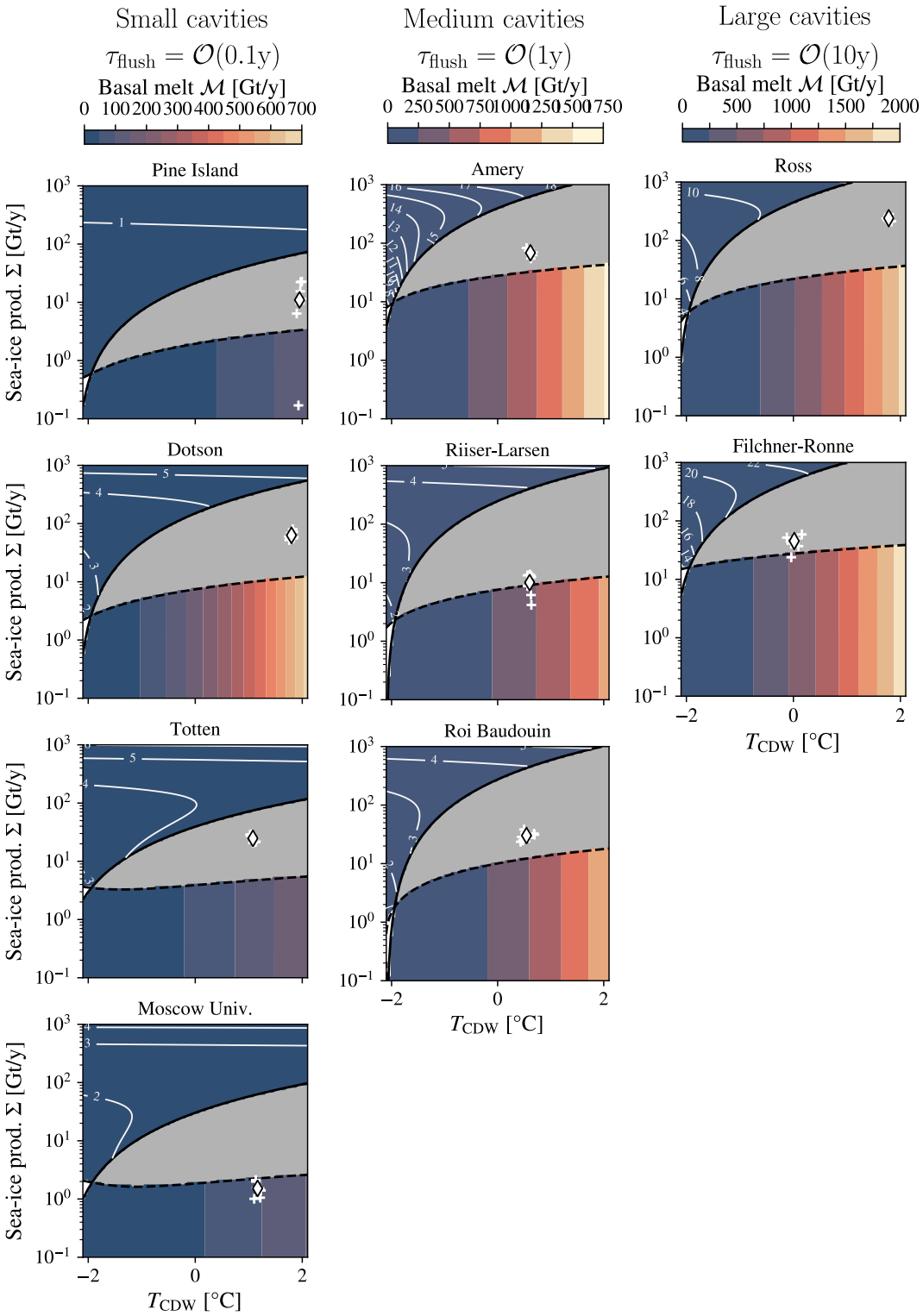

Figure 2.20: Same as Fig. 2.5 but with $q_{\text{cav}} = C_1(\rho_d - \rho_{c,1})$ and $\gamma_T^\star = \Gamma q$.

Continuous PICO model

The aim of this appendix is to study the continuous limit of the PICO model [Reese et al., 2018], which can be obtained in its discrete form with an infinite number of cavity boxes. We consider a 1D model of the ice-ocean interface with the spatial parameter x varying from 0 at the grounding line to L at the calving front. We define the temperature $T(x)$, salinity $S(x)$, and density $\rho(x) = \rho_\star\{-\alpha[T(x - T_\star)] + \beta[S(x) - S_\star]\}$ as key variables changing along the x-axis. The PICO box model uses the $q_{\text{cav}} = C(\rho_d - \rho_{c,0})$ parameterization, which we have to adapt for a continuous model. To this end, we set the overturning circulation in the cavity such that

$$q_{\text{cav}} = -C_2 \frac{\partial \rho}{\partial x}(0), \tag{2.37}$$

where C_2 [m^7/s] characterizes the strength of the cavity overturning. Thus, the spatial variation of the density at the grounding line drives the overturning circulation, as in the original PICO model. We additionally consider the parameterization $\gamma_T^\star = \Gamma q$. Considering a 2-equation thermodynamic formulation of the ice-ocean interface and neglecting the variation of salinity in the parameterization for the interfacial fluxes (hypothesis (H1) in Section 2.4.1), the equation for the temperature $T(x,t)$ in the ocean layer of width W (spanwise) and vertical size e under the ice shelf reads

$$eW\frac{\partial T(x,t)}{\partial t} = -q_{\text{cav}}\frac{\partial T(x,t)}{\partial x} - W\gamma_T^\star[T(x,t) - T_b(x)] \tag{2.38}$$

with $T(0,t) = T_0$ and $T_b(x) = aS_\star + b + c[P_{\text{atm}} + \rho_\star g h(x)]$, $h(x)$ being the local depth of the ice-ocean interface. We rewrite $T_b(x) = T_b(L) - Bh(x)$, with $T_b(L) = aS_\star + b + cP_{\text{atm}}$, and $B = -c\rho_\star g$. Introducing the typical length $l = \frac{q_{\text{cav}}}{W\gamma_T^\star} = (\Gamma W)^{-1}$, and considering the steady state of the system, we obtain the equation for the thermal driving $\theta(x) = T(x) - T_b(x)$:

$$\theta'(x) + \frac{1}{l}\theta(x) = Bh'(x)\,. \tag{2.39}$$

Similarly, the equation at steady state for the salinity reads

$$S'(x) + \frac{1}{l}\frac{c_\star}{\mathcal{L}}\theta(x)S(x) = 0\,. \tag{2.40}$$

We can deduce the overturning circulation from the last two equations as

$$\begin{aligned} q_{\text{cav}} &= -C_2\rho_\star[-\alpha T'(0) + \beta S'(0)] \\ &= \frac{C_2\rho_\star\alpha}{l}(R_\rho - 1)[T_0 - T_b(0)]; \end{aligned} \tag{2.41a}$$

where $R_\rho = \frac{\beta S(0)c_\star}{\alpha\mathcal{L}} = 4.2 > 1$ with $S(0) = 34.2\,\text{g/kg}$. The overturning circulation is thus proportional to the imposed thermal driving $\theta(0) = T_0 - T_b(0)$.

Eqs. (2.39) to (2.41) are sufficient to describe the continuous model for any cavity with a fixed shape $h(x)$. The basal melt rate m can then be computed along the x-axis with

$$m(x) = \frac{\rho_\star}{\rho_{\text{ice}}}\frac{\Gamma C_2\rho_\star}{l}\frac{\alpha c_\star}{\mathcal{L}}(R_\rho - 1)[T_0 - T_b(0)]\theta(x)\,, \tag{2.42}$$

which only requires solving Eq. (2.39).

We now apply the continuous PICO model to a very simple cavity. We consider a linear shape for the depth of the ice-ocean interface, i.e. $h(x) = H - \frac{H}{L}x$, such that $Bh'(x) = -\frac{BH}{L} = -\frac{T_b(L)-T_b(0)}{L}$. Then, we can analytically solve Eq. (2.39) so that

$$\theta(x) = [T_0 - T_b(0)]e^{-x/l} - \frac{l}{L}[T_b(L) - T_b(0)]\left(1 - e^{-x/l}\right) \tag{2.43}$$

From the expression for $\theta(x)$, we find the coordinate x_{freeze} beyond which thermal driving becomes negative, i.e. beyond which basal freezing occurs, as

$$x_{\text{freeze}} = l \log\left(1 + \frac{L}{l}\frac{T_0 - T_b(0)}{T_b(L) - T_b(0)}\right) \tag{2.44}$$

We can also compute the average basal melt rate of the ice shelf. The spatial average of the thermal forcing reads

$$\langle\theta\rangle_x = \frac{1 - e^{-s}}{s}[T_0 - T_b(0)] - \frac{1}{s}\left(1 - \frac{1 - e^{-s}}{s}\right)[T_b(L) - T_b(0)], \tag{2.45}$$

with $s = L/l = \Gamma\mathcal{A}_c$. We plot $\langle\theta\rangle_x$ in Fig. 2.21(a). The average thermal driving is independant of the parameter s for small cavities ($s \ll 1$) but decreases as $1/s$ for large cavities ($s \gg 1$). For comparison, approximating $s = \gamma_T^\star \mathcal{A}_c/q_{\text{cav}}$ and taking values of q_{cav} from [Reese et al., 2018] yields $s \approx 40$ for the Filchner-Ronne ice shelf and $s \approx 0.7$ for the Pine-Island ice shelf. The scaling for the averaged basal melt rate finally reads

$$\begin{cases} \langle m\rangle_x \propto [T_0 - T_b(0)]^2 & \text{when } s \ll 1, \\ \langle m\rangle_x \propto \frac{[T_0 - T_b(0)][T_0 - T_b(L)]}{s} & \text{when } s \gg 1. \end{cases} \tag{2.46}$$

We recover the quadratic scaling as a function of the imposed thermal driving found in [Holland et al., 2008] for small cavities. However, for large cavities, the averaged basal melt rate depends on the liquidus temperature at both the grounding line and at the sea surface. Still, the averaged basal melt scales quadratically with T_0 and decreases with the horizontal area of the cavity.

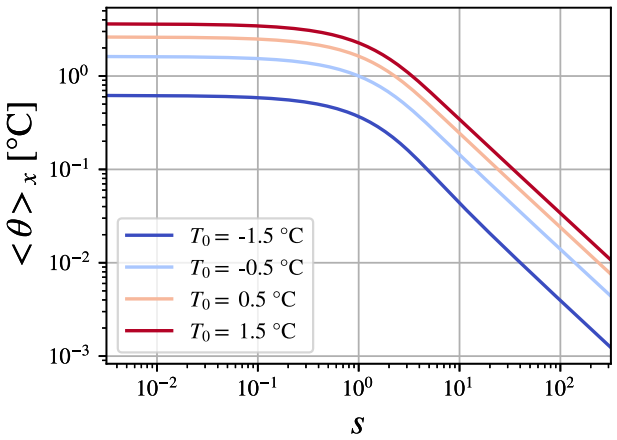

Figure 2.21: (a) Average thermal forcing as a function of the parameter $s = L/l = \Gamma\mathcal{A}_c$ for different (warm) deep water temperatures T_0.

Quadratic scaling of basal melt rate as a function of thermal driving

In this appendix, we aim to derive the quadratic scaling of basal melt rate as a function of thermal driving, when applying the parameterizations $q = C(\rho_d - \rho_c)$, and $\gamma_T^\star = \Gamma q$. We start with the simplified system Eq. (2.16), but we now need to define other dimensionless choices for environmental (Eq. (2.19)) and model (Eq. (2.20)) parameters since they depend on $\gamma_T^\star$ and q. We therefore define

$$\begin{cases} f_S = \frac{\rho_{\text{ice}}}{\rho_\star}\frac{\xi}{\Gamma C \rho_\star} & \text{normalized surface salt flux,} \\ x_{\text{CDW}} = \frac{T_{\text{CDW}} - T_b(S_\star, h_c)}{T_s(S_\star) - T_b(S_\star, h_c)} & \text{normalized CDW temperature,} \\ \Phi = \frac{\mathcal{A}_p}{\mathcal{A}_c} & \text{normalized polynya area,} \end{cases} \tag{2.47}$$

and

$$\begin{cases} k = \frac{\kappa}{\Gamma C \rho_\star} & \text{normalized vertical mixing velocity,} \\ \delta = \frac{c_\star}{\mathcal{L}}(T_s - T_b) & \text{Stefan number of the cold mode,} \\ g = \frac{\tilde{\gamma}_T}{\Gamma C \rho_\star} & \text{normalized surface mixing velocity of box “p”,} \\ s = \frac{\gamma_T^\star \mathcal{A}_c}{q_{\text{cav}}} = \Gamma\mathcal{A}_c & \text{ratio between the interface mixing flux and the overturning flux,} \end{cases} \tag{2.48}$$

which consists in replacing $\gamma_T^\star$ with $\Gamma C \rho_\star$. The normalized overturning has disappeared from the environmental parameters since it is now a dynamical variable, i.e.

$$\chi = \frac{q_{\text{cav}}}{\mathcal{A}_c \Gamma C \rho_\star} = \frac{\sigma_{\text{dc}}}{s} \tag{2.49}$$

with $\sigma_{\rm dc} = \frac{\rho_d - \rho_c}{\rho_\star}$. With these new notations, the equations of the simplified system are still Eq. (2.21) but with matrix M_k now given by

$$M_k = \left(\begin{array}{ccc|ccc} -\frac{\sigma_{\rm dc}}{s} - \Phi k - \Phi g & \Phi k & \frac{\sigma_{\rm dc}}{s} & 0 & 0 & 0 \\ \Phi k & -\frac{\sigma_{\rm dc}}{s} - \Phi k & 0 & 0 & 0 & 0 \\ 0 & 1 & -s-1 & 0 & 0 & 0 \\ \hline 0 & 0 & 0 & -\frac{\sigma_{\rm dc}}{s} - \Phi k & \Phi k & \frac{\sigma_{\rm dc}}{s} \\ 0 & 0 & 0 & \Phi k & -\frac{\sigma_{\rm dc}}{s} - \Phi k & 0 \\ 0 & 0 & -s\delta & 0 & 1 & -1 \end{array}\right),$$

and with the forcing vector

$$F = \begin{pmatrix} \Phi g \\ \frac{\sigma_{\rm dc}}{s} x_{\rm CDW} \\ 0 \\ \Phi f_s \\ 0 \\ 0 \end{pmatrix}. \tag{2.50}$$

The steady state solution is still given by $X_k = -M_k^{-1} F$. However, the solution X_k now depends on $\sigma_{\rm dc}$, which itself depends on X_k. Thus, the full determination of the solution requires solving the self-consistent nonlinear equation

$$\sigma_{\rm dc} = -\tilde{\alpha}[x_d(\sigma_{\rm dc}) - x_c(\sigma_{\rm dc})] + \tilde{\beta}[y_d(\sigma_{\rm dc}) - y_c(\sigma_{\rm dc})]\,, \tag{2.51}$$

where $\tilde{\alpha} = \alpha(T_s - T_b)$, and $\tilde{\beta} = \beta s_\star$. Fortunately, we can deduce from $X_k = -M_k^{-1} F$ the relationships $x_d - x_c = s x_c$ and $y_d - y_c = s\delta x_c$, such that the self-consistent equation reduces to

$$\sigma_{\rm dc} = \tilde{\alpha}(R_\rho - 1) s x_c\,, \tag{2.52}$$

where $R_\rho = \frac{\beta S_\star c_\star}{\alpha \mathcal{L}}$ and x_c depends on $\sigma_{\rm dc}$. Solving this equation is not really of interest since we would get a complex expression for the steady-state solution X_k. However, Eq. (2.52) will be useful to deduce a scaling law for the basal melt rate. The basal melt rate reads

$$m = \frac{\rho_\star}{\rho_{\rm ice}} \gamma_T^\star \delta x_c = \frac{\rho_\star}{\rho_{\rm ice}} (\Gamma C \rho_\star) \delta \sigma_{\rm dc} x_c\,. \tag{2.53}$$

Substituting $\sigma_{\rm dc}$ with Eq. (2.52) then yields a quadratic dependence of the basal melt rate with the thermal driving of the cavity x_c as

$$m = \frac{\rho_\star}{\rho_{\rm ice}} (\Gamma C \rho_\star) s \delta \tilde{\alpha} (R_\rho - 1) x_c^2\,. \tag{2.54}$$

Chapter 3

Bistable dynamics of ice-shelf cavities in an idealized numerical ocean model

Summary

In this chapter, we aim to provide an approach of regime transitions in ice-shelf cavities based on a simple configuration of an ice-shelf cavity with idealized geometry and representation of the influence of the far-field ocean, upon which we impose surface salt fluxes representing sea-ice production in coastal polynyas. A cold regime emerges when the associated buoyancy loss is sufficient to trigger deep convection, whereas a warm regime develops otherwise. The steady response of the system exhibits hysteresis, characteristic of irreversible transitions, and scaling laws are proposed for both melt rates and transition thresholds. We demonstrate that bistability emerges when a gyre occupies the ice-shelf front. The bistable forcing range increases with far-field ocean temperature but decreases with background stratification. We also show that increasing horizontal viscosity limits bistability, which may explain the range of behaviors reported in previous studies.

The content of this chapter mainly comes from an article in preparation.

3.1 Introduction

The high computational cost and complexity of forcing schemes in realistic configurations restrict systematic investigation of the steady response of an ice-shelf cavity to incremental variations of external conditions. As a result, a quantitative understanding of the physical mechanisms and positive feedback driving regime transitions and their thresholds in Antarctic ice shelves is lacking. Specifically, only a limited number of studies have examined the reversibility of these regime transitions. Past works exploring the reversibility of ocean circulations have focused on the Amundsen Sea [Caillet et al., 2023], the Filchner–Ronne ice shelf [Hazel and Stewart, 2020, Haid et al., 2023, Reese et al., 2026, Naughten et al., 2026, Hellmer et al., 2017], the Ross ice shelf [Naughten et al., 2026], and pan-Antarctic configurations [Mathiot et al., 2026], but with diverging conclusions. Although some studies found irreversible dynamics [Hellmer et al., 2017, Naughten et al., 2026, Hazel and Stewart, 2020] or hints of hysteresis behaviors [Haid et al., 2023] for the

case of the Filchner-Ronne ice-shelf cavity, others reported reversible transitions [Mathiot et al., 2026, Reese et al., 2026]. Quantifying the reversibility of cold-to-warm transitions is yet critical for assessing their potential short and long terms impacts, particularly in scenarios where the external forcing may weaken or reverse, or simply exhibits temporal variability.

Here, we adopt a complementary approach to realistic studies by running simulations of a canonical ice-shelf ocean cavity with idealized boundary forcings with the widely-used NEMO ocean code. We focus on regime transitions linked to changes in surface buoyancy fluxes within polynyas at the ice-shelf front. The simulations enable a systematic investigation of the steady response of the ice-shelf cavity circulation to polynya forcing and of the reversibility of the transitions, thus complementing our previous analysis based on a low-dimensional box model [Saddier et al., 2026] with results from a 3D ocean code. Our configuration is inspired from existing idealized ice-shelf cavity configurations [Holland et al., 2008, Holland, 2017, Årthun et al., 2013, Hunter, 2006], and more specifically built upon the intercomparison model ISOMIP+ [Asay-Davis et al., 2016, Yung et al., 2026]. The ISOMIP+ configuration examines the response of the ice-shelf to far field ocean properties. The key difference between ISOMIP+ and our set-up is that we include surface salt forcing at the front of the ice shelf to mimic the formation of sea ice in coastal polynyas and consider a simpler cavity geometry with constant ice-ocean interface slope and a flat seabed.

This chapter is organized as follows. In Section 3.2, we describe the ocean model, the spatial domain, and the forcing schemes. In Section 3.3, we show that our setup allows to recover both the warm and cold circulation modes. We characterize the steady response of the ice-shelf cavity to polynya forcing using quasi-static experiments and demonstrate that our configuration exhibits irreversible dynamics. We propose scaling laws for the basal melt rates in the warm and cold regimes and physics-based predictions for the transition thresholds. In Section 3.4, we present additional experiments exhibiting reversible transitions and demonstrate that the nature of regime changes (i.e. the irreversibility) is sensitive to far-field density stratification, ocean circulation at the front of the ice shelf, and the choice of subgrid-scale dissipation in the horizontal directions. Finally in Section 3.5, we comment the results in light of both recent observations and realistic simulations and discuss model limitations.

3.2 Methods

3.2.1 Model description

We simulate the ocean circulation within an ice-shelf cavity with the ocean component of the Nucleus for European Modelling of the Ocean (NEMO) model [Madec et al., 2024]. We use the version 4.2.1 of the code. The model solves the hydrostatic Boussinesq equations using the method of finite differences. The configuration is built upon the ISOMIP+ ice-shelf-ocean model intercomparison [Asay-Davis et al., 2016, Yung et al., 2026], with the ice-shelf NEMO module [Mathiot et al., 2017]. We use a uniform Arakawa "C" grid (see Fig. 3.1), with z^*-vertical coordinates and partial steps (see Figs. 3.2(b)), with a resolution step of 2 km horizontally and 20 m vertically. The time steps are constant equal to 360 s. Non-diffusive processes are time-stepped with a Leapfrog scheme, and

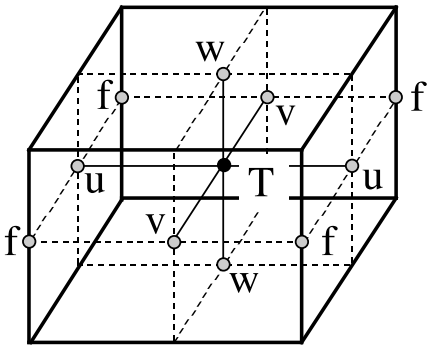

Figure 3.1: Arakawa "C" grid. The tracers (temperature, salinity, density) are defined on the "T" points. Meridional and zonal velocities are defined on the "u" points and the "v" points respectively (Note that our configuration reverses the standard definition). The vertical velocity is defined on the "w" points, and the horizontal vorticity on the "f" points. Figure originating from [Madec et al., 2024].

both tracer and momentum advections are approximated with second order centered schemes. For the diffusive processes, a forward time stepping scheme is adopted for the horizontal diffusion terms, and a backward time stepping scheme for the vertical diffusion terms. The equations are solved on an f-plane ($f = -1.4 \times 10^{-4}$ s^{-1}, corresponding to 75°S latitude). No-slip lateral boundary conditions are applied on the sidewalls, and a quadratic drag with coefficient $C_d = 2.5 \times 10^{-3}$ is applied on the seabed and underneath the ice shelf. The top surface of the open ocean is a rigid lid, thanks to the z*-coordinated framework. The equation of state is linearized at $T_{\text{ref}} = -1$ °C and $S_{\text{ref}} = 34.2$ g/kg, with thermal expansion coefficient $\alpha = 3.733 \times 10^{-5}$ °C^{-1}, and haline contraction coefficient $\beta = 7.843 \times 10^{-4}$ (g/kg)$^{-1}$. Convective patterns are expected to develop when brine is released at the surface of the polynya. An Enhanced Vertical Diffusion scheme (EVD) is therefore used to parameterize convective events. The EVD scheme works as following: if the stratification is stable between two cells, then the Laplacian vertical diffusivity is $\nu_v = 10^{-3}$ m^2/s for the momentum and $\kappa_v = 5 \times 10^{-5}$ m^2/s for the tracers. Otherwise, these coefficients take larger values when the stratification becomes unstable $\nu_v^c = \kappa_v^c = 0.1$ m^2/s. In order to prevent grid-scale noise of the vertical velocity [Garreau, 2021], a biharmonic lateral diffusivity is set for both momentum and tracers with coefficients $\nu_H = \kappa_H = 6.4 \times 10^7$ m^4/s.

3.2.2 Spatial domain and forcing

The spatial domain is sketched in Fig. 3.3. The meridional extent (x-axis, ISOMIP+ convention) is 250 km and the zonal extent (y-axis) is 50 km. The seabed is flat, at depth 600 m. The ice shelf is 100 km long, 50 km large and has a fixed geometry. The ice-ocean interface has an idealized linear shape, as in [Holland et al., 2008, Holland, 2017, Hunter, 2006]. Vertical walls are set at the grounding line and at the front of the ice shelf.

The sloped ice-shelf bottom boundary is interactive (in blue in Fig. 3.3) with basal melt computed and enforced along horizontal surfaces of the ice-ocean interface (not vertical), which has a discrete staircase pattern in the simulations. The ice-ocean interfacial fluxes are modeled with the three-equation model [Holland and Jenkins, 1999], neglecting the diffusion of heat through the ice shelf and ice salinity. The three equations are the

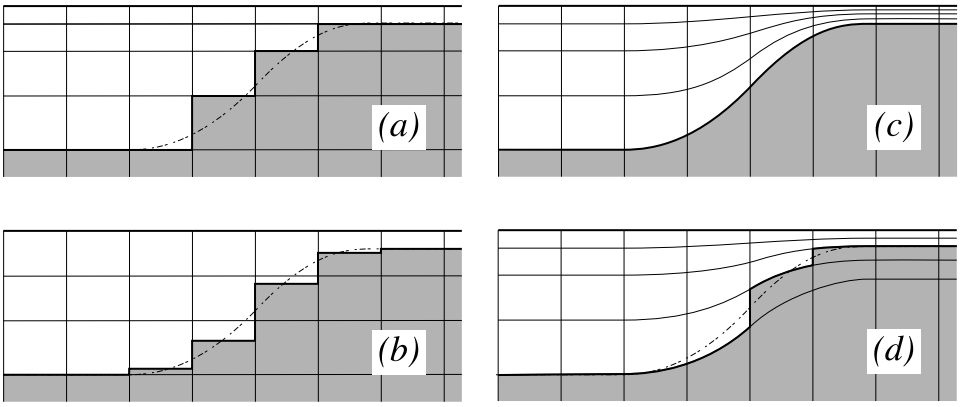

Figure 3.2: Possible vertical coordinates in NEMO. (a) z-coordinates with full step, the topography follows the horizontal levels definition. (b) z-coordinates with partial step. The levels are still flat, but the topography can take intermediate values, thanks to the interpolation of fluxes coming from and entering through the partial cells. It allows a better representation of the topography. Partial steps are used in our configuration for the ice-ocean interface. (c) σ-coordinates. The grid is defined along the topography. The topography and the boundary conditions are well represented. However, these coordinates are more complex to implement. (d) Hybrid coordinate. Figure adapted from [Madec et al., 2024].

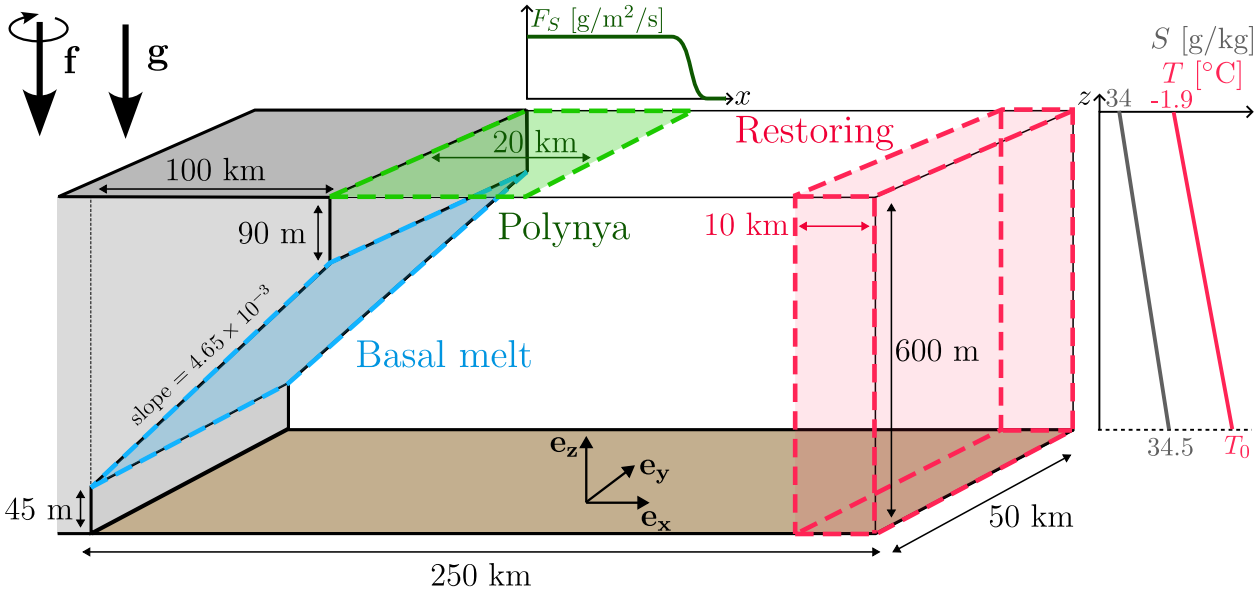

Figure 3.3: Ocean domain schematic. The ocean is bounded between the ice-shelf, atmosphere and seabed. The interactive ice-ocean boundary (basal melt), far-field region (temperature and salinity restoring) and coastal polynya area (surface salt fluxes mimicking sea-ice formation) are highlighted in blue, red and green, respectively.

linearized liquidus of the salt-water binary, the heat conservation equation and the salt conservation equation. They yield the temperature T_b and salinity S_b at the ice-ocean interface as well as the freshwater flux q_{fw} [kg/m^2/s] (positive for melting and negative for freezing) from ocean properties within the ice-ocean boundary layer (also known as

the Losh layer, [Losch, 2008]), denoted by subscript "tbl", as

$$T_b = \lambda_1 S_b + \lambda_2 + \lambda_3 H_{\text{isf}}, \tag{3.1a}$$
$$c_p \rho_{\text{tbl}} \gamma_T (T_{\text{tbl}} - T_b) = -\mathcal{L} q_{\text{fw}}, \tag{3.1b}$$
$$\rho_{\text{tbl}} \gamma_S (S_{\text{tbl}} - S_b) = -S_b q_{\text{fw}}. \tag{3.1c}$$

The temperature T_{tbl}, salinity S_{tbl}, and velocities $\mathbf{u}_{\text{tbl}}$ are averaged (vertically) across the boundary layer, whose width is set to $h_{\text{tbl}} = 30$; H_{isf} [m] is the ice draft and λ_1 [°C/(g/kg)], λ_2 [°C] and λ_3 [°C/m] are liquidus linearization coefficients given by [Asay-Davis et al., 2016], c_p [J/kg/°C] is the ocean specific heat, and $\mathcal{L}$ [J/kg] is the ice latent heat of fusion given in [Madec et al., 2024]. Importantly, γ_T and γ_S [m/s] are the turbulent heat and salt transfer coefficients. They depend on the friction velocity u_* in the top boundary layer such that $\gamma_{T,S} = \Gamma_{T,S} u_*$ [Jenkins et al., 2010], where $u_* = \sqrt{C_d \left(\mathbf{u}_{\text{tbl}}{}^2 + U_{\text{tide}}^2\right)}$, with $U_{\text{tide}} = 0.01$ m/s, a constant tidal velocity ensuring that γ_T and γ_S are always greater than 0. Here, $\Gamma_T = 2.15 \times 10^{-2}$ and $\Gamma_S = 6.14 \times 10^{-4}$ such that the ratio $\Gamma_T / \Gamma_S = 35$, and the Stanton number is worth $\text{St} = \Gamma_T \sqrt{C_d} = 1.1 \times 10^{-3}$, as recommended by [Jenkins et al., 2010]. Evaporation is implemented uniformly at the sea surface to balance exactly the basal melt to prevent drifts of the sea-surface height. In addition, corrections of surface heat and salt fluxes are added to avoid any surface buoyancy flux due to the evaporation [Mathiot et al., 2017].

Brine rejection due to sea-ice formation within the polynya is modeled as a surface salt flux F_S [g/m^2/s] at the front of the ice shelf (highlighted by green area in Fig. 3.3), with a smooth transition at the edge of the polynya along the x-axis such that $F_S(x) = F_{S,0} \frac{\Theta(x - 100\,\text{km})}{2} \left\{1 - \tanh\left[\frac{x - 120\,\text{km}}{3\,\text{km}}\right]\right\}$ [Årthun et al., 2013]. We remark that the surface salt flux is the control parameter in our study, rather than the sea-ice formation rate, which is more readily available from observational studies [Nakata et al., 2021], because it represents the actual forcing in the simulations. Nonetheless, sea-ice formation rates ξ linked to a prescribed F_s value can be easily approximated with $\xi\,[\text{m/y}] \approx 1000 \times F_s$, considering constant a sea-surface salinity of 34.2 g/kg.

We model the far-field ocean as an infinite reservoir of seawater with prescribed temperature and salinity stratification using a finite-width restoring region where temperature and salinity are forced to relax towards imposed linear temperature and salinity profiles (cf. red region in Fig. 3.3). The restoring frequency is 0.1 days^{-1} at the northern boundary and decay linearly to zero 10 km further south. We did not see any qualitative changes of the overturning circulation considering 10 times higher or lower value for the restoring frequency.

Finally, a heat flux is imposed throughout the surface of the open ocean $Q_{\text{surf}} = K(\text{SST} - T_s)$ to restore the Sea Surface Temperature (SST) towards the surface freezing temperature $T_s = -1.9$ °C, with a restoring coefficient $K = -40\,\text{W/m}^2/\text{°C}$.

3.3 Results

3.3.1 Two modes of circulation

We first test the ability of our setup to capture both the warm and the cold circulation regimes. For identical ocean forcing, the atmospheric forcing in the coastal polynya is

expected to control the type of circulation in the ocean cavity [Silvano et al., 2016]. We therefore run two experiments wherein we impose the same restoring conditions in the far field but use different surface salt forcing: a warm-mode experiment without surface fluxes ($F_S = 0$), and a cold-mode experiment with large surface salt fluxes $F_S = 0.075$ g/m^2/s. We note that the cold experiment considers extreme surface salt fluxes as extremal annual values observed around Antarctica range from zero when no sea ice is formed, especially beneath landfast sea ice [Nakata et al., 2021], to 0.03 g/m^2/s in Cape Darnley, which is one of the most active sea-ice production region [Ohshima et al., 2022]. Linear restoring temperature and salinity profiles are imposed in the far field, ranging from -1.9 °C and 34.0 g/kg at the sea surface, to 1 °C and 34.5 g/kg at the seafloor, which fall within the observed range of CDW properties. The resulting density profile is stable because the stably stratified salt profile overcompensates for the unstably stratified temperature profile. The density ratio $R_\rho = \frac{\beta \Delta S}{\alpha \Delta T} = 3.6 > 1$ and the associated Brunt-Väisälä frequency is $N = 2.2 \times 10^{-3}$ s^{-1}. Both the warm- and cold-mode experiments are initialized with a quiescent ocean (zero velocities) and horizontally-uniform temperature and salinity profiles with the same vertical stratification as in the restoring region. We run the simulations for 10 years. Time averages of the last three years of each simulation are shown in Fig. 3.4 for the warm mode experiment and in Fig. 3.5 for the cold mode experiment.

The warm mode experiment reproduces well the Mode II described by [Silvano et al., 2016], and shows strong similarity with the results of [Holland et al., 2008] and [Holland, 2017] whose used similar forcings. The ocean is strongly stratified throughout and a fresh water layer (<34 g/kg), fed by significant meltwater rejections, is seen everywhere at the surface (Fig. 3.4(a)). The Meridional Overturning Circulation (MOC), defined as MOC $= \int_{z'=-H}^{z} \mathrm{d}z' \int_{y=0}^{L_y} \mathrm{d}y u$, shows a single clockwise overturning cell, bringing warm waters from the deep part of the restoring region towards the grounding line of the ice shelf (Fig. 3.4(a)). The intense melting of the ice base sustains and reinforces the overturning cell as the upwelling of relatively fresh waters along the ice-shelf slope pumps CDW into the cavity [Jourdain et al., 2017]. The barotropic stream function, defined as $\Psi = \int_{x'=0}^{x} \mathrm{d}x' \int_{z=-H}^{0} \mathrm{d}z v$, shows the alternance of cyclonic and anti-cyclonic gyres along the channel, starting from the front of the ice shelf (Fig. 3.4(b)). Their extent is comparable to the width of the channel. Similar standing gyres have been observed within Greenland fjords adjacent to marine-terminating glaciers and described as resulting from the interplay between vorticity introduced by the upwelling meltwater plume and vorticity generated through friction along the fjord's topography [Zhao et al., 2023]. Under the ice shelf, a cyclonic circulation is sustained by the upwelling meltwater that deviates towards the West due to the Coriolis force [Hewitt, 2020] and feed the cyclonic gyre at the ice-shelf front. The western intensification of the ice-shelf outflow, which is responsible for the high basal melt rates on the western side of the cavity (Fig. 3.4(c)), is consistent with the topographic beta effect due to the meridional variation of the water-column thickness. As expected, there are no convective patterns under the polynya ($F_s = 0$) and the mean (not shown) and standard deviation of the vertical velocity are weak (cf. Fig. 3.4(d)). The EVD convective scheme is rarely active and only close to the sea surface, due to the surface heat flux temperature restoring (cooling).

The water column is less stratified in salinity, and therefore in density, in the cold mode experiment than in the warm mode experiment (Fig. 3.5(a)). Surface waters are only mod-

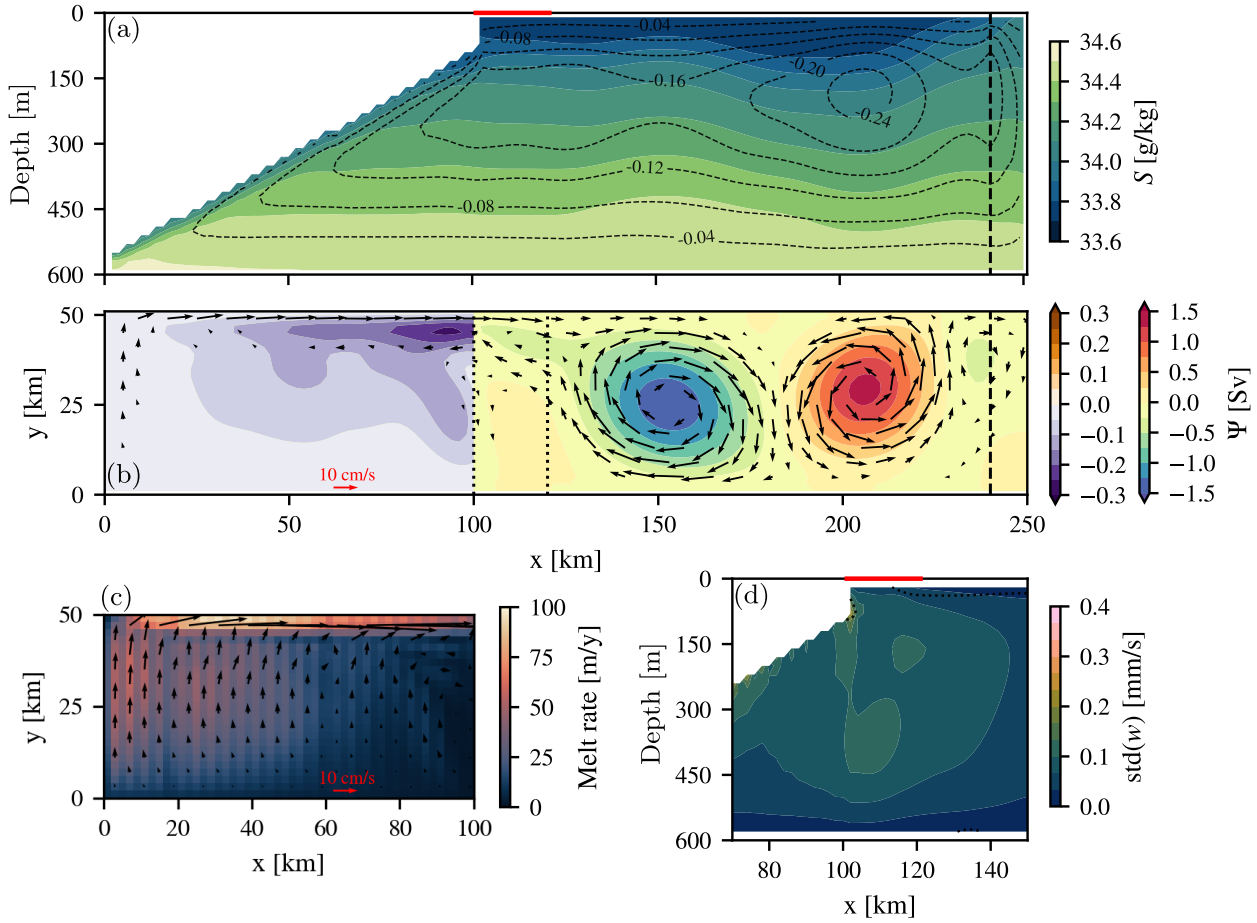

Figure 3.4: Time averages of the last three years of the warm mode experiment. (a) Zonal average of the salinity field. The black contours show the Meridional Overturning Circulation (MOC), in Sverdrup (1 Sv = 10^6 m^3/s). Solid lines denote anticlockwise rotation while dashed lines code for clockwise rotation. The horizontal red line highlights the polynya region. (b) Barotropic stream function Ψ. Two color bars are used to enhance the contrast in the cavity. Black arrows represent the depth-averaged horizontal velocity (plotted only if superior to 2 cm/s). (c) Basal melt rate. Black arrows represent the horizontal velocity $\mathbf{u}_{\text{tbl}}$ in the top boundary layer. (d) Zonal mean of the standard deviation of the vertical velocity w. The dotted contour represents the spatial threshold for which the EVD scheme is active 10% of the time. Note that the melt rate pattern in x at the grid scale visible in (c) is a common artifact in cavity simulations using partial cells and with a staircase representation of the ice base [Losch, 2008].

erately fresh, suggesting weak meltwater rejections. Instead of a single clockwise overturning circulation cell, two counter-rotating overturning cells are observed (Fig. 3.5(a)). On the one hand, we observe a clockwise overturning cell in the ice-shelf cavity, as in the warm mode experiment, although its strength is reduced because of the relatively low meltwater production. On the other hand, an anti-clockwise overturning cell is visible in the open ocean, with net downward volume fluxes from the sea surface towards the bottom of the ocean under the polynya, suggesting DSW invades the cavity instead of CDW, consistent with the Mode I description [Silvano et al., 2016]. The barotropic stream

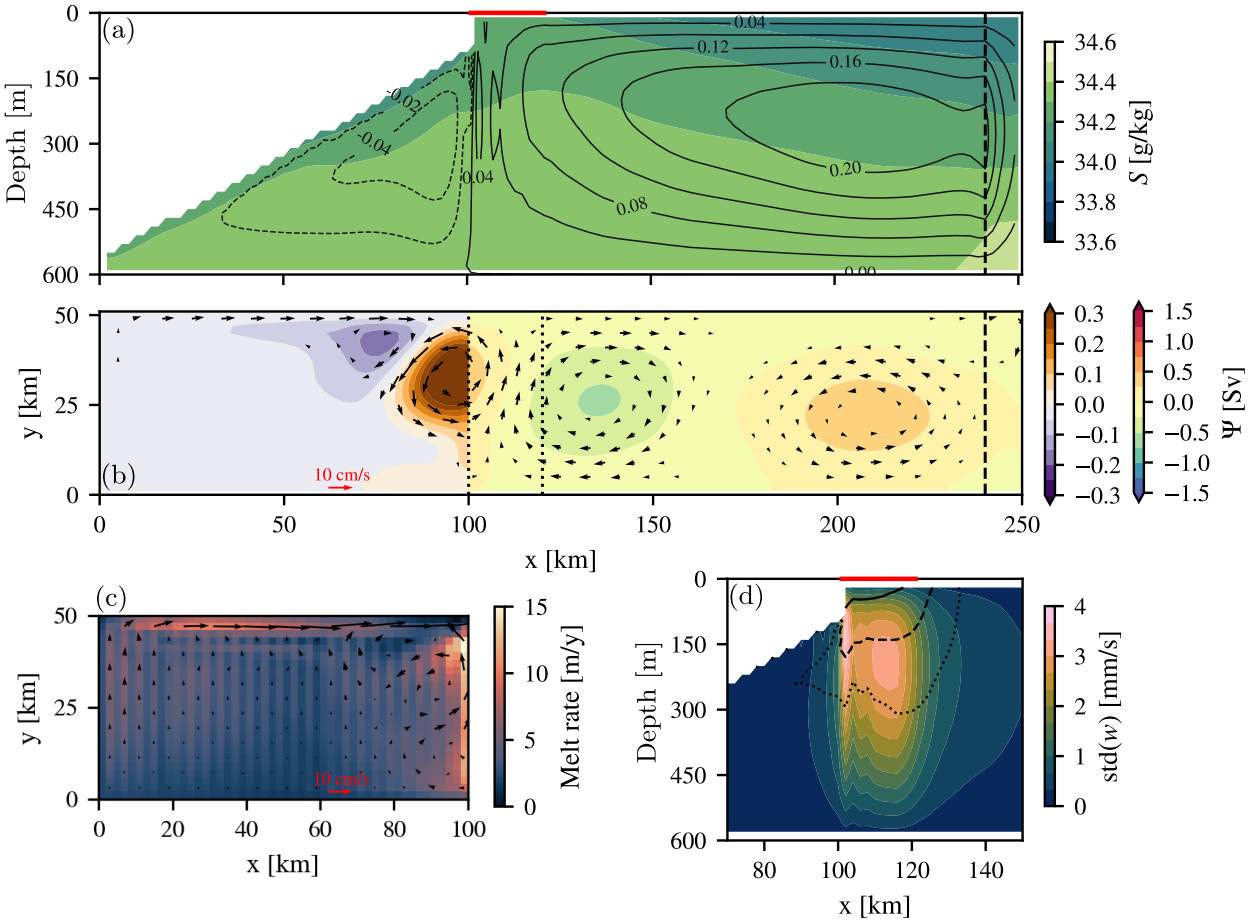

Figure 3.5: Same as Fig. 3.4, but for the cold mode experiment. Note that the scales of the color bars have changed in (c) and (d). In (d), the black contours represent the spatial thresholds for which the EVD scheme is active 10% (dotted), 30% (dashed), and 90% (solid) of the time.

function shows a succession of cyclonic and anti-cyclonic gyres along the channel as in the warm mode experiment, although their strengths are reduced because of the relatively weak meltwater outflow on the western edge of the channel (Fig. 3.5(b)). A gyre that only exists in the cold-mode experiment appears straddling the ice-shelf front. It is driven by the densification of the ocean under the polynya due to the brine releases, resulting in a thermal-wind anticyclonic circulation [Årthun et al., 2013]. The western boundary current still exists but is relatively weak since DSW is cold and drives low basal melt rates. The anti-cyclonic gyre straddling the ice-shelf front allows surface waters to intrude the front of the ice-shelf cavity with high velocities, enhancing local melt rates in a fashion reminiscent of the mode III melting regime that is sometimes observed along the front of ice shelves [Silvano et al., 2016]. Strong vertical velocity signals are observed under the polynya, as expected in deep convective regions (Fig. 3.5(d)). The zonally averaged standard deviation of the vertical velocity is large everywhere under the polynya, as we partially resolve convective chimneys [Xu et al., 2023a]. The mean of the vertical velocity (not shown) is one order of magnitude weaker than the standard deviation. Thus, vertical mixing is the predominant mechanism modifying the deep waters properties, rather than

a net downward volume flux of cold DSW. Fig. 3.5(d) shows that the EVD scheme is frequently active close to the surface of the polynya, where brine rejections destabilize the water column.

Based on thse two regimes of circulation described above, we will refer to a combination of mode I and mode III when employing the term "cold mode", and refer to the mode II when employing the term "warm mode".

3.3.2 Hysteresis experiments

We now investigate the nature of the transitions between the cold and warm modes. To this end, we perform quasi-static experiments that allow to characterize the steady-state response of the ocean cavity to brine rejections in the polynya region. We evaluate the impact of the far-field temperature on the nature of the transitions by considering five distinct quasi-static experiments with similar sea surface temperature $T_s = -1.9\,°\mathrm{C}$ but differing bottom temperature, i.e. $T_0 \in \{-1.9, -1, 0, 1, 2\}\,°\mathrm{C}$ (the restoring profile being always a linear function of depth). The salinity restoring profile is identical in all cases, varying linearly from 34 g/kg at the sea surface to 34.5 g/kg at the seafloor. For each far-field temperature, we test the reversibility of the transition by running two distinct experiments: one with increasing F_s and one with decreasing F_s. When we increase F_s, we probe the warm-to-cold transition and thus initialize the ocean properties with those prescribed in the restoring region (warm initialization). The surface salt flux F_S increases incrementally from $F_s = 0\,\mathrm{g/m^2/s}$ to $F_s = 0.075\,\mathrm{g/m^2/s}$with 0.005 $\mathrm{g/m^2/s}$ increments every 10 years, resulting in a 160-year long simulation. When we decrease F_s, we instead probe the cold-to-warm transition and thus set at the initial time the ocean salinity to its vertically-varying restoring profile but the temperature to a constant low value of -1.9 °C. The surface salt fluxes decrease from $F_s = 0.075\,\mathrm{g/m^2/s}$ to $F_s = 0\,\mathrm{g/m^2/s}$, every 10 years with 0.005 $\mathrm{g/m^2/s}$ salt fluxes increments, also resulting in a 160-year long simulation. We note that steady-state dynamics are usually obtained after a few years, such that they are well represented by ocean properties averaged over the final year of each 10-year increment.

Fig. 3.6(a) and Fig. 3.6(b) show the temporal evolution of the spatially and monthly averaged basal melt rates of the warm-to-cold and cold-to-warm experiments, respectively. The time axis of the cold-to-warm experiment (bottom plot) has been inverted such that F_S increases from left to right, i.e. as for the warm-to-cold case (top plot). The behavior of the melt rate time series depends on the bottom temperature in the restoring zone: for the coldest temperatures ($-1\,°\mathrm{C}$ and $-1.9\,°\mathrm{C}$), the melt rate does not vary much (dark blue curves). As the bottom temperature increases, we start observing transitions between high and low melt rate regimes. The transition becomes more abrupt as the bottom temperature in the restoring zone increases: it occurs over just a few years for the $1\,°\mathrm{C}$ and $2\,°\mathrm{C}$ temperature forcing. We note that the system relaxed to a new steady state by the end of each 10-year segment of the hysteresis experiment for most forcing increments. We show in Fig. 3.6(c) the basal melt rates averaged over the final 3 years of each 10-year increment, as a function of the imposed surface salt flux. Time averaging removes the internal variability and more clearly shows the steady response of the ice-shelf to the coastal polynya forcing. Fig. 3.6(c) highlights that the salt flux thresholds for the abrupt transitions ($1\,°\mathrm{C}$ and $2\,°\mathrm{C}$) are not the same on the increasing (circles) or

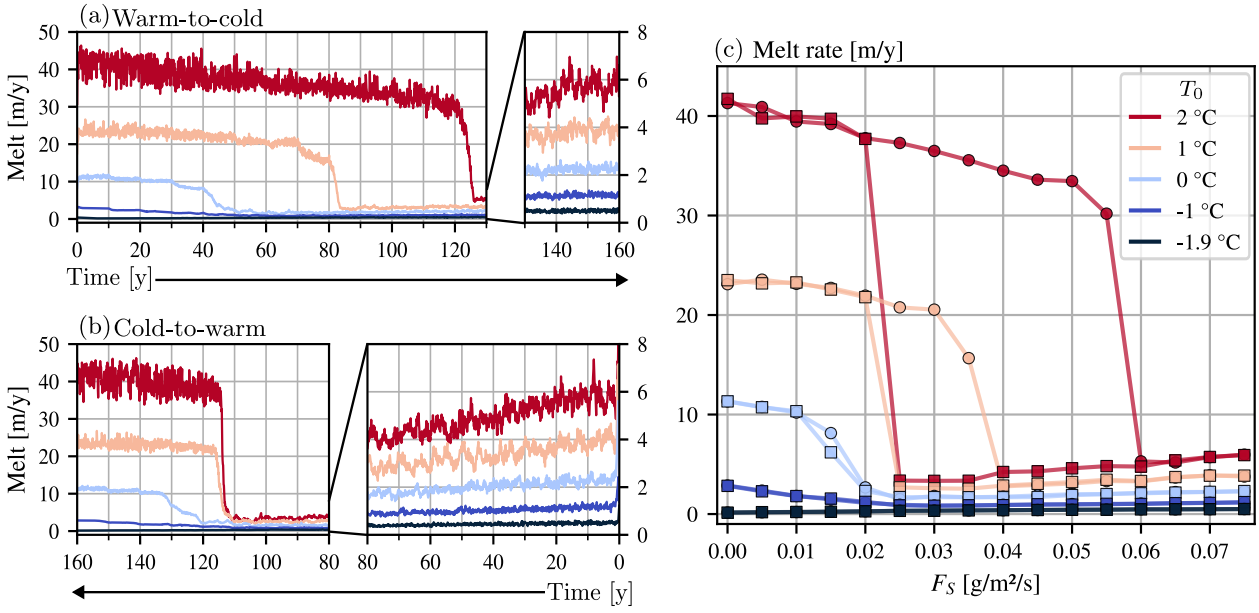

Figure 3.6: (a) Monthly and spatially averaged basal melt rates for the warm-to-cold experiments, plotted as functions of time. The surface salt flux F_S increases from 0 to 0.075 g/m^2/s in 0.005 g/m^2/s increments every 10 years. (b) Same as (a), but for the cold-to-warm experiments, with F_S decreasing from 0.075 to 0 g/m^2/s also with 0.005 g/m^2/s increments every 10 years. (c) Basal melt rates averaged over space and over the final 3 years of each 10-year window plotted against the imposed surface salt flux. Results from the warm-to-cold (resp. cold-to-warm) experiments are shown with circles (resp. squares).

decreasing (squares) F_S branches of the experiment. The basal melt rates then exhibit a hysteresis behavior as a function of F_S and regime transitions are irreversible. Reversible transitions are recovered for low forcing temperatures ($T_0 \in \{0, -1, -1.9\}$ °C), as can be seen from the overlap of the blue circles and squares over the full range of F_s values tested.

The extent of the bistable region in terms of surface salt fluxes increases with the melt rate in the warm regime. Thus, we postulate that the meltwater feedback works in our simulations such that the thick meltwater layer in the warm regime delays deep convection in the polynya region. To verify this hypothesis, we show in Fig. 3.7(a) and Fig. 3.7(b) the temporal evolution of the temperature gradient $\partial_z T$ as a function of depth below the polynya, normalized by the temperature gradient $\partial_z T_{\text{resto}}$ in the restoring region, for the warm-to-cold and cold-to-warm experiments ($T_0 = 1$ °C), respectively. Mixed conditions are highlighted by light blue colors ($(\partial_z T/(\partial_z T)_{\text{resto}} \ll 1$), stratified conditions similar to in the restoring region are highlight by dark blue colors ($(\partial_z T/(\partial_z T)_{\text{resto}} \approx 1$), and strongly-stratified conditions (denoting the presence of a thermocline) are shown in yellow ($(\partial_z T/(\partial_z T)_{\text{resto}} > 1$). The mixed layer is fed by DSW, whereas the stratified layer below the thermocline is supplied by CDW. Thus, the thermocline depth controls which water masses are intruding the cavity. In the warm mode, the thermocline does not reach the bottom of the ocean, and unmodified CDW can intrude the cavity (dark blue colors dominate). In the cold mode, the water column is fully mixed as convective patterns reach the bottom of the ocean. Thus, DSW mix with CDW, resulting in colder waters entering the cavity. The transition from high to low basal melt rates occurs when the mixed layer depth reaches the bottom of the ocean, i.e. at $t \approx 80$ years in both

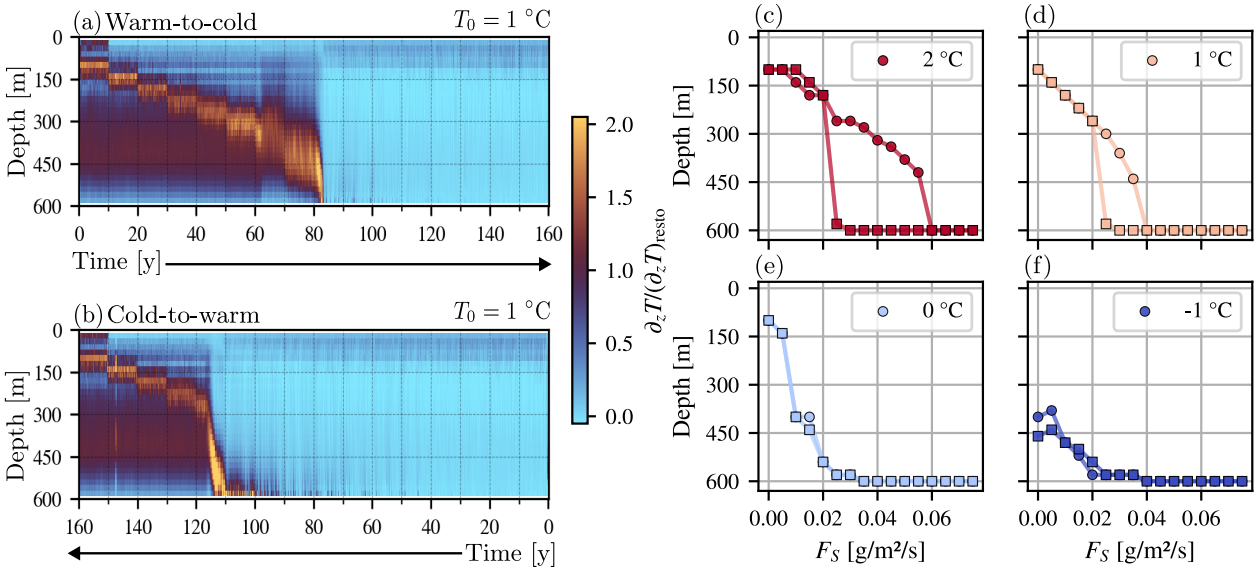

Figure 3.7: (a,b) Ratio between the temperature stratification averaged over the polynya region and every month, and the temperature stratification imposed in the restoring region ($T_0 = 1\,°\text{C}$), plotted as a function of time, for the warm-to-cold experiment in (a), and the cold-to-warm experiment in (b). The time axis of the cold-to-warm experiment has been inverted to show increasing values of F_S from the left to the right in both plots. (c-f) Thermocline depth averaged over the polynya region and over the final 3 years of each 10-year window for warm-to-cold experiments (circle) and cold-to-warm experiments (squares).

Fig. 3.6(a) (orange solid line) and Fig. 3.7(a). Conversely, the transition from low to high basal melt rates occurs when the thermocline rises from the bottom of the ocean, i.e. at $t \approx 110$ years (see Fig. 3.6(b) and Fig. 3.7(b)). Fig. 3.7(c-f) show the depth of the maximum of the temperature gradient averaged over the final 3 years of each 10-year increment (i.e., the depth of the thermocline) as a function of the imposed surface salt flux. Note that if the maximum temperature gradient is inferior to the temperature gradient in the restoring region, we consider that deep convection occurs and set the thermocline to the bottom depth. As previously seen for basal melting, a hysteresis dynamics is observed when the ocean is forced with warm enough waters ($T_0 \in \{1, 2\}\,°\text{C}$), whereas continuous transitions are observed in colder experiments ($T_0 \in \{0, -1\}\,°\text{C}$). In irreversible transitions (Fig. 3.7(c,d)), starting in the warm mode, a linear increase in the depth of the mixed layer is observed first when F_S increases, before it abruptly collapses toward the bottom of the ocean in the warm-to-cold transition. The variability of the thermocline depth increases as the system approaches the transition threshold, as shown in Fig. 3.7(a). In contrast, in the cold mode, decreasing the value of F_S does not affect the depth of the mixed layer, which stays fixed on the sea floor. At the cold-to-warm transition threshold, the thermocline abruptly leaves the seafloor, resulting in an abrupt restratification of the deep part of the ocean. Before the transition, episodic intrusion of warm deep waters are observed (larger values of $\partial_z T/(\partial_z T)_{\text{resto}}$ close to the seafloor) and they become more frequent when approaching the transition threshold, as shown in Fig. 3.7(b).

3.3.3 Scaling laws

In this section we investigate the dependence of the basal melt rates with control parameters and aim to predict the thresholds for regime transitions. The subsequent analysis is based on the results of the simulations discussed in Section 3.3.2 as well as two additional quasi-static experiments with $T_0 \in \{0.5, 1.5\}\,^\circ\mathrm{C}$.

Basal melt rates scaling

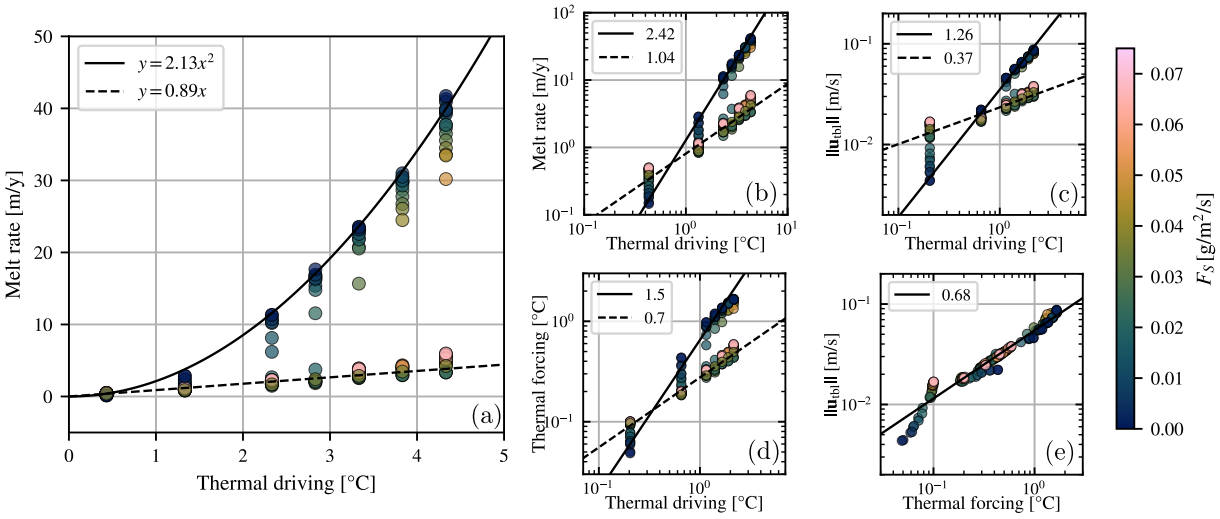

Figure 3.8: (a) Steady-state basal melt rates, as a function of thermal driving $T_0 - T_b(H)$. A quadratic fit is performed for $F_s = 0$ in the warm mode (solid line), and a linear fit is performed for $F_s = 0.04\,\mathrm{g/m^2/s}$ in the cold mode (dashed line). (b) Same but using logarithmic fits with unconstrained power law exponents. (c) Spatial average of the norm of the top boundary layer velocity as a function of thermal driving. (d) Spatial average of the thermal forcing $T_{\mathrm{tbl}} - T_b$ as a function of the thermal driving. (e) Spatial average of the norm of the top boundary layer velocity as a function of thermal forcing.

We first investigate the dependence of the melt rate with thermal driving, which we define based on the bottom temperature T_0 in the restoring region minus the local freezing point $T_b(H)$ (cf. Eq. (3.1a)), i.e. $T_0 - T_b(H)$. Fig. 3.8(a) shows the spatial average of the basal melt rate as a function of thermal driving. The melt rates corresponding to the warm and cold modes are reasonably well captured by two distinct curves. The upper curve approximates melt rates in the warm mode with a quadratic equation $y = ax^2$ (solid line), consistent with [Holland et al., 2008], which can be inferred from Eq. 3.1b. In Eq. 3.1b, the meltwater flux at the ice-ocean interface is proportional to the thermal forcing $T_{\mathrm{tbl}} - T_b$, and to the turbulent heat transfer coefficient γ_T. The coefficient γ_T depends linearly on $\mathbf{u}_{\mathrm{tbl}}$, which, according to meltwater plume theory, itself should vary linearly with the thermal forcing [Hewitt, 2020]. Thus, assuming a linear dependency between the thermal forcing and the thermal driving, the basal melt rates are expected to vary quadratically with thermal driving. In Fig. 3.8(b), a best-fit minimizing the error for the log of the melt rate yields a power law exponent of 2.42 for the warm mode melting scaling. This larger than 2 exponent could be explained because basal freezing occurs under the ice shelf when thermal driving is weak, resulting in a very low spatial

average of the basal melt rate, and a steeper slope for the power law fit. Fitting the basal melt for thermal driving values greater than 2 °C only allows finding a 2.06 power law exponent. On the other hand, the cold mode melt rates are fitted with a linear equation $y = ax$ (dashed line), which seems to be well supported by the logarithmic fit with a 1.04 power law exponent. The fact that the quadratic melting law is not recovered in the cold mode is not surprising since water masses entering the cavity are strongly modified by surface waters when convection is active. Additionally, cold circulations exhibit a Mode III melting regime close to the ice-shelf front, which can be expected to further decrease the sensitivity of the melt rate to the far-field bottom temperature. Thus scaling laws for thermal forcing and $\mathbf{u}_{\mathrm{tbl}}$ should also deviate from those obtained within the meltwater plume theory framework.

In a more generic framework, the relationships between thermal driving, thermal forcing, and boundary-layer velocity is not necessarily linear. We therefore investigate these relationships in Fig. 3.8(c-e). The dependence of the boundary-layer velocity on thermal driving (Fig. 3.8(c)) differs markedly between the two circulation regimes. The scaling is sublinear in the cold regime, with a power-law exponent of 0.37, whereas it is superlinear in the warm regime, with an exponent of 1.26. Similarly, the relationship between thermal forcing and thermal driving (Fig. 3.8(d)) also differs between the two regimes. In the warm regime, the exponent exceeds unity, indicating that the thermal forcing responds more strongly than linearly to changes in thermal driving. This behavior appears to be largely driven by the low thermal driving cases, where basal refreezing strongly reduces the spatially averaged thermal forcing and steepens the fitted power law. In contrast, the thermal forcing exhibits a sublinear dependence on thermal driving in the cold regime. Finally, we examine the relationship between boundary-layer velocity and thermal forcing (Fig. 3.8(e)). In this case, data from both circulation regimes collapse onto a single power law with an exponent of 0.68, suggesting that the local relationship between thermal forcing and boundary-layer velocity is largely independent of the circulation regime. However, this scaling alone cannot explain the distinct scalings observed in Fig. 3.8(c). Indeed, if boundary-layer velocity depended only on thermal forcing, the exponents should combine multiplicatively, yielding $0.68 \times 1.5 \approx 1.0$ and $0.68 \times 0.7 \approx 0.5$, which differ from the measured values of 1.26 and 0.37, respectively. This discrepancy indicates that boundary-layer velocity is influenced not only by the local thermal forcing but also by other processes.

The basal melt rate dependence on F_s is shown in Fig. 3.6. In addition to the sharp decrease obtained when the cavity shifts from warm to cold conditions, we find a decrease (resp. increase) of the basal melt rate with increasing F_S in the warm mode (resp. cold mode). The two trends are opposite because they are dominated by dynamics manifesting in different parts of the cavity. Fig. 3.9 shows the basal mass loss contributions of the deeper part (ice draft $>$ 300 m) and the upper part (ice draft $<$ 300 m) of the cavity. In the warm mode, the deeper part of the cavity, where thermal driving is high, is the primary contributor to meltwater formation. Meltwater masses formed at depth cool as they upwell along the ice shelf, leading to relatively weak basal melt rates in the upper part of the cavity, as predicted by meltwater plume models [Lazeroms et al., 2018, Hewitt, 2020]. The decrease of basal melt rates with increasing F_S in the warm mode is then due to the lowering of thermal driving at depth, which is driven by thermocline deepening (see Fig. 3.7) and deep water mixing with surface water under the polynya. In the cold mode, Fig. 3.9 shows that the basal mass loss in the deeper part of the cavity is weakly

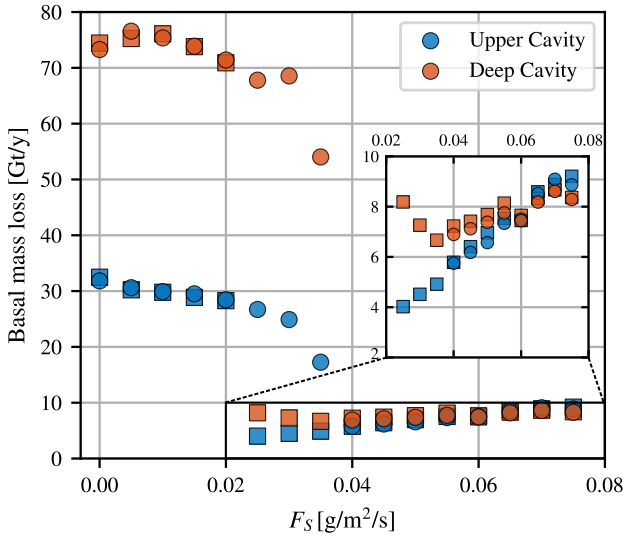

Figure 3.9: Steady-state basal mass losses for the $T_0 = 1\,°\text{C}$ experiment. Red (resp. blue) data points represent average basal mass losses in the deeper (resp. shallower) part of the cavity, using a 300 m depth threshold. Warm-to-cold (resp. cold-to-warm) data points are shown by circles (resp. squares).

impacted by the surface salt fluxes, whereas the upper part basal mass loss increases with F_S (cf. inset). In the deeper part of the cavity, basal melt rates are linked to the mode I circulation, which has deep water masses with surface freezing temperature. As the salinity impacts the freezing temperature rather weakly, the response of the basal mass loss to the surface salt fluxes is very small and nearly constant. In the upper part of the cavity, basal melt rates are instead controlled by a mode III circulation, which features surface waters intruding below the ice-shelf front, with relatively weak thermal forcing but high top boundary layer velocities $\mathbf{u}_{\text{tbl}}$ (see Fig. 3.5(c)). Importantly, the thermal-wind balance underpinning the mode III circulation is driven by the surface salt flux [Årthun et al., 2013]. Thus, the global basal melt increases with F_S in the cold mode due to the increasing contribution from the Mode III circulation.

Transition thresholds and bistability scaling

The identification of regime thresholds in phase space is key to assessing how far a cavity stands from a regime shift and to quantifying irreversibility. Previous low-dimensional studies suggested that a buoyancy (or freshwater) budget analysis could be used to predict the state of a cavity and the range of bistable dynamics [Hazel and Stewart, 2020, Moorman et al., 2023, Finucane and Stewart, 2026, Saddier et al., 2026]. In short, the buoyancy flux budget (or trend) should be negative under the polynya in the convective cold mode, positive in the warm stably stratified mode, and at equilibrium at the transition threshold. Here, the buoyancy flux B_{polynya} [m^4/s^3] associated with the imposed surface salt fluxes reads

$$B_{\text{polynya}} = -\frac{\beta g}{\rho_\star} \mathcal{A}_p F_S, \tag{3.2}$$

where $\mathcal{A}_p$ is the polynya area and g [m/s^2] is the gravity acceleration constant, and the buoyancy flux B_{melt} [m^4/s^3] associated with the meltwater fluxes reads

$$B_{\text{melt}} = \frac{\beta g}{\rho_\star}\mathcal{A}_c\langle S_b q_{\text{fw}}\rangle - \frac{\alpha g}{\rho_\star}\mathcal{A}_c\frac{\mathcal{L}}{c_p}\langle q_{\text{fw}}\rangle, \tag{3.3a}$$

where $\mathcal{A}_c$ is the horizontal area of the ice shelf, $\langle S_b q_{\text{fw}}\rangle$ [g/m^2/s] is the steady-state salt flux at the ice-ocean interface, and $\langle q_{\text{fw}}\rangle$ [kg/m^2/s] is the steady-state freshwater flux at the ice-ocean interface; both boundary fluxes being output of the three-equation model (Eqs. (3.1a) to (3.1c)). Setting Eq. (3.2) equal to Eq. (3.3a) yields a value for the surface salt flux at equilibrium, which depends on the (initial) circulation regime. Setting $B_{\text{polynya}} = B_{\text{melt}}$ for each of the two regimes thus yields two values for F_s describing both regime transitions, i.e.

$$F_S^{\text{cold}\to\text{warm}} = \frac{\mathcal{A}_c}{\mathcal{A}_p}\left(\langle S_b q_{\text{fw}}^{\text{cold}}\rangle - \frac{\alpha\mathcal{L}}{\beta c_p}\langle q_{\text{fw}}^{\text{cold}}\rangle\right), \tag{3.4a}$$

$$F_S^{\text{warm}\to\text{cold}} = \frac{\mathcal{A}_c}{\mathcal{A}_p}\left(\langle S_b q_{\text{fw}}^{\text{warm}}\rangle - \frac{\alpha\mathcal{L}}{\beta c_p}\langle q_{\text{fw}}^{\text{warm}}\rangle\right), \tag{3.4b}$$

where $q_{\text{fw}}^{\text{cold}}$ (resp. $q_{\text{fw}}^{\text{warm}}$) is the freshwater flux just before the cold-to-warm (resp. warm-to-cold) transition.

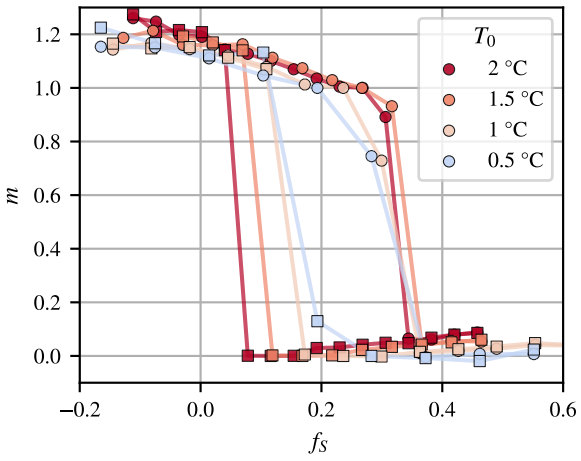

Figure 3.10: Dimensionless melt water flux m as a function of the dimensionless surface salt flux f_S.

We plot a normalized version of the meltwater flux m as a function of the normalized surface salt flux f_S, defined as

$$m = \frac{\langle q_{\text{fw}}\rangle - \langle q_{\text{fw}}^{\text{cold}}\rangle}{\langle q_{\text{fw}}^{\text{warm}}\rangle - \langle q_{\text{fw}}^{\text{cold}}\rangle}, \tag{3.5a}$$

$$f_S = \frac{F_S - F_S^{\text{cold}\to\text{warm}}}{F_S^{\text{warm}\to\text{cold}} - F_S^{\text{cold}\to\text{warm}}}, \tag{3.5b}$$

in Fig. 3.10 for all bistable experiments to test whether transition thresholds in dimensionless space always occur at $f_S = 0$ (resp. $f_S = 1$) for the cold-to-warm (resp. warm-to-cold)

transition, consistent with the buoyancy budget analysis. Note that $q_{\mathrm{fw}}^{\mathrm{cold}}$ and $q_{\mathrm{fw}}^{\mathrm{warm}}$ have been chosen as the second to last meltwater fluxes before each transition, because the values of the last points are more sensitive to their distance to the transition thresholds. The dimensionless curves obtained are almost superimposed for all experiments, suggesting that the buoyancy budget analysis captures reasonably well the sensitivity of basal melt rates and transition thresholds to the far-field temperature. The warm-to-cold transitions collapse on the same master curve but occur at $f_S \approx 0.35$ instead of the predicted value $f_S = 1$. This discrepancy is not surprising since the water column under the polynya is an open system that can have horizontally-diverging buoyancy fluxes when convection sets in. The lower than one f_S threshold suggests that some of the meltwater produced in the cavity is advected away from the polynya region, as already shown by Xu et al. [Xu et al., 2023a, Xu et al., 2023b], and is in good agreement with previous low-dimensional models of ocean cavities that adjusted Eqs. (3.4a) and (3.4b) with a dimensionless coefficient inferior to one to match transition thresholds of numerical simulations [Hazel and Stewart, 2020, Finucane and Stewart, 2026]. The cold to warm transitions show slightly more scatter and occur for values superiors to the predicted threshold $f_S = 0$. This suggests that restratification occurs before reaching an equilibrium buoyancy budget, possibly because of the advection of meltwater outside of the polynya region.

Relative potential energy as a stability criterion

To further characterize the stability of each regime and provide a physical explanation for the transitions, we seek a metric that quantifies the stability of the water column beneath the polynya. The buoyancy budget discussed above is not sufficient for this purpose because buoyancy can be transported into or out of the water column through advection, thereby modifying its stability independently of the local surface forcing. The low-dimensional model developed in the previous chapter suggests that such a metric should be related to the density contrast between the surface and deep waters beneath the polynya. For example, the self-consistent equation for $\sigma = (\rho_p - \rho_d)/\rho_\star$ (see Eq. 2.36) determines the equilibrium states of the system for an arbitrary parameterization of the vertical mixing coefficient $k(\sigma)$. In the three-dimensional simulations, however, defining representative surface and deep densities is somewhat arbitrary because the choice of the reference depth is not unique. Instead, we quantify the stability of the water column through its potential energy per unit horizontal area ($\mathrm{J\,m^{-2}}$), which naturally accounts for the density distribution over the entire water column. To compare experiments with different external forcings, this potential energy must be defined relative to a suitable reference state. A natural choice is the restoring water column, since it represents the state towards which the system would relax in the absence of the other forcings:

$$\mathrm{RPE}_0 = \int_{-H}^{0} \left[\rho(z) - \rho_{\mathrm{resto}}(z)\right] g(z+H)\,\mathrm{d}z. \tag{3.6}$$

Here, ρ [$\mathrm{kg\,m^{-3}}$] denotes the horizontally averaged density beneath the polynya and ρ_{resto} [$\mathrm{kg\,m^{-3}}$] is the restoring density profile. Although physically meaningful, this definition does not reveal a critical value separating the warm and cold regimes across the different experiments.

After exploring several reference states, we found that using the maximum potential energy attainable by complete mixing of the restoring water column provides a much more

robust stability criterion. The resulting relative potential energy is defined as

$$\mathrm{RPE} = \int_{-H}^{0} \left[\rho(z) - \bar{\rho}_{\mathrm{resto}}\right] g(z+H)\,\mathrm{d}z, \tag{3.7}$$

where $\bar{\rho}_{\mathrm{resto}}$ [kg m^{-3}] is the depth-averaged density of the restoring profile. A positive value of RPE therefore indicates that the water column beneath the polynya possesses more potential energy than the fully mixed restoring state. We hypothesize that this threshold represents the energy barrier that must be exceeded for deep convection to develop.

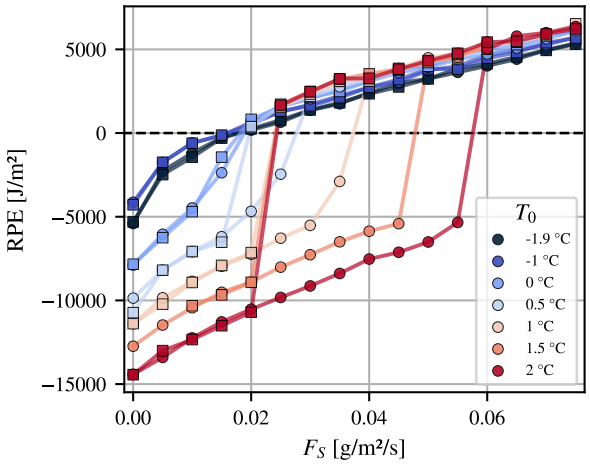

Figure 3.11: Relative potential energy per unit surface, RPE, as a function of the imposed surface salt flux. Simulations with increasing (circles) and decreasing (squares) salt fluxes are shown separately.

Figure 3.11 shows the evolution of RPE as a function of the imposed salt flux F_S for different values of T_0. Positive values of RPE systematically correspond to the cold convective regime (upper branches above the dashed line), whereas negative values characterize the warm stratified regime (lower branches below the dashed line). The warm-to-cold and cold-to-warm transitions correspond to the rightmost and leftmost sloping sections of the hysteresis curves, respectively. In the cold regime, the RPE curves nearly collapse onto a single branch and exhibit the same cold-to-warm transition threshold already identified in Fig. 3.6. In contrast, the warm branches remain separated because the meltwater flux depends strongly on the thermal driving. As T_0 increases, enhanced basal melting freshens the surface layer, thereby reducing its density and decreasing RPE. While the cold-to-warm transition consistently occurs near RPE = 0, the warm-to-cold transition takes place at negative RPE values. Moreover, the corresponding critical value becomes increasingly negative as T_0 increases.

This behaviour is consistent with the predictions of the low-dimensional model when the vertical mixing coefficient is represented by a smooth function $k(\sigma)$ (Fig. 3.12). The physical interpretation is straightforward. Vertical mixing acts as a negative feedback by eroding the density stratification. In the warm regime, this homogenization increases σ in the box model, or equivalently increases RPE in the NEMO simulations, thereby destabilizing the water column and promoting convection. When $k(\sigma)$ is represented by a step function with a very small background diffusivity k_{diff}, this feedback remains

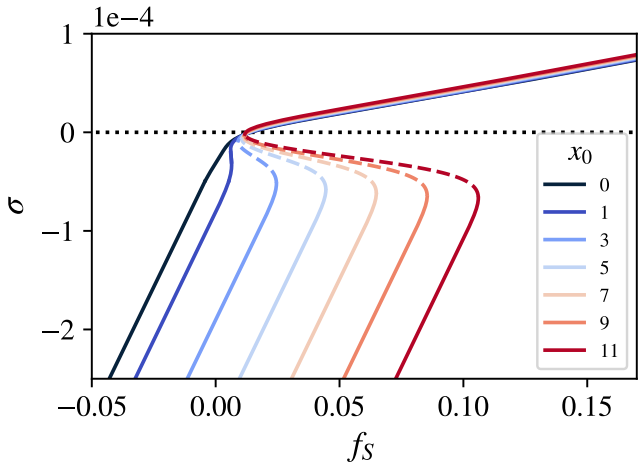

Figure 3.12: Results from the low-dimensional box model presented in the previous chapter. Density difference $\sigma = (\rho_p - \rho_d)/\rho_\star$ as a function of the dimensionless salt forcing f_S for several values of the dimensionless thermal driving x_0. Solid and dashed lines denote stable and unstable equilibria, respectively.

weak until convection is initiated. By contrast, for a smooth parameterization, the mixing intensity increases progressively as σ approaches zero. This stronger destabilizing feedback causes the system to undergo the warm-to-cold transition before complete neutralization of the stratification, explaining why the transition occurs at negative values of RPE.

To further compare the NEMO simulations with the low-dimensional box model, it is natural to seek an analogue of the vertical mixing coefficient $k(\sigma)$. Although such a quantity cannot be directly diagnosed from the model, the vertical kinetic energy (VKE) of the water column provides a useful proxy for the resolved component of vertical mixing. We therefore define the vertically integrated kinetic energy per unit horizontal area ($\mathrm{J\,m^{-2}}$) as

$$\mathrm{VKE} = \int_{-H}^{0} \frac{1}{2}\rho w^2 \,\mathrm{d}z. \tag{3.8}$$

Figure 3.13 shows the evolution of VKE as a function of RPE. The VKE remains weak for RPE < 0, corresponding to the warm stratified regime, but increases rapidly once RPE becomes positive. Remarkably, the data from all experiments collapse onto a single curve, indicating that the relationship between VKE and RPE is largely independent of the restoring temperature T_0. We note that the VKE increases continuously across RPE $= 0$, and no saturation is reached over the range of forcings considered here. This interpretation should nevertheless be treated with caution. The VKE only characterizes the resolved component of the vertical motions, whereas a significant fraction of the vertical mixing is parameterized through the enhanced vertical diffusion (EVD) scheme via the fluxes $\kappa_v \partial_z \rho$. Consequently, VKE cannot be interpreted as a direct measure of the total vertical mixing occurring beneath the polynya.

To conclude this discussion, the proposed RPE provides a consistent measure of the stability of the water column beneath the polynya, although its definition relies on a somewhat ad hoc choice of reference potential energy based on the restoring profile. Whether this definition would remain appropriate in more realistic configurations is still under investigation. Despite this limitation, the RPE appears to be a promising diagnostic. First,

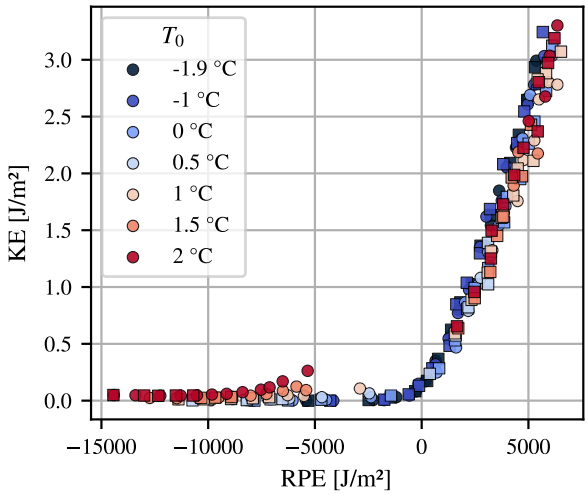

Figure 3.13: Vertical kinetic energy of the polynya water column (VKE, Eq. (3.8)) as a function of its relative potential energy (RPE, Eq. (3.7)).

it provides a predictive indicator of the cold-to-warm transition, since the RPE evolves nearly linearly in the cold regime and the transition consistently occurs near RPE = 0. Second, it offers a natural framework for quantifying the processes governing the stability of the water column by decomposing the RPE tendency into contributions from basal melting, vertical mixing, lateral transport, and surface forcing. Such a decomposition would provide a physically grounded description of the feedback mechanisms operating beneath the polynya and could ultimately lead to a more complete understanding of regime transitions in ice-shelf cavities.

3.4 From irreversible to reversible regime transitions

We now discuss an additional set of simulations aimed at testing the sensitivity of the hysteresis behavior to physical processes (other than the far-field temperature) and modeling choices, including the strength of the salt stratification in the restoring region, the large-scale flow structures at the ice-shelf front and the subgrid-scale dissipation scheme.

3.4.1 Impact of salt stratification

We first test the impact of the salinity field in the restoring region. We restrict our attention to the case of moderate temperature forcing, i.e., $T_0 = 1\,°\mathrm{C}$ (cf. orange curve in Fig. 3.6). Fig. 3.14(a) shows the basal melt rates obtained for three quasi-static experiments with different Sea Surface Salinity (SSS) of 33.8 g/kg, 34.0 g/kg, and 34.2 g/kg but constant Sea Bottom Salinity (SBS) set to 34.5 g/kg. The corresponding Brunt-Väisälä frequencies are $8.5\times10^{-3}\,\mathrm{s}^{-1}$, $2.2\times10^{-3}\,\mathrm{s}^{-1}$, and $1.4\times10^{-3}\,\mathrm{s}^{-1}$, respectively. An increase of the density stratification in the restoring region results in an increase of the cold-to-warm transition threshold (leftmost bifurcation), diminishing the size of the bistable region. For the largest density stratification, the bistable region completely shrinks, and the transition becomes fully reversible. The impact of the restoring density stratification on the

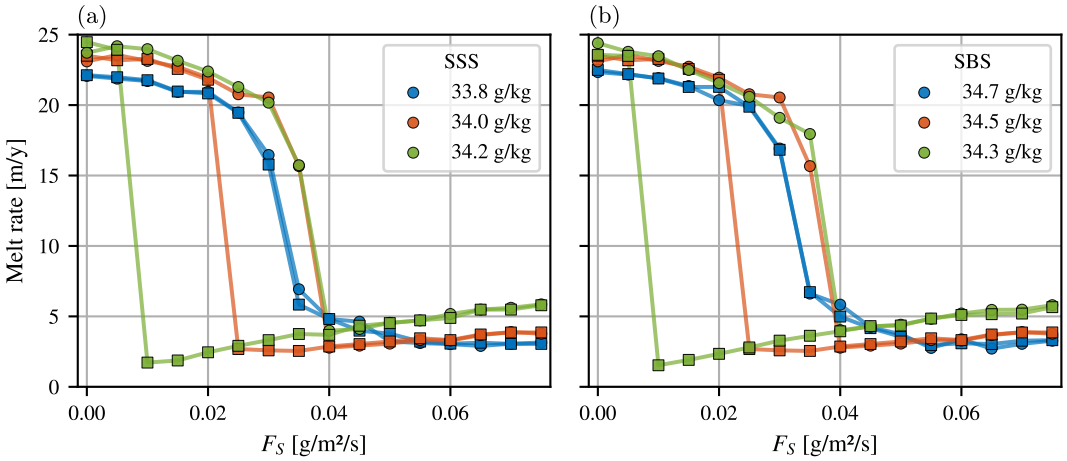

Figure 3.14: Steady-state basal melt rates as a function of surface salt fluxes for $T_0 = 1\,°C$ for different (a) Sea Surface Salinity (SSS) or (b) Sea Bottom Salinity (SBS) values imposed within the restoring region. Circles (resp. squares) denote results obtained with F_s increasing (resp. decreasing). We set SBS = 34.5 g/kg for the experiments shown in (a) and SSS = 34.0 g/kg for those shown in (b), such that the green, orange and blue curves show experiments with weak, reference and strong stratification in both (a) and (b), respectively.

cold-to-warm transition threshold can be understood with a simple argument: stronger density stratification in the restoring region favors restratification in the polynya region, and conversely. On the other hand, the restoring density stratification has no impact on the warm-to-cold transition.

To test whether the Sea Bottom Salinity can similarly impact the dynamics as the Sea Surface Salinity in the restoring region, we show in Fig. 3.14(b) the results of three quasi-static experiments obtained with SBS set to 34.7 g/kg, 34.5 g/kg, and 34.3 g/kg, respectively. The SSS is set equal to 34.0 g/kg, such that the Brunt-Väisälä frequencies are the same as those imposed in the SSS experiments. The experiments with different SBS values give the exact same basal melt rates as those obtained with different SSS values. Thus, the absolute values of the imposed salinities are not important for the dynamics and only the relative values of the imposed salinity profiles play a role, in agreement with recent results from low-dimensional models [Hazel and Stewart, 2020, Moorman et al., 2023, Saddier et al., 2026].

The impact of the salinity stratification on the stability of the cold mode is intuitive. However, it is not clear why the warm mode is not affected in the same way, i.e., stronger restoring density stratification is expected to favor the warm mode. To investigate the regime transitions, we use the potential energy metric defined in Eq. (3.7). Fig. 3.15 shows the evolution of PE as a function of F_S, varying only the SSS restoring. The transitions clearly occur when PE = 0. In the warm mode, the PE curves superimpose, meaning that regardless of the density stratification in the restoring region, the stability of the water column under the polynya has the same evolution. Thus, the PE curves in the warm mode cross the value PE = 0 for the same F_S threshold, and the cold-to-warm threshold is not affected by changes in the restoring density stratification. On the other hand, potential energy curves are disjoint in the cold mode, but still have the same tendency. As a result,

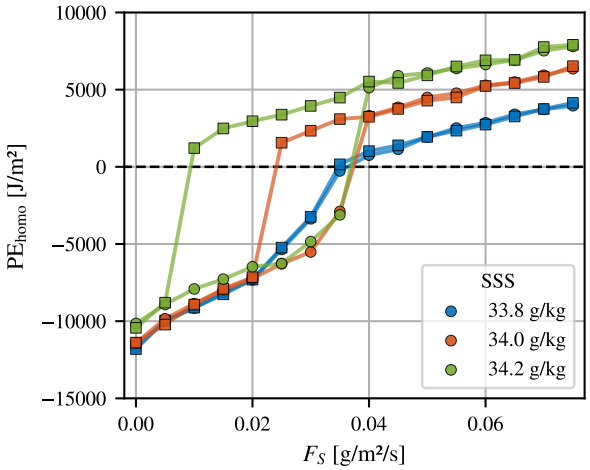

Figure 3.15: Steady-state potential energy per unit surface PE as a function of surface salt fluxes for different SSS values but fixed SBS = 34.5 g/kg in the restoring region and $T_0 = 1\,°C$. Circles (resp. squares) denote results obtained with F_s increasing (resp. decreasing).

their crossing with PE = 0 does not occur for the same F_S thresholds.

We now have a clear understanding of how the restoring water properties affect water-column stability, as quantified by the potential energy metric PE. On the one hand, in the warm mode, the water column is controlled primarily by meltwater released from the ice-shelf cavity and is not directly affected by the restoring region. Nevertheless, the restoring region can indirectly influence water-column stability when higher values of T_0 are imposed (Fig. 3.11), because increased thermal driving enhances basal melt rates. On the other hand, in the cold mode, water-column stability is independent of T_0 (Fig. 3.11) and depends solely on the restoring density stratification (Fig. 3.15). Indeed, the potential energy metric, which quantifies the stability of the water column beneath the polynya, is directly controlled by the density stratification prescribed in the restoring region.

3.4.2 Impact of the large scale circulation: from no-slip to free-slip lateral boundaries

The ocean circulation at the front of the ice self should play an important role on the stability of the water column beneath the polynya since it affects the transport of the meltwater coming from the ice-shelf cavity, the offshore water coming from the restoring region, and the DSW formed at the polynya surface. We discuss the implications of modifying this circulation by changing the lateral boundary conditions at the lateral walls of the spatial domain.

Fig. 3.16 shows the impact of switching the lateral boundary conditions from no-slip (no velocity on the walls) to free-slip (no shear on the wall), for the experiment with $T_0 = 1\,°C$, SST $= -1.9\,°C$, SSS = 34.0 g/kg, and SBS = 34.5 g/kg (again using linear relaxation profiles in the restoring region). The response of the ice shelf to salt surface forcing is completely different between the no-slip and free-slip cases. The basal melt rate transitions continuously and slowly from a warm mode to a cold mode, as shown in

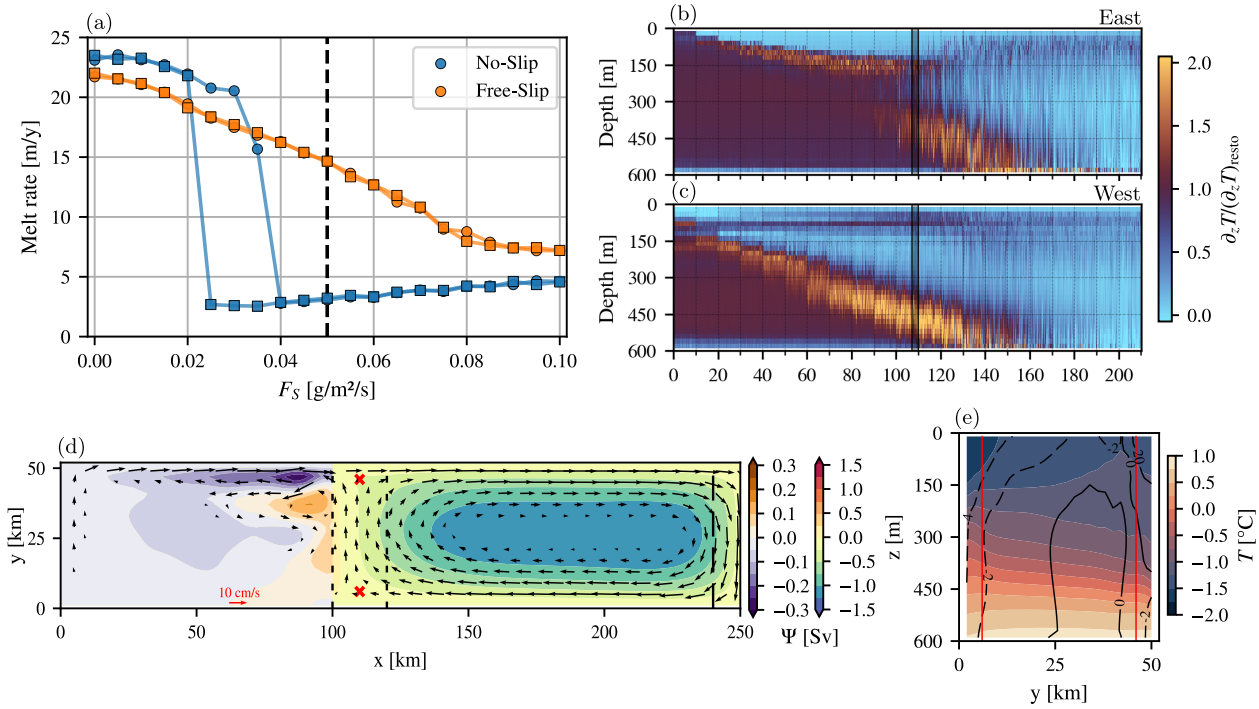

Figure 3.16: Results of the quasi-static experiment with free-slip lateral boundary conditions, $T_0 = 1\,°\text{C}$, SSS $= 34.0\,\text{g/kg}$, and SBS $= 34.5\,\text{g/kg}$. (a) Basal melt rates as a function of the surface salt flux. (b,c) Normalized temperature stratification plotted as a function of time, at $x = 110$ km and $y = 6$ km (eastern side) in (b), and $x = 110$ km and $y = 46$ km (western side) in (c). The thin shaded area in black in the middle represents the time window used for temporal averaging of the variables shown in (d) and (e). (d) Barotropic stream function. Red crosses show the positions of the temperature stratification profiles displayed in (b) and (c). (e) $y - z$ slice of the temperature field at $x = 110$ km. Black contours are meridional velocity contours [cm/s], negative (dashed) when directed towards the cavity, and positive (solid) when directed away from the cavity. Red verticals lines show the positions of the temperature stratification profiles displayed in (b) and (c). The black dashed line in (a) represents the surface salt flux imposed in (d) and (e).

Fig. 3.16(a), and the transition is completely reversible as warm-to-cold and cold-to-warm experiments give the same response (cf. overlapping orange circles and squares). The thermocline depth under the polynya shows a reversible evolution and is therefore only plotted for the warm-to-cold experiment, on the eastern side of the domain in Fig. 3.16(b), and on the western side in Fig. 3.16(c). The mixed layer depth increases with time on both sides, as surface salt fluxes increases. However, the thermocline deepens first more slowly on the eastern side in comparison to the western side, and then relatively abruptly around the year 100, beyond which it matches more closely the western side stratification. It therefore seems that the eastern and western sides of the polynya are not impacted by the same water masses fluxes. Vertical dark bands are visible on both stratification plots in the layer above the thermocline at late times (cold conditions), meaning that the mixed layer is subject to episodic restratification events with warm water intrusions, which likely disrupt the cold mode dynamics. To better understand the change of behavior between

the no-slip and free-slip cases, the barotropic stream function of the free-slip experiment is shown in Fig. 3.16(d), for $F_S = 0.05\,\mathrm{g/m^2/s}$, i.e. when a cold mode circulation arises in the no-slip experiment (see Fig. 3.5). Instead of counter rotating gyres along the x axis, a single strong cyclonic gyre occupies the whole open ocean, from the front of the ice shelf to the restoring region. This modified circulation impacts the water properties at the front of the ice shelf in two ways. Firstly, the meltwater releases on the western side are directly advected towards the restoring region where they transform into more saline water masses. Thus, the meltwater positive feedback is attenuated, and both circulation modes become less self-sustained. Secondly, restoring temperature and salinity profiles are directly advected from the restoring region toward the polynya on the eastern side, favoring restratification, warm water intrusions and hence Mode II dynamics. The east-west asymmetry is further highlighted in Fig. 3.16(e), which shows a $y - z$ slice of the temperature field under the polynya. The direct connection between the restoring and polynya regions is responsible for the restratification events observed in Fig. 3.16(b,c), even when strong surface salt fluxes are applied. In the end, the free-slip experiments show reversible transitions because the domain-scale circulation suppresses the meltwater positive feedback.

3.4.3 Impact of subgrid-scale dissipation: changing the horizontal viscosity

Given its direct influence on boundary currents and tracer transport, we investigate how variations in ν_H affect the transition thresholds and the stability of the two circulation regimes. In fact, the choice of horizontal viscosity is not strongly constrained in ocean models, with coefficients often selected on a combination of physical and numerical grounds that can vary substantially across model configurations [Griffies, 2004].

Fig. 3.17 summarizes the results of a sensitivity analysis varying ν_H. For consistency, the horizontal diffusivity is modified simultaneously as $\kappa_H = \nu_H$. We discuss the results of three quasi-static experiments having the same linear restoring profiles (SSS $= 34.0\,\mathrm{g/kg}$, SBS $= 34.5\,\mathrm{g/kg}$, SST $= -1.9\,^\circ\mathrm{C}$, and $T_0 = 1\,^\circ\mathrm{C}$). The first experiment uses the same viscosity coefficient as in the original set of experiments (orange symbols and curve), the second one has a five times higher coefficient (blue), and the third one has a five times lower coefficient (green). Note that we found it necessary to decrease the time step to 180 s for the two new experiments to ensure numerical stability [Griffies, 2004]. Fig. 3.17(a) shows that the transition thresholds are affected by the viscosity coefficient, and that the bistable region becomes smaller when ν_H either increases or decreases. In the most viscous simulation (blue symbols and lines), the basal melt rates are always weaker than in the other simulations.

We first demonstrate that the lower basal melt rate and warm-to-cold threshold for the higher viscosity simulation is due to a weakening of the meltwater plume. Fig. 3.17(b) represents the norm of the horizontal top boundary layer velocity $\|\mathbf{u}_{\mathrm{tbl}}\|$, at $x = 50$ km (mid-depth in the cavity), for $F_S = 0$. The meltwater boundary current is always visible close to the western boundary ($y = 50$ km). However, its thickness and maximum strength vary with ν_H, specifically, it is thicker and weaker for the higher ν_H case. This result qualitatively agrees with the Munk layer scaling, which predicts a thickness proportional to $(\nu_H/\beta_{\mathrm{topo}})^{\frac{1}{5}}$ and a transport in the layer proportional to $(\beta_{\mathrm{topo}}/\nu_H)^{\frac{1}{5}}$, where β_{topo} [$\mathrm{s^{-1}m^{-1}}$]

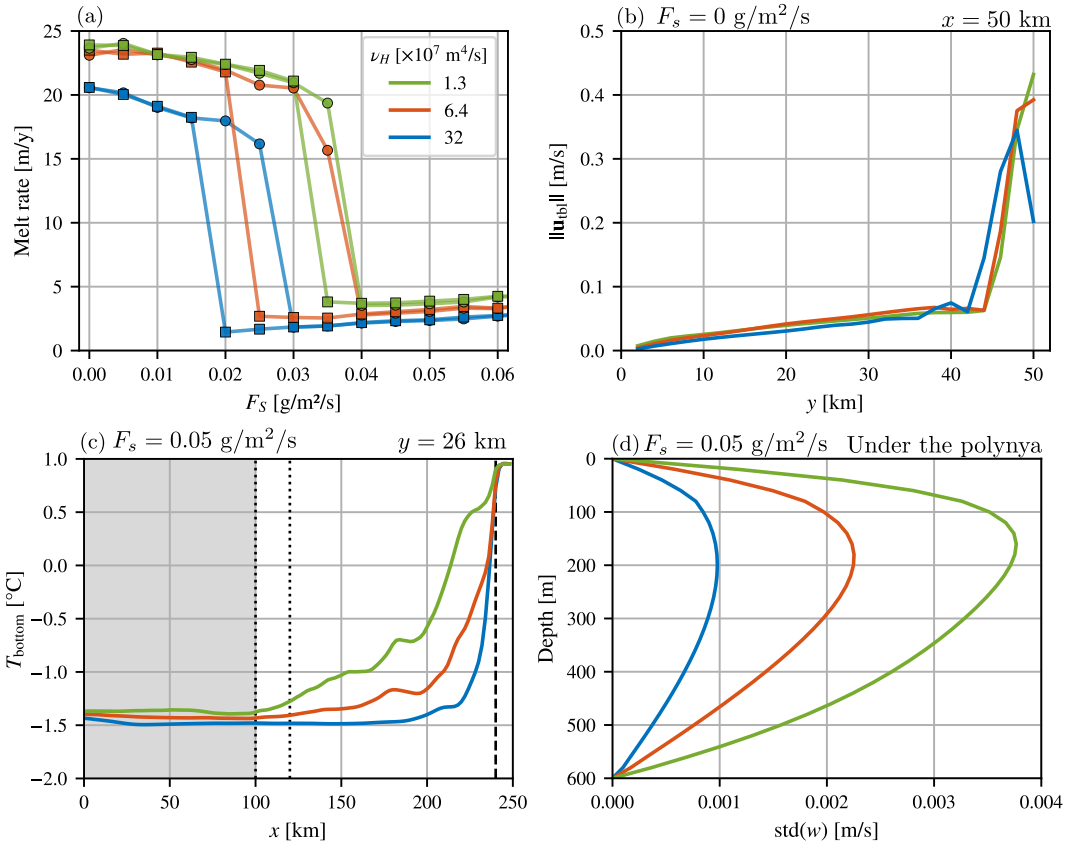

Figure 3.17: Quasi-static experiments varying the horizontal viscosity ν_H and diffusivity κ_H simultaneously ($\kappa_H = \nu_H$). The properties of the restoring region are SSS = 34.0 g/kg, SBS = 34.5 g/kg, SST = −1.9 °C, and T_0 = 1 °C. (a) Basal melt rates as a function of surface salt fluxes with either increasing F_S (circles) or decreasing F_S (squares). (b) Norm of the top boundary layer horizontal velocity at x = 50 km (300 m depth) for F_S = 0 (warm mode). (c) Bottom temperature at y = 26 km with F_S = 0.05 g/m²/s. The gray-shaded area highlights the ice-shelf cavity region, the dotted lines highlight the extent of the polynya region, and the dashed line pinpoints the start of the restoring region. (d) Steady-state standard deviation of the vertical velocity below the polynya when F_S = 0.05 g/m²/s. Note that grid-scale numerical noise are visible in the vertical velocity field in the low viscosity experiment (in green).

is the topographic beta effect coefficient induced by the variable water column thickness in the cavity [Munk, 1950, Cessi et al., 1990, Griffies and Adcroft, 2008]. The increase of the horizontal viscosity thus lowers meltwater production through a decrease of γ_T, which weakens the meltwater feedback and ultimately lowers the warm-to-cold transition threshold, as shown in Fig. 3.17(a). The zonal resolution Δy = 2 km of our configuration only partially resolves the western boundary layer, we would therefore also expect the transition thresholds to depend on Δy. We then demonstrate that the lowering of the cold-to-warm transition threshold with increasing ν_H is linked to the transport of heat from the restoring region towards the cavity. Fig. 3.17(c) shows the bottom temperature for the different experiments at y = 26 km and F_S = 0.05 g/m²/s. When the horizontal viscosity is weak, CDW reach more easily the front of the cavity, due to enhanced horizontal

velocities (not shown). Increasing heat transport into the cavity increases meltwater production, which stabilizes the water column and favors the warm mode, hence the cold-to-warm threshold is pushed to higher values of F_S as ν_H decreases. We finally show in Figure 3.17(d) the vertical profiles of the standard deviation of vertical velocity beneath the polynya for $F_S = 0.05\,\mathrm{g/m^2/s}$, i.e. when the cold mode dominates in each experiment. The standard deviation increases as the horizontal viscosity decreases. However, the increased vertical mixing at low ν_H does not favor the cold mode since Fig. 3.17(a) shows a reduced stability of the cold mode with decreasing viscosity. This suggests that the sensitivity of the cold-to-warm transition to ν_H is primarily linked to its impact on the heat transport at depth rather than on vertical mixing.

3.5 Discussion and conclusion

We have run simulations with the NEMO ocean code to assess the impact of salt rejection in coastal polynyas on the stability of ice-shelf cavity modes I and II (cold and warm, respectively), and investigate the potential for irreversible transitions. Our setup is based on previous idealized numerical configurations that did not impose any surface buoyancy fluxes and thus were focused on the warm circulation regime [Holland et al., 2008, Asay-Davis et al., 2016, Yung et al., 2026]. We highlight four key take-away and discuss model limitations in the next paragraphs.

First take-away: we report irreversible transitions between cold and warm circulation regimes. The emergence of a cold convective circulation regime for high enough surface salt fluxes aligns well with previous studies that demonstrated cold-to-warm regime shifts when the continental shelf freshen, based on both realistic [Caillet et al., 2023, Hazel and Stewart, 2020, Daae et al., 2020, Song et al., 2025, Jin et al., 2025, Naughten et al., 2021, Mathiot and Jourdain, 2023, Hellmer et al., 2017, Haid et al., 2023, Hoffman et al., 2024, Mathiot et al., 2026] and low-dimensional models [Hazel and Stewart, 2020, Moorman et al., 2023, Finucane and Stewart, 2026, Saddier et al., 2026]. The simplicity of our numerical configuration allowed to perform quasi-static experiments with surface salt fluxes increasing or decreasing incrementally, resulting in a succession of statistical steady states for each forcing value in the same fashion as ice-sheet modelling studies that tested the reversibility of the ice-sheet retreat [Rosier et al., 2021, Garbe et al., 2020]. We demonstrated that the system exhibits hysteresis with irreversible transitions when the CDW temperature exceeds 0.5 °C and reversible behavior otherwise. The multistability is supported by a positive meltwater feedback that reinforces both regimes: high basal melt rates stabilize the water column in the warm mode, while low basal melt rates favor deep convection in the cold mode [Hazel and Stewart, 2020, Moorman et al., 2023, Saddier et al., 2026]. Increasing forcing temperatures amplifies this feedback, thereby widening the bistable range of surface salt fluxes. We expect that increasing the exchange coefficients in the basal melt parameterization at the ice–ocean interface would similarly enhance this feedback, and thus shift the warm-to-cold transition threshold to large surface salt fluxes.

Second take-away: the thermocline depth controls regime transitions and basal melt rates. Warm-to-cold (resp. cold-to-warm) transitions occur exactly when the thermocline reaches (resp. lifts from) the seafloor. Furthermore, early warning signals preceding

regime transitions can be detected from the thermocline dynamics: the variability of the thermocline depth increases (Fig. 3.7(a)) prior to warm-to-cold transitions and the frequency of intermittent restratification events increases (Fig. 3.7(b)) before cold-to-warm regime shifts. In contrast, we did not find any early warning signals in basal melting rates prior to transitions (Fig. 3.6(a,b)). In the warm mode, the basal melt rate is modulated by the depth of the thermocline, with weaker basal melt rates when the thermocline deepens, in agreement with realistic studies of the Amundsen Sea [Haigh et al., 2026,O'Connor et al., 2025] and in a low-dimensional model of thermocline dynamics under the Amundsen Sea polynya [Moorman et al., 2023]. In the cold mode, the basal melt rate does not depend on the thermocline depth since convection occurs across the entire water column. Still, basal melt rates decrease with surface salt fluxes before the cold-to-warm transition, consistent with [Naughten et al., 2021], who link the basal melt rates to the barotropic circulation in the cavity. Consistently, we find that surface salt fluxes create an anticyclonic gyre at the front of the ice shelf, which enhances basal melting in the upper part of the cavity [Årthun et al., 2013]. Interestingly, [Jin et al., 2025] observe a current reversal at the front of the Amery ice shelf when transitioning from a cold to a warm mode, which we also have in our model with the reversal of the anticyclonic gyre.

The quadratic melting law as a function of the restoring thermal driving predicted by [Holland et al., 2008] is recovered in the warm mode. In the cold mode, the basal melt rate instead follows a linear scaling with thermal driving as DSW interferes with CDW, lowering the impact of far-field properties on ice losses. This result is in agreement with [Burgard et al., 2022] who found reduced agreement when quadratic melt models are forced with offshore water properties. In line with this, our linear scaling suggests that these formulations may not always be appropriate for estimating basal melt rates from offshore conditions.

Third take-away: the buoyancy budget analysis provides an upper bound for the extent of the bistable region. Rescaling the basal melt rates and the surface salt fluxes according to a buoyancy budget argument put forth in low-dimensional model studies [Finucane and Stewart, 2026, Hazel and Stewart, 2020, Moorman et al., 2023, Saddier et al., 2026], we found a reasonably good collapse of the hysteresis curves obtained with different restoring temperature forcing. However, the rescaling did not lead to the predicted single universal pair of transition thresholds. The bistable range for our simulations is narrower than predicted as the salt flux thresholds for warm-to-cold transitions and salt flux thresholds for cold-to-warm transitions are lower and higher, respectively, than anticipated. The discrepancy can be attributed to the fact that the water column under the polynya is an open system, such that the buoyancy flux balance isn't strictly between the meltwater outflow and air-ocean interface but also with the overall cavity and open ocean [Xu et al., 2023a, Xu et al., 2023b]. Similar observations have already been documented in numerical simulation studies that tried to predict transition thresholds from buoyancy budget arguments [Hazel and Stewart, 2020,Finucane and Stewart, 2026]. We note that interconnections between multiple ice-shelf cavities exchanging meltwater fluxes could also impact the buoyancy budget and modify transition thresholds [Hoffman et al., 2024,Silvano et al., 2018].

We proposed another metric based on the potential energy difference between the polynya water column and the restoring water column (denoted by RPE, see Eq. 3.7)

to infer the transition thresholds. For positive RPE values the water column is in a convective state, whereas for negative RPE values the water column is stably stratified. This metric managed to capture the actual transition thresholds, unlike the simpler proxy based on the density difference between the densest DSW and CDW intruding along the seafloor [Haid et al., 2023], which could not discriminate between the two regimes in our experiments.

Fourth take-away: far-field temperature, stratification and modeling choices impact the nature of the transitions. We have explored several physical effects and modeling pathways that can change the reversibility of regime changes, which remains debated across realistic studies.

We have shown that the properties of the CDW intruding the continental shelf can impact the transition thresholds. On the one hand, low CDW temperature promotes lower warm-to-cold transition thresholds. On the other hand, high CDW density stratification promotes higher cold-to-warm transition thresholds. Weddell Sea ice shelves are subject to colder offshore CDW than the rest of Antarctica [Schmidtko et al., 2014, Narayanan et al., 2023] and Amundsen Sea offshore density profiles are more stratified than other regions of Antarctica [Narayanan et al., 2023]. The impact of temperature and stratification on reversibility acts in opposite direction for both the Amundsen Sea and Weddell Sea regions. Both transition thresholds should occur for relatively high F_S values for the former and low F_S values for the latter. Therefore, it is difficult to conclude on a narrowing or a widening of the bistable zone, and on the reversibility of the transitions for these two Antarctic regions. Other Antarctica regions, which are relatively warm and weakly stratified, can yet be expected to have a relatively large bistable region and thus more prone to irreversible transitions.

We have shown that the ocean circulation in front of the ice shelf can amplify the meltwater positive feedback by trapping the cavity outflow within a coastal gyre. In our idealized configuration, this mechanism promotes the persistence of both circulation regimes and ultimately contributes to the irreversibility of the transitions. The importance of local dynamics was demonstrated by comparing the no-slip simulations with analogue free-slip experiments (no friction on side walls), which do not feature a coastal gyre and experience continuous and reversible transitions. [Xu et al., 2023b] reached similar conclusions by showing that the presence of a headland or ice tongue adjacent to a polynya can induce a gyre that inhibits the export of DSW from the polynya region. More generally, several Antarctic ice shelves are associated with gyre-like circulations near their fronts. Examples include the Pine Island gyre in front of Pine Island ice shelf [Poinelli et al., 2025], the Prydz Bay gyre adjacent to the Amery ice shelf [Jin et al., 2025], and the cyclonic and anticyclonic gyres over the Berkner bank and Filchner trough at the front of the Filchner ice shelf [Naughten et al., 2019]. These circulation features may therefore influence the propensity of ice-shelf cavities to undergo irreversible transitions. However, the role of coastal gyres is likely more complex than the mechanism identified here. Although they can enhance meltwater retention and strengthen positive feedback, they may also reduce the direct influence of far-field water masses by limiting exchanges with the open ocean. In particular, a coastal gyre may shield the ice-shelf front from externally imposed stable stratification, which would otherwise promote restratification beneath the polynya and favor the warm mode.

We finally investigated the role of the horizontal viscosity and showed that it can also modify the transition thresholds. Specifically, increasing the viscosity can affect the heat flux on the continental shelf towards the cavity in cold regimes, the circulation in the ice-shelf cavity, or the vertical velocity associated to convective patterns. Although [Jin et al., 2025], [Mathiot et al., 2026] and [Hazel and Stewart, 2020] used similar horizontal resolution (≈ 8 km), they used horizontal biharmonic viscosity coefficients that differ by an order of magnitude. Thus, our analysis suggest that these studies may not be comparable in terms of transition thresholds and reversibility. A future research avenue would be to test the impact of the horizontal and vertical subgrid scale dissipation schemes (related to both viscosity and diffusivity) in more realistic configurations.

Model limitations. Our idealized configuration was well-suited for long quasi-static forcing experiments, which are typically inaccessible to realistic configurations. However, it lacks physical processes that are considered key to real cavities. First, our configuration does not have a realistic topography for both the ice-shelf draft and the sea floor, even though topographical features, such as troughs, are expected to control circulation patterns and thus basal melting [De Rydt and Naughten, 2024, Bradley et al., 2022]. It also omits continental shelf–break processes, which can modulate CDW inflows onto the shelf through (positive or negative) large-scale feedback [Thompson et al., 2018]. For example, [Si et al., 2023] showed that cross-slope salinity gradients across the shelf break impact the heat transport towards the continental shelf. Another limitation stems from the idealized forcing scheme imposed at the sea surface, which omits surface wind stresses and discards sea-ice coupling. The modeling of surface conditions may yet have a leading order effect on dynamics as [Xu et al., 2023a] showed that the wind driven circulation impact the fluxes of DSW at the front of the ice shelf, and that the extent of the polynya is strongly dependent on the interplay between the sea ice and wind stresses. Freshwater fluxes coming from other ice-shelf cavities could also impact the buoyancy budget at the front of the ice shelf [Hoffman et al., 2024, Silvano et al., 2018]. Finally, our study focuses on the steady response of the ice shelf to coastal polynya forcing, which is an appropriate framework to characterize feedback processes and the nature of regime shifts, hence leaves the question of time scales open. Nevertheless, we remark that our 10 years steps were sufficient to capture full regime transitions, giving a first order of magnitude of the transition time scales in our specific configuration. We expect that the flushing time scales of the cavity [Holland, 2017], and the deepening and lifting time scales of the thermocline [Årthun et al., 2013, Sohail et al., 2020, Xu et al., 2023a] are key quantities to consider when exploring the abruptness of regime shifts.

Take-home messages

1. Three-dimensional idealized numerical simulations show that coastal polynyas can trigger irreversible transitions between cold and warm circulation regimes. Hysteresis emerges from the competition between surface salt rejection and basal meltwater feedback.
2. The thermocline controls both regime transitions and basal melting. Its position provides a better indicator of transitions than basal melt rates.
3. Buoyancy-budget arguments provide an upper bound for the extent of the bistable region.
4. The irreversibility or irreversible nature of the transition depend on both far-field conditions and local dynamics: offshore water properties, coastal gyres, and subgrid-scale parameterizations.

Appendix

Table 3.1: Summary of the main common physical processes in the low-dimensional box model and in the NEMO simulations.

	Physical process	**Box model**	**NEMO**
Forcing parameters	Surface salt flux	$F_S = \rho_{\text{ice}} S_p \xi$	F_S
	Surface heat flux	$F_Q = -\rho_\star c_\star \tilde{\gamma}_T (T_p - T_s)$	$Q_{\text{surf}} = K(\text{SST} - T_s)$
	Far field temperature	T_{CDW}, T_{surf}	$T_{\text{resto}}(z)$
	Far field salinity	S_{CDW}, S_{surf}	$S_{\text{resto}}(z)$
Volume fluxes	Cavity overturning	$q_{\text{cav}} = C(\rho_d - \rho_{c,1})$	Cavity MOC
	Inflow/outflow flux	q_{CDW} or q_{DSW}	Open ocean MOC
	Convective net flux	q_{conv}	$\int\int_{\text{polynya}} w \mathrm{d}x\mathrm{d}y$
Melting processes	Ice-ocean interface	Two-equation model	Three-equation model
	Ice-ocean mixing coeff.	$\gamma_T^\star$	$\gamma_{T,S} = \Gamma_{T,S} u_*(\mathbf{u}_{\text{tbl}})$
Vertical processes	Vertical mixing	κ	EVD, VKE
	Water-column stability	$\rho_p - \rho_d$	N^2, RPE

Chapter 4

Numerical sensitivity of vertical motion and basal melting

Summary

In this chapter, we investigate the numerical aspects of the simulations presented in the previous chapter. This analysis is essential to assess the robustness of the numerical configuration and to distinguish physical processes from numerical artifacts. In particular, we show that grid-scale noise can emerge when centered advection schemes are used without sufficient viscous dissipation. We also investigate the influence of the vertical resolution on basal melt rates. This analysis reveals melt-rate anomalies near the grounding line and in the core of the ice shelf that are associated with topographic Rossby waves.

4.1 Introduction

The previous chapter introduced an idealized three-dimensional configuration of an ice-shelf cavity and demonstrated that coastal polynyas can trigger transitions between cold and warm circulation regimes. Although the forcing and topography were deliberately simplified, using the NEMO ocean general circulation model allowed us to retain essential elements of the three-dimensional ocean circulation.

Such an increase in physical realism, however, comes at the cost of a more complex numerical formulation. The simulated circulation depends not only on the physical parameterizations but also on the numerical schemes used to discretize the governing equations. Choices regarding the advection scheme, viscosity, or grid resolution may alter the representation of vertical motions and basal melting, potentially introducing numerical artifacts or biasing the simulated dynamics. It is therefore essential to assess the robustness of the numerical configuration.

This chapter investigates the sensitivity of our simulations to several numerical choices. We first define in Section 4.2 the truncation errors and stability properties of numerical schemes, exemplified by the advection equation. We then analyze in Section 4.3 how horizontal viscosity influences the representation of vertical motions and convection, with particular emphasis on grid-scale noise. Finally in Section 4.4, we investigate the sensi-

tivity of basal melting to the vertical grid resolution. During this analysis, we uncover the presence of topographic Rossby waves beneath the ice shelf, which redistribute basal melting from the grounding line toward the core of the cavity. Note that Section 4.4 can be read independently from Sections 4.2 and 4.3.

4.2 Numerical schemes: truncation error and stability

The choice of numerical schemes plays a crucial role in both the nature of the truncation errors, which may introduce artificial diffusive or dispersive effects into the numerical solution, and the stability of the simulation.

Let's study the advection schemes. For simplicity, we consider a general variable ϕ that depends only on a spatial axis x, and time t. The equation of advection reads $\partial_t\phi + c\partial_x\phi = 0$, with c an advective velocity. When discretizing the problem, we note $\phi_j^n = \phi(n\Delta t, j\Delta x)$. Using the Leapfrog scheme for time and the second order centered scheme for space, the discrete advection equation therefore reads

$$\frac{\phi_j^{n+1} - \phi_j^{n-1}}{2\Delta t} + c\frac{\phi_{j+1}^n - \phi_{j-1}^n}{2\Delta x} = 0. \tag{4.1}$$

Truncation error

The truncation error is defined as the difference between the discrete implemented equation and its continuous form, and therefore represent the spurious additional term due to discretization. Using expansion of ϕ at the point $(n\Delta t, i\Delta x)$, the truncation error $\mathcal{T}$ reads

$$\begin{aligned}\mathcal{T} &= \frac{\phi_j^{n+1} - \phi_j^{n-1}}{2\Delta t} + c\frac{\phi_{j+1}^n - \phi_{j-1}^n}{2\Delta x} - \left(\partial_t\phi_j^n + c\partial_x\phi_j^n\right) \\ &= \frac{\Delta t^2}{6}\partial_{ttt}\phi_j^n + \frac{c\Delta x^2}{6}\partial_{xxx}\phi_j^n + \mathcal{O}\left(\Delta t^4, \Delta x^4\right).\end{aligned} \tag{4.2a}$$

Using $\partial_t\phi = -c\partial_x\phi \Rightarrow \partial_{ttt}\phi = -c^3\partial_{xxx}\phi$ allows rewriting the truncation error as

$$\mathcal{T} = \frac{c\Delta x^2}{6}(1-\mu^2)\partial_{xxx}\phi_j^n + \mathcal{O}\left(\Delta t^4, \Delta x^4\right), \tag{4.3}$$

where $\mu = \frac{c\Delta t}{\Delta x}$ is the Courant number. The numerical scheme therefore introduces an additional dispersive term in the advection equation, whose magnitude scales with the discretization steps. A key advantage of the second-order centered scheme is the absence of a diffusive contribution proportional to $\Delta x\,\partial_{xx}\phi$, which is typically present in first-order upwind schemes and acts as an artificial viscosity. However, second-order centered schemes are not free from drawbacks: the dispersive term may generate false extrema, leading to grid-scale oscillations if not properly controlled, as shown in Section 4.3.

Absolute stability

The absolute stability of a numerical simulation is defined by whether the solution remains bounded over an infinite time horizon, using a finite time step Δt. A standard

approach to assess absolute stability is the von Neumann analysis. This method consists in decomposing the numerical solution into spatial Fourier modes. In particular, we assume an arbitrary mode of wavenumber k of the form $\phi_j^n = A_n e^{ikj\Delta x}$, where $i = \sqrt{-1}$, and A_n represents the time evolving complex amplitude. Then, Eq. (4.1) can be rewritten

$$\frac{A_{n+1} - A_{n-1}}{2\Delta t} + c\frac{A_n(e^{ik\Delta x} - e^{-ik\Delta x})}{2\Delta x} = 0. \tag{4.4}$$

The aim of the analysis is to determine the ratio $\xi = A_{n+1}/A_n$, whose norm determines if the series (A_n) associated to mode k is diverging ($|\xi| > 1$) or not ($|\xi| \leq 1$). Substituting $A_n = \xi A_{n-1}$ and $A_{n+1} = \xi^2 A_{n-1}$ in Eq. (4.4) allows to obtain the characteristic polynomial equation

$$\xi^2 + i2\mu \sin(k\Delta x)\xi - 1 = 0, \tag{4.5}$$

where $\mu = \frac{c\Delta t}{\Delta x}$ is again the Courant number. The discriminant of the polynomial equation is $\Delta = 4[1 - \mu^2 \sin^2(k\Delta x)]$. The roots of the equation are therefore given by

$$\xi = -i\mu \sin(k\Delta x) \pm \sqrt{1 - \mu^2 \sin^2(k\Delta x)}, \tag{4.6}$$

They have absolute values equal to 1 when $\mu \sin(k\Delta x) \leq 1$ and admit an absolute value strictly superior to 1 otherwise. Thus, the stability condition, regardless of the spatial Fourier mode reads

$$\mu = \frac{c\Delta t}{\Delta x} \leq 1, \tag{4.7}$$

which is also known as the Courant-Friedrichs-Lewy (CFL) condition. In our configuration, it means that our simulation goes unstable if velocity exceeds $\Delta x/\Delta t = 5.6$ m/s. When this condition is satisfied, $|\xi| = 1$, indicating that the method is non-dissipative. This is a desirable property of the centered schemes which preserve conserved physical quantities throughout the numerical integration.

4.3 Vertical motion and horizontal viscosity

4.3.1 Grid-scale noise

In this section, we discuss the representation of vertical motions and convection in hydrostatic ocean models. We became interested in these topics once we realized that our configuration generated numerical noise in vertical velocity fields when implementing the ISOMIP+ model parameters [Asay-Davis et al., 2016], especially when applying surface salt fluxes within the coastal polynya. In the warm regime, when implementing relatively weak surface salt forcing, occasional patterns of vertical velocity mix the ocean close to the sea surface under the polynya, as shown by Fig. 4.1(a). These patterns are horizontally very noisy and have changing signs from cell to cell. They also extend vertically into the ocean over some finite depth. In the cold regime, when implementing higher surface salt fluxes, these patterns appear all the time within the whole polynya, and extend vertically down to the bottom of the ocean (see Fig. 4.1(b)).

These noise patterns are quite insidious because their detection requires looking at specific model outputs. Firstly, the noise is only visible on the vertical velocity component, and not on the horizontal one, as shown by the horizontal velocity streamlines of

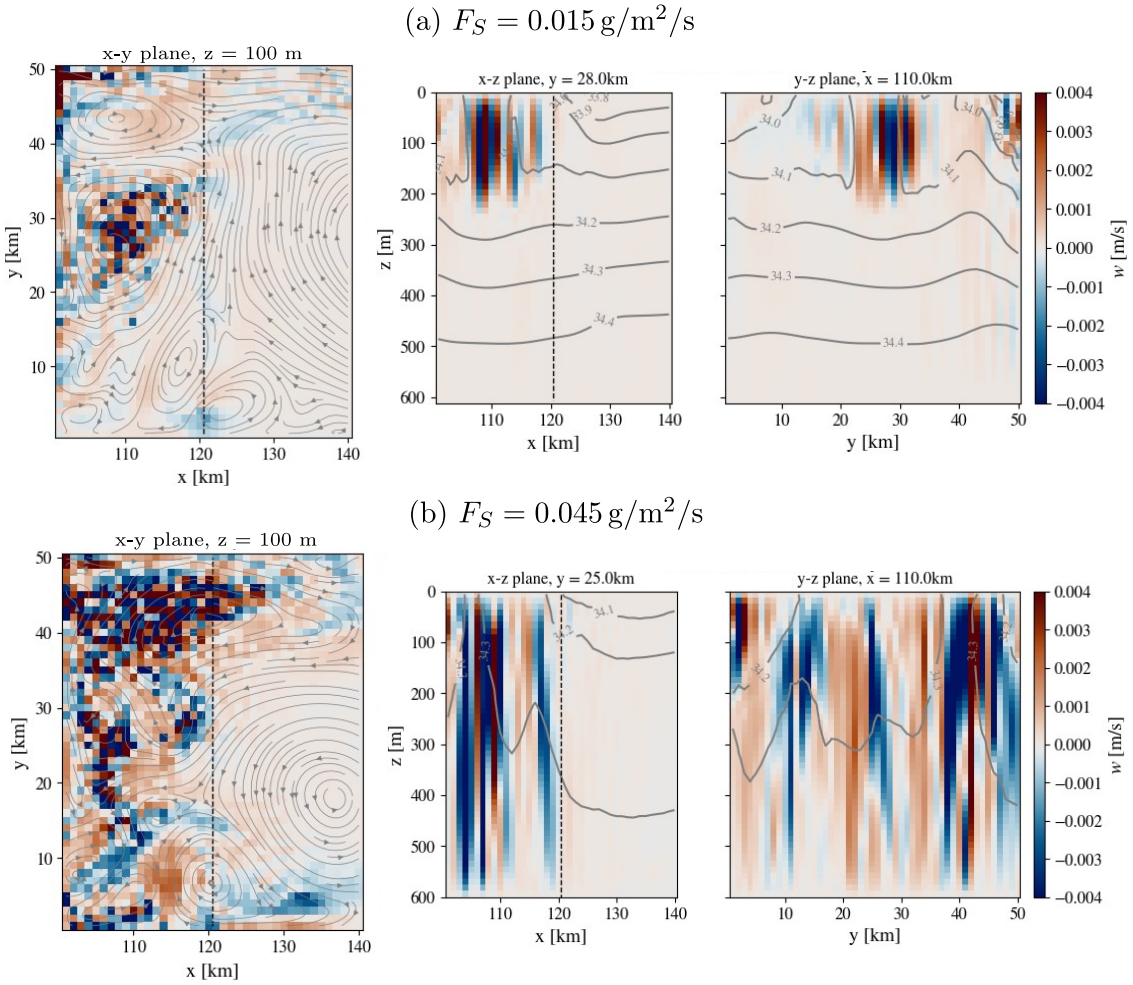

Figure 4.1: Daily average vertical velocity field at the front of the ice shelf for $F_s = 0.015\,\mathrm{g/m^2/s}$ in (a), and $F_s = 0.045\,\mathrm{g/m^2/s}$ in (b). In both plots we set $\Delta x = \Delta y = 1$ km, $\Delta z = 24$ m, $T_0 = 1\,^\circ\mathrm{C}$. The black dashed line shows the rightmost boundary (northernmost) of the polynya region. Horizontal velocity streamlines are superimposed in gray on horizontal slices, and isohaline lines are superimposed on vertical slices [g/kg].

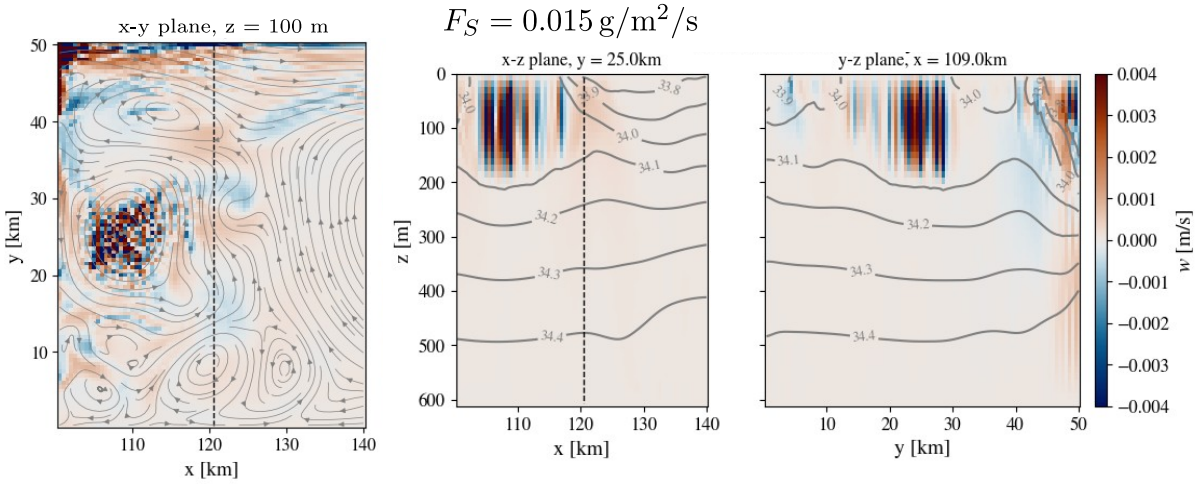

Figure 4.2: Same as Fig. 4.1(a), but using $\Delta x = \Delta y = 500$ m.

Fig. 4.1. In fact, the grid-scale noise is already present in horizontal velocity fields, but it is enhanced by the computation of the horizontal divergence of the flow to obtain the vertical velocity in hydrostatic ocean models. Secondly, when fields are averaged over windows longer than a week, the noise is not visible anymore. This is often the case when working with long simulations, or when being rather interested in the mean state of the ocean, as for quasi-static experiments. Finally and overall, the model remains stable even with the presence of strongly noised signals, which can mislead the ocean modeler as no apparent crash will occur.

In our case, we also show in Fig. 4.2 that even by dividing by two the spatial steps, the noise still appears with a strong alternating pattern from cell to cell. This noise has been in fact well identified by ocean modelers and is often referred as "grid-scale noise" [Garreau, 2021]. It often arises when using centered schemes for the advection. Centered schemes are relevant to conserve physical quantities during the temporal integration, but have however the disadvantage to introduce spurious dispersion terms to the dynamics, as previously shown in Section 4.2, which typically lead to these false extrema. To get some mathematical insights on how the grid-scale noise appears, we follow the derivation proposed in the chapter 16 of [Griffies, 2004], which studies a unidimensional steady advection-diffusion equation for an arbitrary variable ϕ

$$c\partial_x \phi = \kappa \partial_{xx} \phi, \tag{4.8}$$

where c is an advective velocity, and κ is a harmonic diffusion coefficient. Using a second order centered scheme for the advection, the associated discrete equation reads

$$c\frac{\phi_{j+1} - \phi_{j-1}}{2\Delta x} = \kappa \frac{\phi_{j+1} + \phi_{j-1} - 2\phi_j}{\Delta x^2}, \tag{4.9}$$

where $\phi_j = \phi(j\Delta x)$. It can be recast as

$$(R-2)\phi_{j+1} + 4\phi_j - (R+2)\phi_{j-1} = 0, \tag{4.10}$$

where $R = (c\Delta x)/\kappa$ is the grid Reynold number (or grid Péclet number depending on the physical interpretation of ϕ). The characteristic polynomial equation associated to this

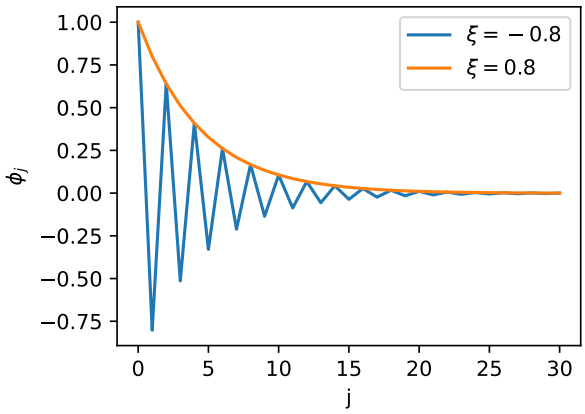

Figure 4.3: (ϕ_j) solutions (Eq. (4.12)) plotted for negative (blue) and positive (orange) values of $\xi = (2+R)/(2-R)$, using the boundary conditions $\phi_0 = 1$ and $\phi_{30} = 0$.

recursive sequence is

$$(R-2)\xi^2 + 4\xi - (R+2) = 0. \tag{4.11}$$

Its discriminant is $\Delta = 4R^2 \geq 0$. The two roots of the equation are therefore 1 and $(2+R)/(2-R)$, such that the solution for the sequence (ϕ_j) reads

$$\phi_j = A_1 + A_2 \left(\frac{2+R}{2-R}\right)^j, \tag{4.12}$$

where A_1 and A_2 are two constants that depend on boundary conditions. From this solution, it is clear that ϕ oscillates at each iteration if $(2+R)/(2-R) < 0$ (see graphical representations of (ϕ_j) in Fig. 4.3). This nonphysical behavior can be avoided by ensuring

$$|R| < 2 \Leftrightarrow \frac{|c|\Delta x}{\kappa} < 2. \tag{4.13}$$

Thus, the viscosity has to be sufficiently high to satisfy this inequality and to damp the spurious oscillations.

In the context of vertical motion and convection, a common way to parameterize vertical mixing is to increase the vertical diffusivity of both momentum and tracers when the density stratification between two cells becomes unstable [Haine and Williams, 2002]. This type of parameterization is called EVD, for Enhanced Vertical Diffusion. In our case, the grid-scale noise typically develops when the water column under the polynya is destabilized by the brine rejections. Thus, EVD looks like the ideal solution to damp the noisy patterns obtained under these conditions. Fig. 4.4 shows the experiment proposed by [Haine and Williams, 2002]. They consider an idealized ocean channel on which they apply negative surface buoyancy flux on one of its half (between 15 and 30 km in across-channel direction). They show that a non-hydrostatic simulation allows capturing convective patterns in this region (Fig. 4.4(a)). They also run a hydrostatic simulation which reproduces similar convective patterns but also develop grid-scale noise (Fig. 4.4(b)). The resulting values of the vertical velocity are overestimated compared to the non-hydrostatic simulation. Indeed, it is not surprising that hydrostatic models fail to appropriately model convection since they approximate the vertical momentum balance with the hydrostatic balance. In Fig. 4.4(c), the authors success to suppress the noise patterns by adding an

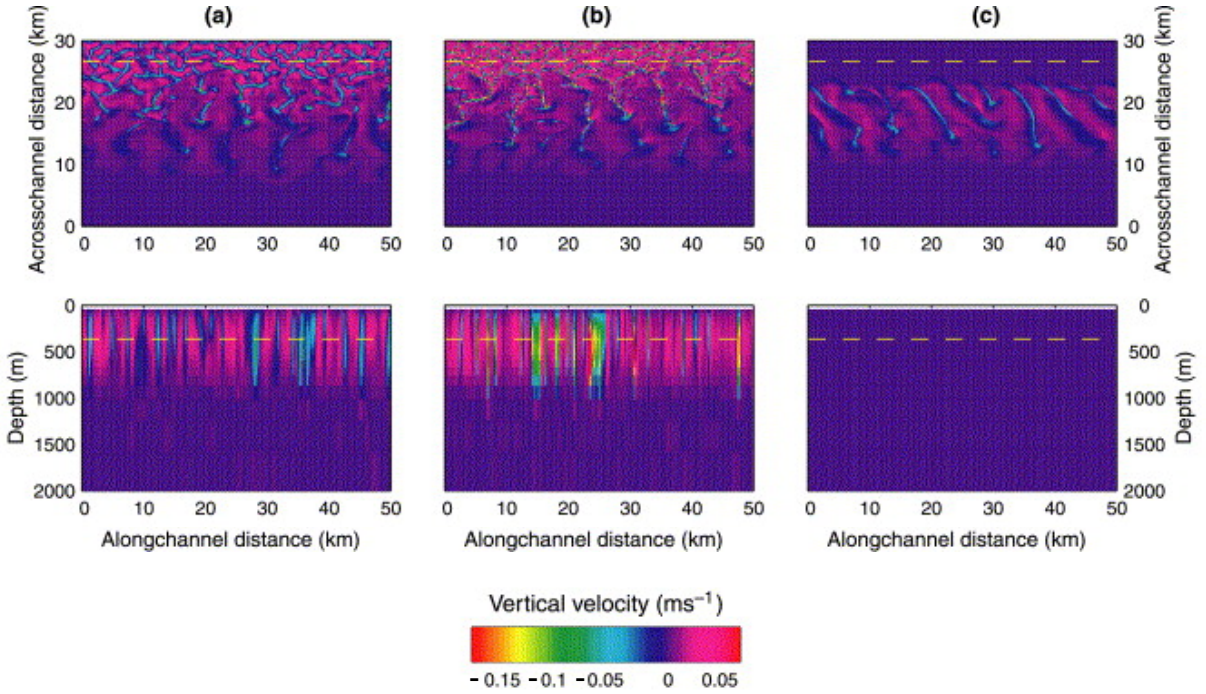

Figure 4.4: Numerical experiments of [Haine and Williams, 2002]. Vertical velocity field in the horizontal plane at 400 m depth (top row), and on a vertical slice at the across-channel distance 27.5 km. (a) Non-hydrostatic experiment. (b) Hydrostatic experiment, EVD deactivated. (c) Hydrostatic experiment, EVD activated.

EVD scheme to the hydrostatic configuration, but they also suppress the resolved vertical motions. In this last case, the vertical mixing is not explicitly resolved and is instead realized by the EVD scheme. The authors report that formed waters with EVD are a bit more homogeneous than in the non-hydrostatic case, and that across-channel eddy fluxes are also underestimated with EVD.

4.3.2 Horizontal viscosity

In our ice-shelf cavity configuration, the EVD parameterization is already applied as it is part of the ISOMIP+ configuration. Thus, its use is not suppressing the noise in our case. In fact, when observing the grid-scale noise, we were using a relatively low harmonic horizontal viscosity $\nu_H = 6$ m^2/s compared to the minimal diffusion $|c|\Delta x/2 \approx 100$ m^2/s identified in Eq. (4.13). To test the behavior of the model to various horizontal viscosity choices, we use a minimalist configuration (see Fig. 4.5). We consider a box with dimensions 60km $\times$ 50km horizontally, and 600 m vertically. The horizontal resolution is $\Delta x = \Delta y = 1$ km and the vertical resolution is $\Delta z = 24$ m. Gaussian-shaped surface salt fluxes are applied in a disk of diameter 20 km at the center of the domain (delineated by the dotted line), and a restoring region that damps salinity toward the initial stratification is set on one edge of the domain (delineated by the dashed line). We test the implementation of increasing values of horizontal harmonic viscosity. Fig. 4.5(a-c) shows the vertical velocity fields 10 days after the beginning of the experiments. When applying high enough horizontal viscosity, the grid-scale noise patterns disappear. However, the

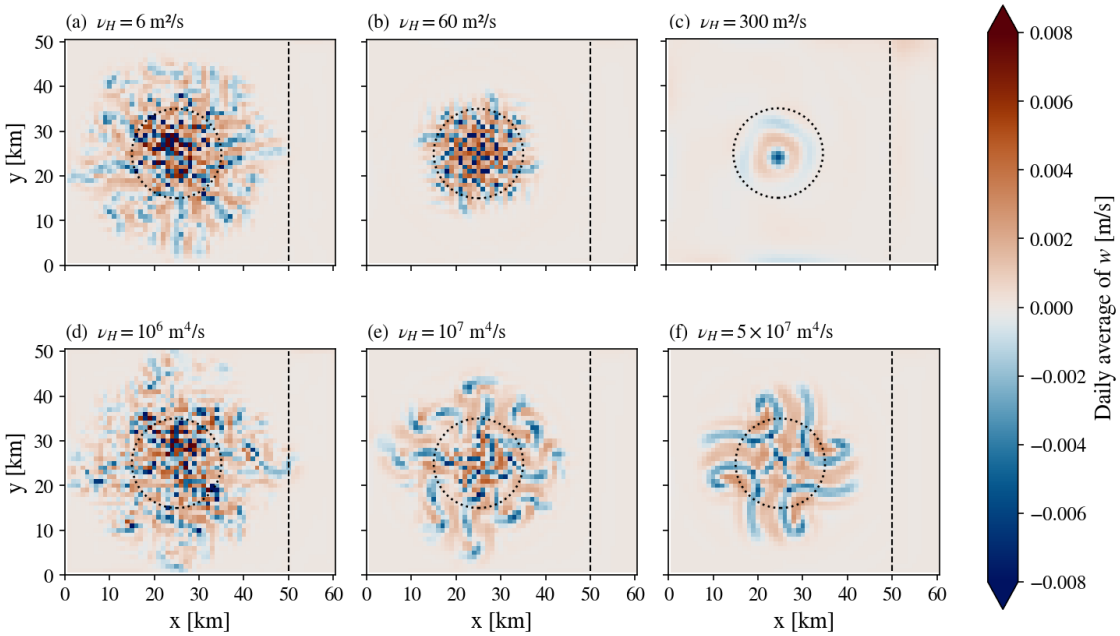

Figure 4.5: Daily average of the vertical velocity 10 days after the beginning of the experiment, at 100 m depth. With harmonic viscosity (a-c), and biharmonic viscosity (d-f). Note that (c) is represented with a lag of 10 days as the convective patterns take more time to emerge in this case. Dotted circles delineate the surface forcing region, and dashed lines delineate restoring regions.

dynamic becomes highly damped, and small-scale dynamics vanishes. Also, the convective pattern takes more time to develop, such that we have to display Fig. 4.5(c) with a lag of 10 days in comparison to the other figures to begin to observe the formation of the convective patterns. Fig. 4.6(a-c) represent vertical slices of the same experiments. The convective pattern becomes more localized when increasing ν_H.

An alternative way to model subgrid-scale horizontal viscosity is to choose a biharmonic representation of the viscous dissipation (which has now [m^4/s] dimension). Consequently, smaller scales are more damped than large scales compared to a harmonic representation of viscosity, which may therefore provide a good alternative to damp grid-scale noise. When using biharmonic viscous dissipation, coherent intermediate-scale patterns can develop even when applying increasing viscosity coefficients, as shown in Fig. 4.5(d-f) and Fig. 4.6(d-f). High enough viscosity coefficients also suppress the grid-scale noise with biharmonic viscosity.

Fig. 4.7(a) show the timely averaged vertical profiles of the vertical velocity standard deviation, which characterizes the vertical motion. Whereas simple averages would be representative of vertical volume fluxes, standard deviations is representative of the resolved vertical mixing. For both harmonic and biharmonic viscosity, the characteristic vertical velocity reaches a maximum between 100 m and 200 m depth. As expected, the vertical velocity decreases when the viscosity coefficient increases. Fig. 4.7(b) shows the activation fraction of the EVD scheme. It is almost always active close to the sea surface where the water column is always unstable due to brine rejections. Except for the larger harmonic viscosity case (dotted blue curve), the EVD activation fractions all follow a

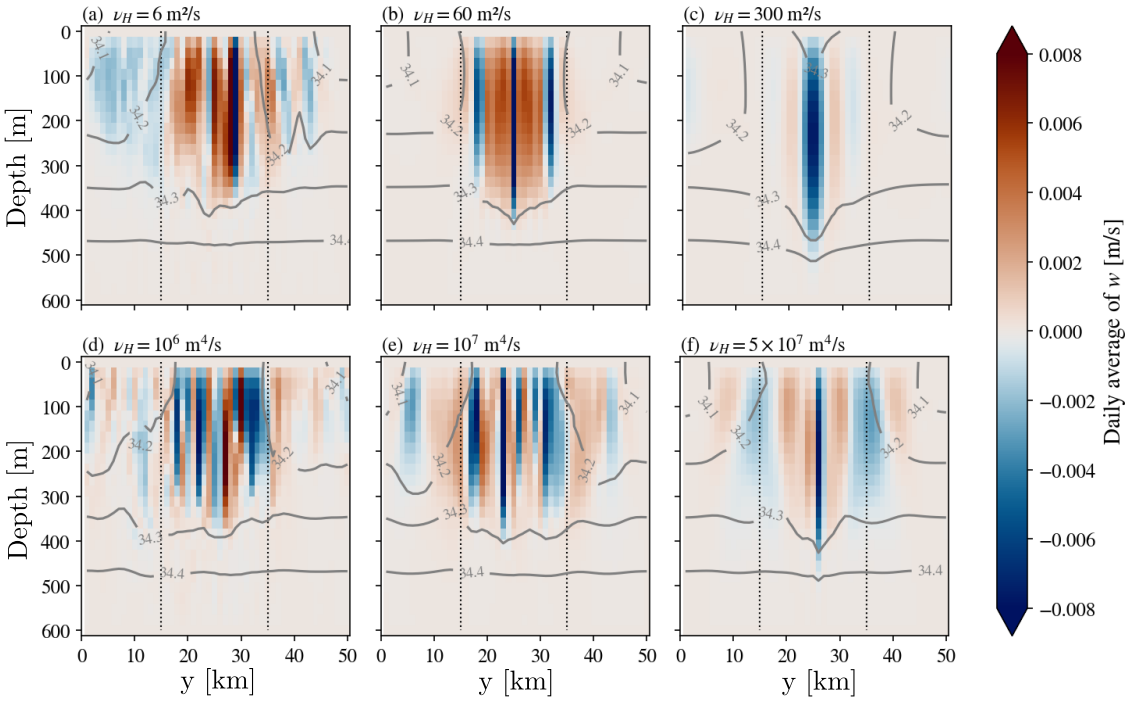

Figure 4.6: Same as Fig. 4.5, but displaying a vertical slice at $x = 25$ km. Note that (c) is represented with a lag of 10 days as the convective patterns take more time to emerge in this case. Dotted lines represent the region under which surface forcing is applied. Isohaline lines are depicted in gray [g/kg].

similar decreasing trend with depth with characteristic length of approximately 150 m. For the case $\nu_H = 300$ m^2/s however, the EVD activation fraction stays of order 0.5 down to 500 m. A plausible explanation is that the vertical motion is so attenuated that it is insufficient to mix the water column adequately to maintain a stable stratification, hence the need for more frequent activation of EVD. In this sense, this experiment looks like the one performed by [Haine and Williams, 2002] (Fig. 4.4) where the addition of EVD removes the resolved vertical motions.

We can mathematically find a condition for which our system does not feature grid-scale noise. Replacing the discrete harmonic operator by the discrete biharmonic operator $(\phi_{j+2} - 4\phi_{j+1} + 6\phi_j - 4\phi_{j-1} + \phi_{j-2})/\Delta x^4$ in Eq. 4.9 yields the characteristic polynomial equation

$$\xi^4 - \left(4 + \frac{R}{2}\right)\xi^3 + 6\xi^2 - \left(4 - \frac{R}{2}\right)\xi + 1 = 0, \tag{4.14}$$

where the biharmonic grid Reynolds number now reads $R = c\Delta x^3/\kappa$. The roots associated to this fourth order polynomial are not trivial (except $\xi = 1$). We therefore use the Routh-Hurwitz stability criterion (as in Chapter 2) to find the condition for which the real part of all roots are positive, to get rid of grid oscillations. After some calculus, this condition simply reads

$$|R| < 8 \Leftrightarrow \frac{|c|\Delta x^3}{\kappa} < 8. \tag{4.15}$$

From the conditions (4.13) and (4.15), we find that a sufficient high viscosity is needed to remove numerical artifacts. However, it is not possible to apply arbitrary high values of

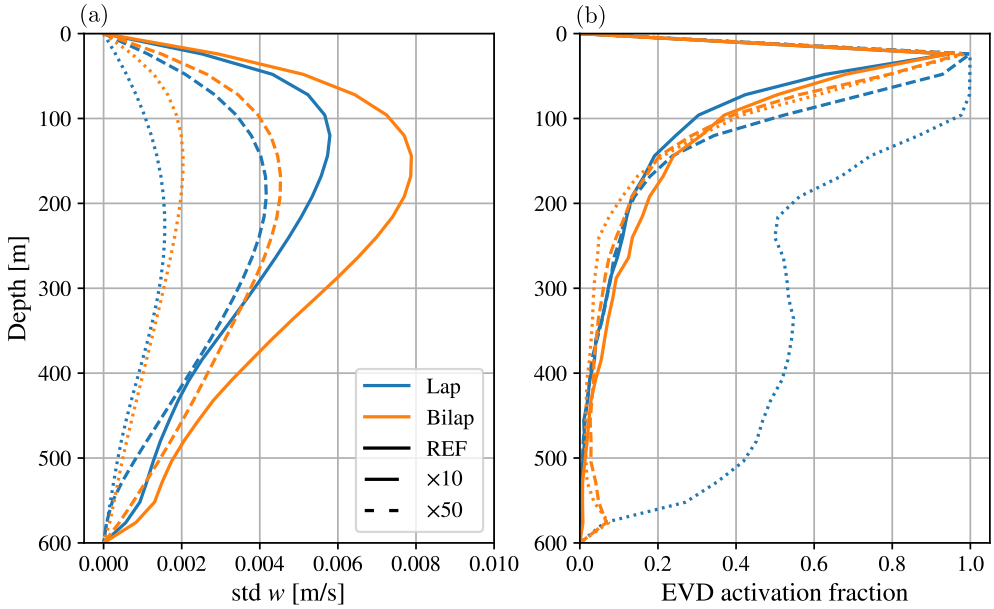

Figure 4.7: (a) One-year average of the vertical velocity standard deviations associated to experiments displayed in Figs. 4.5 and 4.6. Blue curves represent harmonic viscosity cases (REF viscosity is $\nu_H = 6$ m^2/s), while orange curves represent biharmonic viscosity cases (REF viscosity is $\nu_H = 5 \times 10^7$ m^4/s). (b) One-year average of the EVD activation fraction as a function of depth.

viscosity for stability reasons. As in Section 4.2, we can perform a von Neumann analysis of the harmonic diffusion equation $\partial_t \phi = \kappa \partial_{xx} \phi$. In NEMO, the horizontal diffusive processes are time stepped with a forward scheme (a centered scheme is not adapted as it is not dissipative), thus the associated discrete equation reads

$$\frac{\phi_j^{n+1} - \phi_j^{n-1}}{2\Delta t} = \kappa \frac{\phi_{j+1}^{n-1} + \phi_{j-1}^{n-1} - 2\phi_j^{n-1}}{\Delta x^2}, \tag{4.16}$$

where $\phi_j^n = \phi(n\Delta t, j\Delta x)$. We assume an arbitrary mode of wavenumber k of the form $\phi_j^n = A_n e^{ikj\Delta x}$, where $i = \sqrt{-1}$, and A_n represents the time evolving complex amplitude. Defining $\xi^2 = A_{n+1}/A_{n-1}$ the amplification factor, Eq. 4.16 gives the polynomial equation for ξ

$$\xi^2 = 1 - 4\mu_F[1 - \cos(k\Delta x)], \tag{4.17}$$

where $\mu_F = \kappa \Delta t / \Delta x^2$ is the Fourier number, which is analogous to the Courant number, but for diffusive processes. The condition that ensures global stability is $|\xi| < 0$, such that the Fourier number should satisfies

$$\mu_F < \frac{1}{4} \Leftrightarrow \kappa < \frac{\Delta x^2}{4\Delta t}, \tag{4.18}$$

which gives a constraint very similar to the CFL condition (see Section 4.2), but for diffusive processes. Thus, the diffusion should be limited so that time stepping has the time to proagate information to the grid to form a solution. This result generalizes in two

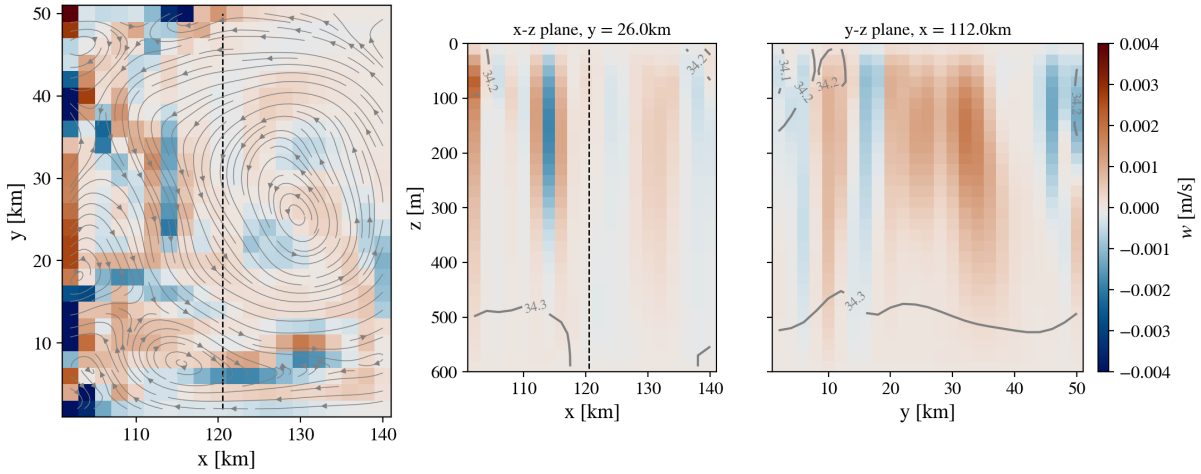

Figure 4.8: Vertical velocity field for $F_S = 0.045\,\mathrm{g/m^2/s}$ (as Fig. 4.1(b)), when imposing the parameters of the simulations displayed in the previous chapter. Biharmonic horizontal viscosity is $\nu_H = 6.4 \times 10^7\,\mathrm{m^4/s}$, and grid resolution $\Delta x = \Delta y = 2$ km and $\Delta z = 20$ m.

dimensions for both harmonic and biharmonic viscosities as [Griffies, 2004]

$$\kappa < \frac{\Delta x^2}{8\Delta t} \text{ for harmonic diffusion,} \tag{4.19a}$$

$$\kappa < \frac{\Delta x^4}{64\Delta t} \text{ for biharmonic diffusion.} \tag{4.19b}$$

Taking these two last stability conditions, as well as the non-oscillatory conditions Eqs. (4.13) and (4.15), we find a range of value of ν_H within our ice shelf cavity configuration ($\Delta x = \Delta y = 2000$ m, $\Delta t = 360$ s, and $c \approx 0.1$ m/s) such that harmonic viscosity should be taken in the range $[100, 1400]$ m^2/s, which clearly exceeds the $6\,\mathrm{m^2/s}$ ISOMIP+ parameter, while for biharmonic viscosity the associated range is $[1 \times 10^8, 7 \times 10^8]$ m^4/s. Our choice $\nu_H = 6.4 \times 10^7\,\mathrm{m^4/s}$ therefore lies a bit under this range, meaning that residual grid-scale noise can appear. Nonetheless, Fig. 4.8 shows that grid-scale noise is much more reduced using this biharmonic coefficient. This choice in fact result from a comparison with other studies modelling deep convection in the Labrador Sea [Zhu et al., 2014, Georgiou et al., 2019] and in the Mediterranean Sea [Herrmann et al., 2008], using biharmonic horizontal viscosity. We identified a scaling $\nu_H \approx 0.008 \times \Delta x^3$ among the viscous coefficients applied in these studies. This scaling in Δx^3 makes sense since it conserves a constant grid Reynolds number $R = c\Delta x^3/\nu_H$ across different resolutions.

To close this section on the numerical implementation of viscosity, we highlight that the EVD scheme could bring stability issues because of the strong increase of the vertical viscosity from $\nu_v = 10^{-3}$ m^2/s to 0.1 m^2/s. The Eq. 4.19a condition reads in the vertical direction $\nu_v < \Delta z^2/(8\Delta t) = 0.14$ m^2/s. Thus, the EVD value is very close to the upper bound that guaranties stability. To overcome stability problems in the vertical direction, a backward time stepping scheme is used instead of the forward scheme implemented for the horizontal viscosity. Backwards time stepping schemes have the disadvantage to be costly as they require to inverse matrices at each iteration steps. As a counterpart to this computational cost, these schemes are unconditionally stable, as can be shown with a von Neumann stability analysis. Using a backward time stepping scheme, the discrete

equation associated to the harmonic diffusion problem becomes

$$\frac{\phi_j^{n+1} - \phi_j^{n-1}}{2\Delta t} = \nu_v \frac{\phi_{j+1}^{n+1} + \phi_{j-1}^{n+1} - 2\phi_j^{n+1}}{\Delta z^2}. \tag{4.20}$$

We assume again the form $\phi_j^n = A_n e^{ikj\Delta x}$, and define $\xi^2 = A_{n+1}/A_{n-1}$ the amplification factor. The polynyomial equation obtained for ξ now reads

$$\xi^2 = \frac{1}{1 + 4\mu_F[1 - \cos(k\Delta x)]}, \tag{4.21}$$

which ensures that $|\xi| \leq 1$ since $1 + 4\mu_F[1 - \cos(k\Delta x)] \geq 1$. Thus, the stability condition is always respected.

Take-home messages

1. Truncation error and absolute stability were illustrated using the advection equation. Centered schemes conserve physical quantities but introduce spurious dispersive errors.
2. Numerical stability requires satisfying the CFL condition, $\mu = c\Delta t/\Delta x \leq 1$.
3. Centered schemes generate grid-scale noise when the grid Reynolds number $R = c\Delta x/\kappa$ becomes too large.
4. Increasing the horizontal viscosity suppresses grid-scale noise. Compared with harmonic viscosity, biharmonic viscosity better preserves intermediate-scale flow structures while damping grid-scale oscillations.

4.4 Vertical resolution and topographic Rossby waves

In this section, we propose to study the basal melt rate dependency to the vertical grid resolution. In our configuration, we did not observe a convergence of the basal mass loss when decreasing the value of Δz, contrary to the finding of [Mathiot et al., 2017] within the ISOMIP configuration [Hunter, 2006], despite the fact we are using the same top boundary layer representation [Losch, 2008]. This led us to investigate the processes that impact melting into the cavity. We find that topographic Rossby waves emerge at intermediate vertical resolutions, and impact the basal mass loss of the ice shelf, especially near its grounding line and in its center. Note that the results presented in this part are preliminaries and should be taken cautiously since standard ISOMIP+ parameters were used. We are therefore using the harmonic horizontal viscosity coefficient $\nu_H = 6$ m^2/s, which is not high enough to suppress grid-scale noise, especially in the meltwater plumes where characteristic velocities are high. Also, the viscosity coefficient does not change when varying the spatial resolution. Consequently, the grid Reynolds number is not constant among experiments, which may alter the computed dynamics.

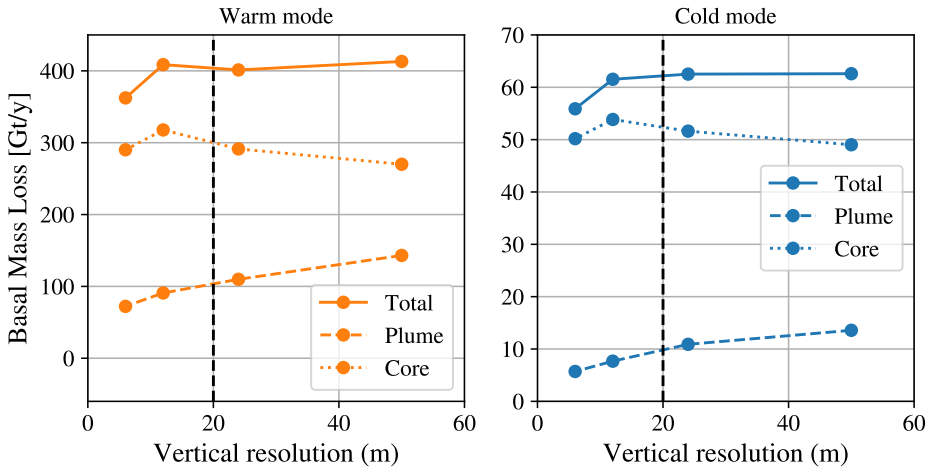

Figure 4.9: Temporal and spatial steady average of the basal mass loss for the warm (orange) and the cold (blue) modes, as a function of the vertical resolution Δz. The black dashed vertical line represents the top boundary layer value $h_{\text{tbl}} = 20$ m. In each plot, the solid line represents the total basal mass loss, whereas the dashed line represents the meltwater plume contribution ($y \in [45, 50]$ km), and the dotted line the complementary core contribution ($y \in [0, 45]$ km).

4.4.1 Impact of the spatial resolution on the basal mass loss

We first test the impact of the vertical spatial step Δz on the basal melt rate. Melting is parameterized thanks to the three-equation thermodynamics formulation of ice-ocean interfaces [Holland and Jenkins, 1999] (see Eq. (3.1) in the previous chapter). The temperature, salinitie, and velocitie fields injected in this model are vertically averaged in a top boundary layer h_{tbl} [Losch, 2008]. We therefore expect different behaviors when $\Delta z > h_{\text{tbl}}$ in which case the top boundary layer is set to the Δz value, or when $\Delta z < h_{\text{tbl}}$ in which case the properties of the cells contained in the top boundary layer are averaged. Within the ISOMIP configuration [Hunter, 2006], Mathiot et al. show that the basal melt rate converges when $\Delta z < h_{\text{tbl}}$ [Mathiot et al., 2017]. To test this result in our configuration, we set the horizontal grid step $\Delta x = \Delta y = 1$ km, and vary $\Delta z \in \{6, 12, 24, 50\}$ m. The top boundary layer is $h_{\text{tbl}} = 20$ m in all cases. We perform a first set of experiments in which $T_0 = 1\,^{\circ}\text{C}$ and $F_S = 0.015\,\text{g/m}^2\text{/s}$ to study the warm mode, and a second set of experiments in which $T_0 = 1\,^{\circ}\text{C}$ and $F_S = 0.045\,\text{g/m}^2\text{/s}$ to study the cold mode.

Fig. 4.9 shows the basal mass loss of the experiments as a function of the vertical resolution. The warm and cold modes show the same melting trends, hence only the warm mode will be discussed here without loss of generality. Contrary to the finding of [Mathiot et al., 2017], the basal mass loss obtained in our configuration does not converge when the vertical resolution is smaller than h_{tbl}. On the contrary, it abruptly decreases when $\Delta z = 6$ m. To further investigate this surprising result, we decompose the basal mass loss into the meltwater plume contribution (dashed lines), and its complementary contribution in the ice-shelf core (dotted lines). The basal mass loss in the meltwater plume decreases when Δz decreases. However, the core contribution of the ice shelf shows a non-monotonic trend. While $\Delta z > h_{\text{tbl}}$, the basal mass loss increases when Δz decreases. When $\Delta z < h_{\text{tbl}}$, the trend reverses and the basal mass loss also decreases for decreasing values of Δz, explaining the abrupt change observed in the total basal mass loss.

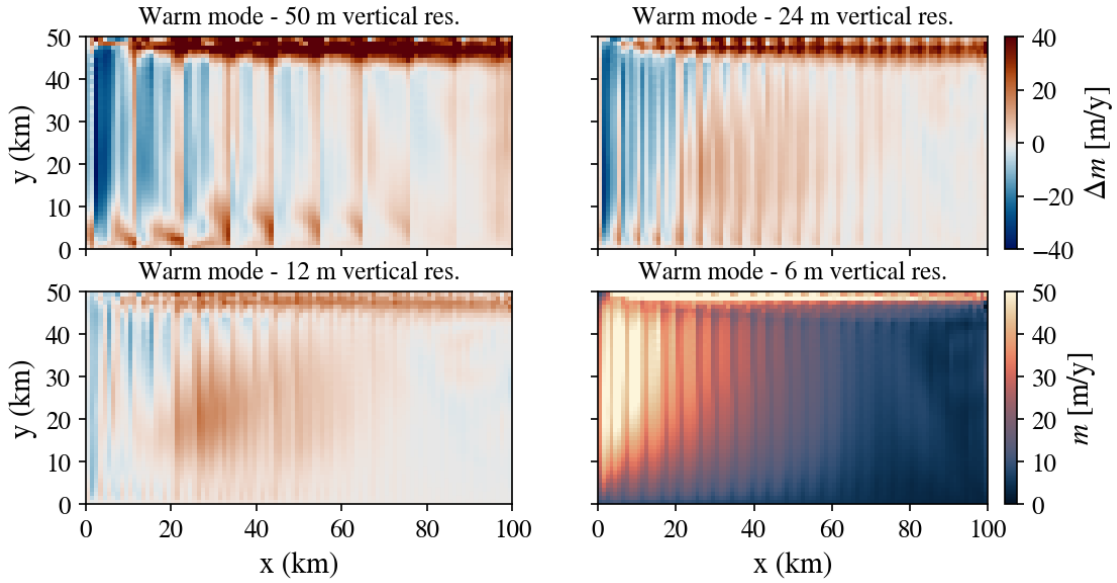

Figure 4.10: Basal mass loss anomaly (warm mode only) taken relatively to the basal mass loss obtained in the $\Delta z = 6$ m experiment (bottom right panel).

Fig. 4.10 shows the basal mass loss anomaly relative to the one obtained setting $\Delta z = 6$ m. Spurious numerical vertical stripes can be observed on these maps. They are located at the vertical ice-ocean interfaces because of the staircase representation of the ice shelf. Losch attributed these patterns to the partial cells representation in z-coordinate models [Losch, 2008]: close to the edge of the staircases, the wet fraction of partial cells is higher, which makes them cool on longer timescales and tends to increase melt rates on these points. The top boundary layer introduced by [Losch, 2008] allows the reduction of this spurious behavior. This is visible in Fig. 4.10, which shows less contrasted cell-to-cell basal melt rates when $\Delta z < h_{\text{tbl}}$ (bottom row). Fig. 4.10 clearly shows an increase of the meltwater plume basal melt rates with increasing Δz. Within the ice shelf, non-negligible meltwater negative anomalies (in blue) are present close to the grounding line, whereas meltwater positive anomalies (in red) are present at intermediate values of x between 20 and 80 km. To investigate these effects, we considered both the top boundary layer velocity (Fig. 4.11) and the thermal forcing (Fig. 4.12) beneath the ice shelf.

Fig. 4.11 shows the relative boundary-layer velocity anomaly $\frac{||\mathbf{u}_{\text{tbl}}|| - ||\mathbf{u}_{\text{tbl}}^{\Delta z=6\text{m}}||}{||\mathbf{u}_{\text{tbl}}^{\Delta z=6\text{m}}||}$. The relative anomaly is more adapted than the absolute anomaly because an order of magnitude is separating plume velocities and core velocities. At smaller Δz, the meltwater plume is better resolved. Thus, the velocity in the top boundary layer is higher when decreasing Δz, which is well observed. In the intermediate resolution cases $\Delta z = 24$ m and $\Delta z = 12$ m, positive velocity anomalies ($\approx +50\%$) are observed in the core of the ice shelf between 20 and 80 km, and negative anomalies (≈ -30 to -50%) closer to the grounding line. They match with the basal melt rates anomaly obtained in Fig. 4.10. A global effect of this anomaly is that near grounding line melt rates are shifted towards the center of the ice shelf, with positive and negative anomalies reaching 20 m/y (see Fig. 4.10 for $\Delta z \in \{24, 12\}$ m). This redistribution of the melt rates could impact the dynamics of the ice-sheet since it would make the ice-shelf core more vulnerable to basal melting, but

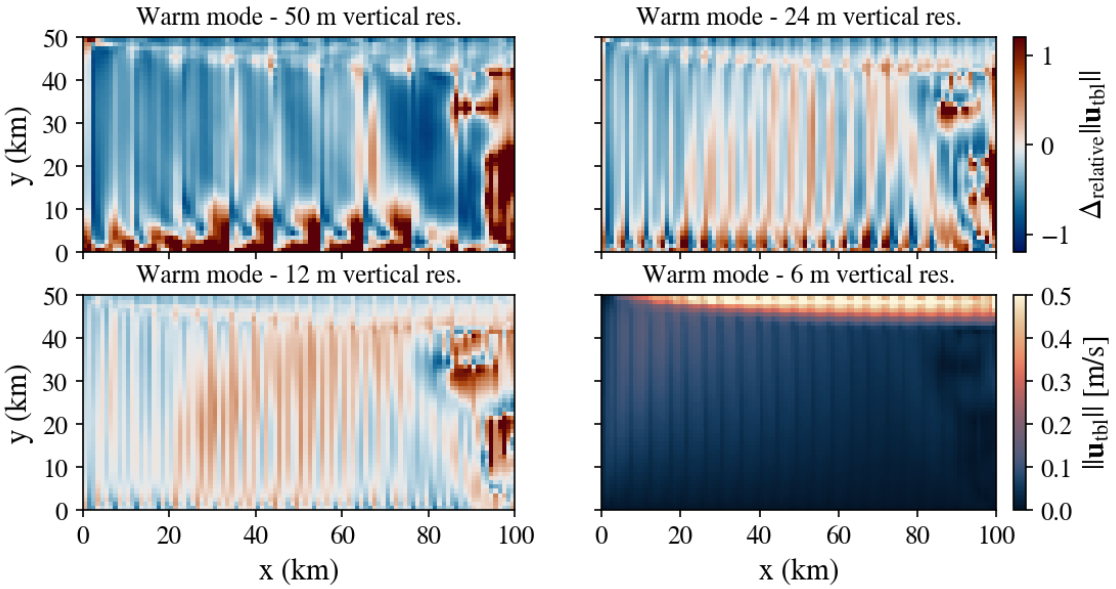

Figure 4.11: Top boundary layer velocity relative anomaly (warm mode only) using the case $\Delta z = 6$ m as reference (bottom right panel).

would decrease the melting close to the grounding line.

To verify that boundary layer velocities are solely responsible for the melt rates anomalies observed among various vertical resolutions, we show in Fig. 4.12 the thermal forcing ($T_{\text{tbl}} - T_b$, T_b being seawater freezing temperature) anomalies. The thermal forcing anomaly increases in the meltwater plume region for increasing values of Δz. This occurs because thicker cells are taking longer time to cool when subject to meltwater fluxes. However, it is difficult to attribute a clear trend for the thermal forcing of the core of the ice shelf. The simulation with $\Delta z = 50$ m shows positive anomalies almost everywhere, except on the eastern edge, whereas intermediate vertical resolutions show the alternance of positive and negative anomalies vertical stripes. Overall, we find that the positive anomalies are more located close to the grounding line, and the negative anomalies are more located within the core of the ice shelf. Thus, these thermal forcing anomalies does not explain the basal melt rates anomalies observed at the core of the ice shelf for intermediate resolutions.

4.4.2 Topographic Rossby waves

Our analyses of processes responsible for basal mass loss anomalies due to changing vertical resolutions allowed us to uncover a type of dynamics at small time scales that has yet not been reported in the literature within ice-shelf cavities: topographic Rossby waves. Fig. 4.13 shows a daily average of the basal melt rate for various vertical resolutions. For $\Delta z = 50$ m, melting patterns at few-kilometer scales are developing on each horizontal step of the staircase shaped ice shelf. These patterns emerge due to the coarse vertical resolution, emphasizing that smaller Δz are needed to capture an accurate ice-ocean interface dynamics. For intermediate vertical resolutions ($\Delta z \in \{24, 12\}$ m), elongated basal mass loss patterns are propagating from the grounding line to the western edge of the spatial domain. For the highest vertical resolution $\Delta z = 6$ m, these melt patterns

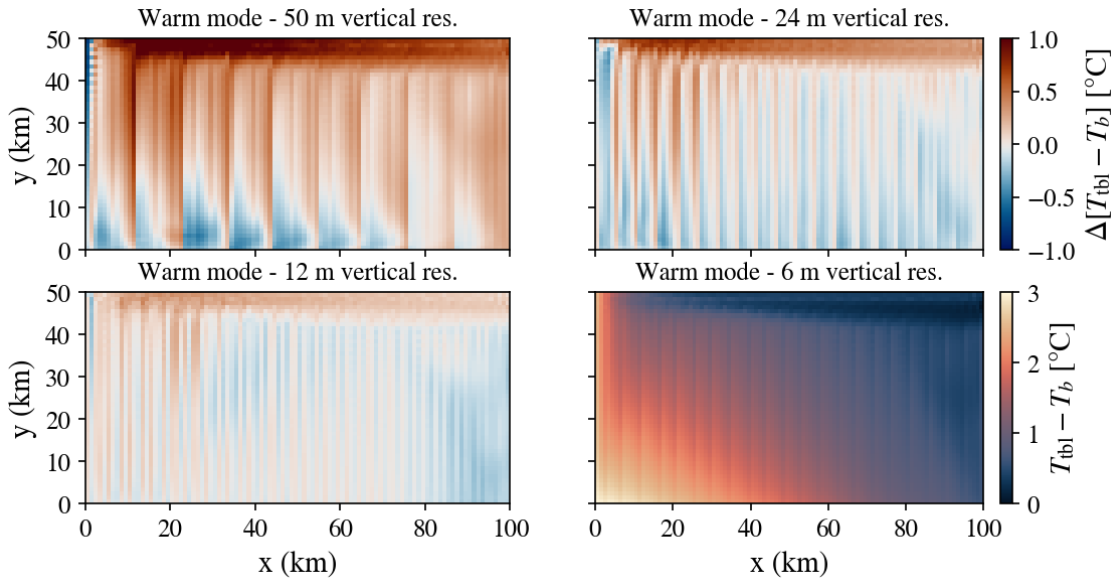

Figure 4.12: Thermal forcing anomaly (warm mode only) using the case $\Delta z = 6$ m as reference (bottom right panel).

vanish and the basal melt rates stay concentrated close to the grounding line and on the western edge.

The result is compelling as it suggests a non-monotonic dependence of the ice-ocean boundary layer to the vertical resolutions. Though, we should take the results of this study with care as the grid Reynolds number R is not the same among the several resolutions tested. Letting a constant diffusivity, R is expected to decrease when increasing the resolution. Thus, it is possible that we are just not capturing the same physics among all experiments. They are also a lot of example for which the triggering of fluids dynamics instabilities is often associated with a critical value of the Reynolds number (see e.g., [Lilly, 1966] for the case of Ekman layer instabilities).

Still, these propagating patterns seem to be responsible for the boundary-layer velocity anomalies observed in Fig. 4.11 near the grounding line and in the core of the ice shelf, that resulted in basal melt rates anomalies in Fig. 4.10. We therefore investigate in detail these melting waves using simulations with resolutions $\Delta x = \Delta y = 1$ km and $\Delta z = 12$ m, which produce these patterns while not showing too strong numerical spurious stripes. Fig. 4.14 shows a daily average of the horizontal velocity in the top boundary layer, from which we have subtracted its yearly average. Thus, this diagnostic only represents the deviation to the mean flow. It becomes now clear that velocity waves are developing under the ice shelf. The velocity field alternates its direction, from pattern to pattern. They form close to the grounding line, on the eastern side, and then propagate diagonally towards increasing values of x and y. They vanish when they meet the meltwater plume.

Previous numerical studies have reported the formation of elongated patterns at the ice-ocean interfaces of ice shelves, using a high resolution MITgcm simulation [Patmore et al., 2023], and a Large Eddy Simulation [Vreugdenhil et al., 2022]. In these two studies, the waves also propagate towards the North-West direction. They also use a linear shaped ice-ocean interface, and a three-equation model representation of basal melting [Holland and Jenkins, 1999]. However, the wavelength associated to their instabilities are about 400

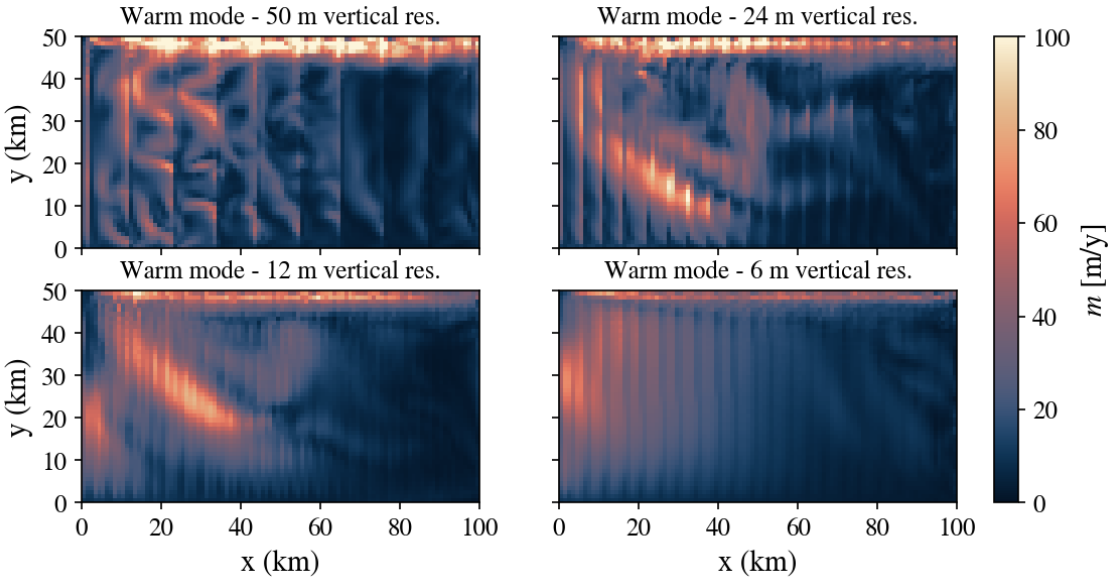

Figure 4.13: Daily average of the basal melt rate for different vertical resolutions (warm mode only).

m whereas our instability wavelength is about 40 km. In these two studies, the observed wave patterns are attributed to Ekman boundary layer instabilities also known as Ekman rolls [Lilly, 1966, Mkhinini et al., 2013], which has wavelengths that scale with the Ekman depth $E_D = \pi\sqrt{\frac{2\nu_v}{f}}$. In our configuration $E_D \approx 10\,\mathrm{m} \ll \Delta x = 1000$ m so we clearly do not observe these Ekman layer instabilities.

Another characteristic of the Ekman rolls observed by [Vreugdenhil et al., 2022] and [Patmore et al., 2023] is that they are localized close to the ice-ocean interface. However, the wave patterns obtained in our configuration have a full-depth signature, as shown by Fig. 4.15 (top row). This figure shows the daily zonal velocity subtracted from its annual mean component, along a vertical column under the ice shelf, as function of time. Positive and negative velocities alternate regularly in time in the whole water column. On the bottom row, we plot the time series obtained at 450 m depth. The oscillations have very regular periods, though their amplitude is modulated in time, alternating between high amplitudes (≈ 0.05 m/s) and low amplitudes (≈ 0.02 m/s) on monthly timescales. The associated Fourier transform is displayed in Fig. 4.16. It shows a very peaked signal at $\omega = 8.5 \times 10^{-6}\,\mathrm{s}^{-1}$, or equivalently at $T = 8.6$ days, which corresponds to the period of the observed waves.

At this point, internal waves and inertial waves are unlikely since their associated characteristic pulsation is much higher ($N = 2.2 \times 10^{-3}\,\mathrm{s}^{-1}$ and $|f| = 1.4 \times 10^{-4}\,\mathrm{s}^{-1}$). Thus, this reinforces the idea that we are in the presence of Rossby waves. This may be counterintuitive since our configuration is run on an f-plane. Nevertheless, the variation of the water-column thickness along the ice-shelf cavity slope impacts the potential vorticity in the same way as the beta effect. This phenomenon is also called the topographic beta effect [Vallis, 2017]. A simple way to demonstrate this effect is to use the shallow-water equations framework. Indeed, the potential vorticity simply reads $Q = \frac{\zeta+f}{h}$ in this case, where ζ is the fluid vorticity, $f = f_0 + \beta x$ is the Coriolis parameter (x denotes the

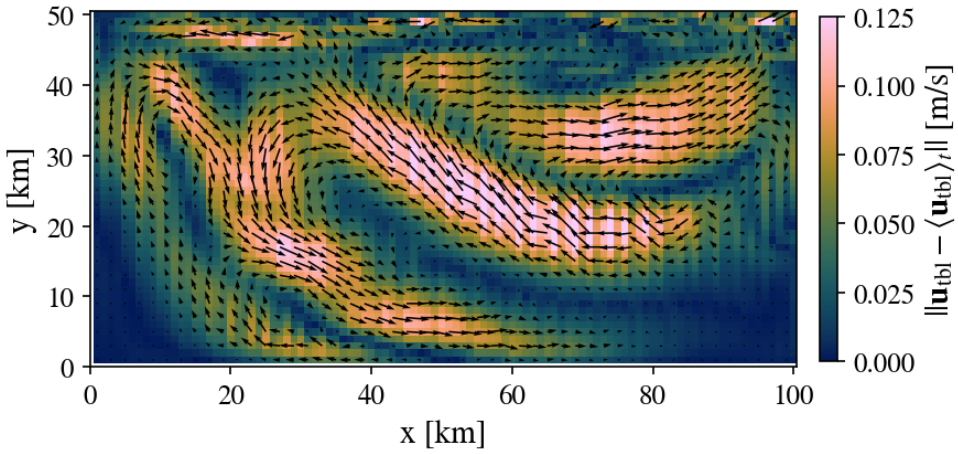

Figure 4.14: Daily average of the top boundary layer horizontal velocity, from which its annual mean field is subtracted.

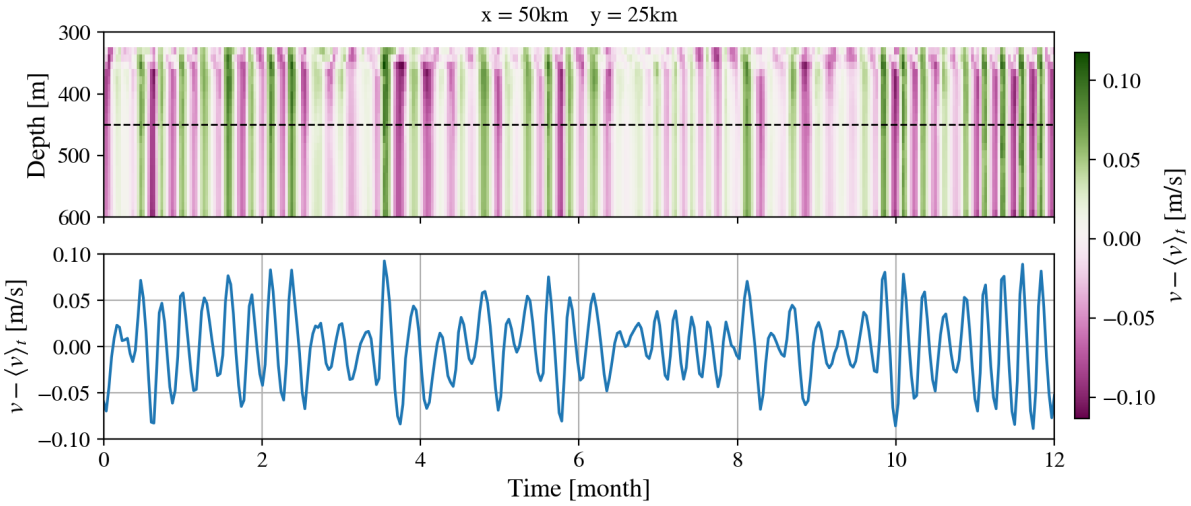

Figure 4.15: Top row: zonal velocity along a water column taken in the middle of the ice shelf at $x = 50$ km and $y = 25$ km. Bottom row: time series of the zonal velocity taken at 450 m depth. The black dashed line in the top row represents this 450 m depth.

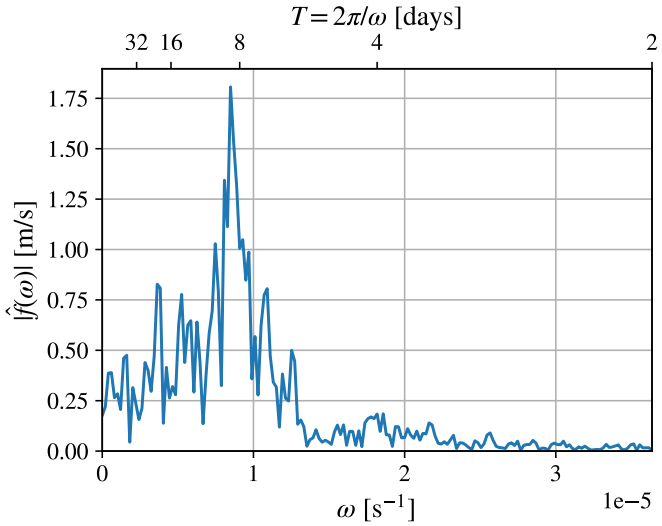

Figure 4.16: Fourier transform of the zonal velocity fluctuations series obtained in the bottom row of Fig. 4.15.

meridional direction), and h is the thickness of the water column. At constant h, the conservation of the potential vorticity reduces to

$$\frac{\mathrm{D}Q}{\mathrm{D}t} = 0 \Leftrightarrow \frac{\mathrm{D}\zeta}{\mathrm{D}t} + \beta u = 0. \tag{4.22}$$

Now imposing f constant and h varying linearly as $h(x) = h_0 + \alpha x$ (as in our configuration), Eq. (4.22) remains valid if replacing β by

$$\beta_{\text{topo}} = -\frac{\alpha f}{h}, \tag{4.23}$$

and considering $\zeta \ll f$.

To identify the observed waves in our configuration as topographic Rossby waves, we studied their dispersion relation. We provide a Hövmoller diagram of the zonal velocity in Fig. 4.17, setting $x = 50$ km and $z = 450$ m, following the propagation of the waves along the y-axis. The phase velocity of the waves along the y-axis is given by the slope of the lines in Fig. 4.17. Taking the two-dimensional Fourier transform of this diagram yields Fig. 4.18(a), where k is the wavenumber associated to the zonal direction y, and ω is the temporal pulsation. The Fourier spectrum reaches a very localized peak for the pair $(k, \omega) = \pm(-1.3 \times 10^{-4}\,\mathrm{m}^{-1}, 8.5 \times 10^{-6}\,\mathrm{s}^{-1})$. The opposite sign of k and ω is consistent with the observed propagation toward the western edge of the spatial domain, at phase velocity $c_\phi^y = |\omega/k| = 6.5 \times 10^{-2}$ m/s. The periods and wavelengths are $T = 8.6$ days (as found previously) and $\lambda_y = 52$ km. It is possible that λ_y is constrained by the zonal extent of the cavity, which is 50 km. We superimpose on this spatiotemporal spectrum the dispersion relation of Rossby waves [Vallis, 2017]

$$\omega = -\frac{\beta_{\text{topo}} k}{k^2 + l^2 + k_d^2}, \tag{4.24}$$

where β_{topo} is given by Eq. (4.23), k is the wave number of the y zonal direction, $l = -1.3 \times 10^{-4}\,\mathrm{m}^{-1}$ is the wavenumber of the x meridional direction (chosen according to

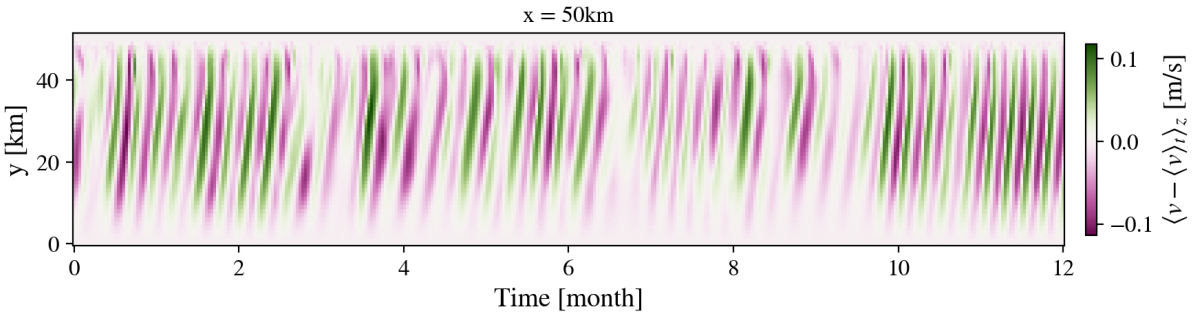

Figure 4.17: Hovmoller diagram of the zonal velocity subtracted from its yearly mean field with $x = 50$ km and $z = 450$ m.

Fig. 4.18(b)), and $k_d = 1/R_D = 3.3 \times 10^{-4}\,\mathrm{m}^{-1}$ is the Rossby deformation frequency. We note that in writing Eq. (4.24) we discard the zonal velocity background (no Döppler effect), which may be disputable since high mean zonal velocities ($\approx 5 \times 10^{-2}$ m/s) can be reached in the top boundary layers despite relatively low zonal velocities elsewhere ($\approx 2 \times 10^{-3}$ m/s). The topographic beta effect coefficient β_{topo} depends on the water column thickness. Thus, we show several dispersion relations of the Rossby waves for different values of h. We find that the pair (k, ω) for the observed waves could be consistent with dispersion relations using values of h ranging between 50 and 100 m, which are conditions that can be found close to the grounding line.

Fig. 4.18(b) shows the two-dimensional spatial Fourier transform of the zonal velocity at 450 m depth. It reaches a maximum for the pair $(k, l) = (-1.3\times10^{-4}, -1.3\times10^{-4})\,\mathrm{m}^{-1}$. The propagation of the waves therefore mainly occurs in a direction that makes an angle 45° with the x-axis, and the wavelength of the Rossby wave is $\lambda = 34$ km. As both l and k are negative, the waves propagate toward increasing values of x and y. Assuming no zonal mean velocity in the background, the values of k and l that satisfy the Rossby waves dispersion relation should be located on circles of center $(k = -\frac{\beta_{\mathrm{topo}}}{2\omega}, l = 0)$, and of radius $-\frac{\beta_{\mathrm{topo}}}{2\omega} + \left[\left(\frac{\beta_{\mathrm{topo}}}{2\omega}\right)^2 - k_d^2\right]^{1/2}$ [Vallis, 2017]. We superimpose in Fig. 4.18(b) several circles corresponding to several values of h. A good agreement is obtained when $h = 110$ m.

To conclude, we have shown that Rossby waves with daily timescales variability are driving basal mass loss anomalies, with lower basal melt rates close to the grounding line, and higher basal melt rates in the core of the ice-shelf. Associated anomalies are up to 20 m/y. These Rossby waves are only obtained for intermediate horizontal resolutions values (12 and 24 m). This preliminary work therefore open a research avenue to better characterize these waves on more realistic context, or with other grid representations (e.g., with s-coordinates). Also, it should be of interest for ice-sheet evolution studies, since the associated basal melt rates anomalies impact the spatial distribution of the basal mass loss, reducing melting close to the grounding line.

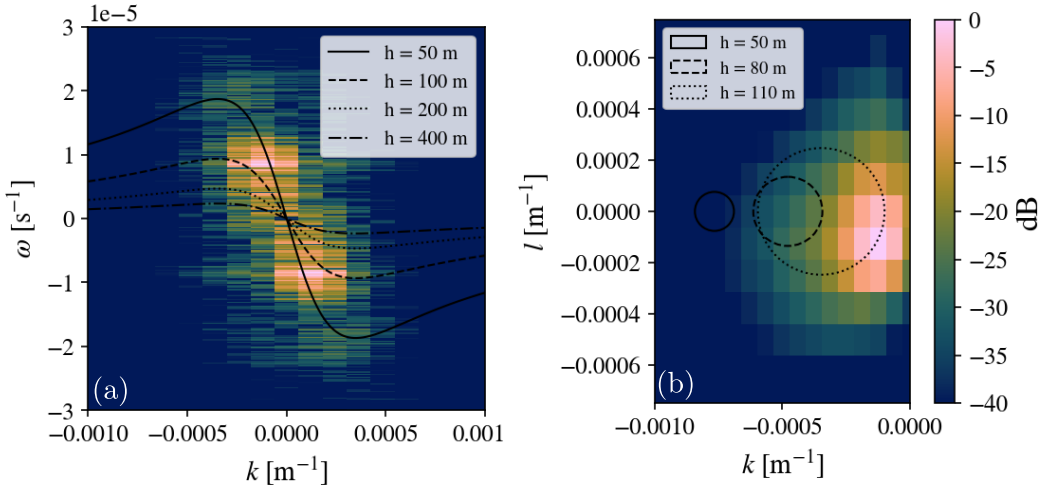

Figure 4.18: (a) Two-dimensional (spatio-temporal) Fourier transform of Fig. 4.17. Several dispersion relations for Rossby waves (Eq. (4.24)) are displayed for various water-column thickness values. (b) Two-dimensional (spatial) Fourier transform obtained from two-dimensional velocity fields taken at 450 m depth. Circle satisfying the dispersion relation Eq. (4.24) are also displayed for various water-column thicknesses.

Take-home messages

1. Basal melt rates do not converge with increasing vertical resolution, despite using a constant Losch top boundary layer thickness.
2. Increasing the vertical resolution reduces basal melting in the meltwater plume due to lower thermal forcing near the ice-ocean interface.
3. Intermediate vertical resolutions produce negative melt anomalies near the grounding line and positive melt anomalies in the core of the ice shelf, relative to the highest-resolution simulations melt rates.
4. These melt anomalies are associated with topographic Rossby waves propagating from the grounding line toward the western edge of the cavity.

Chapter 5

The response of an ice-shelf cavity to time-dependent forcing

Summary

In this chapter, we investigate the response of a bistable ice-shelf cavity to time-dependent polyna forcing. Using both low-dimensional models and idealized NEMO simulations, we identify the adjustment timescales controlling the transient response of the cavity and assess the conditions under which regime transitions occur. We show that rapid forcing is damped whereas slower forcing can trigger transitions between cold and warm circulation regimes, the thermocline time adjustment being the key process separating these two behaviors. We further demonstrate that seasonal forcing weakly modifies the bistable forcing range compared with steady conditions. We finally show that stochastic fluctuations around the seasonal time scale can strongly influence the mean time of first transitions. Specifically, we show that temporally correlated forcing promotes faster regime shifts.

5.1 Introduction

The previous chapters focused on the steady-state response of ice-shelf cavities to quasi-static external forcing and uncovered bistable dynamics. They also shed light on some examples of internal variability occurring under constant external forcing conditions. In Chapter 2, for instance, the low-dimensional model exhibited flip-flop oscillations. They originated from the non-linear dependence of vertical mixing on the density stratification beneath the polynya. The associated variability timescales were controlled by internal processes related to the overturning circulation and the thermocline dynamics. In Chapter 4, we identified topographic Rossby waves within the cavity, providing another example of internal variability. Although the physical mechanism triggering these waves remains unclear, their characteristic timescales are again determined by intrinsic properties of the system through the Rossby wave dispersion relation.

The present chapter now focuses on externally forced variability. Ice-shelf cavities are continuously subjected to fluctuations in coastal polynya forcing, which modify sea-ice production and DSW formation at the ice-shelf front [Golledge et al., 2025]. Because the

ocean cavity has bistable states, its response to time-dependent forcing is not expected to simply follow the forcing signal with some time lags. Instead, the response may depend on the forcing timescale, amplitude, and on the branch of the bistable system that is initially occupied. While we identified abrupt transitions when applying slow changes of the surface forcing in quasi-static experiment in Chapter 3, it is not clear that abrupt changes can be obtained with more realistic time-dependent forcing following, for instance, a strong seasonality.

The variability of sea-ice production in coastal polynyas spans a broad range of timescales associated with different physical processes [Golledge et al., 2025]. At daily to weekly timescales, atmospheric conditions and especially offshore winds control polynya opening and sea-ice production. Offshore winds oscillations with periods of 2 to 5 days have been reported in the Vincennes Bay and Terra Nova Bay polynyas [Xu et al., 2023a, Xu et al., 2023b], while cyclonic atmospheric conditions have been shown to modulate sea-ice production over few days in the Ross Ice Shelf and Terra Nova Bay polynyas [Wang et al., 2023, Wenta and Cassano, 2020]. At seasonal timescales, sea-ice production is strongly modulated by the annual cycle, with 96% of the sea-ice mass production occurring between March and October [Nakata et al., 2021]. From November to February, restratification is instead observed due to sea-ice meltwater carried from offshore regions [Xu et al., 2024]. At interannual to decadal timescales, variability is primarily linked to changes in polynya area [Tamura et al., 2016, Haid and Timmermann, 2013]. Key forcing processes include cryospheric events such as calving, landfast sea-ice formation, and ice-tongue growth, which can modify the geometry of topographic barriers controlling sea-ice motion and thus polynya opening. Larger scale climate modes may also contribute to polynya variability through their influence on winds and sea-ice transport. In particular, the Mertz Glacier polynya has been found to vary with the intensification of the Southern Annular Mode (SAM, a measure of the circumpolar atmospheric meridional pressure gradient) over the last decades [Campagne et al., 2015]. A recent study also correlates East Antarctica polynya growths with positive SAM indexes, and West Antarctica polynya growths with La Niña events (negative phases of El Niño Southern Oscillation) [Ward and Raphael, 2026].

This chapter attempts to address three questions. First, how does a bistable ice-shelf cavity respond to surface-forcing fluctuations occurring over timescales ranging from months to decades? Second, which internal adjustment processes control the cavity response? Third, can ice-shelf cavities undergo regime transitions under realistic stochastic forcing, i.e., representative of combined seasonal and interannual variability?

The chapter is organized as follows. In Section 5.2, we systematically investigate the response of an ice-shelf cavity to oscillating forcing with periods ranging from months to decades. We first gain insight using a box model that accounts only for the cavity dynamics and compare our results with those obtained by [Holland, 2017] with an idealized GCM configuration. We then complement these results with simulations performed using the ocean model presented in Chapter 3, emphasizing the fundamental role of thermocline dynamics. While the experiments presented in this section are designed to investigate the physical processes governing the ice-shelf cavity response from a mechanistic perspective, regardless of the realism of the forcing, Section 5.3 adopts a more realistic representation of the surface forcing in our NEMO configuration by focusing on its seasonal variability. We then introduce stochastic interannual variability in the winter forcing and assess how

the temporal correlation between successive winters affects the mean first transition time.

5.2 Response of an ice-shelf cavity to various forcing timescales

Our steady-state analyses from the previous chapters suggest that two dynamical components may play a central role in the response of the cavity to transient forcing. The first is the thermocline dynamics, which determines whether CDW or DSW intrudes into the cavity. The second is the cavity overturning circulation, which controls the transport of water masses toward the ice-shelf base. Thus, the response of the system should depend on the relative adjustment timescales of these two processes. Here, we first investigate the response of an ice shelf to imposed time-varying properties (temperature and salinity) of the deep water intruding into the cavity, thereby neglecting thermocline dynamics. In this case, the flushing time of the cavity by the overturning circulation is the only relevant adjustment timescale. We test a simplified version of our box model to assess whether it is capable of reproducing the dynamics observed for a similar configuration but with a GCM [Holland, 2017]. Next, we use the NEMO configuration presented in Chapter 3 to explicitly account for surface forcing and the dynamical adjustment of the thermocline. The thermocline depth is influenced by sea-ice production, wind-stress curl, and iceberg melting at the front of Antarctic ice shelves [Hyogo et al., 2026]. Here, we isolate and investigate the specific role of variability in sea-ice production.

5.2.1 Insights from low-dimensional models

We consider a single box model, conserving only the cavity box and removing the deep water and polynya boxes at the front of the ice-shelf to solely focus on the impact of the variation of water properties intruding the cavity. Doing so, we do not obtain bistability within this framework, but it allows us to perform a simple and controlled investigation of the cavity response over a range of forcing timescales. Under hypothesis (H1) described in Chapter 2, the model reduces to two dynamical equations describing the evolution of the temperature T and the salinity S of the ocean cavity box, i.e.

$$\begin{cases} V_{\text{cav}}\dot{T} = q_{\text{cav}}(T_0 - T) - \mathcal{A}_c\gamma_T^\star(T - T_b), \\ V_{\text{cav}}\dot{S} = q_{\text{cav}}(S_0 - S) - \mathcal{A}_c\frac{c_\star}{\mathcal{L}}S_\star\gamma_T^\star(T - T_b), \end{cases} \tag{5.1}$$

where V_{cav} is the volume of the ocean cavity, T_0 and S_0 are the temperature and salinity of the water entering the cavity, q_{cav} is the overturning circulation, $\mathcal{A}_c$ is the area of the ice-ocean interface, $\gamma_T^\star$ is its effective turbulent heat transfer coefficient, $S_\star$ is the reference salinity, $c_\star$ is the specific heat capacity of seawater and $\mathcal{L}$ is its latent heat. The temperature T_b of the ice-ocean interface is the freezing temperature of seawater. To test the impact of periodic forcing, we set T_0 and S_0 to vary according to

$$\begin{cases} T_0(t) = T_\star + \theta\sin(\omega t), \\ S_0(t) = S_\star + \frac{\alpha}{\beta}\theta\sin(\omega t), \end{cases} \tag{5.2}$$

where $T_\star$ and $S_\star$ are constant reference temperature and salinity, and θ is the amplitude of the thermal forcing. The coefficient α and β are the constant thermal expansion and

haline contraction of the linearized equation of state $\rho = \rho_\star[1 - \alpha(T - T_\star) + \beta(S - S_\star)]$. Thus, the amplitude of the salinity forcing is chosen to compensate exactly the variations of density induced by the variations of T_0, as $\rho_0 = \rho_\star[1-\alpha(T_0(t)-T_\star)+\beta(S_0(t)-S_\star)] = \rho_\star$.

Linear low-dimensional box model

The set of equations Eq. (5.1) is easily solved with constant parameters q_{cav} and $\gamma_T^\star$. The characteristic timescale of the system is the flushing time of the cavity, defined as $\tau = V_{\text{cav}}/q_{\text{cav}}$, such that the dimensionless time reads $\tilde{t} = t/\tau$ (and therefore the dimensionless pulsation is $\tilde{\omega} = \omega\tau$). The dynamical variables are redefined with the dimensionless thermal forcing of the cavity $u = \frac{T-T_b}{\Delta T_\star}$ (with $\Delta T_\star$ typically being 3°C) and with the dimensionless buoyancy of the cavity $v = \frac{T-T_\star}{\Delta T_\star} - \frac{S-S_\star}{\frac{\alpha}{\beta}\Delta T_\star}$, such that Eq. (5.1) can be expressed in dimensionless form as

$$\begin{cases} \dot{u} = u_0 - (1 + \chi^{-1})u, \\ \dot{v} = -v + \chi^{-1}(R_\rho - 1)u, \end{cases} \tag{5.3}$$

where $R_\rho = \frac{c_\star}{\mathcal{L}}\frac{\beta}{\alpha}S_\star$ and $\chi = \frac{q_{\text{cav}}}{\mathcal{A}_c\gamma_T^\star}$ are model parameters, and $u_0 = \frac{T_0-T_b}{\Delta T_\star}$ is the forcing parameter. The parameter R_ρ is the density ratio between salinity and temperature effects of meltwater properties. Here, $R_\rho \approx 4 > 1$ ensures that the meltwater release increases the buoyancy of the ocean cavity. The parameter χ is the ratio between the overturning circulation and the mixing flux at the ice-ocean interface. Finally, u_0 represents the thermal driving of water masses entering the cavity.

The steady-state response is obtained when u_0 is constant and reads $(u_\infty, v_\infty) = \left(\frac{\chi}{1+\chi}u_0, \frac{(R_\rho-1)}{1+\chi}u_0\right)$. The Jacobian matrix evaluated at (u_∞, v_∞) is

$$J = \begin{pmatrix} -(1 + \chi^{-1}) & 0 \\ \chi^{-1}(R_\rho - 1) & -1 \end{pmatrix}.$$

Its eigenvalues $\lambda_u = -(1+\chi^{-1})$ and $\lambda_v = -1$ are both negative. Thus, the steady solution (u_∞, v_∞) is stable. The associated basal melt rate is

$$m_\infty = \frac{\rho_\star}{\rho_{\text{ice}}}\gamma_T^\star\delta u_\infty = \frac{\rho_\star}{\rho_{\text{ice}}}\gamma_T^\star\delta\frac{\chi}{1+\chi}u_0, \tag{5.4}$$

with $\delta = \frac{c_\star}{\mathcal{L}}\Delta T_\star$ the Stefan number. The steady basal melt rate scales linearly with u_0.

We now apply the periodic forcing $u_0 = \theta_0 + \theta\sin(\tilde{\omega}\tilde{t})$ introduced with Eq. (5.2). As the dynamical system is linear, we can use the complex notation $\underline{x} - x_\infty = Xe^{-i\phi_x}e^{i\tilde{\omega}\tilde{t}}$ for our dynamical parameters with X and ϕ_x the complex norm and phase of $\underline{x} - x_\infty$, respectively, and x_∞ the steady-state constant solution associated to the thermal driving θ_0. For the complex thermal forcing $\underline{u}$, we find

$$\begin{cases} U = \frac{\theta}{\sqrt{(1+\chi^{-1})^2+\tilde{\omega}^2}}, \\ \phi_u = \arctan\left(\frac{\tilde{\omega}}{1+\chi^{-1}}\right), \end{cases} \tag{5.5}$$

which shows that the response of the system is equivalent to a low-pass filter. The dimensional cutting pulsation above which the fluctuations of thermal driving are damped

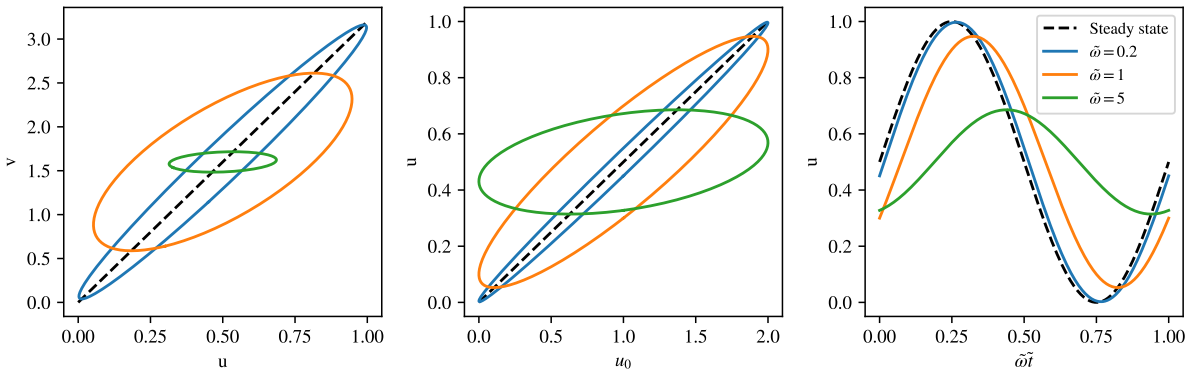

Figure 5.1: Solutions for the linear set of equations Eq. (5.3) using a periodic forcing $u_0 = \theta_0 + \theta \sin(\tilde{\omega}\tilde{t})$. We test $\tilde{\omega} \in \{0.2, 1, 5\}$ and set $\chi = 1$, $R_\rho = 4$, $\theta_0 = 1$ and $\theta = 1$. The steady state is represented by black dashed lines. Left panel: stable periodic responses in the (u, v) plane. Center panel: stable periodic responses in the (u, u_0) plane, which in fact is representative of the basal melt response of the ice shelf to periodic thermal driving. Right panel: temporal evolution of u over one period.

is $\omega_c = \frac{1}{\tau}$, the overturning circulation flushing pulsation. Taking values of q_{cav} from [Reese et al., 2018], we can estimate τ to be equal to 21 years for the Filchner-Ronne ice shelf and 4 months for the Pine Island ice shelf. The seasonal pulsation $\omega_{\text{seas}} = \frac{2\pi}{1\,\text{y}} = 6.3$ $\text{y}^{-1} > \omega_c$ in the two cases. Thus, we expect that seasonal thermal driving fluctuations are damped by the ice-shelf cavities ($U/\theta \approx 0.4$ for Pine Island, and $U/\theta \approx 7 \times 10^{-3}$ for Filchner-Ronne). We show some solutions obtained in Fig. 5.1 when $\tilde{\omega} \in \{0.2, 1, 5\}$. Note that with constant parameters q_{cav} and $\gamma_T^\star$, the dimensionless thermal driving u is also representative of the basal melting dynamics. For slowly varying forcing (blue curves), the response of the system is close to the quasi-static response (black dashed curves). However, for faster forcing (orange and green curves), the response of the system deviates from the quasi-static response. The temporal response is also shifted, with a phase that does not exceed $\pi/2$, as predicted by Eq. (5.5).

These results can be compared with those obtained by Paul Holland [Holland, 2017] within a numerical configuration similar to our NEMO configuration presented in Chapter 3 but without surface forcing. The thermal driving forcing is implemented by varying the properties in the restoring region in their numerical study. Fig. 5.2 shows the basal melt response to varying thermal driving in their configuration and should therefore be compared with the center panel of Fig. 5.1. The gray line in Fig. 5.2 represents the steady-state response and has a quadratic scaling, as predicted by previous idealized numerical studies [Holland et al., 2008]. In comparison, our simple model only captures a linear scaling. In addition, the response to slowly varying thermal driving in the numerical study is asymmetric depending on cold-to-warm or warm-to-cold transitions. This behavior is due to different overturning circulation fluxes between the two modes, which is absent from our one box model as q_{cav} has been set constant. For fast thermal driving fluctuations, the basal melt rates of the numerical configuration do not follow anymore the quasi-static response and are in phase opposition with thermal forcing. The phase shift is clearly visible in Fig. 5.3 where basal melt is plotted as a function of time (the gray dots represent the quasi-static response). However, our simple model only allows a

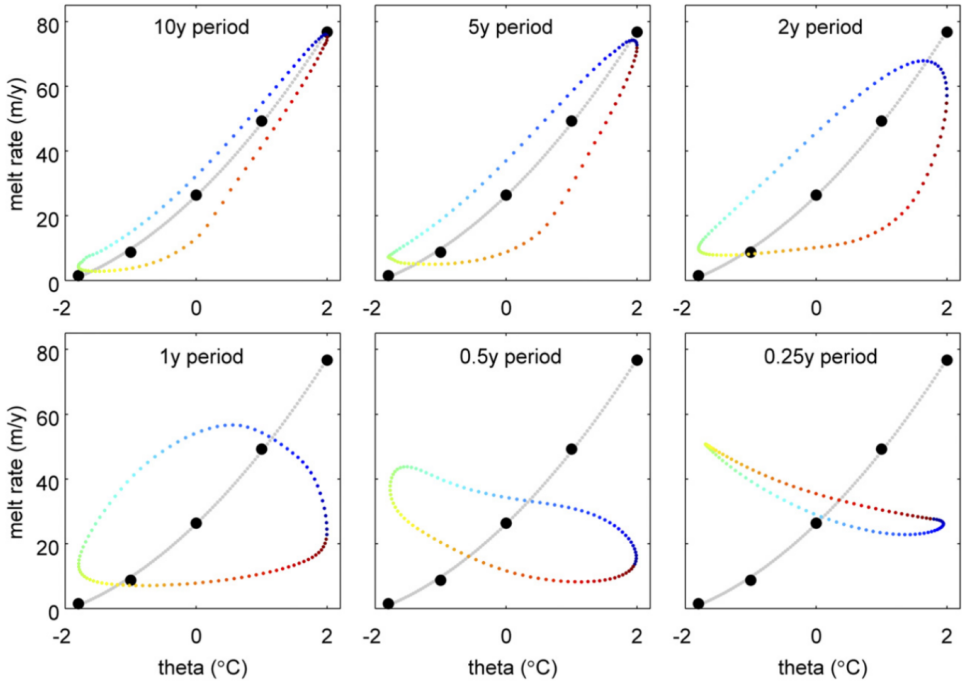

Figure 5.2: Response of the basal melt rates to periodic thermal driving "theta" in an idealized numerical configuration [Holland, 2017]. The numerical configuration is similar to our NEMO configuration presented in Chapter 3 but without polynya forcing. Thus, the only forcing stems from the restoring region wherein temperatures vary periodically. The quasi-static response is shown in gray. Figure from [Holland, 2017].

$\pi/2$ phase shift. We will now demonstrate that better agreement is observed with the simulations results of [Holland et al., 2008] when we relax the assumption of constant q_{cav} and $\gamma_T^\star$.

Nonlinear low-dimensional box model

We now consider parameterizations for the overturning strength and temperature exchange velocity of the form $q = C(\rho_0 - \rho)$ and $\gamma_T^\star = \Gamma q$, respectively. We transform Eq. 5.1 into a dimensionless equation by defining the dimensionless coefficients $s = \Gamma \mathcal{A}_c$ and using the characteristic timescale $\tau = \frac{V_{\text{cav}}}{C\rho_\star \alpha \Delta T_\star}$. The dimensionless equations for u (dimensionless thermal driving) and v (dimensionless buoyancy, which is now interpreted as the dimensionless overturning circulation) as functions of dimensionless time $\tilde{t} = t/\tau$ become

$$\begin{cases} \dot{u} = vu_0 - (1+s)uv, \\ \dot{v} = -v^2 + s(R_\rho - 1)uv. \end{cases} \tag{5.6}$$

Note that the product uv in these nonlinear equations represents the dimensionless basal melt rate, as $m = \frac{V_{\text{cav}}}{\mathcal{A}_c \tau} \frac{\rho_\star}{\rho_{\text{ice}}} \delta s uv$. At constant thermal driving u_0, the fixed point of the system for which $v \neq 0$ is $(u_\infty, v_\infty) = \left(\frac{u_0}{1+s}, \frac{s(R_\rho - 1)}{1+s} u_0\right)$. Thus, we recover the quadratic scaling for the basal melt rate as a function of thermal driving as $u_\infty v_\infty \propto u_0^2$. The

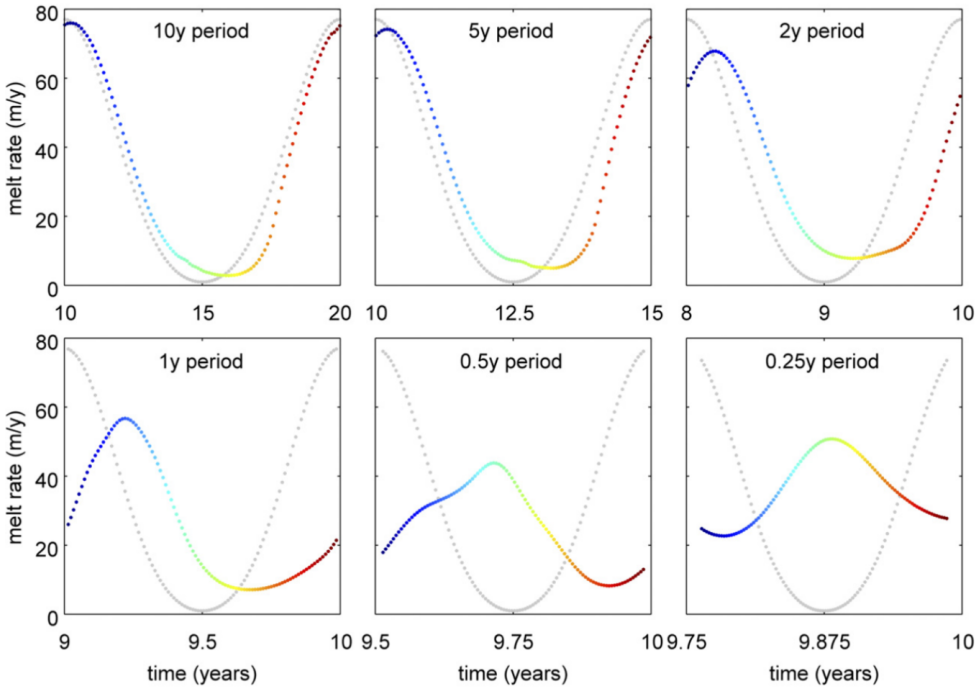

Figure 5.3: Temporal plots of the basal melt rates with time-varying thermal driving in an idealized numerical configuration [Holland, 2017]. The gray dots represent the quasi-static response of the system. Figure from [Holland, 2017].

Jacobian matrix evaluated at (u_∞, v_∞) is

$$J = \begin{pmatrix} -s(R_\rho - 1)u_0 & 0 \\ \frac{s^2(R_\rho-1)^2 u_0}{1+s} & -\frac{s}{1+s}(R_\rho - 1)u_0 \end{pmatrix}.$$

Its eigenvalues $\lambda_u = -s(R_\rho - 1)u_0$ and $-\frac{s}{1+s}(R_\rho - 1)u_0$ are both negative if $R_\rho > 1$, which is the case here as $R_\rho \simeq 4$. Note that we implicitly assumed $u_0 > 0$, meaning that the intruding water temperature is warmer than the freezing temperature. Otherwise, the fixed point (u_∞, v_∞) becomes unstable, and the stable point is another solution that constrains $v = 0$ (which is unstable for $u_0 > 0$).

We show numerical solutions for Eqs. (5.6) in Fig. 5.4, rather than analytical solutions, which are now difficult to obtain since Eqs. (5.6) are nonlinear. As previously, the response to slow variations in thermal driving (blue curves) matches more closely the quasi-static response (black dashed curves) than the response to fast variations in thermal driving (orange and green curves). However, we now recover the quadratic scaling of the basal melt rate uv as a function of u_0, and we also capture the asymmetry of the transition dynamics described by [Holland, 2017]: the warm-to-cold transition is faster than the cold-to-warm transition. For forcing $\tilde{\omega} \leq 1$, we obtain remarkably good qualitative agreement with the findings of [Holland, 2017], despite the simplicity of the model. However, for $\tilde{\omega} > 1$, we still do not recover the phase opposition between the melt uv and thermal driving u_0. Thus, our model still fails to capture the dynamics associated to the small timescales. To be more precise, the observed supplementary phase lag can be associated to a physical process that we do not capture. For example, the ice-ocean interface meltwater plume layer also has a response timescale we neglected here by considering a instantaneous adjustment of

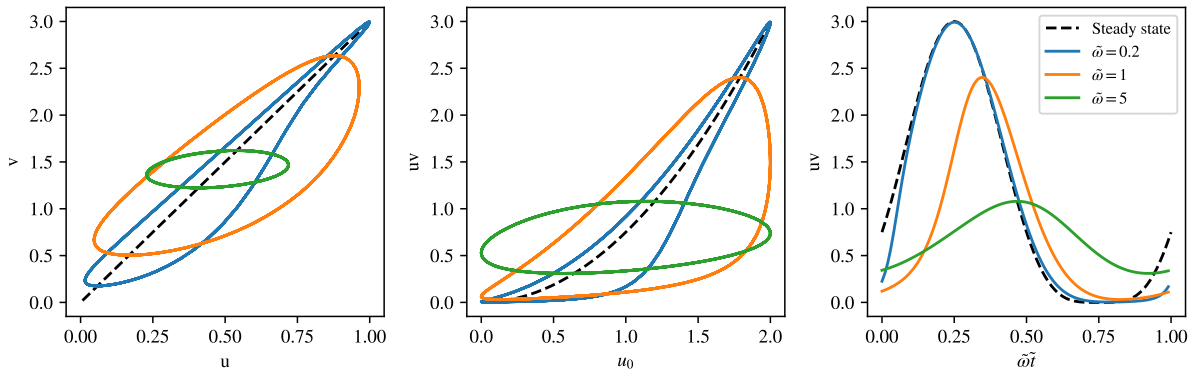

Figure 5.4: Solutions for the nonlinear set of equations Eq. (5.6) using a periodic forcing $u_0 = \theta_0 + \theta \sin(\tilde{\omega}\tilde{t})$. We test $\tilde{\omega} \in \{0.2, 1, 5\}$ and set $s = 1$, $R_\rho = 4$, $\theta_0 = 1$, $\theta = 1$. The steady-state is represented by black dashed lines. On the left plot, we find stable periodic responses in the $u \times v$ plane, which are the two dynamical variables of the system. In the center, we observe stable periodic responses in the $uv \times u_0$ plane, which is representative of the basal melt response of the ice shelf to periodic thermal driving. On the right panel is represented the temporal evolution of the basal melt rate uv on one period.

ice-ocean interface water properties and ocean cavity box properties. A natural way to account for this meltwater plume adjustment would be to integrate a meltwater plume model at the ice-ocean interface [Lazeroms et al., 2018] preserving temporal derivatives in the equations.

5.2.2 Response to transient surface forcing with NEMO simulations

The previous section investigated the response of an ice-shelf cavity to the intrusion of time-dependent water properties. Here, we leverage the more realistic numerical NEMO setup presented in chapter 3 to assess the impact of the thermocline dynamics and bistability on the system response to time-varying sea surface forcing. We set constant far-field ocean properties to focus solely on surface salt forcing. The restoring temperature (resp. salinity) varies linearly from $-1.9\,°\mathrm{C}$ (resp. $34.0\,\mathrm{g/kg}$) at the sea surface to $1\,°\mathrm{C}$ (resp. $34.5\,\mathrm{g/kg}$) at the bottom of the ocean. For this specific restoring condition, we identified in the previous chapter that the cold mode is stable for $F_S > 0.025\,\mathrm{g/m^2/s}$ and that the warm mode is stable for $F_S < 0.035\,\mathrm{g/m^2/s}$. Consequently, the bistable region is obtained between these two forcing bounds.

We investigate the response of the ice-shelf cavity to periodic surface salt forcing of the form

$$F_S(t) = \frac{F_S^{\max}}{2}\left[1 + \cos(\omega t)\right]. \tag{5.7}$$

The surface salt forcing oscillates between 0 and $F_S^{\max}$ with period $T = 2\pi/\omega$. We first test the impact of the forcing period T for fixed $F_S^{\max} = 0.06\,\mathrm{g/m^2/s}$. Thus, the surface forcing covers the whole bistable region and extends into the monostable cold and warm regions. Simulations are initialized from either the warm or the cold equilibrium state in order to assess the sensitivity of the transient dynamics to the initial ocean circulation

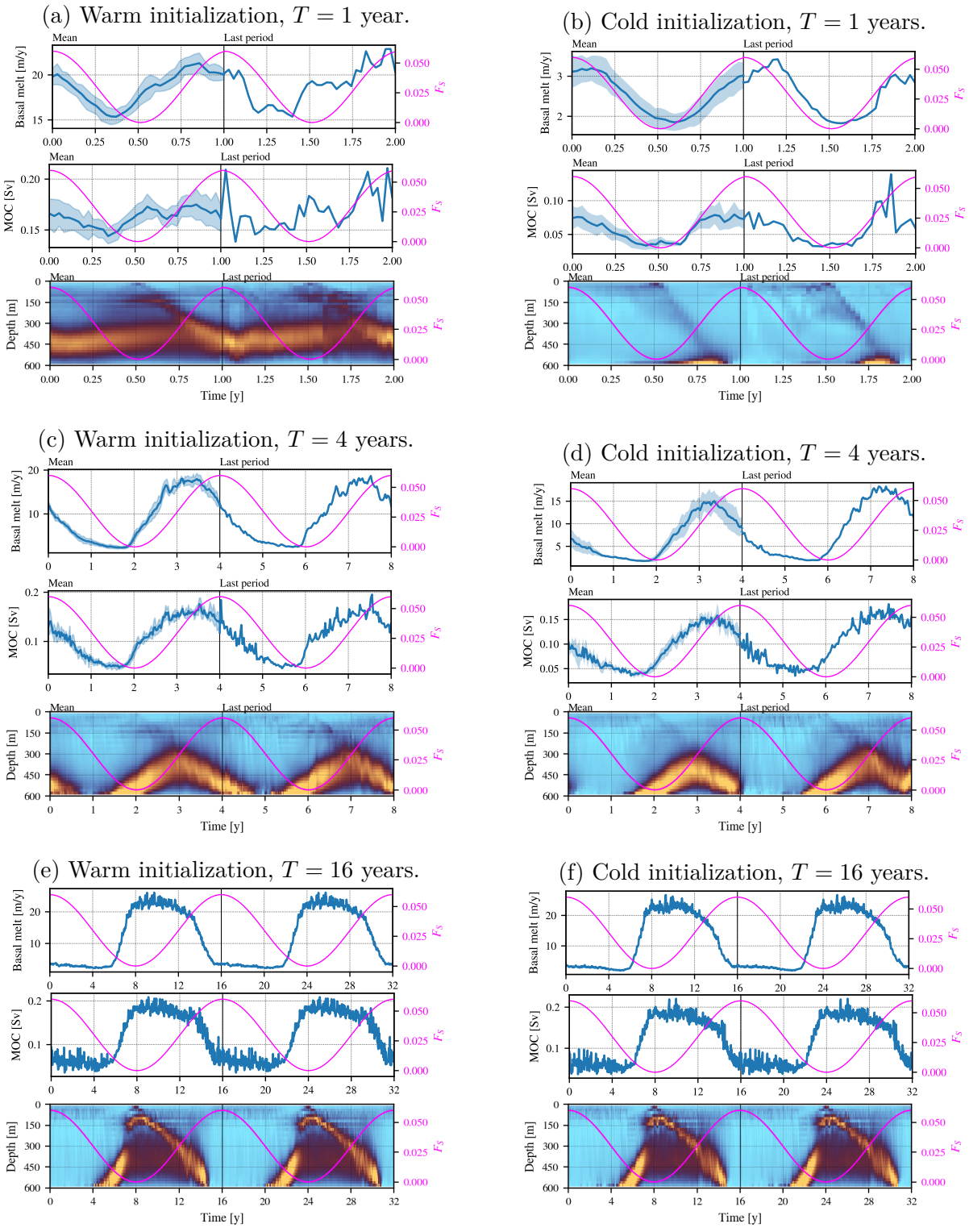

Figure 5.5: Basal melt rate, Meridional Overturning Circulation (MOC, here defined as the maximal |MOC| value within the cavity), and temperature stratification beneath the polynya (the bright yellow shading indicates the depth of the thermocline). The magenta curve shows the imposed surface salt flux. (a,c,e) are initialized from the warm equilibrium state, whereas (b,d,f) are initialized from the cold equilibrium state. In (a-d), the first forcing cycle corresponds to the average over all realized cycles (16 simulated years for each run), while the second corresponds to the final cycle of the simulations. In (e,f), the same cycle is shown twice because only one forcing cycle was realized.

regime. For a warm initialization, F_S starts at $0\,\mathrm{g/m^2/s}$ ($\omega t_0 = \pi$), while for the cold initialization, F_S starts at $0.06\,\mathrm{g/m^2/s}$ ($\omega t_0 = 0$).

Fig. 5.5 shows the temporal evolution of the basal melt rate, the Meridional Overturning Circulation in the cavity (MOC), and the temperature stratification under the polynya, for $T \in \{1, 4, 16\}$ years. These quantities are shown together with the imposed surface salt flux (in magenta). The system exhibits qualitatively different responses depending on the forcing period and initialization of the ocean state. For $T = 1$ year (Fig. 5.5(a,b)), the perturbation is too rapid for a regime transition to occur and the system remains in its initial state throughout the forcing cycle. In contrast, for $T = 16$ years (Fig. 5.5(e,f)), simulations initialized from either warm or cold ocean states converge to the same periodic solution. In this case, the system undergoes regular transitions between the warm and cold circulation modes, indicating that the forcing evolves slowly enough for the ocean circulation to adjust to the changing surface conditions. The simulations with intermediate forcing period $T = 4$ years (Fig. 5.5(c,d)) exhibit comparatively more complex behavior. Transitions between the warm and cold regimes occur but the trajectories depend on the initial ocean state.

For fast varying forcing (e.g., $T = 1$ y), a signal appears close to the surface in the temperature stratification plots when the salt forcing F_S reaches its minimum. This signal may be caused by the restratification of the water column close to the sea surface, which builds up downward over time as the salt surface forcing re-increases.

The basal melt rates of the simulations presented in Fig. 5.5 are also plotted against the surface salt flux F_S in Fig. 5.6. The steady-state melt rates are represented in black as references. For fast varying forcing ($T = 1$ year), we observe a clear dependence on initial conditions as the system remains close to its initial equilibrium branch melting values. We observe a phase opposition between the equilibrium melt rates and the dynamical melt rates obtained for the warm initialized experiment. For $T = 4$ years, this phase opposition is also observed. Finally, for $T = 16$ years, the system evolves slowly and is in phase with the surface forcing: high basal melt rates are obtained for low F_S whereas low basal melt rates are obtained for high F_S. Still, the transition thresholds are overshot due to the inertia of the system.

The dependence of the melt rate to the forcing frequency is summarized in Fig. 5.7(a). The basal melt rate extremums are shown as a function of the forcing frequency ω (bottom axis) and the period T (top axis) for both warm (red) and cold (blue) initializations. At low frequencies, the basal melt rate values obtained are the same independently of the initial ocean state, consistent with the convergence toward a common periodic solution. As the forcing frequency increases, the solutions corresponding to warm and cold initializations separate and converge toward distinct asymptotic values. Figure 5.7(b) shows the melt-rate amplitude Δm, defined as the difference between the melt rates extremums, as a function of ω. For both warm and cold initialized simulations, Δm remains approximately constant for low frequencies before decreasing at shorter periods. The cutoff period is approximately 4 years for the warm initialized simulation, and 8 years for the cold initialized simulations. Below the cutoff periods, the reduction in melt-rate amplitudes with increasingly high forcing frequencies is broadly consistent with a scaling proportional to $1/\omega$ in both cases (black dashed line). For comparison, the flushing time of the cavity $V_{\mathrm{cav}}/\langle|\mathrm{MOC}|\rangle_{\mathrm{cavity}}$ [Holland, 2017] is 8 months for the warm mode steady state and 3 years for the cold mode steady state. Thus, the flushing time of the cavity

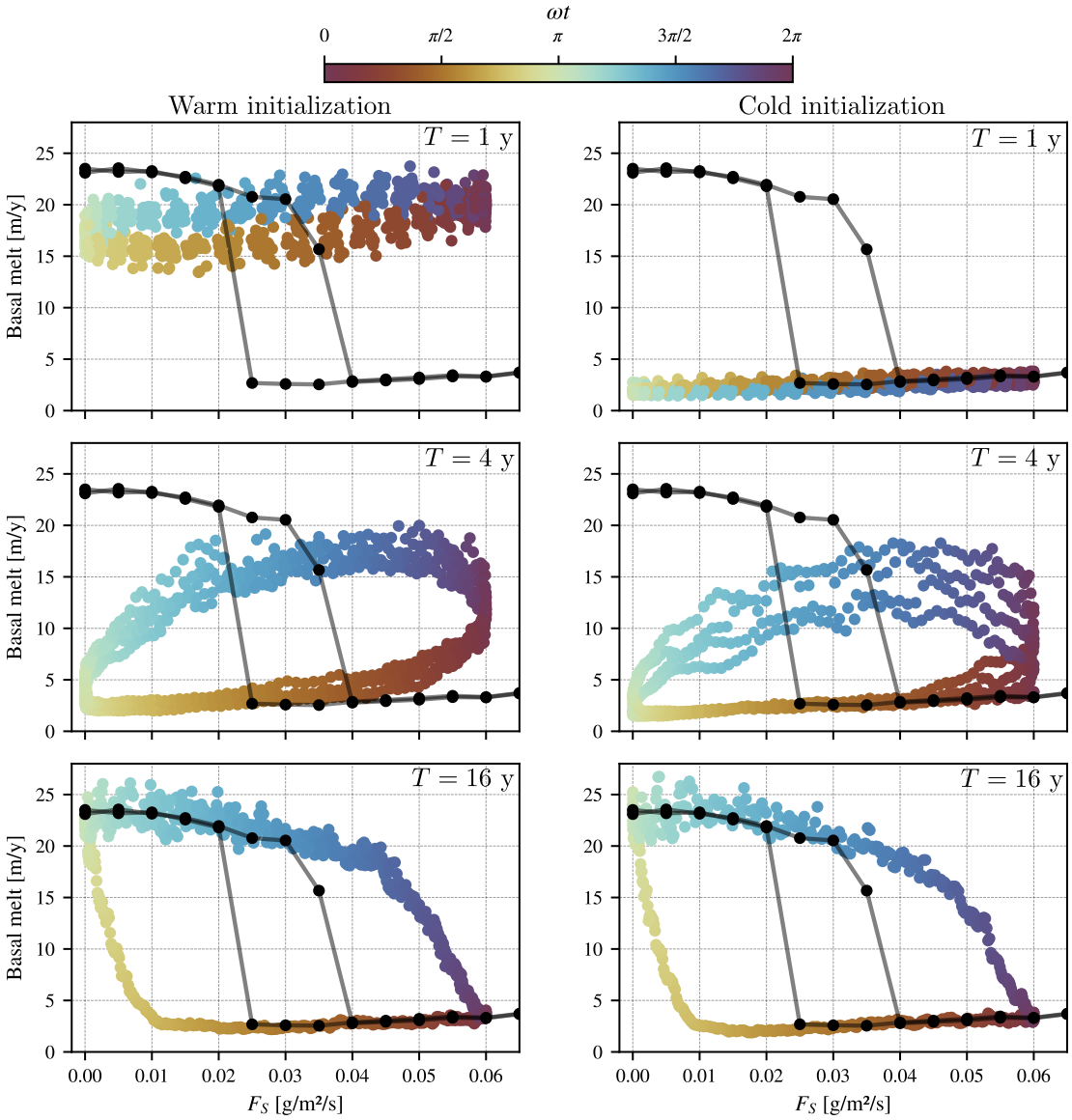

Figure 5.6: Basal melt rate as a function of the imposed surface salt flux F_S. Black curves show the corresponding quasi-static solutions for reference. Panels in the left column are initialized from the warm equilibrium state, while those in the right column are initialized from the cold equilibrium state.

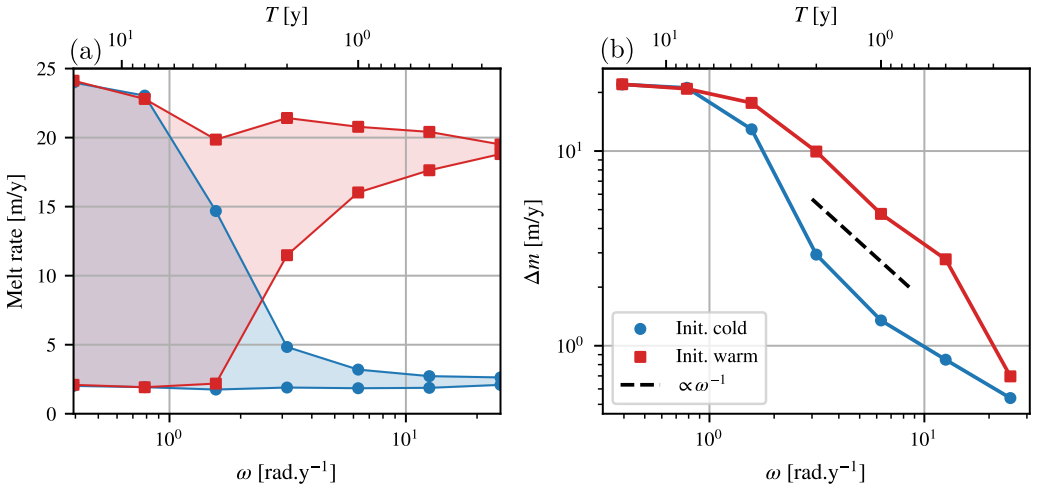

Figure 5.7: Impact of the forcing period on melt rate variations. (a) Range of basal melt rates, highlighted by blue and red shadings, obtained as a function of forcing pulsation ω (bottom x-axis) and forcing period T (top x-axis). Simulations initialized by warm ocean conditions are shown in red, whereas simulations initialized from cold conditions are shown in blue. (b) Amplitude of the basal melt-rate $\Delta m = m_{\max} - m_{\min}$ shown as a function of ω. The black dashed line indicates a $1/\omega$ scaling for reference.

does not seem to be the main limiting time when considering surface flux forcing, contrary to the previous section results that only considered the cavity inertia and discarded thermocline dynamics.

We also represent in Fig. 5.8 the extremum values taken by the MOC (a), as well as its amplitude (b). Here again, the warm and cold initialized simulations encompass the same range of MOC values at small frequencies but converge to different values at high frequencies. Contrary to the basal melt rates, the cutoff frequency seems to be approximately 4 years for both warm and cold initialized simulations. The two same figures are represented in (c) and (d) for the Mixed Layer Depth (MLD, which refers here to the thermocline depth). For low forcing frequencies, both warm and cold initialized simulations span the same range of thermocline depths, with MLD values varying between approximately 100 m and 600 m (maximum depth). In the cold initialized simulations, the maximum MLD remains equal to the ocean depth over the entire range of forcing frequencies, indicating that the system reaches the fully mixed cold state during each forcing cycle. As the forcing frequency increases, the MLD progressively converges toward the bottom depth at all times, suggesting that restratification increasingly vanishes under rapidly varying surface forcing. In contrast, the warm initialized simulations cease to reach the bottom depth for forcing periods shorter than approximately 2 years. Below this threshold, the system fails to access the cold circulation mode, consistent with the disappearance of regime transitions observed at high forcing frequencies. The amplitude of the MLD decreases much faster for the cold initialized simulations, because the allowed range is strongly constrained by the maximum depth of the water column.

To investigate the causal relationships and characteristic timescales governing the system response to transient forcing, we examine the phase differences between the time series of basal melt rate, cavity MOC, thermocline depth, and the imposed surface salt

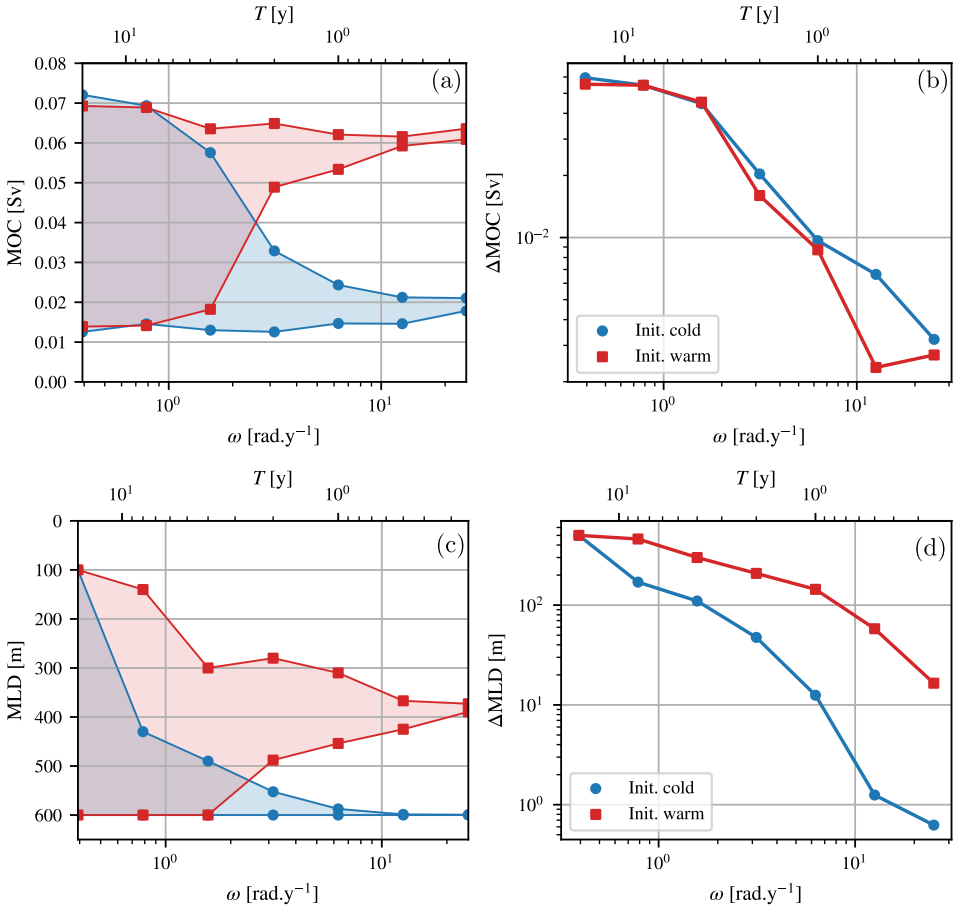

Figure 5.8: (a,b) Same as Fig. 5.7 but for the MOC, here defined as the average of the MOC (which shows less noise compared its maximum) within the cavity. (c,d) Same as Fig. 5.7 but for the Mixed Layer Depth (MLD), here defined as the depth of the thermocline.

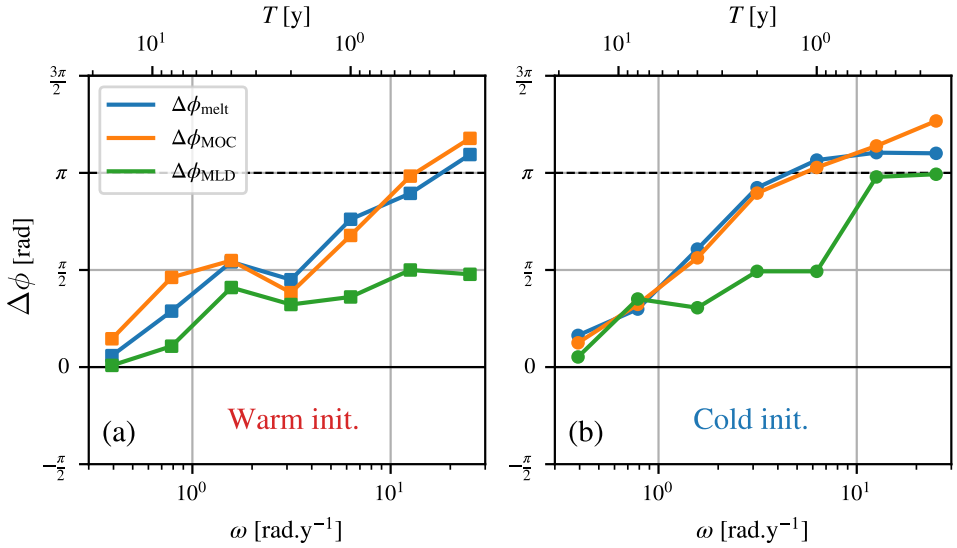

Figure 5.9: Phase lags $\Delta\phi_{\text{melt}}$ (blue), $\Delta\phi_{\text{MOC}}$ (orange), and $\Delta\phi_{\text{MLD}}$ (green) (see Eq. 5.8) as functions of the forcing pulsation ω (bottom x-axis) and period T (top x-axis) for both warm (a) and cold (b) ocean initializations.

flux. Our reference phase ϕ_{F_S} is defined when $F_S = 0$, i.e., which would correspond to a warm state if the forcing would be applied quasi-statically. The warm state is characterized at equilibrium by high basal melt rates, a strong cavity overturning circulation, and a shallow thermocline. Based on these characteristics, we define the associated phases: ϕ_{melt} at maximal basal melt rate, ϕ_{MOC} at maximal cavity MOC, and ϕ_{MLD} at the shallowest thermocline depth, such that for the limit of a quasi-static forcing ($\omega \to 0$) these phases should match with ϕ_{F_S}. Figure 5.9 shows the phase lags

$$\begin{aligned} \Delta\phi_{\text{melt}} &= \phi_{\text{melt}} - \phi_{F_S}, \\ \Delta\phi_{\text{MOC}} &= \phi_{\text{MOC}} - \phi_{F_S}, \\ \Delta\phi_{\text{MLD}} &= \phi_{\text{MLD}} - \phi_{F_S}, \end{aligned} \tag{5.8}$$

as functions of the forcing pulsation ω. We adopt ϕ_{F_S} as the reference phase because the surface salt flux is the externally imposed control parameter and thus provides a natural reference to characterize the ordering of the processes involved. Fig. 5.9(a) and (b) show the results for simulations initialized from the warm state and cold state, respectively. For both initial conditions, all phase lags increase with increasing forcing pulsation. This behavior reflects the finite adjustment times of the physical processes involved: as the forcing varies more rapidly, the system progressively has less time to adapt to the imposed surface conditions. Among the three variables, $\Delta\phi_{\text{MLD}}$ is always the smallest for the entire range of forcing frequencies. Thus, the thermocline depth appears to be the first component of the system to respond to changes in surface forcing. In contrast, the basal melt rate and cavity MOC exhibit larger phase lags. Moreover, $\Delta\phi_{\text{melt}}$ and $\Delta\phi_{\text{MOC}}$ remain very close to one another, making it difficult to conclude on causal links between these two processes. At high forcing frequencies, both $\Delta\phi_{\text{melt}}$ and $\Delta\phi_{\text{MOC}}$ approach π, indicating that the cavity response becomes out of phase with the equilibrium system response. However, the physical mechanisms responsible for this phase opposition differ between the warm and cold initializations. For simulations initialized from the warm state, the cavity remains sensitive to CDW intrusions whose intensity is controlled by the thermocline depth. The phase opposition thus results from the delayed adjustment of the stratification and cavity circulation to the rapidly varying surface forcing. In contrast, for simulations initialized from the cold state, restratification does not occur at high forcing frequencies and the cavity remains predominantly filled with DSW. In this regime, the variability of basal melting is not driven by CDW intrusions. Instead, it originates from the mode III circulation at the ice-shelf front, whose strength is associated with an anticyclonic thermal-wind circulation close to the ice shelf. This circulation intensifies during periods of strong surface salt forcing. As a result, the phase opposition of the basal melt rate in the cold-initialized simulations is not a consequence of the inertia of the MOC or thermocline depth, but rather reflects a more direct response to the imposed surface salt forcing.

5.3 Seasonal and interannual polynya variability

In the previous sections, we investigated the response of an ice-shelf cavity to time-dependent forcing. In particular, we assessed the roles of the overturning circulation and the thermocline depth in the tipping dynamics of the system under forcing periods

ranging from a few months to several years. Using again a sinusoidal surface forcing (Eq. (5.7)), we now fix the period to one year to focus on the seasonal variability of sea-ice production observed in Antarctic coastal polynyas, and seek the thresholds of winter sea-ice production below (resp. above) which the cavity undergoes cold-to-warm (resp. warm-to-cold) transitions. We subsequently investigate the impact of interannual variability in winter sea-ice production on the mean time of first transitions.

5.3.1 Impact of the seasonal cycle on ice-shelf cavity transitions

Since only 4% of annual sea-ice production occurs within coastal polynyas between November and February [Nakata et al., 2021], we set the minimum value of F_S to zero to approximate summer conditions. Under this assumption, the four months with the weakest forcing contribute only to 5.8% of the annual cumulative surface salt flux.

For the forcing period $T = 1$ year and the maximal salt flux $F_S^{\max} = 0.06\,\mathrm{g/m^2/s}$, we showed in the previous section that the basal melt rates obtained starting either from the cold or warm regime are disjoint through the whole forcing cycle (see Fig. 5.7(a)). This observation is a signature of bistable dynamics, as two different stable periodic responses are reached depending on the initial ocean conditions. For a fixed period, it is of interest to know for which values of $F_S^{\max}$ the system converges towards a single stable periodic response, regardless of the initial conditions. Thus we can define dynamical cold-to-warm and warm-to-cold transition thresholds based on the value of $F_S^{\max}$. We first get interested into cold-to-warm transitions. We therefore set several experiments initialized in cold conditions with various values for $F_S^{\max}$. We expect that the system transition irreversibly toward the warm regime below a certain $F_S^{\max}$ threshold.

We are interested in the first transition time of the ice-shelf cavity. Strictly speaking, it depends on the initial state of the system as well as on the threshold considered. Here, denoting X_t the state vector defining the system at time t (which contains temperature, salinity, velocity at each grid point), we define the first cold-to-warm transition time T_1^{ctw} as the time satisfying

$$T_1^{\mathrm{ctw}}(x) = \inf\{t \,|\, m\,(X_t) \geq a_{\mathrm{ctw}}, X_0 = x\}, \tag{5.9}$$

i.e., which is the time when the basal melt in the cavity crosses the a_{ctw} threshold. In practice, we use $a_{\mathrm{ctw}} = 15$ m/y as it corresponds approximately to the melt rate above which the system is attracted by the warm stable periodic orbit for $T = 1$ y (see Fig. 5.7(a)).

Fig. 5.10 shows the time evolution of the basal melt rate for simulations with $F_S^{\max}$ ranging from $0.035\,\mathrm{g/m^2/s}$ to $0.045\,\mathrm{g/m^2/s}$. The simulations are initialized with constant $F_S^{\max}$ surface forcing values during a five-year spin-up (gray shaded zone) to force the system to be in a well-defined cold state initially. For $F_S^{\max} \leq 0.042\,\mathrm{g/m^2/s}$, the system transitions from cold to warm conditions before reaching 100 simulated years. The inset in Fig. 5.10 shows the first cold-to-warm transition time T_1^{ctw}. Note that they have not been averaged over several initial conditions and hence represent single realizations. The first transition time $T_1^{\mathrm{ctw}} \approx 5$ years when $F_S^{\max} \leq 0.039\,\mathrm{g/m^2/s}$ but increases abruptly for higher $F_S^{\max}$ values. In fact, it is even possible that we did not capture transitions occurring at very large time for $F_S^{\max} > 0.042\,\mathrm{g/m^2/s}$. The abrupt increasing of T_1^{ctw} is linked to the internal variability of the system. For example, another run using $F_S^{\max} = 0.040\,\mathrm{g/m^2/s}$ but initialized with a different ocean cold state transitioned at $T_1^{\mathrm{ctw}} = 27$

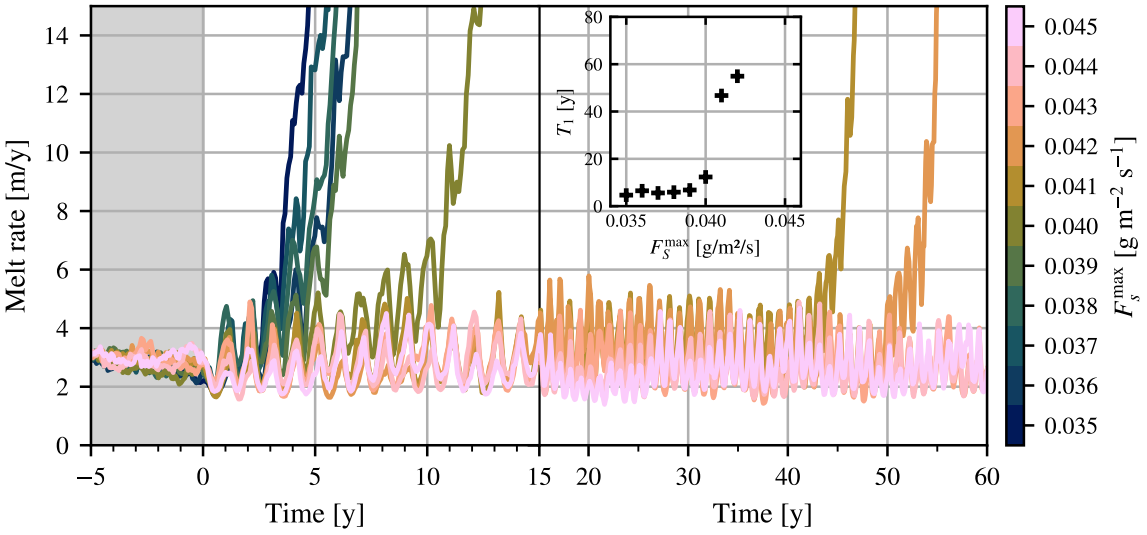

Figure 5.10: Basal melt rate evolution for simulations initialized in the cold regime and subjected to a seasonal surface forcing ($T = 1$ year) with different amplitudes $F_S^{\max} \in [0.034, 0.045]\,\mathrm{g/m^2/s}$. The gray shaded region corresponds to a five-year spin-up during which a constant surface salt flux equal to $F_S^{\max}$ is applied. The inset reports the first transition time $T_1^{\mathrm{ctw}} = \min\{t,\ m(t) \geq 15\,\mathrm{m/y}\}$ as a function of $F_S^{\max}$.

years instead $T_1^{\mathrm{ctw}} = 12$ years obtained in Fig. 5.10 (not shown). As long as T_1^{ctw} has not been averaged over its initial conditions, it is difficult to conclude whether T_1^{ctw} has a vertical asymptote for a finite value of $F_S^{\max}$, or whether $T_1^{\mathrm{ctw}} \to +\infty$ as $F_S^{\max} \to +\infty$. As a preliminary conclusion, we will consider that the cold-to-warm transition threshold can be approximated as $F_S^{\max} = 0.040\,\mathrm{g/m^2/s}$ since below this value T_1^{ctw} has the same order of magnitude.

Fig. 5.11 shows the time evolution of the basal melt rate for simulations with $F_S^{\max}$ ranging from $0.060\,\mathrm{g/m^2/s}$ to $0.075\,\mathrm{g/m^2/s}$ but initialized without surface salt flux during the five-year spin-up to force the system to be initially in the warm state. The first warm-to-cold transition time is now defined as

$$T_1^{\mathrm{wtc}}(x) = \inf\{t \,|\, m\,(X_t) \leq a_{\mathrm{wtc}}, X_0 = x\}, \tag{5.10}$$

where $a_{\mathrm{wtc}} = 5$ m/y is approximately the upper bound of the cold stable orbit (see Fig. 5.7). This time, no transition is detected for $F_S^{\max} \leq 0.065\,\mathrm{g/m^2/s}$ and T_1^{wtc} gradually decreases from 15 to 5 years when $F_S^{\max}$ increases above this threshold. The existence of a vertical asymptote for the warm-to-cold transition at low $F_S^{\max}$ values remains an open question.

Based on the results from Fig. 5.10 and Fig. 5.11, we estimate that both the warm and cold periodic responses remain stable for forcing amplitudes in the range $F_S^{\max} \in [\approx 0.040, 0.065]$ g/m^2/s. In terms of the time-averaged surface forcing, this interval corresponds to $\langle F_S \rangle_t \in [\approx 0.020, 0.033]$ g/m^2/s. Remarkably, this range is very close to the steady-state bistable interval $F_S \in [0.025, 0.035]$ g/m^2/s identified in Chapter 3 for the standard experiments with $T_0 = 1\,^\circ$C. This result suggests that introducing a seasonal periodic forcing does not substantially modify the extent of the bistable regime when viewed in terms of the mean surface forcing. This observation provides support for

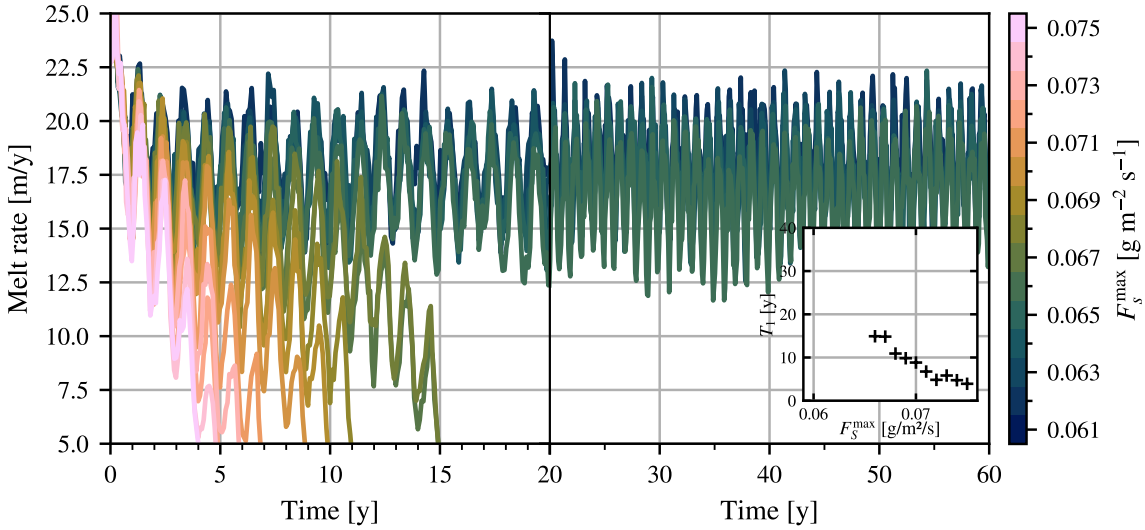

Figure 5.11: Same as Fig. 5.10 but initialized with warm conditions, no surface salt flux during the five-year spin-up, and $F_S^{\max} \in [0.060, 0.075]\,\mathrm{g/m^2/s}$. Here the first transition time is defined as $T_1^{\mathrm{wtc}} = \min\{t,\ m(t) \leq 5\,\mathrm{m/y}\}$.

the yearly-averaged forcing approximation adopted in Chapter 2 to locate Antarctic ice shelves on the stability diagrams of the low-dimensional model.

5.3.2 Interannual stochastic winter surface forcing

We now investigate the impact of interannual variability of the surface forcing on regime transitions within ice-shelf cavities. Large climate interannual variability rarely manifests as a regular periodic signal showing well-defined periods, but is rather described with statistical distributions of amplitude and duration of climate modes. Here, we model interannual variability of surface salt forcing by generating random values of $F_S^{\max}$ each year, which amounts to imposing interannual variability for winter forcing but keeping summer forcing at zero each year. Our stochastic model for winter forcing allows varying the amplitude and correlation time of $F_S^{\max}$ between years, thus enabling investigations of various timescales and strengths of internal variability. We first describe the properties of order-one auto-regressive processes, which are used to draw values of $F_S^{\max}$ each year. We then apply the stochastic surface forcing scheme to cold-initialized ocean states, testing values of $F_S^{\max}$ close to the dynamical cold-to-warm threshold, and assessing the impact of time correlations.

Stochastic model for surface salt flux

One way to model interannual fluctuations of winter salt surface forcing is to choose $F_S^{\max}$ as an auto-regressive process of order one (AR(1)), such that the surface forcing value at year $n+1$ depends on its previous value during year n, i.e.

$$F_{S,n+1}^{\max} = \left(1 - \frac{\Delta t}{\tau}\right) F_{S,n}^{\max} + \epsilon_n, \tag{5.11}$$

with $\Delta t = 1$ year the time lag between two winters, τ the characteristic fluctuation time of $F_S^{\max}$, and ϵ_n identical and independent random variable following a Gaussian probability

distribution. The case $\tau = 1$ year corresponds to draws for $F_S^{\max}$ that are independent and thus described by random Gaussian variables, and the case $\tau \to +\infty$ corresponds to draws for $F_S^{\max}$ following a random walk. In the following, we define $\alpha = \Delta t/\tau$ to simplify the notations. Eq. (5.11) can be applied recursively to obtain

$$F_{S,n}^{\max} = (1-\alpha)^n F_{S,0}^{\max} + \sum_{k=0}^{n-1} (1-\alpha)^k \epsilon_k, \tag{5.12}$$

with $F_{S,0}^{\max}$ the initial value. Thus, $F_S^{\max}$ is a linear combination of Gaussian variables, and consequently also follows a Gaussian distribution (Gaussian distributions being linearly stable). We can deduce from Eq. (5.12) that $F_S^{\max}$ is a stationary process only if $|1-\alpha| < 1$. When $F_S^{\max}$ is stationary, its probability distribution is fully defined by its time-dependent mean $\mu = \mathbb{E}[F_S^{\max}]$ and variance $\sigma^2 = \mathbb{V}[F_S^{\max}]$. The mean and variance of ϵ directly impact those of $F_S^{\max}$. Taking the expectation of both sides of Eq. (5.11), we get

$$\mu = (1-\alpha)\mu + \mathbb{E}[\epsilon] \Leftrightarrow \mathbb{E}[\epsilon] = \alpha\mu. \tag{5.13}$$

Then, since $F_{S,n}^{\max}$ and ϵ_n are uncorrelated ($\mathrm{Cov}[F_{S,n}^{\max}, \epsilon_n] = 0$), taking the variance of Eq. (5.11) simply leads to

$$\sigma^2 = (1-\alpha)^2\sigma^2 + \mathbb{V}[\epsilon] \Leftrightarrow \mathbb{V}[\epsilon] = \alpha(2-\alpha)\sigma^2. \tag{5.14}$$

The process $F_S^{\max}$ is thus generated with prescribed mean μ and variance σ by drawing ϵ_n as identical and independent Gaussian variables of mean $\alpha\mu$ and variance $\alpha(2-\alpha)\sigma^2$. The last property of our stochastic scheme that we will vary is the correlation time τ_c of the AR(1) process, which in our case sets the memory of winter surface forcing to previous realizations. Using Eq. (5.12) with $F_{S,n}^{\max}$ as initial value, the second order moment at lag k reads

$$\begin{aligned}
\mathbb{E}[F_{S,n}^{\max} F_{S,n+k}^{\max}] &= (1-\alpha)^k \mathbb{E}\left[\left(F_{S,n}^{\max}\right)^2\right] + \sum_{j=n}^{n+k-1} (1-\alpha)^{j-n} \mathbb{E}[\epsilon_j F_{S,n}^{\max}] \\
&= (1-\alpha)^k(\sigma^2+\mu^2) + \sum_{j=0}^{k-1} (1-\alpha)^j \alpha\mu^2 \\
&= (1-\alpha)^k\sigma^2 + \mu^2,
\end{aligned} \tag{5.15}$$

where we used the independence of $\epsilon_{j\geq n}$ and $F_{S,n}^{\max}$ in the second equality to compute $\mathbb{E}[\epsilon_j F_{S,n}^{\max}] = \mathbb{E}[\epsilon_j] \times \mathbb{E}[F_{S,n}^{\max}]$. Thanks to the second order moment at lag k, we can express the correlation coefficient r_k between two realizations of $F_S^{\max}$ separated by k years as

$$r_k = \frac{\mathbb{E}[F_{S,n}^{\max} F_{S,n+k}^{\max}] - \mu^2}{\sigma^2} = (1-\alpha)^k = \exp\left(-\frac{k\Delta t}{\tau_c}\right), \tag{5.16}$$

where the correlation time τ_c can be identified as

$$\tau_c = -\frac{\Delta t}{\ln\left(1-\frac{\Delta t}{\tau}\right)}. \tag{5.17}$$

Increasing values of τ lead to higher correlation times τ_c. In the limit $\Delta t/\tau \to 0$, we simply obtain $\tau_c = \tau$. We show in Fig. 5.12 three realizations of $F_S^{\max}$ that all exhibit the same

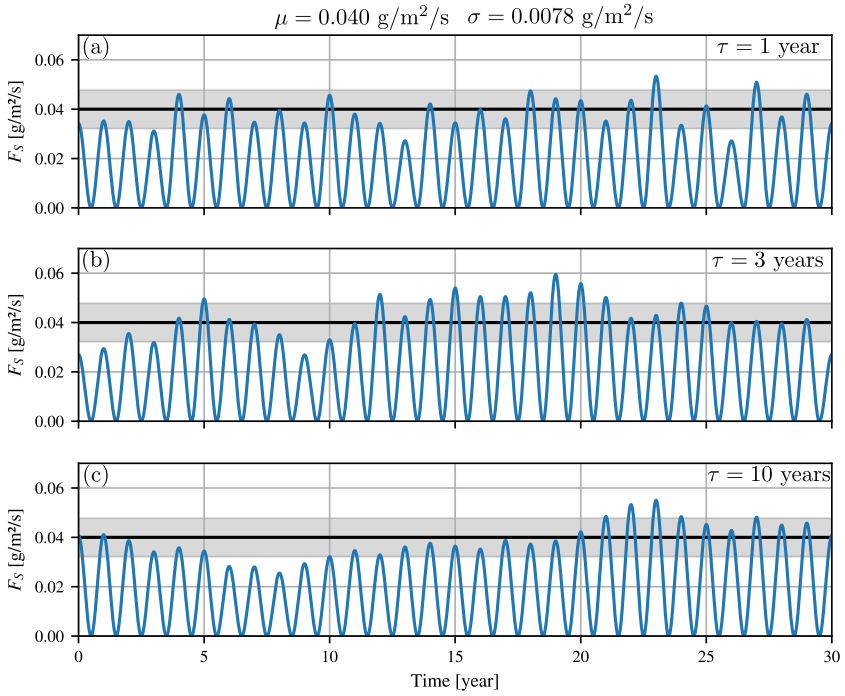

Figure 5.12: Surface forcing time series with $F_S^{\max}$ generated each year from the AR(1) process defined by Eq. (5.11). The three cases have the same stationary Gaussian distribution with mean $\mu = 0.040\,\mathrm{g/m^2/s}$ (black solid line) and standard deviation $\sigma = 0.0078\,\mathrm{g/m^2/s}$ (gray shaded zone) but different characteristic fluctuation time τ: (a) $\tau = 1$ year, corresponding to uncorrelated forcing, (b) $\tau = 3$ years, and (c) $\tau = 10$ years.

stationary probability distribution defined by $\mu = 0.040\,\mathrm{g/m^2/s}$ and $\sigma = 0.0078\,\mathrm{g/m^2/s}$ but have different characteristic times τ ranging from 1 to 10 years. Fig. 5.12(a) corresponds to the limit case $\tau = 1$ for which the realizations of $F_S^{\max}$ are fully uncorrelated ($r_k = \delta_{k,0}$).

Application to cold-to-warm transitions

We now aim to characterize the cold-to-warm transition under stochastic surface forcing. For simplicity, we denote the first cold-to-warm transition time T_1^{ctw} by T_1. Owing to the stochastic nature of the surface forcing scheme, T_1 depends both on the initial state x and the realization of the forcing sequence $(F_{S,t_0}^{\max}, F_{S,t_1}^{\max}, \dots)$. Therefore, we define T_1 such that

$$T_1\left[x, (F_{S,t_0}^{\max}, F_{S,t_1}^{\max}, \dots)\right] = \inf\{t \,|\, m\left[X_t(F_{S,t_0}^{\max}, \dots, F_{S,t}^{\max})\right] \geq a_{\mathrm{ctw}}, X_0 = x\}. \tag{5.18}$$

We will use angled brackets, i.e. $\langle T_1 \rangle$, to denote the expectation of T_1 over both the initial condition x and the forcing sequence $(F_{S,t_0}^{\max}, F_{S,t_1}^{\max}, \dots)$.

We found in Section 5.3.1 that cold-to-warm transitions of 1-year period forced cavities occur when $F_S^{\max} < F_S^{\mathrm{thresh}} \approx 0.040\,\mathrm{g/m^2/s}$. Thus, we use this threshold as reference amplitude when tuning the probability distribution of $F_S^{\max}$. We first investigate the influence of the mean forcing amplitude μ and characteristic timescale τ on the first transition time T_1, for fixed standard deviation σ. The impact of stochastic forcing on T_1 is not straightforward and may either accelerate or delay regime transitions. For example,

when $\mu < F_S^{\text{thresh}}$, a constant forcing equal to the mean value is expected to favor a transition toward the warm state. With the stochastic scheme, occasional years with $F_S^{\max} > F_S^{\text{thresh}}$ may temporarily stabilize the cold mode and thus increase the transition time. Conversely, for $\mu > F_S^{\text{thresh}}$, the mean forcing tends to maintain the cold state and intermittent years with $F_S^{\max} < F_S^{\text{thresh}}$ may instead facilitate the transition and reduce the time required to reach the warm state. As a supplementary effect, the characteristic time τ of the forcing influences how long $F_S^{\max}$ values can be away from the mean of the distribution. As regime transitions occur over several years (see Fig. 5.10), we expect that correlated forcing series favor regime transitions by maintaining the system across the transition threshold over several years.

To test these hypotheses, we build three sets of experiments with μ set to 0.035, 0.040, and $0.0475\,\mathrm{g/m^2/s}$, for fixed $\sigma = 0.0078\,\mathrm{g/m^2/s}$, to capture the response of the system when μ is chosen below, equal or above the transition threshold. We also vary the characteristic timescale $\tau \in \{1, 3, 10\}$ years (the case $\tau = 1$ corresponding to an uncorrelated forcing), such that we have 9 experiments in total. We perform 40 runs for each of the nine chosen forcing pairs (μ, τ), with distinct initial conditions and realizations of surface forcing from Eq. 5.11. A run is stopped when a cold-to-warm transition has occurred ($a_{\text{ctw}} = 15$ m/y) in order to sample the distribution of T_1. We construct a database of plausible ocean conditions by performing 10 to 20 spin-up runs (depending on the duration of the spin-ups) for each forcing pair (μ, τ). These spin-ups are initialized with the equilibrium ocean cold state obtained when $F_S = \mu$ and then evolve under stochastic forcing. We pick from these spin-ups instantaneous states of the ocean during the sequence of winter extrema to constitute a database of plausible ocean states conditioned on $F_S^{\max}$ that we will use to initialize our main runs. More specifically, initial ocean conditions are drawn from the database associated to the couple (μ, τ) and are conditioned on the first realization of $F_S^{\max}$. For example, if the first $F_S^{\max}$ value of a run is $0.047\,\mathrm{g/m^2/s}$, the initial ocean state is drawn from ocean states obtained when subject to $F_S^{\max} \in [0.044, 0.048]\,\mathrm{g/m^2/s}$. Fig. 5.13 shows the basal melt rates realizations (black curves) of simulations obtained with $\mu = 0.035\,\mathrm{g/m^2/s}$ (120 simulations in total). The histograms for T_1 are superimposed on the realizations and the expectation $\langle T_1 \rangle$ is shown by a vertical colored lines in each panel (different τ values). Fig. 5.14 and Fig. 5.15 show the same results but using $\mu = 0.04\,\mathrm{g/m^2/s}$ and $\mu = 0.0475\,\mathrm{g/m^2/s}$, respectively. Note that in the latter case, the subset obtained with $\tau = 1$ year is not displayed as the ocean state rarely transitions toward the warm mode within 100 years based on spin-up simulations and thus was abandoned to save computational cost.

In the following, we gain insights on how often the transition threshold is crossed by considering the probability to obtain a surface forcing value inferior to the cold-to-warm transition

$$\mathbb{P}(F_S^{\max} \leq F_S^{\text{thresh}}) = \frac{1}{2}\left[1 + \operatorname{erf}\left(\frac{F_S^{\text{thresh}} - \mu}{\sqrt{2}\sigma}\right)\right]. \tag{5.19}$$

For $\mu = 0.0350\,\mathrm{g/m^2/s} < F_S^{\text{thresh}}$, this probability is equal to 0.74. Therefore, we should observe very fast transitions. Fig. 5.13 shows that the maximum likelihood of the distribution of T_1 is obtained before 2 years. The expectation of T_1 decreases for higher values of τ (see Fig. 5.16). As the initial realization of $F_S^{\max}$ has 74% chances to be unfavorable to the cold regime, a correlated forcing tends to maintain this initial unfavorable condition in contrast to uncorrelated forcing. That being said, we note that some runs (e.g,

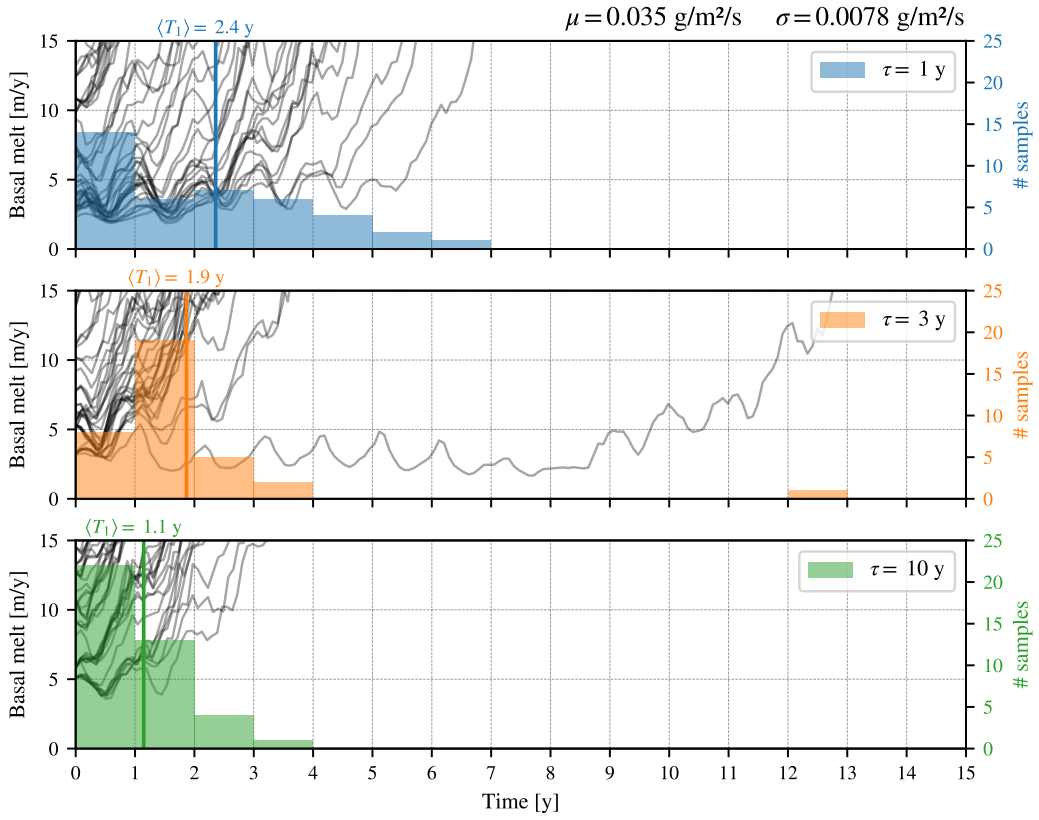

Figure 5.13: Basal melt rates trajectory (black curves) for 40 realizations of surface forcing based on the stochastic AR(1) process (Eq. (5.11)) with mean $\mu = 0.035\,\mathrm{g/m^2/s}$, standard deviation $\sigma = 0.0078\,\mathrm{g/m^2/s}$ and characteristic times $\tau = 1$ year (blue; top panel) corresponding to an uncorrelated forcing, $\tau = 3$ years (orange; middle) and $\tau = 10$ years (green; bottom). The sampled distributions of T_1 (colored histograms) are superimposed on the melt rate realizations (40 for each panel). A value of T_1 is obtained when a the basal melt trajectory crosses the threshold 15 m/y and exits the represented range of basal melt rates. The mean value of T_1 is represented by a vertical line in each panel.

for $\tau = 3$ years) show rare realizations for which the cold state can be maintained over 12 years.

When $\mu = 0.040\,\mathrm{g/m^2/s} = F_S^{\mathrm{thresh}}$, F_S^{max} values are equally distributed below and above the transition threshold. Fig. 5.14 shows that the maximum likelihood of the transition is still obtained at relatively short times (< 6 years). However, more runs exhibit longer T_1 values, especially for the simulations with correlated forcing. This effect is visible in the mean values of T_1, which are larger for increasing values of τ (see Fig. 5.16(b)). Correlated experiments also exhibit larger uncertainty for $\langle T_1 \rangle$, such that it is difficult to conclude whether it converges or not toward a finite value as τ is increasing. This increase of the uncertainty is due to the fact that while the weight of the distribution is strongly concentrated at small T_1, some rare realizations subsist at long time and deviate significantly from the mean value of T_1.

Finally for $\mu = 0.0475\,\mathrm{g/m^2/s} > F_S^{\mathrm{thresh}}$, the transition threshold is crossed only with probability 0.17 each year (which corresponds to a time return of 6 years). Thus, this case represents an interesting configuration to assess the possibility of cold-to-warm

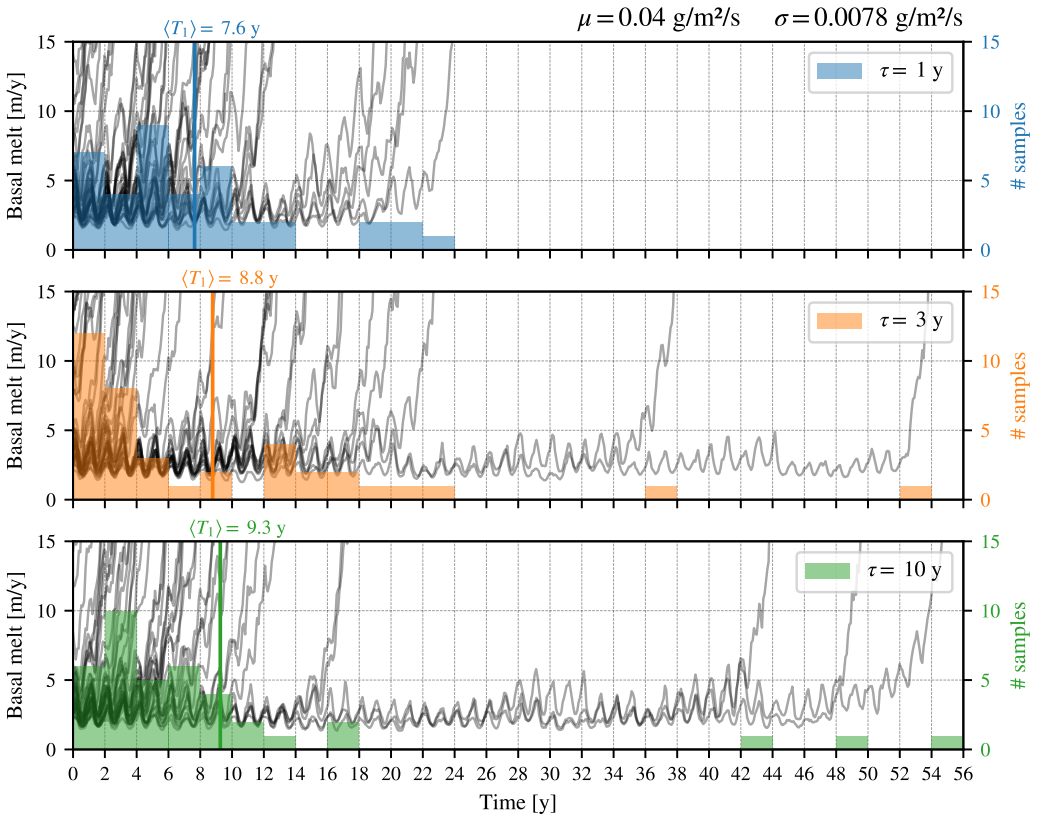

Figure 5.14: Same as Fig. 5.13 but for $\mu = 0.040\,\mathrm{g/m^2/s}$. Note the change of scale for the time axis.

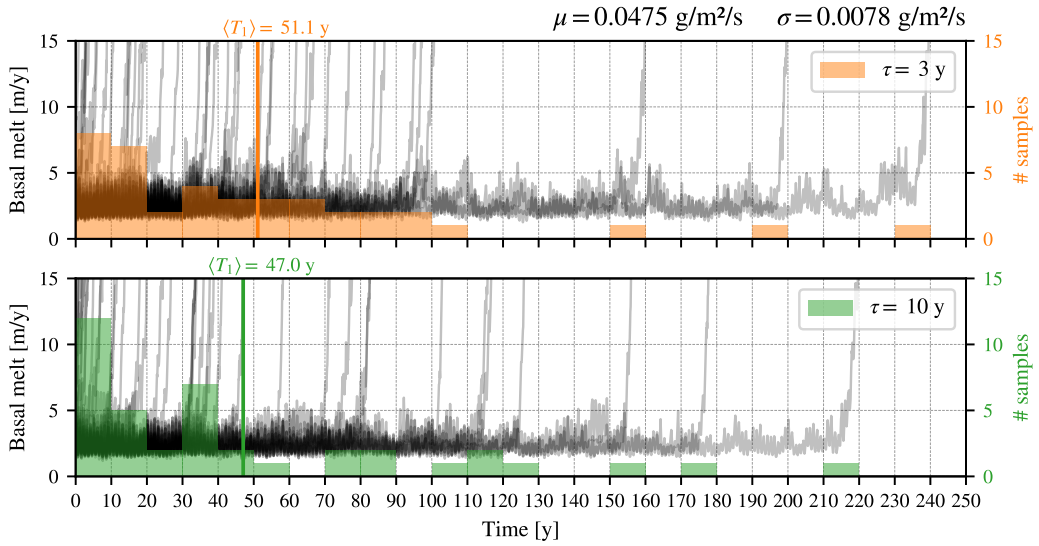

Figure 5.15: Same as Fig. 5.13 but for $\mu = 0.0475\,\mathrm{g/m^2/s}$. Note the change of scale for the time axis. The case $\tau = 1$ year is not displayed because it would have required very long simulations and thus come with a high computational cost.

transitions when the average forcing state remains in cold stable conditions. For this case, uncorrelated and correlated forcing simulations show very different behaviors. In fact, the uncorrelated forced simulations transition after much longer time than correlated simulations, such that we have not been able to sample the distribution of T_1 for $\tau = 1$ year. Approximately 3/4 of the spin-ups did not transition to warm conditions after 100 years for $\tau = 1$ years, while this ratio was 1/10 for $\tau = 3$ year and 1/6 for $\tau = 10$ years. This result highlights that surface forcing correlated on interannual timescales induce faster regime transitions, even when their mean amplitude tends to maintain the initial state. Once again, Fig. 5.15 shows that the T_1 distribution is concentrated at short times (here half of the realizations of T_1 are inferior to 30 years in correlated cases), but rare realizations ($T_1 > 150$ years) spread the distribution. The uncertainty for the mean of T_1 for $\tau = 3$ years and $\tau = 10$ years is thus too high to conclude on the quantitative impact of the correlation time (see Fig. 5.16(c)).

Fig. 5.17 summarizes the results obtained in the last section regarding our investigation of the impact of the amplitude of the surface forcing $F_S^{\max}$ for seasonal variations on cold-to-warm transitions. The results highlight that regardless of the mean value μ of the $F_S^{\max}$ distribution, the average transition time is always lower than the deterministic T_1 value. Thus, we conclude that stochastic forcing favors on average cold-to-warm regime transitions. This observation becomes all the more true for $\mu > F_S^{\mathrm{thresh}}$, as correlated forced simulations drastically decrease the average transition time in comparison to deterministic and uncorrelated forced simulations.

5.4 Conclusion

The dynamical response of an ice-shelf cavity to a time-dependent forcing was investigated in this chapter. We first investigated the adjustments processes occurring in the system

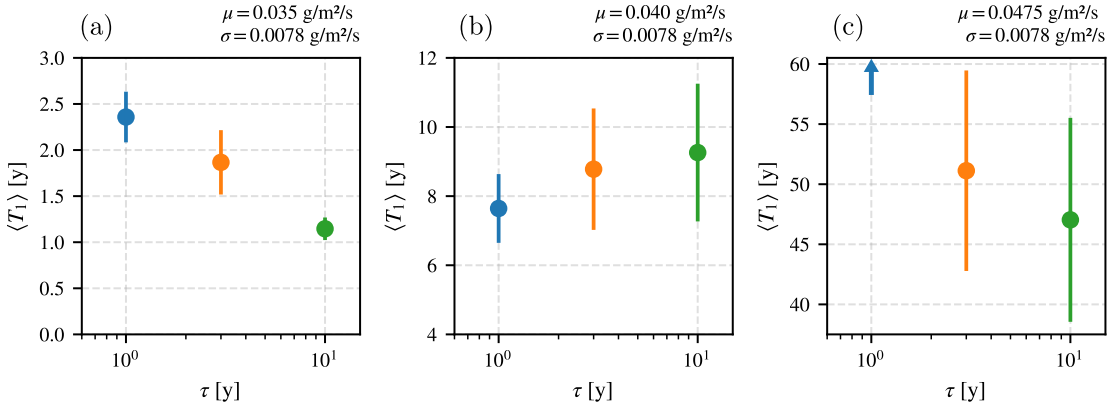

Figure 5.16: Mean first transition time T_1 (defined in Eq. (5.9)) as a function of the characteristic time τ of the $F_S^{\max}$ stochastic process. The dots represent the empirical mean of T_1 while the vertical bars show the associated incertitude, which we obtained by dividing the empirical standard deviation of each distribution by the number of realizations performed. The blue upward arrow in panel (c) indicates that the $\tau = 1$ year case has such a large $\langle T_1 \rangle$ value that we were not able to capture it.

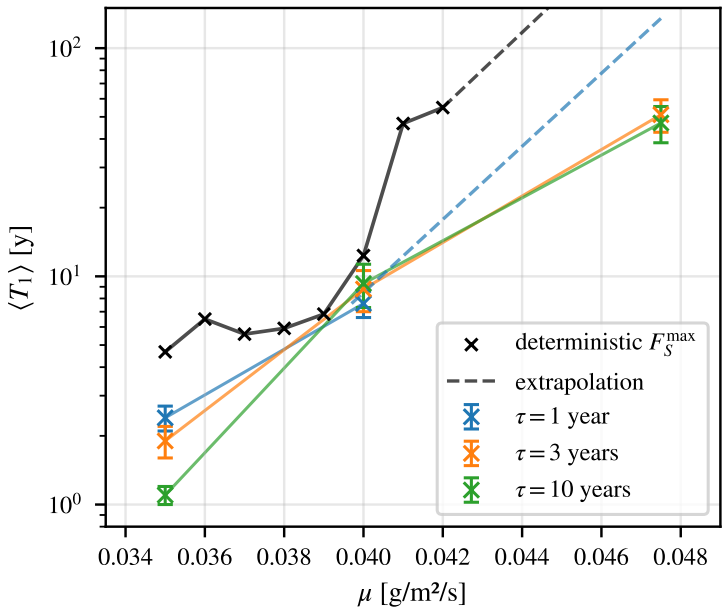

Figure 5.17: Summary of the results obtained when varying the amplitude of the periodic forcing (Eq. (5.7)) on seasonal time scales for cold-to-warm transitions. Black crosses show the first transition time T_1 of deterministic simulations as function of $F_S^{\max}$, which is set constant in each simulation. The colored crosses show the average first transition times $\langle T_1 \rangle$ of stochastic simulations as a function of μ, the mean value of the $F_S^{\max}$ probability distribution, for $\tau = 1$ year (blue), $\tau = 3$ years (orange) and $\tau = 10$ years (green). Dashed lines are arbitrary extrapolations to underline that T_1 values increase abruptly and are unknown at high values of μ.

when implementing periodic forcing. We evaluated the ability of low-dimensional box models to reproduce results from a previous ocean GCM study that evaluated the impact of temporally oscillating intruding water properties [Holland, 2017]. The low-dimensional model showed surprisingly good qualitative agreement with GCM simulations, exhibiting for example asymmetric cold-to-warm and warm-to-cold transition times due to the different overturning strengths values in cold and warm modes. However, it failed to capture the response to fast oscillating forcing, probably due to the lack of physical processes at the ice-ocean interface that may add inertia to the system. To take into account the dynamics of the thermocline, we then used the numerical NEMO configuration presented in Chapter 3. We designed numerical experiments complementary to [Holland, 2017], i.e., setting constant far field ocean properties, but varying periodically in time the surface salt flux. We tested the impact of the forcing period at constant surface salt forcing amplitude, in such a way that we spanned bistable and monostable cold and warm forcing regions that we identified in Chapter 3 with quasi-static experiments. For low forcing frequencies, the ice-shelf cavity had enough time to adapt to the surface forcing conditions, resulting in dynamical hysteresis. The system oscillated in phase with the surface forcing between the warm and the cold modes, regardless of the initial ocean state. However, for high frequencies, the circulation regime depended on the initial state of the ocean. We showed that the cutoff timescale that differentiates these two regimes (about 4 to 8 years) was linked to the thermocline dynamics. For larger forcing periods, the thermocline reached and lifted periodically from the bottom of the ocean, allowing oscillations between cold and warm modes. For lower forcing periods, the thermocline either stayed at mid-depth for warm initialized simulations, or at the bottom of the ocean for cold initialized simulations. The system thus kept a memory of the initial conditions and did not transition toward another regime. The flushing time of the cavity was evaluated at about 8 months to 3 years and delayed the intrusion of CDW into the cavity, but was not the limiting timescale for the regime transitions.

We then set the forcing period to one year to mimic a seasonal cycle of sea-ice production and characterized the response of the ice-shelf to a more realistic forcing. The minimal values of sea-ice production was set to $0\,\mathrm{g/m^2/s}$ during summer and we tested the impact of the maximal winter value $F_S^{\max}$. For $T = 1$ year, the forcing was too fast to allow for regime oscillations. Thus, transitions were irreversible when they occurred. Cold-to-warm transitions were obtained for $F_S^{\max} \lesssim 0.040\,\mathrm{g/m^2/s}$, whereas warm-to-cold transition were obtained for $F_S^{\max} > 0.065\,\mathrm{g/m^2/s}$. Thus, both warm and cold stable periodic responses could be reached between these two forcing values, which can be interpreted as dynamical bistability. The bounds of the bistable range, when taken in terms of mean forcing values $\langle F_S \rangle_t$ instead of amplitude value $F_S^{\max}$, were close to the steady-state bounds obtained in the previous chapter.

Finally, we continued the investigation of the impact of $F_S^{\max}$ on the transition, but drawing $F_S^{\max}$ from random distributions, to assess the impact of multiannual winter variability on the cavity circulation regimes. We used Gaussian distributions with various means for fixed standard deviation. We reported that stochastic forcing favors on average cold-to-warm regime transitions as their averaged first transition time was always shorter than obtained with deterministic forcing. We also tested the impact of temporal correlations in $F_S^{\max}$ and showed that more strongly correlated forcing time series induced much faster cold-to-warm transitions, particularly when the mean forcing favored the cold

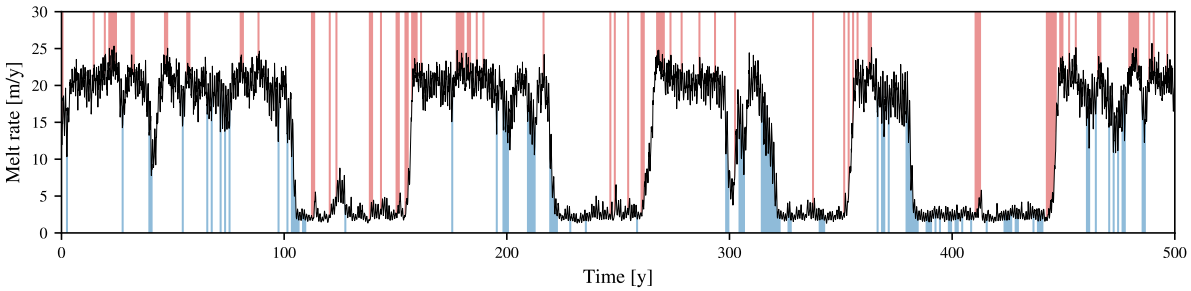

Figure 5.18: Spatially averaged basal melt rates (displayed at monthly resolution) from a 500-year simulation in which $F_S^{\max}$ follows a first-order auto-regressive process (see Eq. (5.11)) with parameters $\tau = 3$ y, $\mu = 0.0525$ g/m^2/s and $\sigma = 0.015$ g/m^2/s. With these parameters, the probability that $F_S^{\max}$ exceeds the warm-to-cold threshold or falls below the cold-to-warm threshold is 0.2 each year. Periods during which these thresholds are crossed are shown in blue and red, respectively.

regime. This could be due to the preconditioning of the ocean conditions over several years before the transition when using correlated surface forcing.

As a perspective, it would be interesting to investigate the long-term dynamics of a bistable ice-shelf cavity, rather than focusing solely on the first transition time, under continuously varying stochastic forcing. Long integrations such as the one shown in Fig. 5.18 reveal successive spontaneous switches between the warm and cold circulation regimes. This raises several questions regarding the statistical properties of these transitions, such as the distribution of residence times in each regime. Such an analysis would provide a more complete characterization of the stochastic dynamics of bistable ice-shelf cavities and could provide insight into the mechanisms underlying longer term variability in ocean circulation beneath Antarctic ice shelves.

Take-home messages

1. The response of a bistable ice-shelf cavity to time-dependent surface forcing depends on the adjustment timescales of the thermocline and overturning circulation. Fast forcing is damped whereas slower forcing can trigger regime transitions.

2. The thermocline dynamics adjusts faster than the cavity circulation and basal melt rates, suggesting it is the primary process controlling regime transitions.

3. Seasonal variability slightly modifies the bistable forcing range compared with steady forcing, supporting the use of annually averaged forcing to track the ice-shelf stability regimes on interannual scales.

4. Interannual stochastic variability strongly affects mean first transition times. Temporally correlated forcing promote faster regime transitions than uncorrelated fluctuations by preconditioning the ocean circulation over several years.

Conclusion

The future contribution of the Antarctic Ice Sheet to global sea-level rise depends critically on the stability of its floating extensions, the ice shelves. Because ocean-driven basal melting controls the weakening of these ice shelves, understanding the mechanisms governing ocean circulation within ice-shelf cavities has become a major challenge to better constrain sea level rise projections.

Throughout this thesis, we investigated whether Antarctic ice-shelf cavities can undergo tipping behaviour under variations in the forcing exerted by coastal polynyas, the sea-ice-free regions located at the front of many Antarctic ice shelves. In particular, we examined whether currently cold cavities could transition abruptly and irreversibly toward a warm state. Such a transition would substantially increase basal melt rates, weaken ice-shelf buttressing, and ultimately enhance the Antarctic contribution to sea-level rise.

To address this question, we deliberately adopted models with lower complexity than the realistic regional and pan-Antarctic simulations used in previous studies (e.g. [Hellmer et al., 2012, Hazel and Stewart, 2020, Caillet et al., 2023, Haid et al., 2023, Mathiot and Jourdain, 2023], among many others). Rather than reproducing a specific ice-shelf cavity as accurately as possible, our models were designed to systematically characterize the response of ice-shelf cavities to variations in coastal-polynya forcing. This approach enabled us to isolate the physical feedbacks that either promote or inhibit irreversible transitions and, in particular, to determine under which conditions bistable circulation regimes can emerge. We focused on the steady-state response of ice-shelf cavities to constant forcing (Chapters 2 and 3), as well as their dynamical response to periodic and stochastic forcing (Chapter 5).

A first approach consisted of a low-dimensional box model coupling an ice-shelf cavity to the adjacent continental shelf. Building upon previous conceptual models of ice-shelf cavities [Olbers and Hellmer, 2010, Reese et al., 2018] and front-ice-shelf dynamics [Hazel and Stewart, 2020, Moorman et al., 2023], the model was designed as a generic framework wherein observations of ice-shelf geometry, CDW properties [Burgard et al., 2022], and coastal-polynya characteristics [Nakata et al., 2021] could be easily incorporated as forcing parameters.

A second approach consisted of an idealized three-dimensional numerical configuration based on the ocean general circulation model NEMO and inspired by the ISOMIP+ framework [Asay-Davis et al., 2016, **?**]. Although the geometry and forcing were deliberately simplified, this configuration retained most of the relevant ocean dynamics and therefore provided a suitable framework to investigated the physical mechanisms identified by the

conceptual model.

While addressing the same principal question "Can sea-ice production in coastal polynyas promote a bistable ocean circulation in Antarctic ice-shelf cavities?", these two modelling approaches provided complementary insights, and answered different aspects of the problem. The low-dimensional model made it possible to explore a large parameter space and construct stability diagrams describing the response of real Antarctic ice shelves under different environmental conditions. Using these diagrams, we found that all presently cold cavities considered in this study lied within bistable regions, suggesting that they could be susceptible to irreversible cold-to-warm transitions. The three-dimensional numerical model, in contrast, resolved processes absent from the conceptual model and revealed the important role played by thermocline dynamics and large-scale eddies at the ice-shelf front in controlling the intrusion of different water masses into the cavity.

Both models identified the meltwater feedback generated beneath the ice shelf as the principal mechanism promoting bistability. In both cases, enhanced basal melting strengthened the surface stratification at the ice-shelf front, thereby reducing Dense Shelf Water formation at the sea surface and favoring further intrusions of warm Circumpolar Deep Waters. However, the two approaches provided different perspectives on the processes capable of mitigating this positive feedback. Within the box model, the dependence of vertical mixing on the density stratification emerged, by construction, as the primary control on the reversibility of regime transitions. In the three-dimensional numerical model, the impact of vertical mixing could not alone explain reversible transitions. The reversibility also appeared to depend on processes such as the development of an ocean gyre at the ice-shelf front, the density stratification of offshore waters, and the model viscosity. These findings may help explain why previous realistic simulations have reached contrasting conclusions regarding the reversibility of regime transitions in Antarctic ice-shelf cavities [**?**, Hazel and Stewart, 2020].

The development of the numerical configuration also required careful evaluation of the numerical schemes and parameterizations in order to minimize spurious numerical artifacts. This led to the implementation of biharmonic diffusivity to suppress grid-scale numerical noise. Furthermore, investigating the influence of vertical resolution on basal melting revealed the presence of topographic Rossby waves at intermediate resolutions, which modified the spatial distribution of basal melting beneath the ice shelf.

Finally, we extended the numerical experiments to time-dependent forcing to consider the temporal variability of coastal-polynya activity, on seasonal timescales in particular. We investigated the response of bistable ice-shelf cavities to variations in both the amplitude and the period of the forcing. When the forcing varied more rapidly than the thermocline adjustment timescale, the system remained dependent on its initial state, reflecting its underlying bistability. Conversely, for slower forcing, the cavity periodically transitioned between cold and warm circulation regimes. Interestingly, under seasonal forcing, the annual-mean transition thresholds were found to be remarkably close to those obtained from steady-state simulations. This result supports the use of annually averaged forcing parameters to assess the long-term stability of Antarctic ice shelves, as we previously did in the context of the box model. Finally, inspired by the interannual variability of winter sea-ice production, we investigated the impact of correlated-in-time variable forcing using a stochastic scheme. We found that the temporal correlation substantially reduced the time required for cold cavities to transition toward the warm regime, emphasizing that

climate variability may trigger regime transitions faster than expected.

Future prospects

A natural extension of this work would be to turn to more realistic model configurations to test whether processes identified here remain important for determining the reversibility of the transitions. The standardized MISOMIP2 framework [De Rydt et al., 2024] for the Amundsen Sea and Filchner-Ronne ice shelves could provide a good starting point for increasing the realism of our numerical experiments. This framework also makes it possible to account for several processes that were neglected in this thesis. First, the continental shelf break plays a fundamental role in controlling the intrusion of Circumpolar Deep Water onto the continental shelf. Both positive and negative feedbacks affecting the heat transport have been linked to the shelf break and the Antarctic Slope Current [Si et al., 2023, Thompson et al., 2018]. Including this region of the ocean would therefore improve our understanding of how heat reaches ice-shelf cavities. More specifically, determining whether these feedbacks have a stabilizing or destabilizing influence on the cavity circulation would help assess their impact on the extent of the bistable regime. Second, another direction could be to include ice-sheet dynamics, that would be a major change leading to greater level of realism. An evolving ice sheet may indeed modify the ocean circulation through changes in cavity geometry and bathymetry [De Rydt and Naughten, 2024], potentially affecting the meltwater feedback in ice-shelf cavities.

A broad consensus has now emerged across the hierarchy of climate models that Antarctic ice-shelf cavities can undergo abrupt transitions from cold to warm circulation states. Beyond the questions of bistability and the reversibility of these transitions, a key remaining challenge is to understand their predictability, which is essential for better constraining future climate projections. Within the framework of bifurcation-induced tipping points, dynamical systems theory predicts that Early Warning Signals (EWS) should precede bifurcations-induced tipping points because of the critical slowdown of the system [Scheffer et al., 2009]. As a system approaches a saddle-node bifurcation, its recovery from perturbations becomes progressively slower, leading to increases in both variance and autocorrelation. In the context of our quasi-static numerical experiments, we observed enhanced variability of the thermocline depth prior to both cold-to-warm and warm-to-cold transitions (see Fig. 3.7(a,b) in Chapter 3), which could be interpreted as an EWS. However, we did not investigate this direction further by performing a detailed temporal analysis of the thermocline-depth signal to quantitatively assess its predictive skill. Several interesting questions therefore remain open. For instance, does this EWS exhibit the same signature for reversible and irreversible transitions? If not, it could also provide an indicator of irreversibility. Another important question concerns its spatial distribution: where is the EWS strongest? Answering this question could help determine the optimal locations for deploying oceanographic moorings. For example, our simulations revealed a pronounced asymmetry in thermocline variability between the eastern and western sides of the ice-shelf front for some configurations. To move closer to realistic conditions, seasonal and interannual variability in sea-ice production could also be included to assess whether such EWS remains robust under more realistic forcing.

Finally, another research direction emerging from this thesis concerns the role that to-

pographic Rossby waves highlighted in Chapter 4 may play. Although this phenomenon does not appear to be directly related to regime transitions, it is nevertheless of interest because of its influence on the spatial redistribution of basal melt beneath the ice shelf. Our simulations suggest that these waves reduce basal melt rates near the grounding line–where the impact on ice-sheet dynamics is expected to be greatest–while increasing melt rates in the center of the cavity. Since topographic Rossby waves have not yet been investigated in ice-shelf cavities, many research avenues remain open. First, the mechanism responsible for their generation is still not understood, although they may be primarily excited by instabilities within the boundary layer at the ice-ocean interface. A question could be whether these waves need an ice interface to develop. If so, this would provide an interesting fundamental problem involving a tilted boundary layer that generates buoyancy fluxes while interacting dynamically with the underlying ocean circulation. On the one hand, simplified theoretical frameworks, such as quasi-geostrophic models including surface buoyancy forcing (surface quasi-geostrophic models [Lapeyre, 2017]) could provide a valuable starting point for investigating these processes. On the other hand, increasing the realism of our numerical simulations would make it possible to assess if such wave patterns can develop in real ice-shelf cavities.

Bibliography

[Abram et al., 2025] Abram, N. J., Purich, A., England, M. H., McCormack, F. S., Strugnell, J. M., Bergstrom, D. M., Vance, T. R., Stål, T., Wienecke, B., Heil, P., Doddridge, E. W., Sallée, J.-B., Williams, T. J., Reading, A. M., Mackintosh, A., Reese, R., Winkelmann, R., Klose, A. K., Boyd, P. W., Chown, S. L., and Robinson, S. A. (2025). Emerging evidence of abrupt changes in the Antarctic environment. *Nature*, 644(8077):621–633.

[Armstrong McKay et al., 2022] Armstrong McKay, D. I., Staal, A., Abrams, J. F., Winkelmann, R., Sakschewski, B., Loriani, S., Fetzer, I., Cornell, S. E., Rockström, J., and Lenton, T. M. (2022). Exceeding 1.5°C global warming could trigger multiple climate tipping points. *Science*, 377(6611):eabn7950.

[Asay-Davis et al., 2016] Asay-Davis, X. S., Cornford, S. L., Durand, G., Galton-Fenzi, B. K., Gladstone, R. M., Gudmundsson, G. H., Hattermann, T., Holland, D. M., Holland, D., Holland, P. R., Martin, D. F., Mathiot, P., Pattyn, F., and Seroussi, H. (2016). Experimental design for three interrelated marine ice sheet and ocean model intercomparison projects: MISMIP v. 3 (MISMIP +), ISOMIP v. 2 (ISOMIP +) and MISOMIP v. 1 (MISOMIP1). *Geoscientific Model Development*, 9(7):2471–2497.

[Bennetts et al., 2024] Bennetts, L. G., Shakespeare, C. J., Vreugdenhil, C. A., Foppert, A., Gayen, B., Meyer, A., Morrison, A. K., Padman, L., Phillips, H. E., Stevens, C. L., Toffoli, A., Constantinou, N. C., Cusack, J. M., Cyriac, A., Doddridge, E. W., England, M. H., Evans, D. G., Heil, P., Hogg, A. M., Holmes, R. M., Huneke, W. G. C., Jones, N. L., Keating, S. R., Kiss, A. E., Kraitzman, N., Malyarenko, A., McConnochie, C. D., Meucci, A., Montiel, F., Neme, J., Nikurashin, M., Patel, R. S., Peng, J.-P., Rayson, M., Rosevear, M. G., Sohail, T., Spence, P., and Stanley, G. J. (2024). Closing the Loops on Southern Ocean Dynamics: From the Circumpolar Current to Ice Shelves and From Bottom Mixing to Surface Waves. *Reviews of Geophysics*, 62(3):e2022RG000781.

[Bett et al., 2026] Bett, D. T., Bradley, A. T., Miles, B. W. J., Williams, C. R., Holland, P. R., and Arthern, R. J. (2026). Modelling the evolution of Thwaites Glacier over the 20th century. *EGUsphere*, pages 1–43.

[Beylat et al., 2024] Beylat, S., Coquereau, A., Priol, C., Marino, T., and Saddier, L. (2024). La science des points de bascule. *La Météorologie*.

[Bradley et al., 2022] Bradley, A. T., Bett, D. T., Dutrieux, P., De Rydt, J., and Holland, P. R. (2022). The Influence of Pine Island Ice Shelf Calving on Basal Melting. *Journal of Geophysical Research: Oceans*, 127(9):e2022JC018621.

[Bretherton and Blossey, 2017] Bretherton, C. S. and Blossey, P. N. (2017). Understanding Mesoscale Aggregation of Shallow Cumulus Convection Using Large-Eddy Simulation. *Journal of Advances in Modeling Earth Systems*, 9(8):2798–2821.

[Burgard et al., 2022] Burgard, C., Jourdain, N. C., Reese, R., Jenkins, A., and Mathiot, P. (2022). An assessment of basal melt parameterisations for Antarctic ice shelves. *The Cryosphere*, 16(12):4931–4975.

[Caillet et al., 2023] Caillet, J., Jourdain, N. C., Mathiot, P., Hellmer, H. H., and Mouginot, J. (2023). Drivers and Reversibility of Abrupt Ocean State Transitions in the Amundsen Sea, Antarctica. *Journal of Geophysical Research: Oceans*, 128(1):e2022JC018929.

[Campagne et al., 2015] Campagne, P., Crosta, X., Houssais, M. N., Swingedouw, D., Schmidt, S., Martin, A., Devred, E., Capo, S., Marieu, V., Closset, I., and Massé, G. (2015). Glacial ice and atmospheric forcing on the Mertz Glacier Polynya over the past 250 years. *Nature Communications*, 6(1):6642.

[Cessi, 1994] Cessi, P. (1994). A Simple Box Model of Stochastically Forced Thermohaline Flow. *Journal of Physical Oceanography*, 24(9):1911–1920.

[Cessi et al., 1990] Cessi, P., Condie, R., and Young, W. (1990). Dissipative dynamics of western boundary currents. *Journal of Marine Research*, 48(4).

[Cessi and Young, 1992] Cessi, P. and Young, W. R. (1992). Multiple equilibria in two-dimensional thermohaline circulation. *Journal of Fluid Mechanics*, 241:291–309.

[Cimatoribus et al., 2014] Cimatoribus, A. A., Drijfhout, S. S., and Dijkstra, H. A. (2014). Meridional overturning circulation: Stability and ocean feedbacks in a box model. *Climate Dynamics*, 42(1):311–328.

[Collin et al., 2026] Collin, B., Couston, L.-A., Joubaud, S., and Volk, R. (2026). Ice melting in saltwater: Formation of a stratified system in laboratory experiments. *European Journal of Mechanics - B/Fluids*, 119:204518.

[Couston, 2024] Couston, L.-A. (2024). Turbulent Ice–Ocean Boundary Layers in the Well-Mixed Regime: Insights from Direct Numerical Simulations. *Journal of Physical Oceanography*, 54(8):1705–1717.

[Daae et al., 2020] Daae, K., Hattermann, T., Darelius, E., Mueller, R. D., Naughten, K. A., Timmermann, R., and Hellmer, H. H. (2020). Necessary Conditions for Warm Inflow Toward the Filchner Ice Shelf, Weddell Sea. *Geophysical Research Letters*, 47(22):e2020GL089237.

[De Rydt et al., 2024] De Rydt, J., Jourdain, N. C., Nakayama, Y., van Caspel, M., Timmermann, R., Mathiot, P., Asay-Davis, X. S., Seroussi, H., Dutrieux, P., Galton-Fenzi, B., Holland, D., and Reese, R. (2024). Experimental design for the Marine Ice Sheet–Ocean Model Intercomparison Project – phase 2 (MISOMIP2). *Geoscientific Model Development*, 17(18):7105–7139.

[De Rydt and Naughten, 2024] De Rydt, J. and Naughten, K. (2024). Geometric amplification and suppression of ice-shelf basal melt in West Antarctica. *The Cryosphere*, 18(4):1863–1888.

[Dijkstra, 2013] Dijkstra, H. A. (2013). *Nonlinear Climate Dynamics*. Cambridge University Press.

[Dinniman et al., 2016] Dinniman, M. S., Asay-Davis, X. S., Galton-Fenzi, B. K., Holland, P. R., Jenkins, A., and Timmermann, R. (2016). Modeling Ice Shelf/Ocean Interaction in Antarctica: A REVIEW. *Oceanography*, 29(4):144–153.

[Donohue et al., 2016] Donohue, K. A., Tracey, K. L., Watts, D. R., Chidichimo, M. P., and Chereskin, T. K. (2016). Mean Antarctic Circumpolar Current transport measured in Drake Passage. *Geophysical Research Letters*, 43(22):11,760–11,767.

[Eyring et al., 2021] Eyring, V., Gillett, N. P., Achutarao, K. M., Barimalala, R., Barreiro Parrillo, M., Bellouin, N., Cassou, C., Durack, P. J., Kosaka, Y., McGregor, S., Min, S.-K., Morgenstern, O., and Sun, Y. (2021). Human influence on the climate system. In Masson-Delmotte, V., Zhai, P., Pirani, A., Connors, S. L., Péan, C., Berger, S., Caud, N., Chen, Y., Goldfarb, L., Gomis, M. I., Huang, M., Leitzell, K., Lonnoy, E., Matthews, J. B. R., Maycock, T. K., Waterfield, T., Yelekci, O., Yu, R., and Zhou, B., editors, *Climate Change 2021: The Physical Science Basis. Contribution of Working Group I to the Sixth Assessment Report of the Intergovernmental Panel on Climate Change*, pages 423–552. Cambridge University Press, Cambridge, United Kingdom and New York, NY, USA.

[Favier et al., 2014] Favier, L., Durand, G., Cornford, S. L., Gudmundsson, G. H., Gagliardini, O., Gillet-Chaulet, F., Zwinger, T., Payne, A. J., and Le Brocq, A. M. (2014). Retreat of Pine Island Glacier controlled by marine ice-sheet instability. *Nature Climate Change*, 4(2):117–121.

[Feldmann and Levermann, 2015] Feldmann, J. and Levermann, A. (2015). Collapse of the West Antarctic Ice Sheet after local destabilization of the Amundsen Basin. *Proceedings of the National Academy of Sciences*, 112(46):14191–14196.

[Finucane and Stewart, 2026] Finucane, G. and Stewart, A. (2026). A Theory of Meltwater- Versus Polynya -Dominated Ice Shelf Cavities. *ESS Open Archive*.

[Finucane and Stewart, 2024] Finucane, G. and Stewart, A. L. (2024). A Predictive Theory for Heat Transport Into Ice Shelf Cavities. *Geophysical Research Letters*, 51(10):e2024GL108196.

[Fowler and Ng, 2020] Fowler, A. and Ng, F. (2020). *Glaciers and Ice Sheets in the Climate System: The Karthaus Summer School Lecture Notes*. Springer Nature.

[Fox-Kemper et al., 2021] Fox-Kemper, B., Hewitt, H. T., Xiao, C., Aðalgeirsdóttir, G., Drijfhout, S. S., Edwards, T. L., Golledge, N. R., Hemer, M., Kopp, R. E., Krinner, G., Mix, A., Notz, D., Nowicki, S., Nurhati, I. S., Ruiz, L., Sallée, J.-B., Slangen, A. B. A., and Yu, Y. (2021). Ocean, cryosphere, and sea level change. In Masson-Delmotte, V., Zhai, P., Pirani, A., Connors, S. L., Péan, C., Berger, S., Caud, N., Chen, Y., Goldfarb, L., Gomis, M. I., Huang, M., Leitzell, K., Lonnoy, E., Matthews, J. B. R., Maycock, T. K., Waterfield, T., Yelekçi, O., Yu, R., and Zhou, B., editors, *Climate Change 2021: The Physical Science Basis. Contribution of Working Group I to the Sixth Assessment Report of the Intergovernmental Panel on Climate Change*, pages 1211–1362. Cambridge University Press, Cambridge, United Kingdom and New York, NY, USA.

[Galton-Fenzi et al., 2025] Galton-Fenzi, B. K., Fricker, H. A., Bassis, J. N., Crawford, A. J., Gomez, N., and Schoof, C. (2025). The Antarctic Ice Sheet and Sea Level: Contemporary Changes and Future Projections. In *Antarctica and the Earth System*. Routledge.

[Garbe et al., 2020] Garbe, J., Albrecht, T., Levermann, A., Donges, J. F., and Winkelmann, R. (2020). The hysteresis of the Antarctic Ice Sheet. *Nature*, 585(7826):538–544.

[Garreau, 2021] Garreau, P. (2021). Modélisations, Observations : Contribution à la dynamique fine échelle de la Méditerranée Nord-Occidentale.

[Georgiou et al., 2019] Georgiou, S., van der Boog, C. G., Brüggemann, N., Ypma, S. L., Pietrzak, J. D., and Katsman, C. A. (2019). On the interplay between downwelling, deep convection and mesoscale eddies in the Labrador Sea. *Ocean Modelling*, 135:56–70.

[Giordani et al., 2020] Giordani, H., Bourdallé-Badie, R., and Madec, G. (2020). An Eddy-Diffusivity Mass-Flux Parameterization for Modeling Oceanic Convection. *Journal of Advances in Modeling Earth Systems*, 12(9):e2020MS002078.

[Golledge et al., 2025] Golledge, N. R., Keller, E. D., Gossart, A., Malyarenko, A., Bahamondes-Dominguez, A., Krapp, M., Jendersie, S., Lowry, D. P., Alevropoulos-Borrill, A., and Notz, D. (2025). Antarctic coastal polynyas in the global climate system. *Nature Reviews Earth & Environment*, 6(2):126–139.

[Griffies, 2004] Griffies, S. M. (2004). *Fundamentals of Ocean Climate Models*. Princeton University Press.

[Griffies and Adcroft, 2008] Griffies, S. M. and Adcroft, A. J. (2008). Formulating the equations of ocean models. In Hecht, M. W. and Hasumi, H., editors, *Geophysical Monograph Series*, volume 177, pages 281–317. American Geophysical Union, Washington, D. C.

[Grosfeld et al., 1997] Grosfeld, K., Gerdes, R., and Determann, J. (1997). Thermohaline circulation and interaction between ice shelf cavities and the adjacent open ocean. *Journal of Geophysical Research: Oceans*, 102(C7):15595–15610.

[Gudmundsson et al., 2019] Gudmundsson, G. H., Paolo, F. S., Adusumilli, S., and Fricker, H. A. (2019). Instantaneous Antarctic ice sheet mass loss driven by thinning ice shelves. *Geophysical Research Letters*, 46(23):13903–13909.

[Gülk et al., 2024] Gülk, B., Roquet, F., Naveira Garabato, A. C., Bourdallé-Badie, R., Madec, G., and Giordani, H. (2024). Impacts of Vertical Convective Mixing Schemes and Freshwater Forcing on the 2016–2017 Maud Rise Polynya Openings in a Regional Ocean Simulation. *Journal of Advances in Modeling Earth Systems*, 16(5):e2023MS004106.

[Hadamard, 1898] Hadamard (1898). Les surfaces à courbures opposées et leurs lignes géodésiques. *Journal de Mathématiques Pures et Appliquées*, 4:27–73.

[Haid and Timmermann, 2013] Haid, V. and Timmermann, R. (2013). Simulated heat flux and sea ice production at coastal polynyas in the southwestern Weddell Sea. *Journal of Geophysical Research: Oceans*, 118(5):2640–2652.

[Haid et al., 2023] Haid, V., Timmermann, R., Gürses, O., and Hellmer, H. H. (2023). On the drivers of regime shifts in the Antarctic marginal seas, exemplified by the Weddell Sea. *Ocean Science*, 19(6):1529–1544.

[Haigh et al., 2026] Haigh, M., Holland, P. R., Harrison, T. C., and Dutrieux, P. (2026). Wind-Driven Coastal Polynya Variability Drives Decadal Ice-Shelf Melt Variability in the Amundsen Sea. *Geophysical Research Letters*, 53(2):e2025GL118546.

[Haine and Williams, 2002] Haine, T. W. N. and Williams, P. D. (2002). The role of nonhydrostatic dynamics in controlling development of a surface ocean front. *Ocean Modelling*, 4(2):121–135.

[Hattermann et al., 2021] Hattermann, T., Nicholls, K. W., Hellmer, H. H., Davis, P. E. D., Janout, M. A., Østerhus, S., Schlosser, E., Rohardt, G., and Kanzow, T. (2021). Observed interannual changes beneath Filchner-Ronne Ice Shelf linked to large-scale atmospheric circulation. *Nature Communications*, 12(1):2961.

[Hazel and Stewart, 2020] Hazel, J. E. and Stewart, A. L. (2020). Bistability of the Filchner-Ronne Ice Shelf Cavity Circulation and Basal Melt. *Journal of Geophysical Research: Oceans*, 125(4):e2019JC015848.

[Held, 2005] Held, I. M. (2005). The Gap between Simulation and Understanding in Climate Modeling. *Bulletin of the American Meteorological Society*, 86(11):1609–1614.

[Hellmer et al., 2012] Hellmer, H. H., Kauker, F., Timmermann, R., Determann, J., and Rae, J. (2012). Twenty-first-century warming of a large Antarctic ice-shelf cavity by a redirected coastal current. *Nature*, 485(7397):225–228.

[Hellmer et al., 2017] Hellmer, H. H., Kauker, F., Timmermann, R., and Hattermann, T. (2017). The Fate of the Southern Weddell Sea Continental Shelf in a Warming Climate. *Journal of Climate*, 30(12):4337–4350.

[Herman et al., 2020] Herman, A., Dojczman, M., and Świszcz, K. (2020). High-resolution simulations of interactions between surface ocean dynamics and frazil ice. *The Cryosphere*, 14(11):3707–3729.

[Herrmann et al., 2008] Herrmann, M., Somot, S., Sevault, F., Estournel, C., and Déqué, M. (2008). Modeling the deep convection in the northwestern Mediterranean Sea using an eddy-permitting and an eddy-resolving model: Case study of winter 1986–1987. *Journal of Geophysical Research: Oceans*, 113(C4).

[Hewitt, 2020] Hewitt, I. J. (2020). Subglacial Plumes. *Annual Review of Fluid Mechanics*, 52(1):145–169.

[Hirano et al., 2023] Hirano, D., Tamura, T., Kusahara, K., Fujii, M., Yamazaki, K., Nakayama, Y., Ono, K., Itaki, T., Aoyama, Y., Simizu, D., Mizobata, K., Ohshima, K. I., Nogi, Y., Rintoul, S. R., van Wijk, E., Greenbaum, J. S., Blankenship, D. D., Saito, K., and Aoki, S. (2023). On-shelf circulation of warm water toward the Totten Ice Shelf in East Antarctica. *Nature Communications*, 14(1):4955.

[Hoffman et al., 2024] Hoffman, M. J., Branecky Begeman, C., Asay-Davis, X. S., Comeau, D., Barthel, A., Price, S. F., and Wolfe, J. D. (2024). Ice-shelf freshwater triggers for the Filchner–Ronne Ice Shelf melt tipping point in a global ocean–sea-ice model. *The Cryosphere*, 18(6):2917–2937.

[Holland and Jenkins, 1999] Holland, D. M. and Jenkins, A. (1999). Modeling Thermodynamic Ice–Ocean Interactions at the Base of an Ice Shelf. *Journal of Physical Oceanography*, 29(8):1787–1800.

[Holland, 2017] Holland, P. R. (2017). The Transient Response of Ice Shelf Melting to Ocean Change. *Journal of Physical Oceanography*, 47(8):2101–2114.

[Holland et al., 2008] Holland, P. R., Jenkins, A., and Holland, D. M. (2008). The Response of Ice Shelf Basal Melting to Variations in Ocean Temperature. *Journal of Climate*, 21(11):2558–2572.

[Hunter, 2006] Hunter, J. R. (2006). Specification for Test Models of Ice Shelf Cavities.

[Hyogo et al., 2026] Hyogo, S., Nakayama, Y., Ohshima, K. I., Fujii, M., Onishi, H., Tamura, T., Abe-Ouchi, A., and Aoki, S. (2026). What maintains the deep thermocline off Totten glacier?

[Janout et al., 2021] Janout, M. A., Hellmer, H. H., Hattermann, T., Huhn, O., Sültenfuss, J., Østerhus, S., Stulic, L., Ryan, S., Schröder, M., and Kanzow, T. (2021). FRIS Revisited in 2018: On the Circulation and Water Masses at the Filchner and Ronne Ice Shelves in the Southern Weddell Sea. *Journal of Geophysical Research: Oceans*, 126(6):e2021JC017269.

[Jenkins et al., 2001] Jenkins, A., Hellmer, H. H., and Holland, D. M. (2001). The Role of Meltwater Advection in the Formulation of Conservative Boundary Conditions at an Ice–Ocean Interface. *Journal of Physical Oceanography*, 31(1):285–296.

[Jenkins et al., 2010] Jenkins, A., Nicholls, K. W., and Corr, H. F. J. (2010). Observation and Parameterization of Ablation at the Base of Ronne Ice Shelf, Antarctica. *Journal of Physical Oceanography*, 40(10):2298–2312.

[Jin et al., 2025] Jin, J., Payne, A. J., and Bull, C. Y. S. (2025). Current reversal leads to regime change in the Amery Ice Shelf cavity in the 21st century. *The Cryosphere*, 19(5):1873–1896.

[Jourdain et al., 2017] Jourdain, N. C., Mathiot, P., Merino, N., Durand, G., Le Sommer, J., Spence, P., Dutrieux, P., and Madec, G. (2017). Ocean circulation and sea-ice thinning induced by melting ice shelves in the Amundsen Sea. *Journal of Geophysical Research: Oceans*, 122(3):2550–2573.

[Kashinath et al., 2021] Kashinath, K., Mustafa, M., Albert, A., Wu, J.-L., Jiang, C., Esmaeilzadeh, S., Azizzadenesheli, K., Wang, R., Chattopadhyay, A., Singh, A., Manepalli, A., Chirila, D., Yu, R., Walters, R., White, B., Xiao, H., Tchelepi, H. A., Marcus, P., Anandkumar, A., Hassanzadeh, P., and Prabhat (2021). Physics-informed machine learning: Case studies for weather and climate modelling. *Philosophical Transactions of the Royal Society A: Mathematical, Physical and Engineering Sciences*, 379(2194):20200093.

[Khrulev et al., 2025] Khrulev, C., Aschwanden, A., Bueler, E., Brown, J., Maxwell, D., Albrecht, T., Reese, R., Mengel, M., Martin, M., Winkelmann, R., Zeitz, M., Levermann, A., Feldmann, J., Garbe, J., Haseloff, M., Seguinot, J., Hinck, S., Kleiner, T., Fischer, E., Damsgaard, A., Lingle, C., van Pelt, W., Ziemen, F., Shemonski, N., Mankoff, K., Kennedy, J., Blum, K., Habermann, M., DellaGiustina, D., Hock, R., Kreuzer, M., Degregori, E., and Schoell, S. (2025). Parallel ice sheet model (PISM). Zenodo.

[Kirtman et al., 2014] Kirtman, B., Power, S. B., Adedoyin, A. J., Boer, G. J., Bojariu, R., Camilloni, I., Doblas-Reyes, F., Fiore, A. M., Kimoto, M., Meehl, G., Prather, M., Sarr, A., Schar, C., Sutton, R., van Oldenborgh, G. J., Vecchi, G., Wang, H.-J., Bindoff, N. L., Cameron-Smith, P., Chikamoto, Y., Clifton, O., Corti, S., Durack, P. J., Fichefet, T., Garcia-Serrano, J., Ginoux, P., Gray, L., Guemas, V., Hawkins, E., Holland, M., Holmes, C., Infanti, J., Ishii, M., Jacob, D., John, J., Klimont, Z., Knutson, T., Krinner, G., Lawrence, D., Lu, J., Murphy, D., Naik, V., Robock, A., Rodrigues, L., Sedlacek, J., Slater, A., Smith, D., Stevenson, D. S., van den Hurk, B., van Noije, T., Vavrus, S., Voulgarakis, A., Weisheimer, A., Wild, O., Woollings, T., and Young, P. (2014). *Near-Term Climate Change: Projections and Predictability*, volume 9781107057999.

[Kreuzer et al., 2021] Kreuzer, M., Reese, R., Huiskamp, W. N., Petri, S., Albrecht, T., Feulner, G., and Winkelmann, R. (2021). Coupling framework (1.0) for the PISM (1.1.4) ice sheet model and the MOM5 (5.1.0) ocean model via the PICO ice shelf cavity model in an Antarctic domain. *Geoscientific Model Development*, 14(6):3697–3714.

[Kulessa et al., 2014] Kulessa, B., Jansen, D., Luckman, A. J., King, E. C., and Sammonds, P. R. (2014). Marine ice regulates the future stability of a large Antarctic ice shelf. *Nature Communications*, 5(1):3707.

[Kusahara et al., 2010] Kusahara, K., Hasumi, H., and Tamura, T. (2010). Modeling sea ice production and dense shelf water formation in coastal polynyas around East Antarctica. *Journal of Geophysical Research: Oceans*, 115(C10):2010JC006133.

[Lanham et al., 2025] Lanham, J., Mazloff, M., Naveira Garabato, A. C., Siegert, M., and Mashayek, A. (2025). Seasonal regimes of warm Circumpolar Deep Water intrusion toward Antarctic ice shelves. *Communications Earth & Environment*, 6(1):168.

[Lapeyre, 2017] Lapeyre, G. (2017). Surface Quasi-Geostrophy. *Fluids*, 2(1).

[Lazeroms et al., 2018] Lazeroms, W. M. J., Jenkins, A., Gudmundsson, G. H., and van de Wal, R. S. W. (2018). Modelling present-day basal melt rates for Antarctic ice shelves using a parametrization of buoyant meltwater plumes. *The Cryosphere*, 12(1):49–70.

[Legay et al., 2025] Legay, A., Deremble, B., and Burchard, H. (2025). Derivation and Implementation of a Non-Local Term to Improve the Oceanic Convection Representation Within the k–epsilon Parameterization. *Journal of Advances in Modeling Earth Systems*, 17(1):e2024MS004243.

[Lenton et al., 2008] Lenton, T. M., Held, H., Kriegler, E., Hall, J. W., Lucht, W., Rahmstorf, S., and Schellnhuber, H. J. (2008). Tipping elements in the Earth's climate system. *Proceedings of the National Academy of Sciences*, 105(6):1786–1793.

[Li et al., 2023] Li, T., Dawson, G. J., Chuter, S. J., and Bamber, J. L. (2023). Grounding line retreat and tide-modulated ocean channels at Moscow University and Totten Glacier ice shelves, East Antarctica. *The Cryosphere*, 17(2):1003–1022.

[Lilly, 1966] Lilly, D. K. (1966). On the Instability of Ekman Boundary Flow. *Journal of the Atmospheric Sciences*, 23(5):481–494.

[Lorenz, 1963] Lorenz, E. N. (1963). Deterministic Nonperiodic Flow. *Journal of the Atmospheric Sciences*, 20(2):130–141.

[Losch, 2008] Losch, M. (2008). Modeling ice shelf cavities in a z coordinate ocean general circulation model. *Journal of Geophysical Research: Oceans*, 113(C8).

[Madec et al., 2024] Madec, G., Bell, M., Benshila, R., Blaker, A., Boudrallé-Badie, R., Bricaud, C., Bruciaferri, D., Carneiro, D., Castrillo, M., Calvert, D., Chanut, J., Clementi, E., Coward, A., de Lavergne, C., Dobricic, S., Epicoco, I., Éthé, C., Fiedler, E., Ford, D., Furner, R., Ganderton, J., Graham, T., Harle, J., Hutchinson, K., Iovino, D., King, R., Lea, D., Levy, C., Lovato, T., Maisonnave, E., Mak, J., Sanchez, J. M. C., Martin, M., Martin, N., Martins, D., Masson, S., Mathiot, P., Mele, F., Mocavero, S., Moulin, A., Müller, S., Nurser, G., Oddo, P., Paronuzzi, S., Paul, J., Peltier, M., Person, R., Rousset, C., Rynders, S., Samson, G., Schroeder, D., Storkey, D., Storto, A., Téchené, S., Vancoppenolle, M., and Wilson, C. (2024). NEMO ocean engine reference manual.

[Manabe and Wetherald, 1967] Manabe, S. and Wetherald, R. T. (1967). Thermal Equilibrium of the Atmosphere with a Given Distribution of Relative Humidity. *Journal of the Atmospheric Sciences*, 24(3):241–259.

[Marino et al., 2026] Marino, T., Byrne, M. P., and Herbert, C. (2026). Climate Impacts of Forced Equatorial Superrotation in an Idealized GCM. *Journal of Climate*, 39(4):1119–1136.

[Mascolo et al., 2025] Mascolo, V., Lovo, A., Herbert, C., and Bouchet, F. (2025). Gaussian Framework and Optimal Projection of Weather Fields for Prediction of Extreme Events. *Journal of Advances in Modeling Earth Systems*, 17(6):e2024MS004487.

[Masson-Delmotte et al., 2021] Masson-Delmotte, V., Zhai, P., Pirani, A., Connors, S. L., Péan, C., Berger, S., Caud, N., Chen, Y., Goldfarb, L., Gomis, M. I., Huang, M., Leitzell, K., Lonnoy, E., Matthews, J. B. R., Maycock, T. K., Waterfield, T., Yelekci, O., Yu, R., and Zhou, B., editors (2021). *Climate Change 2021: The Physical Science Basis. Contribution of Working Group I to the Sixth Assessment Report of the Intergovernmental Panel on Climate Change*. Cambridge University Press, Cambridge, United Kingdom and New York, NY, USA.

[Mathiot et al., 2017] Mathiot, P., Jenkins, A., Harris, C., and Madec, G. (2017). Explicit representation and parametrised impacts of under ice shelf seas in the z star coordinate ocean model NEMO 3.6. *Geoscientific Model Development*, 10(7):2849–2874.

[Mathiot and Jourdain, 2023] Mathiot, P. and Jourdain, N. C. (2023). Southern Ocean warming and Antarctic ice shelf melting in conditions plausible by late 23rd century in a high-end scenario. *Ocean Science*, 19(6):1595–1615.

[Mathiot et al., 2026] Mathiot, P., Jourdain, N. C., Urruty, B., Gillet-Chaulet, F., Gagliardini, O., and Durand, G. (2026). Transition to a much warmer climate for the global ocean and Antarctic Ice Sheet coupled system, and its reversibility.

[Menthon et al., 2025] Menthon, M., Bakker, P., Quiquet, A., Roche, D. M., and Reese, R. (2025). Comparison of calibration methods of a PICO basal ice shelf melt module implemented in the GRISLI v2.0 ice sheet model. *EGUsphere*, pages 1–36.

[Meredith, 2022] Meredith, M. P. (2022). Carbon storage shifts around Antarctica. *Nature Communications*, 13(1):3400.

[Miles et al., 2016] Miles, T., Lee, S. H., Wåhlin, A., Ha, H. K., Kim, T. W., Assmann, K. M., and Schofield, O. (2016). Glider observations of the dotson ice shelf outflow. *Deep Sea Research Part II: Topical Studies in Oceanography*, 123:16–29.

[Mkhinini et al., 2013] Mkhinini, N., Dubos, T., and Drobinski, P. (2013). Secondary instability of the stably stratified Ekman layer. *Journal of Fluid Mechanics*, 728:29–57.

[Moorman et al., 2020] Moorman, R., Morrison, A. K., and Hogg, A. M. (2020). Thermal Responses to Antarctic Ice Shelf Melt in an Eddy-Rich Global Ocean–Sea Ice Model. *Journal of Climate*, 33(15):6599–6620.

[Moorman et al., 2023] Moorman, R., Thompson, A. F., and Wilson, E. A. (2023). Coastal Polynyas Enable Transitions Between High and Low West Antarctic Ice Shelf Melt Rates. *Geophysical Research Letters*, 50(16):e2023GL104724.

[Mora et al., 2017] Mora, C., Dousset, B., Caldwell, I. R., Powell, F. E., Geronimo, R. C., Bielecki, C. R., Counsell, C. W. W., Dietrich, B. S., Johnston, E. T., Louis, L. V., Lucas, M. P., McKenzie, M. M., Shea, A. G., Tseng, H., Giambelluca, T. W., Leon, L. R., Hawkins, E., and Trauernicht, C. (2017). Global risk of deadly heat. *Nature Climate Change*, 7(7):501–506.

[Munk, 1950] Munk, W. H. (1950). ON THE WIND-DRIVEN OCEAN CIRCULATION. *Journal of the Atmospheric Sciences*, 7(2):80–93.

[Nakata et al., 2021] Nakata, K., Ohshima, K. I., and Nihashi, S. (2021). Mapping of Active Frazil for Antarctic Coastal Polynyas, With an Estimation of Sea-Ice Production. *Geophysical Research Letters*, 48(6):e2020GL091353.

[Narayanan et al., 2023] Narayanan, A., Gille, S. T., Mazloff, M. R., du Plessis, M. D., Murali, K., and Roquet, F. (2023). Zonal Distribution of Circumpolar Deep Water Transformation Rates and Its Relation to Heat Content on Antarctic Shelves. *Journal of Geophysical Research: Oceans*, 128(6):e2022JC019310.

[Narayanan et al., 2024] Narayanan, A., Roquet, F., Gille, S. T., Gülk, B., Mazloff, M. R., Silvano, A., and Naveira Garabato, A. C. (2024). Ekman-driven salt transport as a key mechanism for open-ocean polynya formation at Maud Rise. *Science Advances*, 10(18):eadj0777.

[Naughten et al., 2021] Naughten, K. A., De Rydt, J., Rosier, S. H. R., Jenkins, A., Holland, P. R., and Ridley, J. K. (2021). Two-timescale response of a large Antarctic ice shelf to climate change. *Nature Communications*, 12(1):1991.

[Naughten et al., 2019] Naughten, K. A., Jenkins, A., Holland, P. R., Mugford, R. I., Nicholls, K. W., and Munday, D. R. (2019). Modeling the Influence of the Weddell Polynya on the Filchner–Ronne Ice Shelf Cavity. *Journal of Climate*, 32(16):5289–5303.

[Naughten et al., 2026] Naughten, K. A., Mitcham, T., Smith, R., Holland, P. R., Liddicoat, S. K., Jones, C., and Payne, A. J. (2026). Limiting global warming can prevent tipping points beneath Antarctica's two largest ice shelves.

[Noel et al., 2025] Noel, M., Masson, S., and Rousset, C. (2025). Atmospheric Response to Antarctic Coastal Polynyas. *Journal of Geophysical Research: Atmospheres*, 130(14):e2025JD043319.

[Nøst et al., 2011] Nøst, O. A., Biuw, M., Tverberg, V., Lydersen, C., Hattermann, T., Zhou, Q., Smedsrud, L. H., and Kovacs, K. M. (2011). Eddy overturning of the Antarctic Slope Front controls glacial melting in the Eastern Weddell Sea. *Journal of Geophysical Research: Oceans*, 116(C11).

[Ohshima et al., 2022] Ohshima, K. I., Fukamachi, Y., Ito, M., Nakata, K., Simizu, D., Ono, K., Nomura, D., Hashida, G., and Tamura, T. (2022). Dominant frazil ice production in the Cape Darnley polynya leading to Antarctic Bottom Water formation. *Science Advances*, 8(42):eadc9174.

[Olbers and Hellmer, 2010] Olbers, D. and Hellmer, H. (2010). A box model of circulation and melting in ice shelf caverns. *Ocean Dynamics*, 60(1):141–153.

[O'Connor et al., 2025] O'Connor, G. K., Nakayama, Y., Steig, E. J., Armour, K. C., Thompson, L., Hyogo, S., Berdahl, M., and Shimada, T. (2025). Enhanced West Antarctic ice loss triggered by polynya response to meridional winds. *Nature Geoscience*, 18(9):840–847.

[Paolo et al., 2015] Paolo, F. S., Fricker, H. A., and Padman, L. (2015). Volume loss from Antarctic ice shelves is accelerating. *Science*, 348(6232):327–331.

[Patmore et al., 2023] Patmore, R. D., Holland, P. R., Vreugdenhil, C. A., Jenkins, A., and Taylor, J. R. (2023). Turbulence in the Ice Shelf–Ocean Boundary Current and Its Sensitivity to Model Resolution. *Journal of Physical Oceanography*, 53(2):613–633.

[Poincaré, 1890] Poincaré, H. (1890). Sur le problème des trois corps et les Équations de la dynamique. *Acta mathematica*, 13(1):A3–A270.

[Poinelli et al., 2025] Poinelli, M., Siegelman, L., Nakayama, Y., Rignot, E., Seroussi, H., Fenty, I., and Larour, E. (2025). Small-Scale, High-Frequency Ice, and Ocean Processes in the Amundsen Sea Embayment, West Antarctica. *Journal of Advances in Modeling Earth Systems*, 17(11):e2025MS005098.

[Rahmstorf, 2024] Rahmstorf, S. (2024). FEATURE ARTICLE • Is the Atlantic Overturning Circulation Approaching a Tipping Point? *Oceanography*, 37(3):16–29.

[Rahmstorf et al., 2005] Rahmstorf, S., Crucifix, M., Ganopolski, A., Goosse, H., Kamenkovich, I., Knutti, R., Lohmann, G., Marsh, R., Mysak, L. A., Wang, Z., and Weaver, A. J. (2005). Thermohaline circulation hysteresis: A model intercomparison. *Geophysical Research Letters*, 32(23).

[Reese et al., 2018] Reese, R., Albrecht, T., Mengel, M., Asay-Davis, X., and Winkelmann, R. (2018). Antarctic sub-shelf melt rates via PICO. *The Cryosphere*, 12(6):1969–1985.

[Reese et al., 2026] Reese, R., Rydt, J. D., and Naughten, K. A. (2026). Ice-Sheet–Ocean Interactions and the Reversibility of a Regime Shift Beneath Filchner-Ronne Ice Shelf. *Journal of Geophysical Research: Oceans*, 131(6):e2025JC023952.

[Rignot et al., 2013] Rignot, E., Jacobs, S., Mouginot, J., and Scheuchl, B. (2013). Ice-Shelf Melting Around Antarctica. *Science*, 341(6143):266–270.

[Rintoul et al., 2026] Rintoul, S. R., Stewart, A. L., Johnson, G. C., Zhou, S., Foppert, A., Li, Q., Morrison, A. K., Silvano, A., Gunn, K. L., England, M. H., Nihashi, S., and Aoki, S. (2026). Antarctic Bottom Water in a changing climate. *Nature Reviews Earth & Environment*, 7(2):86–102.

[Robel et al., 2019] Robel, A. A., Seroussi, H., and Roe, G. H. (2019). Marine ice sheet instability amplifies and skews uncertainty in projections of future sea-level rise. *Proceedings of the National Academy of Sciences*, 116(30):14887–14892.

[Rosevear et al., 2024] Rosevear, M. G., Gayen, B., Vreugdenhil, C. A., and Galton-Fenzi, B. K. (2024). How Does the Ocean Melt Antarctic Ice Shelves? *Annual Review of Marine Science*.

[Rosier et al., 2021] Rosier, S. H. R., Reese, R., Donges, J. F., De Rydt, J., Gudmundsson, G. H., and Winkelmann, R. (2021). The tipping points and early warning indicators for Pine Island Glacier, West Antarctica. *The Cryosphere*, 15(3):1501–1516.

[Saddier et al., 2026] Saddier, L., Herbert, C., Bull, C. Y. S., and Couston, L.-A. (2026). Irreversible Transitions of the Ocean Circulation in Antarctic Ice-Shelf Cavities. *Geophysical Research Letters*, 53(4):e2025GL118278.

[Sallée et al., 2008] Sallée, J. B., Speer, K., and Morrow, R. (2008). Response of the Antarctic Circumpolar Current to Atmospheric Variability. *Journal of Climate*, 21(12):3020–3039.

[Scheffer et al., 2009] Scheffer, M., Bascompte, J., Brock, W. A., Brovkin, V., Carpenter, S. R., Dakos, V., Held, H., van Nes, E. H., Rietkerk, M., and Sugihara, G. (2009). Early-warning signals for critical transitions. *Nature*, 461(7260):53–59.

[Schmidt et al., 2023] Schmidt, C., Morrison, A. K., and England, M. H. (2023). Wind– and Sea-Ice–Driven Interannual Variability of Antarctic Bottom Water Formation. *Journal of Geophysical Research: Oceans*, 128(6):e2023JC019774.

[Schmidtko et al., 2014] Schmidtko, S., Heywood, K. J., Thompson, A. F., and Aoki, S. (2014). Multidecadal warming of Antarctic waters. *Science*, 346(6214):1227–1231.

[Schoof, 2007] Schoof, C. (2007). Ice sheet grounding line dynamics: Steady states, stability, and hysteresis. *Journal of Geophysical Research: Earth Surface*, 112(F3).

[Si et al., 2023] Si, Y., Stewart, A. L., and Eisenman, I. (2023). Heat transport across the Antarctic Slope Front controlled by cross-slope salinity gradients. *Science Advances*, 9(18):eadd7049.

[Silvano et al., 2023] Silvano, A., Purkey, S., Gordon, A. L., Castagno, P., Stewart, A. L., Rintoul, S. R., Foppert, A., Gunn, K. L., Herraiz-Borreguero, L., Aoki, S., Nakayama, Y., Naveira Garabato, A. C., Spingys, C., Akhoudas, C. H., Sallée, J.-B., de Lavergne, C., Abrahamsen, E. P., Meijers, A. J. S., Meredith, M. P., Zhou, S., Tamura, T., Yamazaki, K., Ohshima, K. I., Falco, P., Budillon, G., Hattermann, T., Janout, M. A., Llanillo, P., Bowen, M. M., Darelius, E., Østerhus, S., Nicholls, K. W., Stevens, C., Fernandez, D., Cimoli, L., Jacobs, S. S., Morrison, A. K., Hogg, A. M., Haumann, F. A., Mashayek, A., Wang, Z., Kerr, R., Williams, G. D., and Lee, W. S. (2023). Observing Antarctic Bottom Water in the Southern Ocean. *Frontiers in Marine Science*, 10.

[Silvano et al., 2016] Silvano, A., Rintoul, S. R., and Herraiz-Borreguero, L. (2016). Ocean-Ice Shelf Interaction in East Antarctica. *Oceanography*, 29(4):130–143.

[Silvano et al., 2018] Silvano, A., Rintoul, S. R., Peña-Molino, B., Hobbs, W. R., Van Wijk, E., Aoki, S., Tamura, T., and Williams, G. D. (2018). Freshening by glacial meltwater enhances melting of ice shelves and reduces formation of Antarctic Bottom Water. *Science Advances*, 4(4):eaap9467.

[Sohail et al., 2020] Sohail, T., Gayen, B., and Hogg, A. M. (2020). The Dynamics of Mixed Layer Deepening during Open-Ocean Convection. *Journal of Physical Oceanography*, 50(6):1625–1641.

[Song et al., 2025] Song, P., Scholz, P., Knorr, G., Sidorenko, D., Timmermann, R., and Lohmann, G. (2025). Regional conditions determine thresholds of accelerated Antarctic basal melt in climate projection. *Nature Climate Change*, pages 1–7.

[Srokosz and Bryden, 2015] Srokosz, M. A. and Bryden, H. L. (2015). Observing the Atlantic Meridional Overturning Circulation yields a decade of inevitable surprises. *Science*, 348(6241):1255575.

[Stewart et al., 2019] Stewart, C. L., Christoffersen, P., Nicholls, K. W., Williams, M. J. M., and Dowdeswell, J. A. (2019). Basal melting of Ross Ice Shelf from solar heat absorption in an ice-front polynya. *Nature Geoscience*, 12(6):435–440.

[Stommel, 1961] Stommel, H. (1961). Thermohaline Convection with Two Stable Regimes of Flow. *Tellus*, 13(2):224–230.

[Stommel, 1989] Stommel, H. (1989). Why We Are Oceanographers. *Oceanography*, 2(2):48–54.

[Suganuma et al., 2025] Suganuma, Y., Itaki, T., Haneda, Y., Kusahara, K., Obase, T., Ishiwa, T., Omori, T., Ikehara, M., McKay, R., Seki, O., Hirano, D., Fujii, M., Kato, Y., Amano, A., Tokuda, Y., Iwatani, H., Suzuki, Y., Hirabayashi, M., Matsuzaki, H., Yamagata, T., Iwai, M., Katsuki, K., Jimenez-Espejo, F. J., Matsui, H., Seike, K., Kawamata, M., Nishida, N., Ito, M., Sugiyama, S., Okuno, J., Sawagaki, T., Abe-Ouchi, A., Aoki, S., and Miura, H. (2025). Antarctic ice-shelf collapse in Holocene driven by meltwater release feedbacks. *Nature Geoscience*, pages 1–8.

[Tamsitt et al., 2021] Tamsitt, V., England, M. H., Rintoul, S. R., and Morrison, AK. (2021). Residence time and transformation of warm Circumpolar Deep Water on the Antarctic continental shelf. *Geophysical Research Letters*, 48(20):e2021GL096092.

[Tamura et al., 2016] Tamura, T., Ohshima, K. I., Fraser, A. D., and Williams, G. D. (2016). Sea ice production variability in Antarctic coastal polynyas. *Journal of Geophysical Research: Oceans*, 121(5):2967–2979.

[Thompson et al., 2018] Thompson, A. F., Stewart, A. L., Spence, P., and Heywood, K. J. (2018). The Antarctic Slope Current in a Changing Climate. *Reviews of Geophysics*, 56(4):741–770.

[Thompson et al., 2020] Thompson, L., Smith, M., Thomson, J., Stammerjohn, S., Ackley, S., and Loose, B. (2020). Frazil ice growth and production during katabatic wind events in the Ross Sea, Antarctica. *The Cryosphere*, 14(10):3329–3347.

[Tinto et al., 2019] Tinto, K. J., Padman, L., Siddoway, C. S., Springer, S. R., Fricker, H. A., Das, I., Caratori Tontini, F., Porter, D. F., Frearson, N. P., Howard, S. L., Siegfried, M. R., Mosbeux, C., Becker, M. K., Bertinato, C., Boghosian, A., Brady, N., Burton, B. L., Chu, W., Cordero, S. I., Dhakal, T., Dong, L., Gustafson, C. D., Keeshin,

S., Locke, C., Lockett, A., O'Brien, G., Spergel, J. J., Starke, S. E., Tankersley, M., Wearing, M. G., and Bell, R. E. (2019). Ross Ice Shelf response to climate driven by the tectonic imprint on seafloor bathymetry. *Nature Geoscience*, 12(6):441–449.

[Trenberth, 2011] Trenberth, K. E. (2011). Changes in precipitation with climate change. *Climate Research*, 47(1/2):123–138.

[Trenberth et al., 2009] Trenberth, K. E., Fasullo, J. T., and Kiehl, J. (2009). Earth's Global Energy Budget. *Bulletin of the American Meteorological Society*, 90(3):311–324.

[Trusel et al., 2015] Trusel, L. D., Frey, K. E., Das, S. B., Karnauskas, K. B., Kuipers Munneke, P., van Meijgaard, E., and van den Broeke, M. R. (2015). Divergent trajectories of Antarctic surface melt under two twenty-first-century climate scenarios. *Nature Geoscience*, 8(12):927–932.

[Ushio and Wakatsuchi, 1993] Ushio, S. and Wakatsuchi, M. (1993). A laboratory study on supercooling and frazil ice production processes in winter coastal polynyas. *Journal of Geophysical Research: Oceans*, 98(C11):20321–20328.

[Vallis, 2017] Vallis, G. K. (2017). *Atmospheric and Oceanic Fluid Dynamics: Fundamentals and Large-Scale Circulation*. Cambridge University Press, Cambridge, 2 edition.

[van Westen and Baatsen, 2025] van Westen, R. M. and Baatsen, M. L. J. (2025). European Temperature Extremes Under Different AMOC Scenarios in the Community Earth System Model. *Geophysical Research Letters*, 52(12):e2025GL114611.

[van Westen et al., 2025] van Westen, R. M., Kliphuis, M., and Dijkstra, H. A. (2025). Collapse of the Atlantic Meridional Overturning Circulation in a Strongly Eddying Ocean-Only Model. *Geophysical Research Letters*, 52(6):e2024GL114532.

[von Schuckmann et al., 2023] von Schuckmann, K., Minière, A., Gues, F., Cuesta-Valero, F. J., Kirchengast, G., Adusumilli, S., Straneo, F., Ablain, M., Allan, R. P., Barker, P. M., Beltrami, H., Blazquez, A., Boyer, T., Cheng, L., Church, J., Desbruyeres, D., Dolman, H., Domingues, C. M., García-García, A., Giglio, D., Gilson, J. E., Gorfer, M., Haimberger, L., Hakuba, M. Z., Hendricks, S., Hosoda, S., Johnson, G. C., Killick, R., King, B., Kolodziejczyk, N., Korosov, A., Krinner, G., Kuusela, M., Landerer, F. W., Langer, M., Lavergne, T., Lawrence, I., Li, Y., Lyman, J., Marti, F., Marzeion, B., Mayer, M., MacDougall, A. H., McDougall, T., Monselesan, D. P., Nitzbon, J., Otosaka, I., Peng, J., Purkey, S., Roemmich, D., Sato, K., Sato, K., Savita, A., Schweiger, A., Shepherd, A., Seneviratne, S. I., Simons, L., Slater, D. A., Slater, T., Steiner, A. K., Suga, T., Szekely, T., Thiery, W., Timmermans, M.-L., Vanderkelen, I., Wjiffels, S. E., Wu, T., and Zemp, M. (2023). Heat stored in the Earth system 1960–2020: Where does the energy go? *Earth System Science Data*, 15(4):1675–1709.

[Vreugdenhil et al., 2022] Vreugdenhil, C. A., Taylor, J. R., Davis, P. E. D., Nicholls, K. W., Holland, P. R., and Jenkins, A. (2022). The Ocean Boundary Layer beneath Larsen C Ice Shelf: Insights from Large-Eddy Simulations with a Near-Wall Model. *Journal of Physical Oceanography*, 52(8):1903–1926.

[Wang et al., 2023] Wang, X., Zhang, Z., Dinniman, M. S., Uotila, P., Li, X., and Zhou, M. (2023). The response of sea ice and high-salinity shelf water in the Ross Ice Shelf Polynya to cyclonic atmosphere circulations. *The Cryosphere*, 17(3):1107–1126.

[Ward and Raphael, 2026] Ward, J. and Raphael, M. N. (2026). Multi-Temporal Influences of Large-Scale Atmospheric Patterns On Antarctic Coastal Polynyas. *EGUsphere*, pages 1–25.

[Weertman, 1974] Weertman, J. (1974). Stability of the Junction of an Ice Sheet and an Ice Shelf. *Journal of Glaciology*, 13(67):3–11.

[Welander, 1982] Welander, P. (1982). A simple heat-salt oscillator. *Dynamics of Atmospheres and Oceans*, 6(4):233–242.

[Wenta and Cassano, 2020] Wenta, M. and Cassano, J. J. (2020). The Atmospheric Boundary Layer and Surface Conditions during Katabatic Wind Events over the Terra Nova Bay Polynya. *Remote Sensing*, 12(24).

[Xu et al., 2023a] Xu, Y., Zhang, W. G., Maksym, T., Ji, R., and Li, Y. (2023a). Stratification Breakdown in Antarctic Coastal Polynyas. Part I: Influence of Physical Factors on the Destratification Time Scale. *Journal of Physical Oceanography*, 53(9):2047–2067.

[Xu et al., 2023b] Xu, Y., Zhang, W. G., Maksym, T., Ji, R., and Li, Y. (2023b). Stratification Breakdown in Antarctic Coastal Polynyas. Part II: Influence of an Ice Tongue and Coastline Geometry. *Journal of Physical Oceanography*, 53(9):2069–2088.

[Xu et al., 2024] Xu, Y., Zhang, W. G., Maksym, T., Ji, R., Li, Y., and Walker, C. (2024). Influence of Physical Factors on Restratification of the Upper Water Column in Antarctic Coastal Polynyas. *Journal of Geophysical Research: Oceans*, 129(3):e2023JC020762.

[Yung et al., 2026] Yung, C. K., Asay-Davis, X. S., Adcroft, A., Bull, C. Y. S., De Rydt, J., Dinniman, M. S., Galton-Fenzi, B. K., Goldberg, D., Gwyther, D. E., Hallberg, R., Harrison, M., Hattermann, T., Holland, D. M., Holland, D., Holland, P. R., Jordan, J. R., Jourdain, N. C., Kusahara, K., Marques, G., Mathiot, P., Menemenlis, D., Morrison, A. K., Nakayama, Y., Sergienko, O., Smith, R. S., Stern, A., Timmermann, R., and Zhou, Q. (2026). Results of the second Ice Shelf–Ocean Model Intercomparison Project (ISOMIP+). *The Cryosphere*, 20(4):2053–2088.

[Zemp et al., 2017] Zemp, D. C., Schleussner, C.-F., Barbosa, H. M. J., Hirota, M., Montade, V., Sampaio, G., Staal, A., Wang-Erlandsson, L., and Rammig, A. (2017). Self-amplified Amazon forest loss due to vegetation-atmosphere feedbacks. *Nature Communications*, 8(1):14681.

[Zhao et al., 2023] Zhao, K. X., Stewart, A. L., McWilliams, J. C., Fenty, I. G., and Rignot, E. J. (2023). Standing Eddies in Glacial Fjords and Their Role in Fjord Circulation and Melt. *Journal of Physical Oceanography*, 53(3):821–840.

[Zhou et al., 2014] Zhou, Q., Hattermann, T., Nøst, O. A., Biuw, M., Kovacs, K. M., and Lydersen, C. (2014). Wind-driven spreading of fresh surface water beneath ice shelves in the Eastern Weddell Sea. *Journal of Geophysical Research: Oceans*, 119(6):3818–3833.

[Zhu et al., 2014] Zhu, J., Demirov, E., Zhang, Y., and Polomska-Harlick, A. (2014). Model simulations of mesoscale eddies and deep convection in the Labrador Sea. *Advances in Atmospheric Sciences*, 31(4):743–754.

[Årthun et al., 2013] Årthun, M., Holland, P. R., Nicholls, K. W., and Feltham, D. L. (2013). Eddy-Driven Exchange between the Open Ocean and a Sub–Ice Shelf Cavity. *Journal of Physical Oceanography*, 43(11):2372–2387.

Abstract:

The response of the Antarctic ice sheet to climate change is one of the main sources of uncertainty in climate projections. It has been losing mass at an increasing rate during the last few decades through increasing discharges of ice and meltwater into the Southern Ocean. Importantly, the discharge of land ice contributes directly to sea-level rise while the meltwater production may impact the global ocean circulation. Antarctic ice shelves, the floating extension of grounded Antarctic glaciers, play a key role in controlling the mass loss of the Antarctic ice sheet. Their fate primarily depends on the properties of the waters intruding ice-shelf cavities, as melt rates at the bottom ice-ocean interface largely exceeds those at the top air-ice boundary. Recent regional numerical studies provide increasing evidence for the possibility of abrupt transitions from cold to warm ocean circulation modes in ice-shelf cavities, which would considerably enhance the basal mass loss of ice shelves. However, a quantitative understanding of the feedback processes is lacking, in part because the high computational cost of realistic simulations prevents a detailed and systematic analysis of the underlying physics. This thesis puts forth two research projects that aim at deciphering the mechanisms underlying abrupt regime transitions in Antarctic ice-shelf cavities, as well as their potential reversibility, in ways that are inaccessible to realistic ocean simulations. Specifically, leveraging a low-dimensional ocean box model and an idealized numerical ocean configuration, this thesis systematically explores the steady-state response of the ocean to changes in far-field ocean and atmospheric conditions, which is needed to characterize the thresholds and the reversibility of the transition. Together, the two approaches allow building a high-level understanding of the key physical processes controlling the nature of the transitions, which is crucial to assess how confident we can be in the projections of Earth System Models. We first develop a low-dimensional box model representing two competing ocean circulation regimes: a warm mode dominated by Circumpolar Deep Water (CDW) intrusion, and a cold mode sustained by Dense Shelf Water (DSW) formed in coastal polynyas, where sea-ice formation induces surface salt fluxes that increase the density of surface waters. The model uncovers bistability over a wide range of sea-ice formation rates and CDW temperatures. Applied to nine Antarctic ice-shelf cavities, it suggests that most of them are in a bistable regime under realistic forcing and thus susceptible to irreversible transitions. This model also demonstrates that the vertical mixing parameterization plays a key role in determining whether transitions are irreversible. Building on these results, we then introduce an idealized three-dimensional numerical configuration of an ice-shelf cavity, using the ocean code NEMO. Consistent with the box-model results, the NEMO simulations exhibit hysteresis and bistability between warm and cold circulation regimes. The simulations further reveal that CDW properties strongly influence whether transitions are reversible or irreversible. They highlight the important role of the large-scale ocean circulation outside of the cavity and the model viscosity, which are two processes that are not explicitly represented in the box model. The sensitivity of steady-state circulations to forcing and model parameters provides some explanations for the different behaviors obtained in previous studies featuring either irreversible or reversible dynamics. We finally investigate the impact of time-dependent forcing and notably assess the influence of the seasonal cycle. We show that the characteristic time scales associated with the cavity overturning and with the thermocline deepening are key to predict whether the system is susceptible to irreversible transitions when subject to one or a few exceptionally mild winters.

Résumé :
La réponse de la calotte glaciaire antarctique au changement climatique est l'une des principales sources d'incertitude dans les projections climatiques. Sa perte de masse s'est accélérée au cours des dernières décennies, avec des flux croissant de glace et d'eau douce se déversant dans l'Océan Austral. Ces apports contribuent à l'élévation du niveau de la mer, mais pourraient également impacter la circulation globale de l'océan. Les plateformes de glace antarctique, qui sont les extensions flottantes des glaciers reposant sur le continent, jouent un rôle clé dans la perte de masse de la calotte antarctique. Leur interface basale avec l'océan est principalement responsable de la fonte de la glace, qui dépend donc fortement des propriétés des eaux pénétrant dans ces cavités sous glaciaires. De récentes modélisations numériques régionales ont montré que des cavités actuellement froides pourraient abruptement basculer vers des conditions plus chaudes, ce qui entraînerait une augmentation considérable de la fonte basale des plateformes de glace. Dans ce contexte, cette thèse étudie les mécanismes à l'origine de telles transitions abruptes, ainsi que leur réversibilité. Les modèles régionaux réalistes sont coûteux numériquement et utilisent des forçages complexes. Cela fait qu'ils sont peu adaptés à l'exploration systématique de la réponse stationnaire de l'océan dans la cavité, pourtant nécessaire pour caractériser les seuils et la réversibilité des transitions. Ce travail adopte donc une approche complémentaire fondée sur des cadres idéalisés, combinant un modèle réduit d'océan « en boîte » et une configuration numérique idéalisée. Ces modèles permettent d'obtenir un haut niveau de compréhension des processus physiques contrôlant la nature des transitions, ce qui est crucial pour évaluer le niveau de confiance associé aux projections des modèles de climat globaux. Nous développons d'abord un modèle réduit « en boîte » représentant deux régimes de circulation en compétition: un mode chaud caractérisé par l'intrusion d'eaux profondes circumpolaires; et un mode froid entretenu par l'intrusion d'eaux denses formées dans les polynies côtières, où la formation de glace de mer induit des flux de sel qui densifient les eaux de surface. Le modèle met en évidence une circulation bistable pour une large gamme de taux de formation de glace de mer et de températures des eaux circumpolaires. Appliqué à neuf cavités antarctiques, il suggère que la plupart d'entre elles se trouvent dans un régime bistable sous des forçages réalistes, les rendant susceptibles à des transitions irréversibles. Ce modèle souligne également que le mélange vertical devant les plateformes de glace joue un rôle clé sur la réversibilité des transitions. Dans la continuité de ces résultats, nous introduisons une configuration numérique idéalisée de cavité sous glaciaire avec le code d'océan NEMO. En accord avec les résultats du modèle réduit, les simulations NEMO reproduisent la bistabilité des modes de circulation de la cavité. En outre, elles montrent aussi l'importance qu'ont la circulation devant la cavité et la viscosité du modèle dans la nature des transitions, qui sont des processus non explicitement représentés dans un modèle en boîtes. Ces résultats donnent ainsi des éléments de réponses vis-à-vis de conclusion divergente dans de précédentes études concernant la réversibilité des transitions. Enfin, nous étudions l'impact de forçages temporels sur le système, notamment afin d'évaluer l'influence du cycle saisonnier. Nous montrons que le temps caractéristique de vidange de la cavité, ainsi que celui associé à la convection profonde sont des paramètres essentiels pour conclure sur la possibilité du système à basculer irréversiblement quand il subit un ou plusieurs hivers exceptionnellement plus doux.

ENS DE LYON

Résumé de thèse

Louis SADDIER

Bistable dynamics of the ocean circulation in Antarctic ice-shelf cavities

Dynamique bistable de la circulation océanique sous les plateformes de glace antarctiques

---

Abstract

Antarctic ice shelves are the floating extensions of the grounded ice sheet. They limit the contribution of Antarctic land ice to sea level rise but may disappear over time due to their melting at their bottom ice-ocean interface. Recent studies have shown that ice-shelf cavities currently cold could abruptly transition toward warm conditions. In this context, this thesis investigates the mechanisms underlying abrupt transitions in ice-shelf cavities, as well as their reversibility. We develop both a simple model with a handful of equations predicting the evolution of large ocean "boxes", and a three-dimensional numerical configuration solving the equations of motion on a relatively high resolution grid. The two models help identify sea-ice formation rates at the ocean surface as drivers of regime changes and demonstrate that reversibility depends on both physical conditions and modelling choices.

Résumé

Les plateformes de glace antarctique sont les extensions flottantes des calottes glaciaires reposant sur le continent. C'est à la base de ces plateformes en contact avec l'océan qu'a lieu la majorité de la fonte de la calotte antarctique. De récentes études ont montré que des cavités sous glaciaires actuellement froides pouvaient abruptement basculer vers des conditions chaudes. Dans ce contexte, cette thèse étudie les mécanismes à l'origine de ces transitions abruptes, ainsi que leur réversibilité. Nous développons parallèlement un modèle réduit d'équations divisant l'océan en « boîtes », ainsi qu'une configuration numérique résolvant les vrais équations du mouvement de l'océan mais dans une cavité simplifiée. Ces deux modèles mettent en évidence que la transition d'un régime à un autre peut être irréversible, et dépend de la formation de glace de mer à la surface de l'océan.

Thèse préparée à l'École normale supérieure de Lyon
École Doctorale N° 52 — PHAST, Physique et Astrophysique